

Electrically Conductive Composite Materials from Carbon Nanotube Decorated Polymer Powder Particles



Dissertation with the aim of achieving a doctoral degree (Dr. rer. nat.)
Faculty of Mathematics, Informatics and Natural Sciences

Department of Chemistry
University of Hamburg

Submitted by

Christian Otto

University of Hamburg

2017

This work was done between May 2013 and August 2016 at the Institute of Polymer Research of Helmholtz-Zentrum Geesthacht under the supervision of Prof. Dr. Volker Abetz.

First Evaluator: Prof. Dr. Volker Abetz

Second Evaluator: Prof. Dr. Gerrit A. Luinstra

Date of Disputation: 14.11.2017

Table of Contents

| | |
|---|----|
| 1. Introduction | 1 |
| 1.1. Motivation | 1 |
| 1.2. Strategy of the Research and Outline of the Thesis | 3 |
| 2. Theoretical Background | 5 |
| 2.1. Fundamentals of Membrane Filtration Processes | 5 |
| 2.2. Polymer Composites Using MWCNT | 17 |
| 2.3. Sintering | 22 |
| 3. Materials | 29 |
| 3.1. Polyetherimide | 29 |
| 3.2. Ultra-High Molecular Weight Polyethylene | 30 |
| 3.3. Polypropylene | 31 |
| 3.4. Decorated Powder Particles | 31 |
| 4. Polymer and Composite Processing | 34 |
| 4.1. Compression Moulding | 34 |
| 4.2. Sintering | 38 |
| 4.2.1. Sintering of PEI and PEI/MWCNT Membranes | 39 |
| 4.2.2. Sintering of UHMWPE and UHMWPE/MWCNT Membranes | 41 |
| 4.2.3. Sintered Rectangular Samples | 43 |
| 5. Polymer and Composite Analysis | 44 |
| 5.1. Thermogravimetric Analysis (TGA) | 44 |
| 5.2. Differential Scanning Calorimetry (DSC) | 44 |
| 5.3. Optical Microscopy | 45 |
| 5.4. Scanning Electron Microscopy (SEM) | 45 |
| 5.5. Rheological Analysis | 45 |
| 5.6. Capillary-Flow Porometry | 48 |
| 5.7. Wet-Dry Method | 50 |

| | | |
|--------|---|-----|
| 5.8. | Water Flux Measurements | 50 |
| 5.9. | Electrical Conductivity Measurements | 51 |
| 5.10. | Conductive Atomic Force Microscopy | 53 |
| 5.11. | Tensile Testing | 54 |
| 6. | Results and Discussion..... | 55 |
| 6.1. | Thermal Analysis | 55 |
| 6.1.1. | Thermogravimetric Analysis..... | 55 |
| 6.1.2. | Differential Scanning Calorimetry | 58 |
| 6.2. | Morphology of Powders..... | 62 |
| 6.2.1. | Polyetherimide | 62 |
| 6.2.2. | Ultra-High Molecular Weight Polyethylene | 68 |
| 6.2.3. | Polypropylene | 73 |
| 6.2.4. | Summary for Morphology of Powders | 74 |
| 6.3. | Rheology of Polymers and Composites | 75 |
| 6.3.1. | Polyetherimide and Composites..... | 76 |
| 6.3.2. | Ultra-High Molecular Weight Polyethylene and Composites | 78 |
| 6.3.3. | Polypropylene and Composites..... | 83 |
| 6.4. | Sintering and Morphology of Sintered Membranes..... | 85 |
| 6.4.1. | Sintering of PEI and PEI/MWCNT Powder | 86 |
| 6.4.2. | Sintering of UHMWPE and UHMWPE/MWCNT Powder..... | 91 |
| 6.4.3. | Sintering of Polyetherimide Membranes | 95 |
| 6.4.4. | Summary for Sintered PEI and PEI/MWCNT Membranes | 107 |
| 6.4.5. | UHMWPE..... | 108 |
| 6.4.6. | Summary for the UHMWPE and UHMWPE/MWCNT membranes | 120 |
| 6.5. | Wet-Dry Method for Determination of Porosity..... | 122 |
| 6.5.1. | Polyetherimide | 122 |
| 6.5.2. | Ultra-High Molecular Weight Polyethylene | 123 |
| 6.6. | Porometry..... | 124 |

| | |
|---|-----|
| 6.6.1. Polyetherimide Membranes | 125 |
| 6.6.2. Ultra-High Molecular Weight Polyethylene Membranes | 127 |
| 6.7. Pure Water Membrane Permeability | 129 |
| 6.7.1. Polyetherimide | 129 |
| 6.7.2. Ultra-High Molecular Weight Polyethylene | 132 |
| 6.8. Electrical Conductivity..... | 134 |
| 6.8.1. Polyetherimide | 134 |
| 6.8.2. Ultra-High Molecular Weight Polyethylene | 140 |
| 6.8.3. Polypropylene | 145 |
| 6.9. Tensile Testing | 146 |
| 6.9.1. Polyetherimide | 146 |
| 6.9.2. Ultra-High Molecular Weight Polyethylene | 152 |
| 7. Summary | 159 |
| 8. Outlook..... | 163 |
| 9. Zusammenfassung..... | 165 |
| 10. Acknowledgements | 169 |
| 11. Appendix | 171 |
| 11.1. Results Tensile Testing | 171 |
| 11.1.1. Polyetherimide | 171 |
| 11.1.2. Ultra-High Molecular Weight Polyethylene | 174 |
| 12. References | 179 |

List of Abbreviations

| Abbreviation | Meaning |
|--------------------------------------|--|
| AFM | Atomic force microscopy |
| BSE | Back-scattered electron (contrast) |
| C-AFM | Conductive atomic force microscopy |
| CCVD | Catalytic chemical vapour deposition |
| CNT | Carbon nanotube |
| CVD | Chemical vapour deposition |
| DSC | Differential scanning calorimetry |
| MWCNT | Multi-walled carbon nanotube |
| PA 12 | Polyamide 12 |
| PE | Polyethylene |
| PEEK | Poly(ether ether ketone) |
| PEI | Polyetherimide |
| PP | Polypropylene |
| PP/MWCNT, PEI/MWCNT, UHMWPE/MWCNT | Respective polymer with added MWCNT |
| SE | Secondary electrons (contrast) |
| SEM | Scanning electron microscopy |
| SLS | Selective laser sintering |
| SWCNT | Single-walled carbon nanotube |
| TGA | Thermogravimetric analysis |
| UHMWPE | Ultra-high molecular weight polyethylene |

1. Introduction

1.1. Motivation

Worldwide, sweet water makes up only around 2.5% of water with most of it is in form of clouds and ice on the polar caps and mountainous regions.^[1] As the growing world population and agriculture are increasing the demand for drinkable water worldwide, membrane filtration processes increase in importance and urgency. Membrane filtration offers high efficiency and filtration performance in the purification of water and general filtration processes of liquids and gases, compared to conventional methods such as distillation and adsorption.^[2] Membranes are widely used in different separation processes such as gas separation, dialysis, reverse osmosis, nanofiltration, ultrafiltration and microfiltration.^[3] Especially ultra- and often in conjunction microfiltration are increasing in importance to filter contaminated water. For example, they remove particles, microbes and parasites.^[4] Microfiltration separates particles, parasites and partially microbes from the water before it flows to the ultrafiltration step. The use of microfiltration before ultrafiltration is one way to reduce the deposition of material on or in the membranes.

Tortuous microfiltration membranes without a defined screen layer act as depth-filters and are widely used in a large variety of applications. For example, they are used in the cold-sterilisation of liquids, particle filtration in liquids and gases, oil droplet filtration and general water purification. Microfiltration membranes can also be used as a foundation for “dynamic membranes”.^[5] Dynamic membranes are alternatively called “second membranes” or “dynamic layer” and are equal to filtration cakes, which deposit on the surface of membranes. In filtrates, where more than one specific particle diameter is present, larger particles tend to settle on the membrane surface and form a cake layer. The filtrate now has to flow between the particles in the cake layer, which preferably form pores smaller than the pores of the membrane. This increases the selectivity of the membrane, while decreasing the permeability. Therefore, highly permeable membranes with relatively large pores for the application are preferred for this method, as they provide a very high base permeability that compensates the decrease through the “dynamic membrane”.

Microfiltration membranes are easily manufactured on large scales through different methods such as phase inversion through temperature or immersion, sintering, bi-axial stretching and chemical etching. A typical microfiltration range is 0.1 – 10 μm .^[3] It is important to note, that this means the size of the separated material, not automatically the pore size. Tortuous

membranes usually have larger surface pores and filter smaller objects than their medium inner pore size, because the long and twisted pore channels capture objects through adsorption or mechanical inhibition. This constricts the diameter of the pore channels, allowing for further capture of following particles. To a certain degree, this is desired, but after a given amount of time, the pores are too constricted to allow for an efficient permeate flow through the membrane. From this point, the pores are becoming increasingly clogged; the membrane performance is decreasing. If a depth-filtration membrane is too saturated with filtered media, the flow of the media out of the membrane is too high for efficient filtration. The general process of material deposition on or in a membrane is called membrane fouling.

A special type of membrane fouling is through living biological material in the form of biofouling.^[6] These are in most cases bacteria and other one-cellular lifeforms. As they share the special property of living beings to reproduce, one bacterium in or on the membrane can quickly multiply through mitosis. This will happen for as long as the bacteria are provided with enough nutrients and proper environmental conditions. This case is true for a great variety of filtration processes, as bacteria are characterised by simplicity, toughness, adaptability and a high survivability under conditions that are deadly for other lifeforms.

In the last years, bacteria have become resistant against more and more antibiotics and other antimicrobial chemicals or materials.^[7, 8] The adaptation of bacteria as a whole was faster than the development or discovery of new effective chemicals and materials. Single-wall carbon nanotubes (SWCNT) were potential anti-microbial additives for liquids, but some microbes were found that adapted to the anti-microbial mechanisms of SWCNT, rendering them less effective.^[8]

So far, microbes were not found to be resistant against sufficiently high electric voltages. In fact, a voltage as low as 3 V can suffice to neutralize a large number of microbes.^[9] Electrically conductive membranes or filtration assemblies with opposed electrodes are also the topic of general anti-fouling research. They were found to be able to be cleaned through electrostatic and electrophoretic repulsion of charged particles in a watery suspension.^[10-12]

The objective of this work is to investigate the processing of the solvent-free sintering of MWCNT-decorated polymer powder particles to produce tortuous microfiltration membranes with an appropriate electrical conductivity that could be potentially used for initially small-scale applications. With the used solvent-free method, no chemical waste is produced during sample preparation, offering a contribution to a reduced amount of chemical waste. As most

organic solvents are toxic, this membrane production method reduces the risk of hazardous exposure. Additionally, the electrical conductivity of compression moulded and sintered plates is analysed to give a reference frame for effectiveness of the sintering process. Samples were strictly prepared in purely thermo-mechanical processes to avoid organic solvents or other chemicals.

1.2. Strategy of the Research and Outline of the Thesis

The production of electrically conductive polymer composites most importantly depends on the distribution of the filler. To achieve good electrical conductivity a maximisation of inter-filler contacts is of highest priority.

The goal of this work was to investigate the use of MWCNT-decorated polymer powder particles as innovative materials with a high potential for large scale production of conductive composite materials with a segregated MWCNT network. The main processing focus was sintering for open-porous structures that could be used as microfiltration membranes. The surface-presence of the MWCNT in the decorated powder already places the MWCNT at a primed location for excellent contact in a segregated network in the finished composite material. Apart from the presence of carbon nanotubes, the decorated powder can generally be handled like common polymer powder, given some safety limitations due to the presence of MWCNT.

To cover a large range of polymer properties, polyetherimide and ultra-high molecular weight polyethylene were chosen for this work. Polyetherimide is an amorphous thermoplastic polymer with high a Young's modulus and is widely used in membrane and other applications. Ultra-high molecular weight polyethylene is a typical semi-crystalline polymer for sintering with excellent elongation at break, ultimate tensile strength and is significantly softer than polyetherimide.

Additional results for polypropylene were also used in this work, extending the results related to rheological and electrical conductivity properties. Part of the work on polypropylene was performed in close cooperation with Mrs. Nina Beckmann during her work on her master thesis. Polypropylene is a semi-crystalline polymer with good ductility, relatively low melt viscosity and excellent processability.

The decorated powder was used to investigate the formation of a segregated MWCNT network to achieve a distribution for high electrical conductivity values. Because of this, it was assumed that minimal deformation of pressed-together powder particles should lead to the highest

conductivity values. This assumption was investigated through two of the most common solvent-free methods: Sintering and compression moulding. Sintering was performed without external pressure and represents the processing method with the least amount of shear flow of the polymer matrix. Compression moulding was performed in the typical way for flash-type moulds, with a melting phase and a compression phase under externally applied uniaxial pressure.

Different processing methods can result in different melt flow, material deformation and ultimately different morphologies of an identical polymer. A strong characteristic of polymers is their modifiability through processing. As such, the MWCNT were also exposed to varying amounts of general deformation and especially shear forces, which are intrinsic to the sintering and compression moulding processes.

As is known from the literature, comparable concentrations of CNT can lead to significant differences in electrical conductivity, depending on the chosen polymer as the matrix.^[13] As will be discussed in this work, notable differences caused by the processing method for the materials were found, corresponding to their intrinsic properties.

The comparison of the achieved electrical conductivity values together with the morphology in this work will give a significant insight into the effectiveness of the MWCNT decorated powder particles.

The main focus of this work was the pressureless and solvent-free sintering of electrically conductive membranes, with the set goal to achieve open-porous structures that can be seen as microfiltration membranes with comparable properties to what can be expected in comparison to commercially available types. The addition of compression moulding was chosen to acquire further insight into the influence of the processing on the formation of the expected MWCNT network and therefore the electrical conductivity of the material.

Samples were separated into membranes and compression moulded samples. Analysis was chosen accordingly and directly compared where possible.

2. Theoretical Background

2.1. Fundamentals of Membrane Filtration Processes

Liquid phase separation membranes most commonly filter particles, droplets (non-miscible liquid) or generally colloids down to a certain size from a liquid. A membrane is a type of filter that operates at filtration sizes below 10 μm . In liquid phase separation, membranes are usually categorised as microfiltration, ultrafiltration, nanofiltration or reverse osmosis membranes. Microfiltration membranes operate between 10 μm and 0.1 μm .^[3] In porous membranes, the separation is done through the name-giving pores that separate the particles or other colloids through a geometric size selection (see **Figure 1**). The size and geometry of the pore decides what can pass through it. Liquid phase separation is most commonly performed in two methods: Dead-end filtration and cross-flow filtration.^[3, 14]

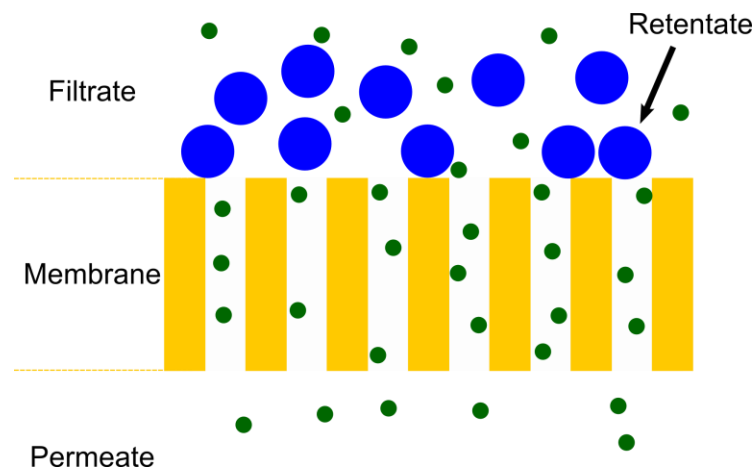


Figure 1: General principle of the filtration process of a porous membrane with a separation layer. The membrane pore size limits the size of the particles that can pass through it.

Matter that is small enough to pass through the porous structure passes through the membrane as permeate. Anything that is too large to pass through the pores is deposited on the membrane as retentate and can form a filtration cake. This is the most common type of membrane selectivity for porous membranes, which is called size selectivity.^[3] The formed filtration cake on top is compacted with more deposited material over time due to its initial looseness and the applied pressure. As the filtration cake grows denser and thicker, water flow through the filtration cake becomes increasingly more difficult.

The flow rate through a formed filtration cake can be described by Darcy's law (in varying forms) for viscous flows through a porous medium, when the flow rate is low enough for laminar flow ^[15-18]:

$$\frac{\dot{V}}{A} = \frac{\kappa \cdot \Delta p}{\eta \cdot d} \Leftrightarrow \kappa = \frac{\dot{V} \cdot \eta \cdot d}{A \cdot \Delta p} \quad (1)$$

Darcy's law connects the volumetric flow rate \dot{V} per permeable area A with the permeability κ of the porous medium (here the filtration cake), the pressure difference across the membrane Δp , the viscosity of the liquid phase η and the thickness of the porous medium or here the filtration cake d .

For the characterisation of porous membranes for liquid phase separation, a simple experiment is the measurement of the volumetric flow rate of a liquid through a membrane.

$$\dot{V} = \frac{dV}{dt} \quad (2)$$

The volumetric flow rate value is directly dependent on the specifically used set-up. A membrane with a larger diameter will allow for a larger flow rate. To allow for a comparison of different membranes with each other, the water flux value is more beneficial. The water flux is the volumetric flow rate, divided by the permeable surface area of the membranes.^[3]

$$J = \frac{\dot{V}}{A} = \frac{1}{A} \cdot \frac{dV}{dt} \quad (3)$$

The water flux value is often called J given in the unit $\text{L h}^{-1} \text{m}^{-2}$ and is directly dependent on the transmembrane pressure as the main driving force behind most common filtration processes. Therefore the used transmembrane pressure has to be given for a measured water flux value to allow for a proper comparison with other membranes. Through measuring a water flux curve for a set amount of time or number of filtration cycles, changes in the filtration system can be monitored. This includes potential swelling of the membrane, fouling, membrane damage, etc.

In dead-end filtration, the filtrate is driven towards the membrane (see **Figure 2**), while in cross-flow filtration, the filtrate is driven across the membrane (see **Figure 3**).^[3, 14, 19] For dead-end filtration, the particles or colloids in the filtrate are directly deposited on the membrane and held there by the pressure gradient. This is a simple approach that requires relatively small amount of components and can be easily used in systems as small as a handheld syringe. The fast and continuous fouling of the membrane leads to an equally fast loss of permeate flow.

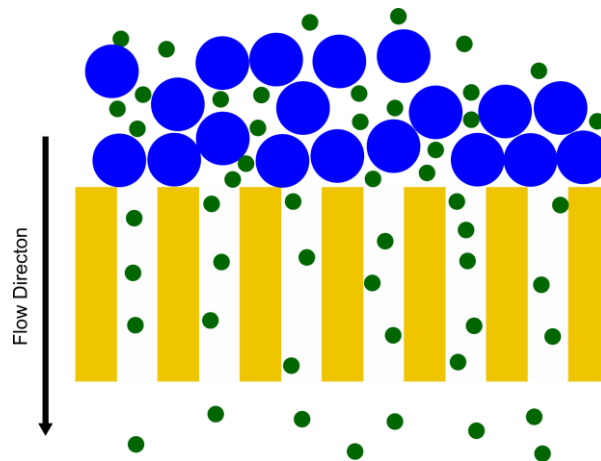


Figure 2: Schematic of the dead-end filtration process. The filtrate is driven towards the membrane. The permeate can pass through the membrane, while particles that are too large remain pressed against the membrane and form a filtration cake.

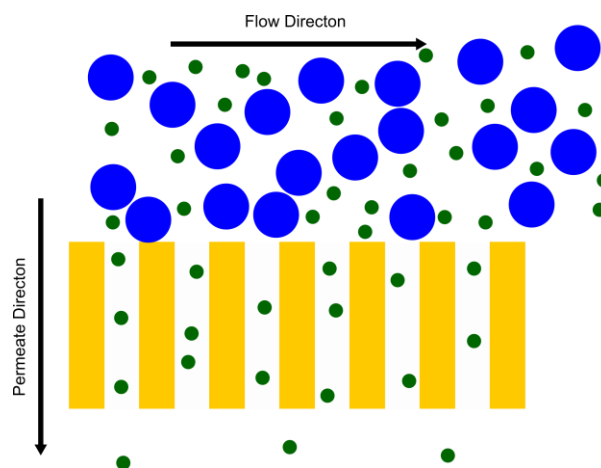


Figure 3: Schematic of the cross-flow process. The filtrate is driven across the membrane in a circular flow. Part of the permeate pass through the membrane, while the rest flows with the rest of the filtrate.

Due to this, dead-end filtration is efficient for filtrates with up to typically around 0.1 wt% concentration of particles or colloids.^[3] With higher concentrations, the performance loss of the membrane is too fast to be efficient. For concentrations up to typically around 0.5 wt% cross-flow filtration is predominantly used.^[3] As the filtrate is forced across the membrane, it can carry along the particles or colloids and significantly hinder the formation of a dense filtration cake. To enhance this effect, the set-up is controlled in such a way to induce turbulent flow of the filtrate. Over time, the concentration in the filtrate increases. At a certain increased concentration, the retentate is disposed off and a fresh volume of filtrate is introduced into the filtration system.^[3, 14, 19] Therefore cross-flow filtration can handle higher concentrations in the filtrate, but requires a more complex system with higher base costs.

Given enough time, a large quantity of permeate can be collected and if the filtrate has a finite volume, a relatively low amount of liquid is left in the filtration cake. In a purification process, this is not of importance because the permeate is collected. A collection process of the retentate, for example a synthesized product in a suspension, is made easier with an as small as possible amount of retained liquid, as this will speed up a following drying step.

The filtration cake can be seen in completely different perspectives, depending on the type of process. In a collection process, the filtration cake formation is the desired goal. In a purification step, the filtration cake is seen as membrane fouling that decreases the performance of the overall filtration process with increasing thickness of the cake.

Membrane fouling for porous membranes is defined as the deposition of particles or colloids on a membrane surface or inside the porous structure of the membrane, leading to a decreased overall permeate flow and decrease in membrane performance.^[3] The decrease in permeate flow happens by increasing the hydraulic resistance through partial or complete pore blocking and/or filtration cake formation. The pore blocking can happen either directly “on top” of the pore or through gradual deposition of matter on the inner walls of the pore channel, until it is severely constricted or fully blocked. Membranes with a distinct separation layer on the top surface to the filtrate side predominantly foul through cake formation and pore blocking on top. Membranes, such as sintered ones, are depth filters and are predominantly fouled by internal pore blocking and cake formation. Surface fouling and internal fouling can occur for both membrane types, but with different distinctiveness. The biggest difference between both fouling types is that surface fouling can be reversed through cleaning techniques, while internal fouling for screen filters is irreversible or only partially reversible.^[3]

Filtration cake formation is a pronounced property of porous membranes with a separation layer. These types of membranes are also called “screen filters”.^[3] Ideally, the separation layer with its small enough pores holds back the appropriate larger particles, while the spongy support layer remains free from fouling. Another type of filters is a “depth filter”. Here, the pore size usually is larger than at least a part of the particles and there is no distinct separation layer. An illustrative comparison of the filter structures is shown in **Figure 4**.

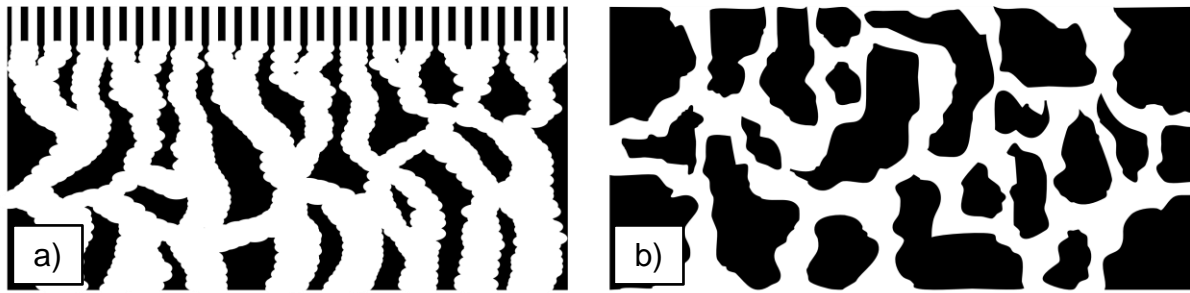


Figure 4: Schematic comparison between membranes with a distinct separation layer (a) and a tortuous membrane (b). Membranes with a separation layer usually have a spongy structure underneath with larger pores and a more tortuous structure. The illustrations are not to scale. Depth filters usually have much larger pore channels than separation layer membranes.

No type is intrinsically better than the other, but each has their own properties that make them effective for different purposes. While separation layer membranes excel at size selection and therefore separation performance, filtration cake formation can quickly lead to a large loss in permeate flow rate. Depth filters do not have a distinct separation layer, but rather filter through their whole porous and often tortuous volume. The pore channel diameters can be larger than the particle which they filter out, but through the channel geometry have a chance per length segment to trap a particle inside. This can happen through simple sieving by geometric blocking of the particle or through adsorption on the filter walls. The adsorption on the filter walls can happen, for example, through electrostatic attraction. The classical size sieving can be the smallest contributor of the filtration process in depth filters, because especially the smaller particles are prone to adsorption on the filter walls. This can lead to the effect, that the largest and the smallest fractions in the filtrate show the highest filtration performance, while medium sized particles are the most likely to pass through the depth filter.^[3] A depth filter can either be a classical filter such as sand columns or a microfiltration membrane.^[3]

Both screen-filters and depth filters can be symmetric or asymmetric filters. A symmetric filter possesses approximately the same morphology over the whole membrane volume. An asymmetric filter shows a distinct change in morphology typically with in the depth of the filter volume. Screen-filters generally benefit from an increased pore channels size and connectedness past the filtering screen, as this lowers the hydraulic resistance of the filter.

The main advantage of a depth filter is that they can tolerate a significantly larger amount of inner fouling before the permeate flow becomes too low to be feasible. On the other hand, they are not perfect filters, so a part of the permeate can still contain to be filtered particles. Additionally, when the depth filter is too highly loaded with particles, the rate of particles breaking free from the filter and contaminating the permeate increases.

An illustration for the different filtration mechanisms of screen filters compared to depth filters is shown in **Figure 5**. For better comparison, the identical particle shapes are used for both sides. This illustrates that screen filters are not efficient for applications with large particle or colloid concentrations, while depth filters do not have the same high selectivity performance as screen filters.

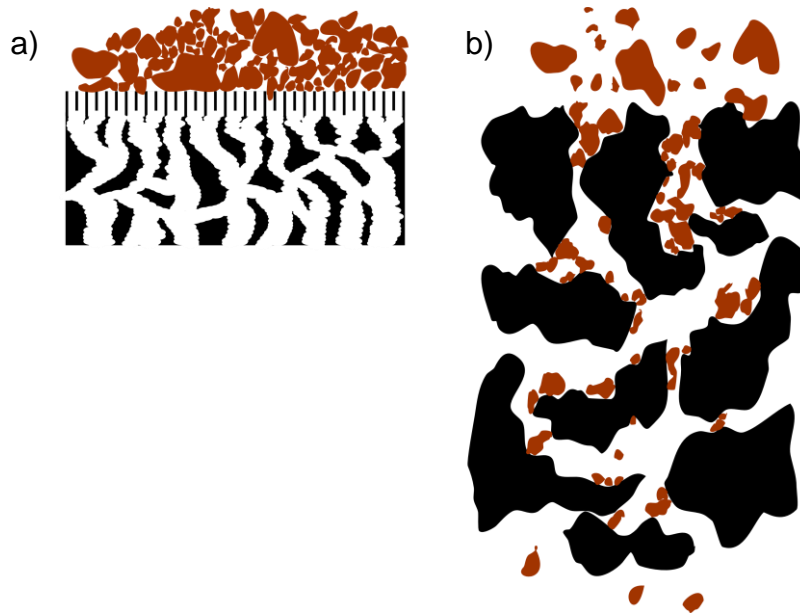


Figure 5: Comparison of the working principle and fouling mechanisms between an asymmetric membrane with (a) a distinct separation layer (b) and a symmetric tortuous depth filtration membrane.

The formation of a filtration cake can also be deliberately initiated by filtering a coating suspension with a permeable liquid and particles of a desired diameter.^[20] Alternatively, the formation of a cake layer through the filtrate can be planned and used for increases in permeability.^[20] Here the particles form a filtration cake with pore channels sufficient for the actual filtration process. This filtration cake now acts as a dynamic membrane and traps pollutants and fouling material away from the fixed micro- or ultrafiltration membrane.^[21] After a certain amount of time, the dynamic membrane is removed together with the pollutants and the rest of the retentate. This significantly reduces the fouling of the fixed membrane.^[20, 21]

Above in the part about filtration cakes, Darcy's law was mentioned to express the change in volumetric flow rate per cross section area related to the properties of the porous medium and the liquid flowing through it. Above the permeability was defined by Equation (1):

$$\kappa = \frac{\dot{V} \cdot \eta \cdot d}{A \cdot \Delta p} \quad (1)$$

The term permeability in different scientific fields is used to express similar, but in their specificity, different quantities. This includes different disciplines of physics, chemistry, geology, medicine and specifically membrane filtration and separation science. For sediments of soil or sand in geology and for dense membranes, dynamic membranes or porous membranes with filtration cakes in membrane and filtration science, permeability is directly linked to the thickness of the membrane or deposited material. For asymmetric porous membranes or membranes with highly irregular pore structures, where a fixed repeatable length segment cannot be confidently identified, linking the thickness directly to the permeability is more challenging. Due to this, in large parts of the literature, the permeability P of a porous membrane is fixed to the specific membrane and, only for pure water, is equivalent to the pure water flux J divided by the transmembrane pressure difference Δp with the same unit (usually written as $\text{L h}^{-1} \text{m}^{-2} \text{bar}^{-1}$).

$$P = \frac{J}{\Delta p} \quad (4)$$

This only holds true for pure water in porous membranes without any noticeable quantity of fouling or changes in the membrane morphology. With the addition of fouling agents, the permeability of the system is no longer only determined by the membrane itself, but by the formed system of filtration cake or fouling component inside the pores and the membrane structure. Here, the water flux, or less commonly the specific water flux, is used as the appropriate quantifiable term for simple water flux experiments.

This unfortunately resulted in a noticeable amount of confusion in the published research, leading to deviation of the units, calculation for the water flux value and the overall difference between pure water permeability or specific water flux and water flux itself. Lately, the terms “pure water permeability” or “specific water flux” are more often found in porous membrane related publications for the above mentioned term.^[22-27] The pure water permeability $P = J/\Delta p$ will also be used in this work.

One of the largest motivators for emerging new membranes or membrane filtration processes is the persisting problem of fouling. Fouling of membranes demands either the frequent exchange of the membrane or membrane module, which is only reasonable for small-scale and/or very low concentrations in the filtrate, or cleaning techniques, which are necessary for the economic application at larger scales.^[28, 29] Cleaning techniques usually involve one or

multiple of the following: Forward flush, backward flush, backwashing, sponge ball cleaning, air flushing or chemical cleaning.^[28]

These techniques are effective and prolong the lifespan of the membrane or whole membrane module, but may not be applicable for all membrane types or, in the case of chemical cleaning, may damage the membrane over time.^[28] While these techniques require further research along with the fouling mechanisms themselves, nonconventional cleaning techniques are also gaining interest. Ultrasonic irradiation, magnetic fields and electric fields are still researched and further developed.^[28, 30-34]

Electrical conductive membranes are still an emerging field. While electrical conductivity is an important parameter for dense ion exchange membranes due to the presence of mobile charges in form of counter ions, the intrinsic conductivity of porous membranes is comparatively slowly gaining interest.

Electric fields offer the possibility to affect more materials than magnetic fields and a more compact system compared to ultrasonic irradiation. Many particles and colloids are negatively or positively charged in a liquid suspension. Electrically charged particles can be submitted to an electrophoretic force generated through the electric field between two oppositely charged electrodes. Additionally, a charged membrane or electrode behind the membrane can deflect a particle or colloid of the same charge. The last sentence implies that the application of an electric field can be approached differently. As mentioned before, an electric charge can also affect microbes either through electrophoresis or electrostatic repulsion or electrochemically. To reduce fouling through electrophoresis, the membranes themselves do not necessarily have to be conductive themselves.

The process of using electrophoresis in filtration processes is sometimes referred to as “electrofiltration”¹. Solid electrodes behind the support structure of the membranes can generate sufficiently strong electric fields. Hofman et al developed a double dead-ended filtration set-up with two membranes opposite of each other, the electrodes separately behind the membranes and a flushing channel between them.^[34] They showed that such a set-up can successfully filter biopolymers from a water suspension with a high concentration of the biopolymer on the anode side. The concept proved promising enough to allow a pilot-scale module.^[35] As the anode

¹ This should not be confused with an “electrofilter”, which is an electrically charged mesh to filter dust and other particles from air.

collects the material as a filtration cake, the cathode side showed a drastically reduced filtration cake formation.

Research also investigates the use of an electrically conductive membrane as the anode or cathode to either decrease the distance between the electrodes or provide an electrochemically active surface to the filtrate or the fouling material. Electrically conductive membranes offer the advantage that they themselves can act as an electrode, which minimizes the distance to the counter electrode.

The electric field strength between two plates can be calculated from the following equation:

$$E = \frac{U}{d} \quad (5)$$

with the electric field strength E , the potential difference between the plates U and the distance between them d . With the electric field strength inversely proportional to the distance between the electrodes, the closer the electrodes are, the stronger is the electric field strength and therefore also the electrophoretic force. This is illustrated in **Figure 6** for electrofiltration in cross-flow.

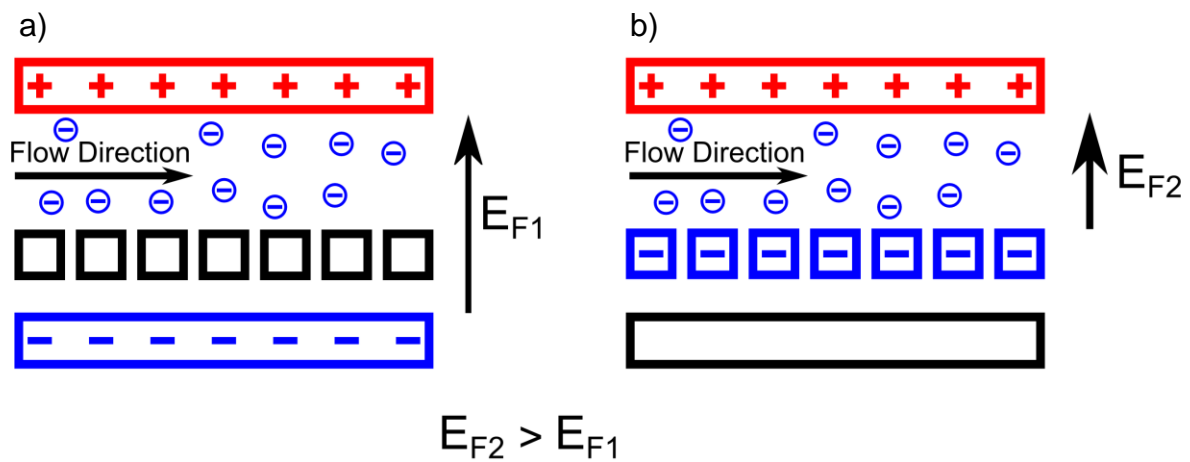


Figure 6: Schematic drawing of the difference between an electrically non-conductive and a conductive membrane in an electrofiltration set-up with a solid anode on the opposite side (a). If the membrane itself is the cathode (b), the electrophoretic force at equal potential difference is increased through decrease of the gap between the electrodes.

Rashid et al prepared self-supporting ultrafiltration membranes from MWCNT which either had carboxylic acid or amine groups.^[36] The MWCNT were dispersed using a surfactant and ultrasonification and then vacuum filtered. This formed the MWCNT into a porous bucky-paper. The produced membranes were hydrophilic with a contact angle between 28° and 55° and showed extremely high conductivity values of up to 5,800 S/m. Due to the very small diameter of MWCNT, the average pore diameters were between 20 and 26 nm. The mechanical

properties were analysed using the tensile test. The tensile testing allows for the determination of the Young's modulus and elastic and plastic deformation behaviour of a material in elongation. The membranes achieved an elongation at break below 1.2% and Young's moduli between 0.34 and 1.3 GPa. Self-supporting CNT bucky-paper membrane were also produced by Dumée et al, once with pristine MWCNT and once with functionalised MWCNT, without measurement of the electrical conductivity.^[37, 38]

Dudschenko et al performed electrofiltration in a cross-flow set-up with an electrically conductive membrane for which they also produced a highly conductive membrane.^[39] Concerning the membrane, they produced it from cross-linked poly(vinyl alcohol) and carboxylated multi-walled carbon nanotubes through sequential depositing and cross-linking with glutaraldehyde as the agent. The poly(vinyl alcohol) and MWCNT were pressure deposited onto a PS-35 membrane support through an aqueous suspension and afterwards cross-linked. The conductive layer showed a significant 2,500 S/m and reduction of the membrane fouling by 33% at -3 V and 51% at -5 V, respectively. In terms of membranes from the combination of carbon nanotubes with polymers, this achieved conductivity value is exceptionally high.

Even higher conductivity values were achieved by de Lonay et al two years earlier, also using poly(vinyl alcohol) and carboxylated MWCNT, and also deposited from suspensions for each with a concentration of 1 wt%.^[40] They as well deposited PVA and the MWCNT on a support membrane and cross-linked the PVA, but had a high MWCNT concentration in the conductive layer of 20 wt% with respect to PVA to achieve extremely high 3,597.0 S/m. They used succinic acid to cross-link the PVA and carboxylated MWCNT.

The approach of depositing a layer of highly conductive CNT on a support membrane was also taken by Hashaiekh et al by using 1 wt% sodium lauryl sulfate (SDS) as a surfactant for the MWCNT in a suspension of 0.05 wt% of MWCNT in an aqueous solution.^[41] The MWCNT suspension was then pressure-driven through a support membrane and a layer of MWCNT with a thickness of 3 - 4 μm was deposited. They also showed that the membrane can be cleaned of deposited yeast cells through electrolysis at 2 V for 3 min. Up to 80% of the flux could be recovered repeatedly this way.

Zhang and Vecitis investigated the use of a conductive CNT-PVDF membrane for capacitive organic fouling reduction.^[42] In their study, they also investigated the effect of different set-ups concerning the electrodes. They compared set-ups with no electrode, negative surface charge

only, electric field and electric field combined with a negative surface charge. They found that the optimal electrode-membrane configuration to reduce organic fouling involved the permeate to first flow through a porous anode and then pass on to the negatively charged CNT-PVDF cathode and then to also used PES ultrafiltration membrane.

More moderate conductivity values were achieved by Hu et al using bacterial cellulose and polyaniline.^[43] Using HCl as a dopant for polyaniline, they achieved a conductivity of up to 5 S/m. They also reported very good mechanical properties with a Young's modulus of 5.6 GPa and tensile strength of 95.7 GPa.

An electrically conductive polymer was also used by Liu et al to produce a conductive composite membrane. Polypyrrole was polymerised from the liquid phase and vapour phase onto a blank tyrelene cloth filter for antifouling experiments in a membrane bioreactor. The vapour phase polymerised membrane achieved the highest electrical conductivity of 0.04 S/m. A very small applied electrical field of 0.2 V/cm was sufficient to reduce fouling through electrophoresis and electrocoagulation.

Xu et al also used a polypyrrole but with anthraquinone to modify a polyester membrane for fouling reduction in a membrane bioreactor. The specific conductivity of the membrane was 0.002 S/m with a very small contact angle of 5.1°. The very high hydrophilicity of the modified membrane still allowed for a moderate decrease of the water flux by 9.2%, due to reduction of the pore size by the coverage with polypyrrole of the blank membrane. Interestingly, the voltage to charge the membrane negatively came from the bioreactor itself through a microbial fuel cell, generating a voltage between 0.2 and 0.05 V. Again the fouling of the membrane was reduced and allowed for longer time intervals between physical cleaning of the membranes.

A conductive membrane was produced by Vecitis et al, again by depositing dispersed MWCNT onto a support membrane through vacuum filtration.^[9] The pore size of the support membrane was 5 µm and the average pore diameter of the deposited MWCNT layer was 93 ± 38 nm. While they did not provide a conductivity value, they showed the effect of an applied voltage on the filtration performance for *E. coli* bacteria and MS2 bacteriophages² as well as on their culturability. The membrane was not used as an electrode, instead the electrical current passed through the membrane in a closed circuit. The *E. coli* bacteria were screen-filtered on the surface while the viruses were depth-filtered by the around 22 µm thick MWCNT layer. Due

² Bacteriophages are viruses that target bacteria.

to this, the bacteria were completely removed from the permeate, while not all viruses could be removed. For the viruses, plaque forming units could be found in the permeate, but the membrane reduced the number by two orders of magnitude compared to the filtrate suspension. When electrochemical filtration was performed with an applied voltage of 2 V, no culturable virus could be found in the permeate. Bacteria and viruses were collected from the membrane. Nearly all deposited bacteria and viruses could be completely deactivated at a voltage of 3 V for 30 s.

A composite membrane was produced by Zhu et al through membrane casting using a solution of polysulfone with functionalised MWCNT in a solvent. The solution was cast onto a glass plate using a doctor knife. After 30 s evaporation time, the composite membrane was placed in a water bath for 30 min to complete the phase inversion. The size of most surface pores was between 1 and 3 μm and the membrane thickness was around 100 μm . Electrical conductivity values were 0.1 S/m for 2.5 wt% of MWCNT and 2.5 S/m for 6.0 wt%. When an alternating current of 3 mA at 0.5 W/h was passed through the membrane, more than 99.999% of *E. coli* bacteria were deactivated within 20 min. This showed that lower conductivity values can be effective against microbes.

A different approach of a composite membrane was taken by Huang et al.^[44] A PVDF solution was used to coat a stainless steel mesh assembled on a polyester non-woven. The membrane was then formed through precipitation in a non-solvent bath. While they did not provide a electrical conductivity, they found the ohmic resistance of the membranes to be around 2.6 Ω . An applied electrical field with 2 V/cm proved effective at fouling reduction and reduction of necessary membrane cleaning intervals in a continuous-flow membrane bioreactor.

In the literature, a general trend is that membranes from electrically conductive polymers are more difficult to produce and show lower conductivity values than MWCNT composite membranes. Yet they offer more morphological flexibility through polymerisation onto a support membrane. Composite membranes with MWCNT so far are mostly either deposited sheets of MWCNT onto a support membrane or mixed into a casting solution for the membrane formation through phase inversion. The membranes with sheets or buckypaper of MWCNT on the support membrane show the highest conductivity values, but only very limited flexibility and controllability of the morphology of the separation layer. In contrast, the phase-inverted composite membranes offer more flexibility, but show significantly lower conductivity values.

Still, the literature overview shows that conductive membranes in general can offer notable improvements in the fouling behaviour, filtration performance and/or deactivation of microbes and viruses through an either applied electric field or flowing electrical current. Conductivity is primarily an issue of energy loss through heat and charge distribution with increasing membrane dimension.

Flexibility in the processing, dimensions and geometries of electrically conductive membranes is still to be improved. While flat membranes can be easily produced with the methods found in the literature, cylindrical or other geometries are still to be desired.

2.2. Polymer Composites Using MWCNT

Carbon nanotubes (CNT) are allotropes of carbon. Their structure is a cylindrical nanostructure in a hexagonal lattice with different structures (see **Figure 7**). Carbon nanotubes generally resemble a graphene sheet that is folded around and connected to itself.

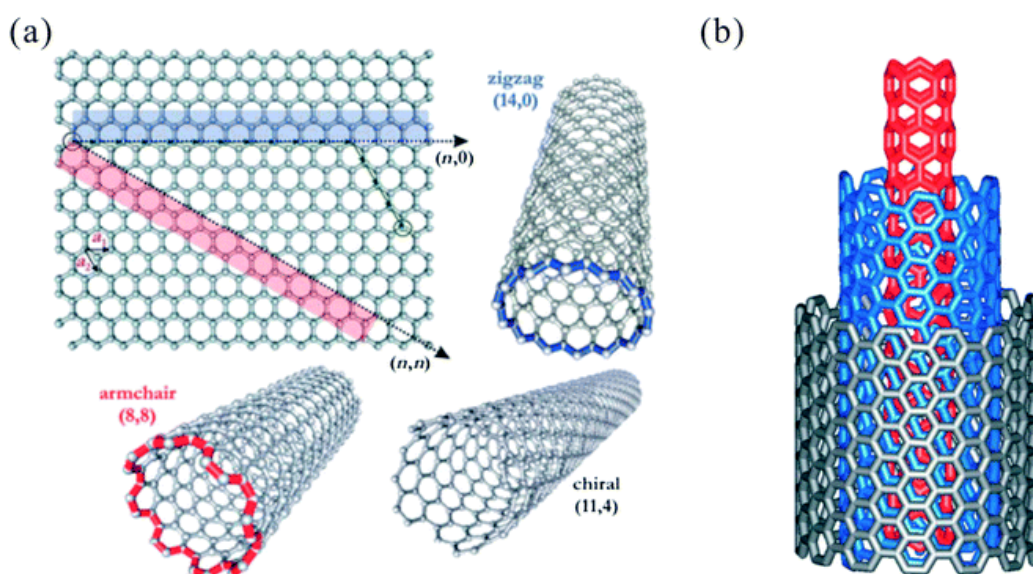


Figure 7: Illustration of (a) the three structures of single-walled CNT and (b) side-view of a multi-walled carbon nanotube with three walls. In (b) the black is armchair, blue is chiral and red is zigzag pattern.^[45]

They can be synthesised in typical diameters between 1 nm and 30 nm, but with varying lengths up to micron dimensions.^[46] With one tube layer, CNT are classified as single-walled carbon nanotubes (SWCNT). If they possess more than one tube layer, they are classified as multi-walled carbon nanotubes (MWCNT) (see **Figure 8**).

Defect-free SWCNT possess some of the most extreme properties of any material. Their Young's modulus is reported around 1 TPa with a tensile strength of up to 52 GPa.^[47, 48] In comparison, MWCNT show a lower mechanical strength with a Young's modulus between 270

and 950 GPa, a tensile strength between 11 and 63 GPa and varying elongation at break.^[49] The lowered Young's modulus is an effect of the low wall interaction inside the MWCNT, leading to comparatively easy gliding of the walls relative to each other and easier transition to plastic deformation.^[50] Realistically, cost-efficient large quantities of defect-free CNT are not yet available and a certain number of defects is common, which notably lowers the extreme properties of the CNT.^[51]

The electrical conductivity of a carbon nanotube greatly depends on its wall structure. It strongly varies, depending on the CNT type and its amount of defects. As the upper extreme: Defect-free, metallic conducting CNT can show a electrical conductivity of up to 10^7 S/m at room temperature.^[52]

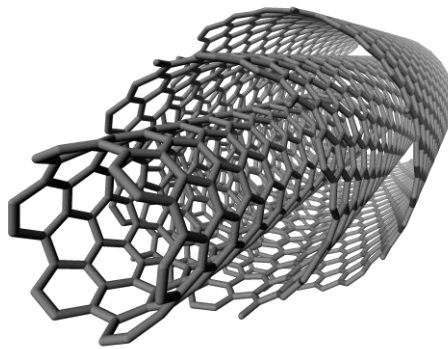


Figure 8: Perspective illustration of a MWCNT with armchair structure and three walls.

From a commercial perspective, MWCNT are easier and cheaper to synthesize.^[53] Therefore, more cost-efficient and large-scale synthesis can be relatively easily performed via catalytic chemical vapour deposition (CCVD) using an iron or cobalt catalyst.^[51] This process produces CNT with relatively large amounts of defects compared to arc discharge and laser ablation, resulting in a noticeable lower quality.^[51]

In terms of mechanical properties, the high aspect ratio makes an excellent ratio of CNT-matrix interaction possible.^[54] For a spherical particle, the vast majority of the volume does not interact with the matrix, but only the outer shell. For SWCNT, the whole wall or for MWCNT the outside wall interact with the matrix, leading to all or a high percentage of the CNT atoms in contact with the matrix. This leads to a noticeable increase in mechanical properties at relatively low concentrations of CNT.^[54-57] Further, if the CNT are aligned in the direction of an applied tensile stress, they carry a large fraction of stress of the matrix and effectively strengthen the overall composite.^[58] This is analogue to the strengthening effect of aligned fibres in fibre-reinforced polymers.

For an improvement of the isotropic mechanical properties, a homogenous distribution with ideally no agglomerates in the matrix is desired (see **Figure 9** for an illustration).^[57] This means a minimal amount of inter-CNT contacts and a maximal amount of individual CNT surrounded by the matrix with strong CNT-matrix interactions. The interaction of the CNT with the polymer matrix can be increased by appropriate functionalisation of the CNT.^[59, 60] Further, low affinity of the matrix to the CNT promotes the formation of agglomerates in form of aggregates through their entanglement and van der Waals forces.^[60]

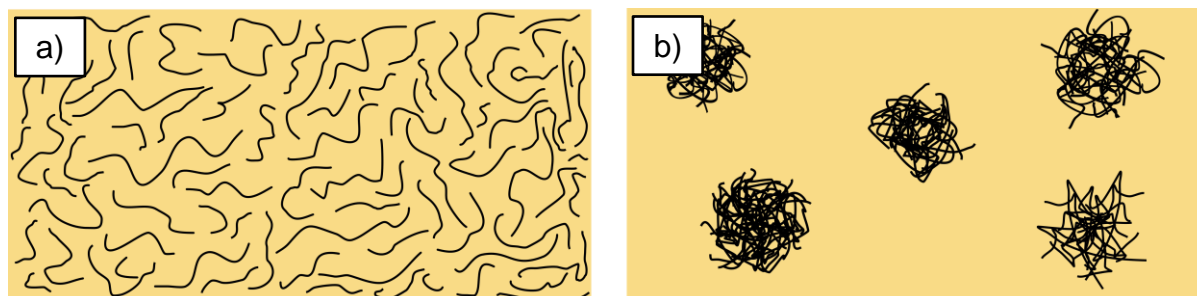


Figure 9: Illustration of (left) well dispersed CNT compared to (right) similar number of CNT in agglomerates.

Carbon nanotubes offer interesting properties for electrically conductive composite materials. For one, their very high aspect ratio allows for a conductive network while occupying a small volume or area. This is illustrated in **Figure 10**. In the illustration a spherical particle with approximately the same diameter as the length of a given CNT will occupy a significantly larger area and volume than the nanotubes. Not shown in the illustration is that the free area in the CNT case can be occupied with further CNT, increasing the inter-CNT contacts and contact volume, providing significantly larger “bottle necks” for the electrical flow which makes higher current densities possible. Therefore, the overall electrical conductivity can be significantly higher for an equal weight concentration of CNT compared to spherical particles of identical conductivity to the nanotubes.

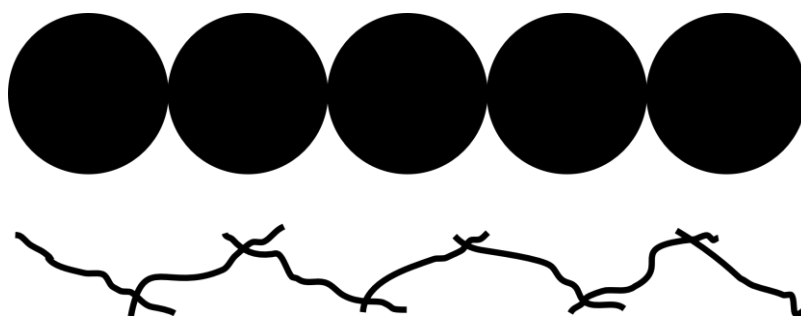


Figure 10: Illustration for comparison of conductive networks. Spherical particles of identical diameter to MWCNT length cover a much larger area.

For the improvement of the electrical properties, CNT agglomerates and low CNT-matrix interaction are also not desired.^[57, 58, 61] Yet, the priorities are not identical. While an effective dispersion of the CNT without agglomerates is still optimal, the amount of inter-CNT contacts should be maximized. If the CNT form a conductive network inside the matrix, the whole composite is called electrically conductive. The conventional way to achieve this network is the increase of the CNT concentration. At a given concentration the CNT start to be randomly in contact with other CNT, forming continuous conductive pathways through the matrix.^[62] This depends on the CNT type, the matrix and the process used for the composite production. If the number of contacts is high enough, a conductive network with a relatively low amount of inter-MWCNT in the beginning is achieved. This point is the percolation threshold.

Above this concentration, the electrical conductivity of the composite increases drastically, following a power-law with increasing CNT concentration and therefore increasing number of contacts between CNT^[61]:

$$\sigma = \sigma_0 \cdot (\Phi - \Phi_c)^t \quad (6)$$

In this equation, σ is the conductivity of the composite, σ_0 is a scaling factor comparable to the effective conductivity of the filler, Φ is the volume concentration, Φ_c is the percolation threshold concentration and t is the critical exponent that governs the conductivity increase. The percolation threshold can be found by using a graph of $\log \sigma$ against $\log \Phi - \Phi_c$ and adjusting t and Φ_c until a linear function on the logarithmic scale fits the experimental data.

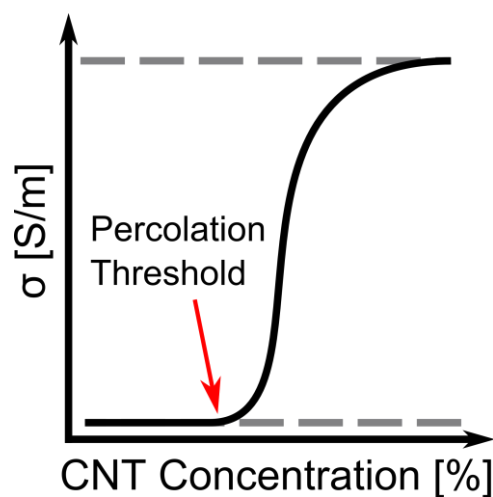


Figure 11: Qualitative curve shape of the increase of the electrical conductivity with increasing CNT content. When the percolation threshold is reached, the conductivity increase is very high with relatively small increases of the CNT concentration. After a certain CNT concentration, diminishing returns lead to an approach of a plateau for the conductivity.

The classic assumption in the formation of the conductive network of CNT inside the matrix included the necessity of direct physical contact between two CNT. This corresponds to a typical electron transfer between conductive elements. Recently, the electron transfer through the quantum tunnelling effect has been added as a plausible supportive mechanism.^[63] With decreasing distance between two CNT, the tunnelling probability increases.^[64]

At a certain CNT concentration, the increase in electrical conductivity is significantly lower with increasing CNT concentration. At this point it can be assumed that the maximum conductivity of the composite is close to be achieved and nearly all CNT are part of an interconnected network.^[62]

Apart from the random distribution, a different approach can be used to improve the percolation of the CNT before the composite is fully formed. The formation of a segregated network of the conductive filler is currently the most promising (see **Figure 12**).^[65] The segregated network approach so far shows the strongest lowering of the percolation threshold and increase in the electrical conductivity in thermosetting and thermoplastic polymers.^[65]

Here, “segregated” does not mean a full exclusion of the matrix between the CNT forming the network, but rather a minimized, partial envelopment of the CNT with the matrix. This makes it necessary to pre-locate the CNT or other filler in a network structure before the finished composite is formed. A very low percolation threshold and maximum conductivity at lower concentrations for different polymers were achieved this way, as inter-CNT interaction is increased with a reduced influence of the polymer matrix.^[65-67]

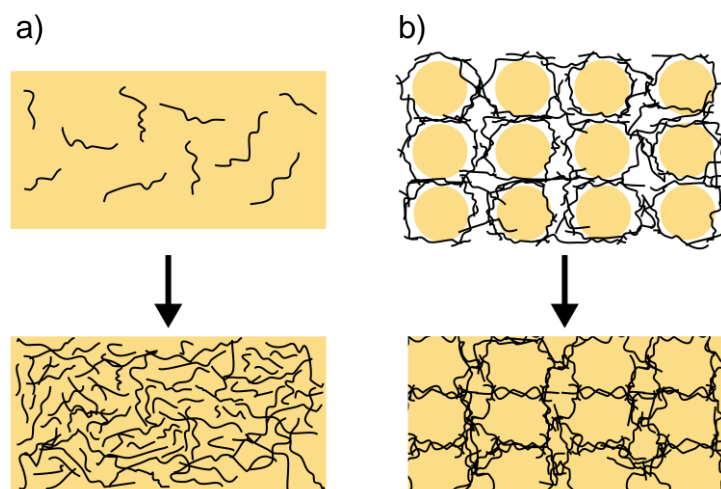


Figure 12: Comparison between percolation through random network formation (a) and approach through segregated network formation (b). The MWCNT are randomly in contact with other MWCNT for random network formation at a certain concentration. For the segregated network approach, the MWCNT are already assembled

into a network that is kept as intact as possible or improved in inter-MWCNT contact through processing to a composite.

For thermoplastic polymers or rubbers before vulcanisation for example, this can be achieved by dispersing polymer powder particles and CNT in a suspension or in a dry mixing process, through evaporation with ultrasonification or CNT deposit on top and in-between powder particles.^[67-70] Through compression moulding, the loose powder-CNT mixture under low-shear conditions preserves the CNT network, while fixing it inside the polymer matrix.

In any approach to produce a segregated CNT network, the stresses during the final processing steps have to be minimized to avoid disruption as much as possible.

The approach that allows for easier handling is the predispersion on the surfaces of powder particles. This can be either performed through agitation of a CNT-polymer suspension or dry mixing of CNT agglomerates with polymer particles.^[65, 69-72] Independent of the process, the shear or impact forces on the CNT aggregates have to be high enough to de-agglomerate them, without causing significant damage to the structure. Additionally, the CNT need to have a high enough affinity to the polymer surfaces to physically attach to them. In case of ball-milling, the CNT can be worked into the outer shell of the polymer volume, if impact energies are high enough.^[72] Surface-covered particles are often referred to as “decorated” in the literature.

These methods offer the advantage of an easier to handle composite powder or pellet material for further processing. Furthermore, this opens up the use of pressureless sintering for porous structures as well as easier compression into green bodies, with a lowered disruption of the dispersed CNT on the particle surfaces. A loosely assembled powder of CNT and polymer powder particles does not lend itself to shape and tap compaction.

2.3. Sintering

The surface energy dependant process of fusing particles together at elevated temperature, through the combined processes of coalescence and densification, is known as “sintering”.^[73] Sintering is a technological key process in the powder technology of ceramics and metals.^[74] In the case of polymer melts as viscoelastic fluids, the surface tension is the equivalent to surface free energy.^[75]

Coalescence in this sense means the merging of two or more particles into one particle. Densification means the reduction of porosity. As even a compressed powder possesses gaps and open tortuous channels inside of it, there is always a certain amount of densification

happening. The densification does not necessarily overlap with the coalescence from the beginning. Particles may fuse together, but the overall porosity of the observed system initially does need not change due to material flow, thermal expansion or changes in particle alignments. In contrast, densification can still occur even though the coalescence is finished. One can imagine four particles aligned in a square: They initially start to fuse together without a significant decrease in the diameter of the hole in the middle, as the viscous material flow is small enough to happen only on the outer layers of the particles. As they continue to fuse together, viscous material flow of the whole particle volumes occurs, leading to a decrease in the diameter of the hole in the middle and an overlap between coalescence and densification. Continuing, the particles fuse together into a single circular string, while in the middle there is still a hole left. Over more time, this hole is progressively filled through viscous material flow, without the string coalescing with something else. Due to this, coalescence initiates the sintering and densification finishes it.

Sintering as a technological process is characterised by an overlap of physical processes depending on the material.^[74] The classical sintering materials are ceramics and metals. Here, most commonly the diffusion of single atoms leads to the fusion of separate particles. This is a relatively large difference compared to polymers, where the diffusion and rearrangement of whole polymer chains in a viscous melt flow is happening.^[76-79] Because the solid state diffusion of polymers is not an effective way to induce macroscopic material deformation, thermoplastic polymers are sintered above the glass transition temperature (amorphous polymers) and the melting temperature (semi-crystalline polymers).^[73] Sintering as a pressureless thermal process is only available for thermoplastic polymers. With the introduction of applied pressure, sintering was also shown to be applicable for the recycling of thermosetting polymer rubbers.^[80] With applied pressure, the process becomes very similar to compression moulding, showing only variation in the process sequences. In sintering with applied pressure, the powder is first put under pressure and then heated, while in compression moulding it is first heated and then the pressure is applied.

To illustrate the complexity of the physical processes during the sintering process, a brief description of the development of physical models is presented in the following paragraphs.

Most of the literature concerning sintering is about metals and ceramics, which are generally sintered at temperatures below their melting temperatures. As mentioned above, for these materials the sintering happens through solid state diffusion. The first formulated sintering model by Frenkel et al was published in 1945. Frenkel stated that the material transport during

solid-state diffusion is equivalent to viscous flow of a Newtonian liquid.^[81] As later experimental data showed, this may only be true for metals, ceramics or generally the initial stage of sintering, where the behaviour can be approximated to be Newtonian.^[78, 79, 82, 83]

Four years later, Eshelby et al improved the model on the theoretical level to fulfil the continuity equation, which is why the model often is referred to as Frenkel-Eshelby model.^[84] Afterwards, other models were developed for the complete fusion process in different systems and with material properties, including numerical simulation models.^[85] The model developed by Bellehumeur et al so far proved to be the most accurate and adaptable analytical model for the sintering of viscoelastic materials such as polymers.^[78] It introduced the influence of the viscoelastic properties and balanced it with the work of the surface tension to acquire a better model for polymers. For example, compared to Frenkel's model, Bellehumeur's model can be used to predict the lower sintering rate of more elastic polymer melts compared to less elastic ones.^[78]

Most studies observed the sintering of two individual powder particles to analyse the sintering behaviour. While this is an adequate approach, a few studies showed the influence of the particle number in contact and their orientation to each other. Lately it was shown that the sintering of multi-particle systems cannot be accurately predicted by models developed for two-particle systems and lead to adaptations of Bellehumeur's model.^[73, 77]

The development of sintering models is not only a history of improvements, but lately also of specific adaptations. Still, the available models are generally developed from simple systems of two or a few particles. This limits their usability for the more complex technological sintering process of multiple particles in more complex three-dimensional arrangements, possibly in contact with different surfaces. Further, these models do not account for strong interactions of the polymer melt with the substrate surface, which was mentioned above as an important factor for technological processing.

In the technological process of sintering the wetting behaviour of polymers to the surface of the substrate material is an important process parameter.^[73] While the sintering is performed above the melting temperature (semi-crystalline polymers) or glass transition temperature (amorphous polymers), the polymer melt may or may not have a very small contact angle to the substrate. With a small contact angle, the polymer melt will spread on the substrate surface while simultaneously fusing with the neighbouring polymer particles, which are also spreading. This is illustrated in **Figure 13**. For dense products, this accelerates the overall sintering process

while decreasing the risk of air bubbles and other defects. This is beneficial for rotational moulding but not for the sintering of porous structures. With a large contact angle, the polymer particles have a larger fraction of their material flow contributing to direct fusion at the neck to a neighbouring particle while initially retaining a large fraction of their original shape.

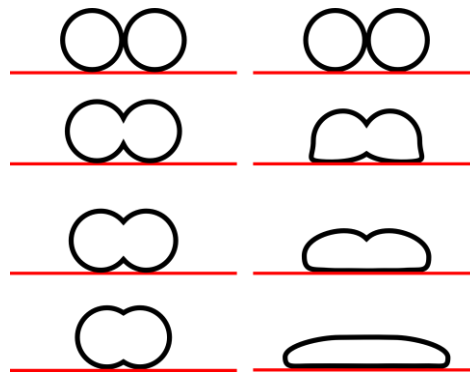


Figure 13: Comparison of the idealised sintering behaviour of two particles. The red line represents a heated surface. If the particle materials have a very large contact angle to the substrate (left) the particles predominantly coalesce together. If the contact angle is small, the fusion is overlapped with the spread of the material across the substrate surface.

For the direct observation of the sintering process, usually two or only a few particles are observed through an optical microscope. The experiments are usually performed on a transparent substrate such as glass and in a heatable chamber with a window. To characterise the fusion of the particles, the dimensionless neck radius is used. Usually, the dimensionless neck radius is named as x/r . Here, x is the radius at the neck at a given time t , while r is the radius of the particles at the time t . An illustration of the dimensions and their changes can be seen in **Figure 14**. Only in ideal cases are the radii of two particles identical, but for most available polymer powders, this is not the case. Then two similar particles have to be found and the radius of one of the particles has to be used.

For irregular particle shapes, observing the change in the approximated diameters is significantly easier, because the neck and particle centre do not have to be identified. Instead the edges of the neck and particle can be used and approximated with a circular overlay. Since the diameter and radius only differ in the factor 2, the measured dimensionless neck diameter, here called y/d , can easily be converted to the dimensionless neck radius.

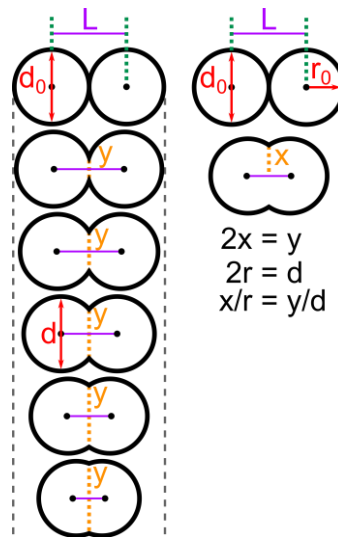


Figure 14: Schematic of the fusion of two perfect spheres. The fusion is shown in progression from top to bottom on the left. The material flow leads to a decrease of the centre-to-centre distance “ L ” between the two spheres, resulting in an increase of the neck diameter “ y ”. The initial diameter “ d_0 ” also changes over time as a value “ d ”. In the observation of particle fusion, usually the dimensionless neck diameter “ x/r ” is used. The right side illustrates, that for purely observational purposes the dimensionless neck diameter “ y/d ” can be used interchangeably.

The diameter of the particles changes over time. Therefore, the diameter has to be measured after every chosen time interval. The initial particle diameter d_0 is larger than the transient diameter d . As two particles completely fuse together, the final diameter of the new particle is larger than d_0 . Because the diameter d is measured after every time interval together with the neck diameter y , y/d can only approach the value 1 and never be larger. At $y/d = 0$, the sintering did not yet begin. With the first increase in y/d , the coalescence of the particles is initiated. As y/d is getting closer to the value 1, the centre-to-centre distance L between two particles at a certain time also starts to decrease. The reduction in the centre-to-centre distance is the initiation of the densification part of the sintering.

A qualitative curve shape for the growth rate of x/r depending on the time t in a pressureless sintering process for a viscoelastic polymer melt is illustrated in **Figure 15**. The shape is similar to that of other, inorganic materials, but for the description afterwards it should be assumed for polymer melts.

The initial sintering rate is highest in the beginning, when the coalescence starts. Depending on the particle material and shape, the initial dimensionless neck radius x/r does not have to be 0, but may near-instantaneously jump to a value $x/r \neq 0$. An initial swelling of the particles due to thermal expansion or sudden decreased density due to the melting of a crystalline phase can result in such a jump. At the initial stage, the reduction of the surface energy as the driving force of the sintering process is the highest. The surface curvature and therefore the Laplace

pressure around the contact area is the highest in the beginning and the two molten surfaces of two particles in contact rapidly fuse to form the fusion neck.

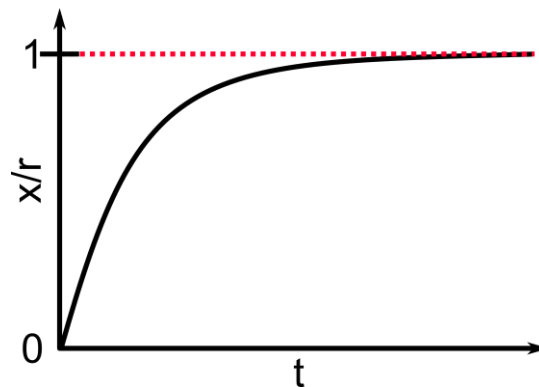


Figure 15: Illustrative curve for the general qualitative shape of the change of the dimensionless neck diameter x/a over the time according in an ideal situation, according to sintering models. The fusion is fastest in the beginning and slows down when y/a approaches 1. Close to 1, the fusion is nearly complete, which is accompanied by a significant reduction in driving force behind the fusion.

From here on the Laplace pressure at and around the neck is still high, but decreases with an increasing value of y and therefore y/r . The overall curvature and area of the surface shared between the two fusing particles at the fusion neck is reduced further and further as the sintering process continues. This leads to the reduction in surface area and therefore surface energy. As the tension decreases, the resistance of the polymer melt in form of its elastic and viscous properties is larger in relation, leading to a decrease in the sintering rate at the later stage.

In the technological process of sintering, the chosen powder for the process is often compressed into a green body to minimize the porosity between the particles and increase the contact point number and size of the contact areas between particles through elastic deformation. Depending on the material and execution of the process, this green body can be composed solely of the compressed powder or the powder mixed with an added binder. Any shape that can be geometrically given through a two-part mould is possible with enough applied pressure.

A special processing technique that is emerging is selective laser sintering (SLS). With it, very complex three dimensional structures can be produced in incremental process by sintering polymer powder layer-by-layer through applying heat through a small-focus laser. So far SLS allows for the production of the most complex structures available to powder technological processes. Still, it has major drawbacks in form of limited quality and smoothness of the finished product and the relatively slow production rate limits its ability for upscaling. Additionally, only polyamide 12 (PA 12) is currently adequately usable for SLS at the current level of technology, leading to a share of 90% of used polymer for SLS.^[86] The reason is a need

for a large enough temperature gap between the lowest temperature of the melting range and the highest temperature of the crystallisation range of the polymer. The powder bed during laser sintering is kept 2 - 4 °C below the melt peak, to increase the melting rate through the laser and decrease its energy demands.^[87] To be able to technologically control the bed temperature below the melt peak and above the crystallisation peak, the temperature gap has to be large enough, this gap is called the “processing window”.^[87] So far only PA 12 has a sufficiently large enough processing window and desired material properties.

For the conventional sintering of dense components and materials, complete coalescence and densification are desired. The polymer should have a relatively low melt viscosity and an easily compressible powder. The application of an external pressure strongly increases the sintering rate. External pressure can be applied through a piston or other mechanical device to the mould or through centrifugal force, such as in rotational moulding.

A polymer with a high melt viscosity and also easily compressible powder is preferred for sintering of porous components and materials. The high melt viscosity slows down the sintering rate of the particles.

Most thermoplastic polymers can be sintered to dense components and materials, as the process is very similar to compression moulding, if external pressure is added. The above mentioned rotational moulding is an established and widely used industrial production process up to large scale products.^[88]

The sintering of open-porous components and materials is less common for the usual industrial polymer range. The classical polymers for sintering of porous materials and components are polytetrafluorethylene and ultra-high molecular weight polyethylene. Their high melt viscosity excludes classical melt processing with screw-driven methods such as extrusion and injection moulding. Instead ram-driven extrusion and injection moulding with high forces have to be used. This high melt viscosity makes it possible to sinter them relatively easily inside or outside of a mould and allows for products with an adjustable porosity.

3. Materials

3.1. Polyetherimide

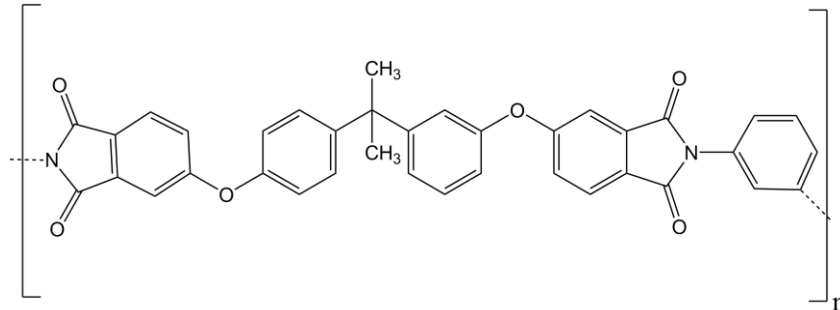


Figure 16: Chemical structure of polyetherimide

Polyetherimide is an amorphous high-performance thermoplastic that is commercially available on an industrial scale. In membrane applications it is widely used as a material for dense gas separation membranes and porous filtration membranes. The membranes are usually produced via different methods from a solution.^[14, 89-91] The polymer stands out due to its excellent mechanical properties³ with a Young's modulus of 3,580 MPa^[92], resilience against heat and flames with low amount of smoke formation, a pronounced yielding after 7% extension and a break elongation of 60% through neck formation.^[92] It is resilient against many solvents, but with a significant weakness against halogenated ones such as chloroform and dichloromethane.^[93] Additionally, polyetherimide has a high hydrolysis resistance, making it well-suited for long-term use in water separation applications.^[94]

The used commercial powder was Ultem™ 1000P, the powdered and non-filled version of Ultem™ 1000. The particle size distribution is relatively large with 90% of the particles below 206 μm (as measured by laser diffraction, see Chapter 6.2.1). The powder shows good flowability for handling and a good ability for green body compression.

³ The number values correspond to the commercial, unfilled product Ultem™ 1000P

3.2. Ultra-High Molecular Weight Polyethylene

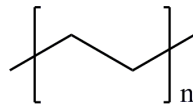


Figure 17: Chemical structure of polyethylene.

Polyethylene is a semi-crystalline thermoplastic polymer and is the polymer with the largest amount of industrial production^{4, [95]} It is available in a large range of modified versions such as high-density PE, low-density PE, linear low-density PE, cross-linked PE and ultra-high molecular weight PE (UHMWPE). UHMWPE is a high-performance polyolefin with exceptional mechanical properties and chemical resistance, which separate it from most other high-performance polymers with polar groups in their chemical structure. Available UHMWPE usually has a very high molecular weight between 2 and 9 million g/mol, resulting in extremely long chains.

The van der Waals forces between individual segments of the chains are low, but due to their very large number and the resulting distinctive entanglement, UHMWPE is tremendously resilient to mechanical stress and abrasion, shows well developed strain-hardening and very high elongation at break of up to 525%.^[96] As a simple polyolefin, it is also highly stable in most organic solvents, bases and acids. The lack of polar groups also results in a low affinity to water and a low uptake of humidity. Mechanical properties differ, depending on the molecular weight, but generally a Young's modulus of around 720 MPa, yield stress of 20 MPa, ultimate tensile strength of 32 MPa and elongation at break of around 300% are common.^[96-99]

The used commercial powder GUR[®] 2126 is a fine powder with 90% of the particles below 57 μm (as measured by laser diffraction, see Chapter 6.2.2). The powder shows a very low flowability and high ability for green body compression. The material shows a very high viscosity in the melt and therefore cannot be injection moulded or extruded with conventional screw-driving machines. Instead, usually rams with very high applied forces are used in ram injection moulding and ram extrusion.

⁴ Combined for all types of PE.

In filtration applications, UHMWPE is used in the production of porous filters for liquids and air filters. These filters and membranes are usually either produced via direct sintering of the processed UHMWPE powder or by extrusion of the UHMWPE melt together with a porogen.

3.3. Polypropylene

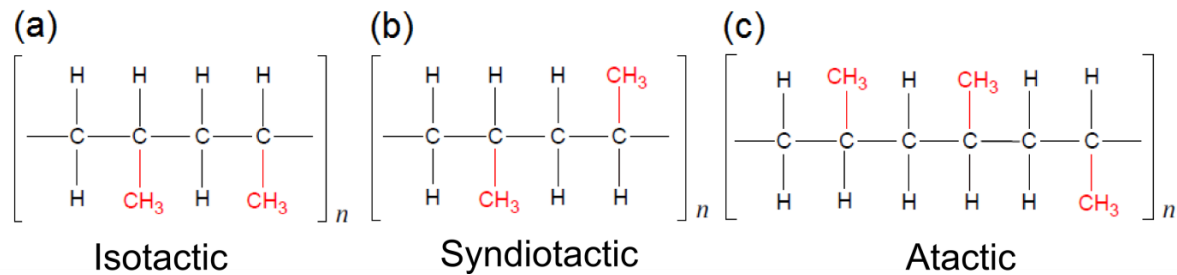


Figure 18: Chemical structure of polypropylene with its three types of tacticity.^[100]

Polypropylene is the singular most produced type of commercial polymers in the world, only overtaken by PE if all different types are not counted separately.^[95]

The used powder Moplen[®] HF 500 H by LyondellBasell-Industries (Rotterdam, Netherlands) is a commercially available non-filled powder of polypropylene. Unlike the powders for UHMWPE and PEI, this powder has large particles with a broad particle size distribution mostly between 0.355 mm and 1.800 mm, with these dimensions this powder is excluded from the sintering experiments because it cannot produce a reasonable membrane. Nevertheless, with its round spherical shape and large particle size for a powder, this product shows excellent flowability and can be easily poured by hand or mechanical methods with little residue. This is desirable for powder delivery for extrusion or injection moulding and filling of larger moulds in compression moulding. Due to its flowability and particle size and shape, the powder cannot be compressed into a green-body. The Young's modulus, ultimate tensile strength and elongation at break are not provided by the manufacturer. Usually a Young's modulus of 1300 MPa and elongation at break of around 800% can be expected.^[101, 102]

Therefore, this powder served as an addition to the compression moulding experiments to cover a larger range of polymer properties. The powder was separated through vibration sieving into two contingents of particle sizes. The first one is particles from 0.355 mm to 1.0 mm and the second one from 1.0 mm to 1.8 mm. With this, the difference in surface area at same weight was taken into account for the decoration process.

3.4. Decorated Powder Particles

The used material in this work is polymer powder particles. Depending on the material, the particle size varies. Parts of these powders were processed to electrically conductive MWCNT-polymer composites. As the main focus was the increase in electrical conductivity, a segregated network approach with MWCNT was used.

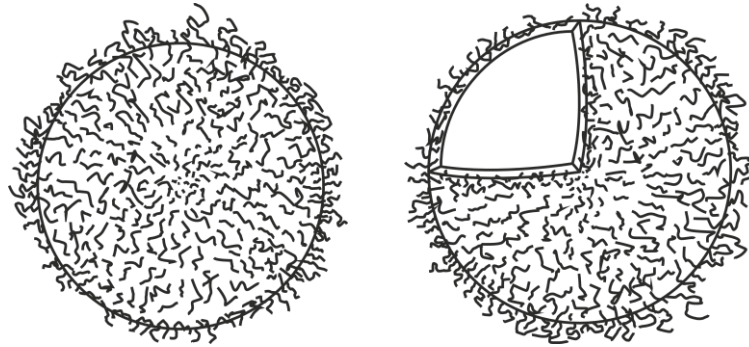


Figure 19: Schematic of decorated powder particles, here shown as perfect spheres. The black wavy lines are MWCNT, oriented on the powder particle surface, while partially pointing away from the surface which is here shown in exaggeration. With the exception of the outer-most layer of the powder, the volume of the particles is pristine polymer.

The dispersion of the MWCNT was achieved by high-energy dry mixing of MWCNT aggregates with the polymer powders, which realizes a “decoration” of the powder particles with the MWCNT (see **Figure 19**). Decoration of the powder particles was performed by the project partner at FutureCarbon GmbH, using their patented process.^[103]

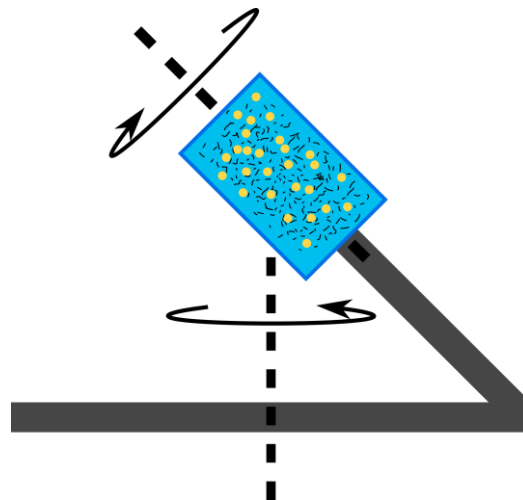


Figure 20: Illustration of the geometry and rotation direction of a dual asymmetric centrifugal mixing process with powder particles and MWCNT.

The high-energy dry mixing is performed using a SpeedMixer™ (Hauschild & Co KG, Hamm, Germany) device. A SpeedMixer™ imposes large centrifugal forces on the material in the mixing container through dual asymmetric centrifugal mixing (see **Figure 20** for an

illustration). The cylindrical mixing container rotates around its central axis, it is eccentrically mounted on a base plate at an angle of 45° and the base plate rotates in the counter-direction of the mixing container. The process is bladeless and has near-zero vibrations, avoiding turbulent air flows in the mixing container.

The energy and shear forces are high enough to break up the MWCNT aggregates and cause MWCNT to physically attach to the polymer powder particles. The effectiveness of the process depends on the powder particle properties such as polymer density, particle size and shape. If the particle properties are appropriate, the powder particles can be fully covered in mostly individual MWCNT if the weight fraction is high enough.

Details of the process, including the specifics of the used parameters, remain with the project partner company.

4. Polymer and Composite Processing

4.1. Compression Moulding

Compression moulding was performed to prepare samples for shear rheological measurements, two-probe electrical conductivity measurements and for uniaxial tensile testing.

The parameters and the overall process went through several iterations to pinpoint the necessary adaptations of the compression moulding process and parameters for each material and sample shape. It was found very early on that the use of flat flash-type moulds with two openings has several limitations, which could not be fully solved because of the necessary sample variety and the available equipment. Schematic illustrations of the different used moulds and cavity shapes are shown in **Figure 21**. The moulds were flat and the cavities for the ample shapes are holes going through the full thickness of the moulds. The draw-back result from this, as conventionally moulds for compression moulding are made of two parts with actual cavities and one part sinking into the shape, applying pressure to the melt from start to finish.^[104]

Firstly, excessive overfilling of the mould may guarantee complete filling of the mould cavity, but it also induces large material flow and therefore shear flow on top of it, combined with a large flash. An illustration is shown in **Figure 22**. Apparently, the larger material flow on top induces severe problems. The large shear flow appears to disrupt the percolation of the MWCNT and causes strong envelopment with the non-conductive matrix at least on the surfaces. This manifested in preliminary tests as non-conductive samples with the decorated powders. Conventionally, the mould is slightly overfilled with the powder, heated to melt the material and then pressed into shape in the main compression step with a large force. This lead to samples without a conductive surface and appeared as electrical isolators to measurement attempts.

The compression force only is applied on the melt until the pressing plates are in full contact with the mould. While this still works efficiently for pristine PP and for PP/MWCNT, the shear flow of the melt in the flash created a specific problem for UHMWPE. Due to its very high viscosity and pronounced elastic properties in the melt, the overflow and flash appeared to restrict the compression of the material in the mould. It was found that with excessive overfilling the polymer and composites would not flow completely out into a flash, but rather most of the overflowing material is staying between the mould and the pressing plate on top.

This overflown constricted elastic melt apparently reduced the pressure on the shrinking melt in the mould cavity, leading to faulty samples through reduced plastic material flow.

This problem was solved by adaption of the process as close as possible to sintering under pressure. The mould was filled as much as possible with the powder with minimal overfilling, put under a small force of 10 kN during the powder melting phase to sinter the molten powder particles together and into the mould and then the main pressing step to completely fill out the mould. This method produces conductive samples for UHMWPE/MWCNT and PEI/MWCNT. For so far unclear reasons, this specific problem did not occur for PP/MWCNT, where no difference between the methods could be found.

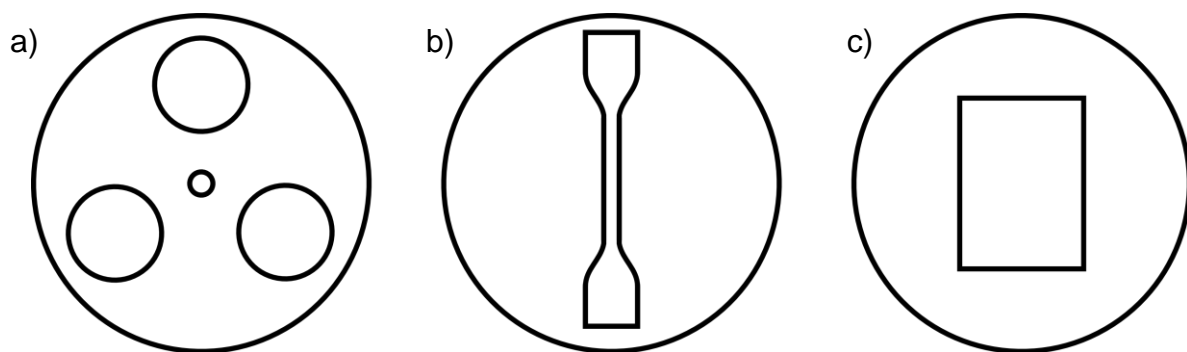


Figure 21: Schematic illustrations of the top-down view of the three types of moulds used for compression moulding. The cavities are cut-out from the mould and are in fact holes. The moulds are 2 mm thick. Shown are a) the cylindrical shapes, b) a dog-bone shaped shape for tensile testing c) one a flat rectangular plate for electrical conductivity measurements via two-probe method.

Secondly, demoulding was a severe problem for the composites from varying MWCNT concentrations depending on the polymer matrix. Generally, brittleness would increase with MWCNT concentration, leading to problems with the available demoulding methods. For the soft PP and UHMWPE, locally increased brittleness, cohesion of the material in the mould and the flash, and adhesion to the mould walls would lead to partial or complete fracture of the samples, independent of shape. Therefore improper demoulding could easily damage the samples. This problem was greatly increased for the already brittle and hard PEI samples. One could easily fracture the samples by simply applying pressure in small areas with a fitting demoulding cylinder. As the cohesion to the strongly adhered flash makes demoulding significantly more difficult, scissors and a scalpel were used to manually cut the flash as closely as possible to the sample volume. For the cylindrical samples for the shear rheological analysis, a demoulding cylinder with a properly sized polymer layer in form of a polyether ether ketone (PEEK) foil between it and the sample solved the problem and reduced sample loss to a few attempts. The square shaped samples for the two-probe conductivity measurement and heating

measurement needed a similar method, but with a significantly smaller demoulding cylinder and carefully incrementally and in alteration applied force around the four corners of the sample. While effective, some samples still had small pieces broken off, which was compensated for by cutting these samples to a defect free square geometry.

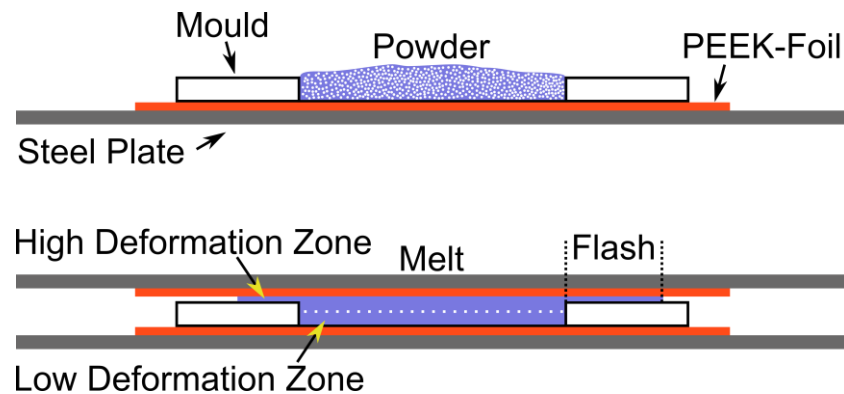


Figure 22: Schematic illustration of the compression moulding with the flat moulds with hole-cavities.

Compression moulding of the flat samples for tensile testing of the composites showed additional problems. Due to the geometry of the samples, the thin middle part posed a weak spot in the geometry. For PP, this problem could be very efficiently avoided by punch-cutting the sample shape from a larger rectangle. This was not possible for UHMWPE and PEI, as both were far too resilient against the cutting force. Therefore, both materials had to be directly compression moulded into the desired sample shape. This was relatively easy for UHMWPE, due to its very high toughness and bendability. Care only had to be taken to not bend the samples too far out of the mould on one part, so not to deform the shape which could lead to errors during tensile testing.

The compression moulding of flat samples for the brittle PEI/MWCNT caused more significant problems in demoulding, as the thin part in the middle of the bone samples was the fracture area of all unsuccessful demoulding attempts with a demoulding cylinder or any other available object. Demoulding was possible for pristine PEI without loss of samples. The procedure was therefore adapted by taking a pristine PEI flat dog-bone sample and grinding all sides, except the upper and lower surfaces, of the sample down until around 0.5 mm was taken off on all side. This grinded-down sample was then used as the demoulding shape to apply uniform pressure on as much of the samples as possible. This efficiently solved the fracturing of the bone samples for PEI/MWCNT and was afterwards used for UHMWPE/MWCNT for easier demoulding with unbent samples.

Powders used for compression moulding were dried for at least 24 h in a vacuum oven to remove absorbed or trapped moisture in it. The drying temperature for polyetherimide was 150 °C and for both ultra-high molecular weight polyethylene and polypropylene 70 °C.

Polyetherimide and UHMWPE were precompressed at room temperature in a cylindrical mould with a diameter of 20 mm, to remove as much air between the powder particles as possible and close gaps between them. This step was necessary for the two finer powders to avoid the development of bubbles in the finished samples. The used pressure was 3.9 GPa, which was applied for 10 seconds. For the production of samples for the shear rheological analysis, the precompressed powder pellet was put into in cylindrical moulds with a diameter of 24 mm and a thickness of 2 mm. For polypropylene, the powder was directly filled into the compression moulds, because the relatively large powder particles could not be pre-compressed.

The rectangular mould for the rectangular samples for the measurement of the electrical conductivity had the dimensions 40 x 50 mm and a thickness of 1 mm.

The temperature of the heatable press at the top and bottom part was set to 320 °C for PEI and PEI/MWCNT, 220 °C for UHMWPE and UHMWPE/MWCNT, 180 °C for pristine PP and 200 °C for PP/MWCNT.

A disc-shaped brass plate contained three of these moulds in a rotational symmetric alignment. The brass plate with the moulds was placed on top of a PEEK foil on an aluminium plate approximately 1 mm thick. The PEEK foil provides a smooth and easy to remove surface, while the aluminium shields the surfaces in the pan from compression damage. A second PEEK foil and second aluminium plate were put on top of the filled-in powder.

A powder mass of 1.4 g was used for the 2 mm thick moulds. This amount of mass was used to provide enough excess material to compensate for the flash formation and still fill the mould during the process. The initial samples were samples of PEI, PEI/MWCNT, PP and PP/MWCNT for rheological analysis. The initial samples were produced in a three-step process (vacuum process), using a pan with a lid and medium vacuum. The process was as follows:

1. Filling the powder (PP) or putting the pre-compressed pellet (PEI and UHMWPE) into the mould and putting the mould into the pan with the lid.
2. Putting the assembly into the heated press.
3. With the lid on, pre-heating the assembly for 3 min at 10 kN applied uniaxial force from the top and bottom.

4. Turning on a vacuum pump to acquire medium vacuum condition in the pan chamber and waiting for 3 min.
5. Pressing the pan and therefore the samples at 60 kN (PP and PEI) or 120 kN (UHMWPE) for 5 min.
6. Transferring the assembly to an identical cooling press and cooling the assembly for 15 min back to around room temperature.

The applied force of 60 kN equals 60 MPa for the rectangular moulds and 44 MPa *per* round mould with 24 mm diameter.

This process was also used for the production of samples of PP and PP/MWCNT for rectangular samples for measurement of electrical conductivity.

Later samples for rheological analysis were produced in a more simplified process without the use of a vacuum. The same mould type and temperatures were used, but instead of the pan two steel plates were used. The mould was placed on PEEK foil on top of one of the steel plates. After the mould was filled, a second PEEK foil was placed on top of the mould and afterwards a second steel plate on top. The steps were as follows:

1. Filling the powder (PP) or putting the pre-compressed pellet (PEI and UHMWPE) into the mould and placing the second PEEK foil and subsequently the second steel plate on top.
2. Putting the assembly into the heated press.
3. Pre-heating the assembly for 5 min at 10 kN applied uniaxial force from the top and bottom.
4. Compressing the assembly at 60 kN (PP and PEI) or 120 kN (UHMWPE) for 5 min.
5. Transferring the assembly to an identical cooling press and cooling the assembly for 10 min back to around room temperature.

This simplified process was also used for the production of rectangular samples for conductivity measurements and flat samples for tensile testing of PEI, PEI/MWCNT, UHMWPE and UHMWPE/MWCNT, as well as the samples for rheological analysis of UHMWPE.

4.2. Sintering

For the sintering, a two-part mould out of hardened steel with a removable compression cylinder was designed to allow for high flexibility in the sample preparation process. The mould consists of a cylindrical bottom part, with a smaller cylindrical elevation in the centre with a diameter of 47 mm. The upper part is a cylindrical ring that fits onto the bottom part and has an inner

centre hole with a diameter of 47 mm to fit onto the bottom part and a raised wall around the hole. The compression cylinder has a diameter of 46.5 mm to fit into the hole of the upper part with a sufficient geometric tolerance.

Preliminary experiments showed that simple loose stacking of the powder in a more simple mould combined with knock density and varied parameters did not produce useable samples, due to irregularities in the powder distribution. Precompression into a green body with uniaxial force offered the desired regular shape, but for the vast majority of attempts did not produce any undamaged samples. The compressed green body is densely packed and during the heating step in the sintering, the thermal expansion caused cracks and defects, due to the lack of cohesion between the powder particles. This happened in the sintering of free-standing green bodies and green bodies compressed in the used cylindrical mould, which was open on the top. Consequently, geometrical restriction that left only one direction open was also not applicable. Continuous restriction in all directions leads to an increased pressure inside the powder during sintering which causes the open-porous structure of the green body to change into a close-porous structure.

Therefore, the thermal expansion of the powders had to be restricted appropriately. This varied for the two sintered material PEI and UHMWPE, as both materials had very different particle sizes, melt properties and different degree of shrinkage during solidification.

4.2.1. Sintering of PEI and PEI/MWCNT Membranes

The sintering of PEI and PEI/MWCNT went through many attempts and adaptations until the following procedure was developed to reproducibly produce samples without defects, with consistency of sample dimensions and appropriate firmness for handling and characterisation.

Due to its particle size distribution, one-dimensional geometrical green body restriction through placing a steel plate under and on top of the green body led to cracks in radial direction to its centre. This was caused by outwards expansion of the powder.

The sintering process was performed in three steps (illustrated in **Figure 23**): Pre-sintering, cooling and sintering. Before the sintering process started, the weighed powder of 1.4 g was placed into the mould (bottom and upper part combined) and brought to shake and tap density. The compression cylinder was then placed on top of the powder, rotated and a small pressure of 6 MPa was applied. A compression force of 69 MPa was then applied in the cold press, which was also used in the compression moulding process.

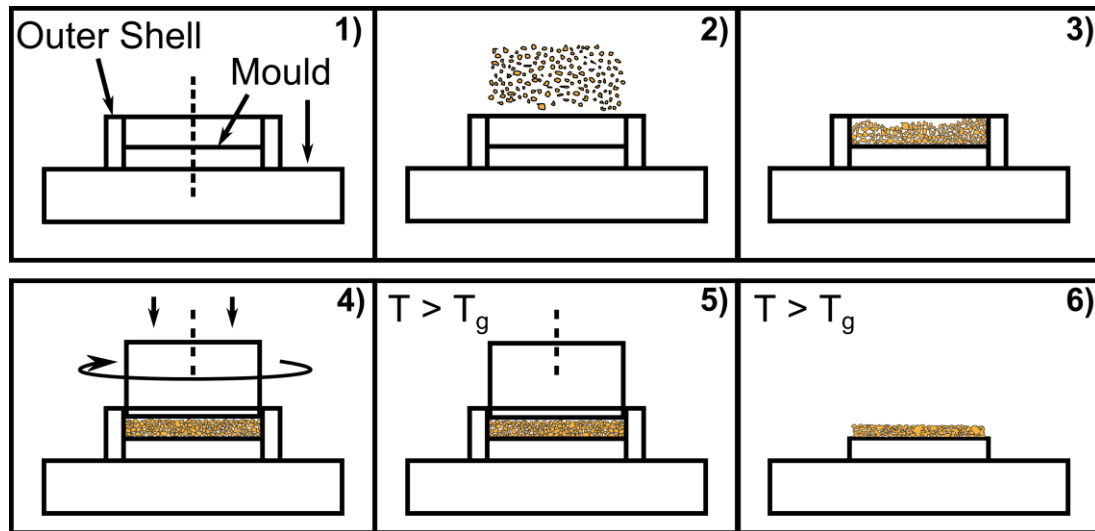


Figure 23: Schematic of the sintering process. From top left to bottom right: The mould is (1) assembled. The powder is then (2) filled into the mould, (3) brought to tap and knock density, (4) compressed using the compression cylinder that is rotated several times, then (5) heated with a cylinder in the pre-sintering step, (5) cooled with the cylinder in the cooling step and (6) sintered with removed cylinder and upper part of the mould.

In the pre-sintering step, while the cylinder was left on top the green body, the assembly was placed under 300 °C for 6 min for PEI and PEI/MWCNT with the MWCNT concentrations up to 1.5 wt%. For PEI/MWCNT with the concentrations 2.0 wt% to 3.0 wt%, the time had to be increased to 9 min (time changes for 2.0 wt% and higher will be discussed further down). Afterwards, the assembly was placed in the cooling press at 9 °C for 3 min with an applied pressure of 11 MPa. The compression cylinder and the upper part of the mould were then removed. The pre-sintered body now had enough cohesion to sinter free-standing without cracks and still a large porosity with open pores. The sintering step was then performed with the pre-sintered body on the bottom part of the mould at 300 °C for 6 min for PEI and PEI/MWCNT with concentrations up to 1.5 wt%. The concentrations of 2.0 wt% and higher were sintered for 12 min. Afterwards the samples were cooled to room temperature and then fully demoulded. Finished samples had a thickness of 1.0 mm for PEI and MWCNT concentrations up to 1.5 wt% and 0.8 mm for 2.0 wt% and higher.

The sintering times had to be varied for different MWCNT concentrations due to increases in viscosity and overall changes in the sintering behaviour through the surface localisation of the MWCNT. The same lower sintering times (6 min, 3 min and 6 min) led to unsatisfying results for PEI/MWCNT with 2.0 wt% MWCNT and higher concentrations. Samples lacked desired cohesion with pronounced brittleness, showed defects like pin holes and small cracks, and easily fractured during the demoulding step. Therefore sintering times had to be increased to 9 min, 3 min and 12 min, to allow for a more pronounced fusion and thicker sintering bridges

between former particles. Reversely, using the longer sintering times for MWCNT concentrations of 1.5 wt% and lower led to completely or mostly dense samples that were mostly impermeable for water.

While it would have been possible to eventually find the optimal sintering parameters to assure identical pore sizes and porosity for all samples, this was not feasible due to time restrictions. The main goal of this part of the research was to investigate the differences in the sintering behaviour, which could also be performed by comparing the results for a set of sintering parameters that led to porous membranes for a set of MWCNT concentrations. As one set of parameters did not produce porous membranes for all MWCNT concentrations, the set of parameters were increased to two which was sufficient to produce porous membranes for all MWCNT concentrations. Therefore, the two sintering times were chosen to keep the comparability of the samples as high as possible.

The sintering process was innovative enough to lead to an accepted European patent (EP 2982492). It allows for control over the dimensions of the sample and the sintering of an open-porous structure with pristine polymer powder or powder decorated with non-sintering material.

4.2.2. Sintering of UHMWPE and UHMWPE/MWCNT Membranes

The sintering of UHMWPE and UHMWPE/MWCNT membranes did not share the same problems as for PEI and PEI/MWCNT, but needed its own process specifications and parameters.

The experimental approach was overall initially based on the experiences from PEI and PEI/MWCNT. The same method produced non-porous samples, independent of set times. UHMWPE is much softer than PEI, the pre-compression, small pressure and spatial restriction of the compression cylinder in the pre-sintering step led to a much faster fusion rate of the powder particles. As the compression into the green body stores a certain amount of elastic energy and with the spatial restriction through compression cylinder during the thermal expansion of the powder particles, the amount of stored energy in the system was relatively higher than for PEI. The stored energy is converted into plastic deformation of the UHMWPE melt, leading to the faster fusion rate.

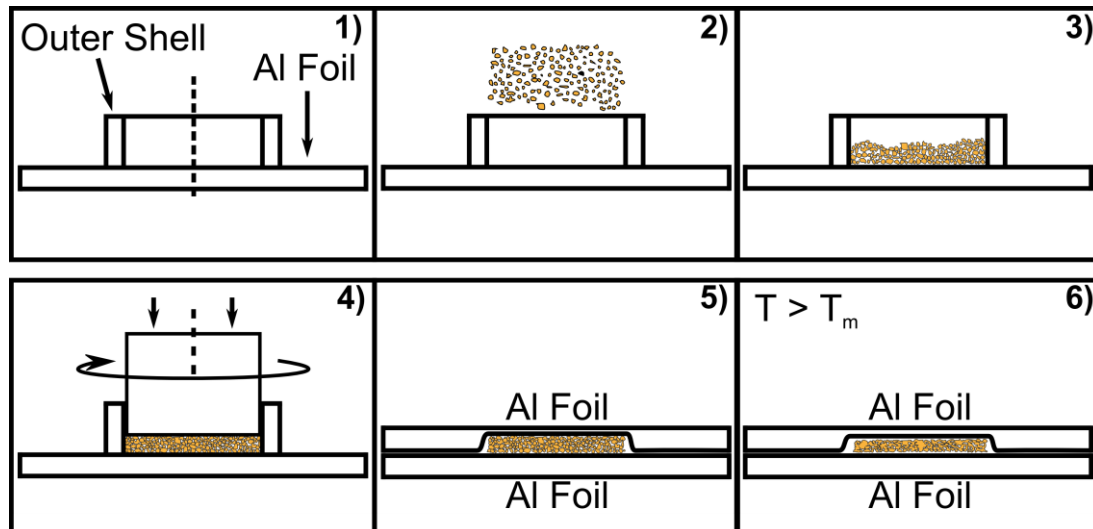


Figure 24: Schematic of the sintering process. From top left to bottom right: The upper part of the original mould is (1) placed on top of aluminium foil. The powder is then (2) and (3) filled into upper part of the mould, (4) compressed using the compression cylinder that is rotated several times, then (5) a second layer of aluminium foil is placed on top the green body and the assembly is then (6) again compressed and afterwards cooled to room temperature.

Additionally, UHMWPE showed a strong adhesion to the previously used PEEK foil, making the separation of PEEK and UHMWPE impossible without damaging the sample. This was avoided by using a thick aluminium foil instead of a PEEK foil. The UHMWPE was easily separated from the aluminium foil. Through several iterations the overall sintering process was adapted for UHMWPE and UHMWPE/MWCNT into its shape for this work (see **Figure 24**).

The upper part of the mould was used as an outer shell and placed on aluminium foil on top of a PEEK foil on a steel plate. A mass of 0.5 g of UHMWPE or UHMWPE/MWCNT powder was put into the outer shell and spread out using a spatula. The compression cylinder was placed on top of the powder, rotated and with a light pressure of around 6 MPa smoothed. Then a pressure of 69 MPa was applied to compress the powder into a green body. Afterwards a second aluminium foil was placed on top of the green body. The final part of the assembly was a second PEEK foil and a second steel plate that were placed on top. The whole assembly was then compressed again at a pressure of 69 MPa on the green body to allow for maximum contact between green body and the aluminium foils. The membrane was then sintered in a single sintering step at a temperature of 220 °C for 2 h in air atmosphere.

Afterwards, the membrane was separated from the aluminium foil. The outer parts of the sample showed a brown colour, resulting from thermal degradation and oxidation. For this reason, a sample with a diameter of 24 mm was cut out from the centre, using a cutting punch.

The decoration of the powder particles with MWCNT did not have a significant influence on the sinterability of the powder in the macroscopic scale. Therefore, the same sintering parameters could be used for pristine UHMWPE and all UHMWPE/MWCNT powders, independent of MWCNT concentration. With identical parameters, a comparison on the microscopic scale is more effective.

4.2.3. Sintered Rectangular Samples

Rectangular samples were sintered in the same mould as was used for the compression moulding of the rectangular samples for conductivity measurements. The sintering was kept significantly simpler compared to the membranes. The rectangular mould was put on a PEEK foil for PEI and aluminium foil for UHMWPE on top of a steel plate. The powders of PEI and UHMWPE were filled into the centre of the rectangular moulds. A second PEEK or aluminium foil and steel plate were placed on top. The powder was compressed in the cooling press with 69 MPa pressure. The assembly was then sintered at the same sintering times and temperatures for PEI for UHMWPE. This produced rectangular samples in the middle section of the mould. Commonly defects appeared on the outer areas of samples and were cut out in such a way to keep the samples rectangular. With this assembly, control is not sufficient enough for an open-porous structure comparable to the membranes, but rendered samples with homogenous geometries necessary for the calculation of the electrical conductivity.

5. Polymer and Composite Analysis

5.1. Thermogravimetric Analysis (TGA)

The thermogravimetric analysis was performed in a temperature range between 25 °C and 1000 °C with a heating rate of 10 K/min in the TGA device Netzsch TG209 F1 Iris with a constant argon atmosphere of 1 bar and a constant flow rate of 29 mL/min. The dried powder was filled into an Al₂O₃ crucible.

It was used for analysis of changes in the thermal degradation process of the decorated powder particles. As the MWCNT concentration never exceeded 5.0 wt%, the accuracy of the machine prohibited an exact determination of the actual MWCNT concentration of the powders due to sensitivity limitations.

Polyetherimide and polypropylene could be measured with conventional approaches, while it was found for UHMWPE that the material taken with the gas stream have a significant tendency to block the filter at the outgoing end of the oven chamber. This would lead to a complete blocking of the following measurement with an UHMWPE material and failure of this measurement. To compensate for this, after each measurement the filter had to be changed.

5.2. Differential Scanning Calorimetry (DSC)

The DSC-Device DSC 1 (STAR^e System) from Mettler Toledo was used to study the thermal transitions of the polymer and MWCNT decorated powders in the temperature range between 30 °C and 300 °C for polyetherimide, -150 °C to 220 °C for ultra-high molecular weight polyethylene and -50 °C to 270 °C for polypropylene. The gas atmosphere was pure N₂ with a constant flow rate of 60 mL/min. The heating rate was 10 K/min for all materials. For the calculation of the crystallinity of UHMWPE and PP, the following equation was used:

$$X_C = 100\% \cdot \frac{\Delta H_m}{\Delta H_m^0} \quad (7)$$

Here the symbols are the percentage of crystallinity X_C , the heat of fusion⁵ for the theoretically 100% crystalline polymer ΔH_m^0 and the determined heat of fusion from the DSC

⁵ The heat of fusion is here identical to the melting enthalpy of the crystalline structures.

measurement ΔH_m . The used value of ΔH_m^0 for UHMWPE was 288 J/g and for PP 207 J/g.^[105, 106]

5.3. Optical Microscopy

A DMLM optical microscope (Leica Camera AG, Wetzlar, Germany) with a Leica DFC320 camera was used for the direct observation of the sintering of two particles of selected materials. This was achieved using a THMS 600 hot stage (Linkam Scientific, Waterfield, United Kingdom). The hot stage can be operated in temperature ranges between 30 °C and 600 °C, if appropriate cooling is provided. The chassis of the heatable table was water cooled through the use of an external thermostat, using pure water at initially room temperature. The heatable table was operated at 220 °C for UHMWPE and UHMWPE/MWCNT 5.0 wt%, and 300 °C for PEI and PEI/MWCNT 3.0 wt%. Significantly longer operating times were possible for the lower temperature of 220 °C compared to 300 °C. At 300 °C, the pure water volume of the external thermostat became increasingly warmer of time, leading to a connective tube at the chassis of the heatable table to become warm and soften. To avoid spillages and possible damage to the microscope, the experimental operating time had to be limited to a maximum of 40 min for 300 °C.

5.4. Scanning Electron Microscopy (SEM)

Scanning electron microscopes Merlin and LEO Gemini 1550 VP both from Zeiss (Oberkochen, Germany) were used for analysis of powder and the surface and cross section of the sintered membranes. Used detectors were for back-scattered electron, conventional secondary electrons and in-lens secondary electrons. Where appropriate, either a signal was used or a combination of two different ones.

5.5. Rheological Analysis

Rheological analysis was performed in dynamic shear rheology of the polymer and composite melts in plate-plate geometry. The rotational shear rheometers ARES (Rheometric Scientific, Piscataway (NJ), USA) and MCR 502 (Anton Paar, Graz, Austria) were used for the experiments. The rheological experiments of PEI and PP was performed on the ARES rheometer, while the experiments for UHMWPE were performed on the MCR 502 rheometer.

The diameter of the plates was 25 mm, one millimetre larger than the used samples to compensate for the thermal expansion. The experiments were performed in three parts. The first

part was an amplitude sweep with a fixed angular frequency of 10 rad/s. The amplitude was increased from 1 to 10% for PEI and PP and from 0.2 to 2% for UHMWPE. The samples for PEI and PP behaved like conventional homopolymer melts with predominantly viscous behaviour at lower deformation rates, while UHMWPE showed a significant elastic behaviour.

In the first amplitude sweep, the linear viscoelastic range for each material was found and an amplitude value for each material for the second step was chosen. In the linear viscoelastic range, the dynamic moduli do not depend on the values of the deformation or stress. That means that in the linear viscoelastic range, the dynamic moduli of the material are the same for the whole deformation range (amplitude) at each frequency step of a frequency sweep. This is usually the case for very small amplitude values.

The shear-rate dependant dynamic viscosity $\eta(\dot{\gamma})$ of a material in shear is defined as:

$$\eta(\dot{\gamma}) = \frac{\sigma_{xy}}{\dot{\gamma}} \quad (8)$$

with the shear stress σ_{xy} and the shear rate $\dot{\gamma}$. The shear modulus of a material is defined as:

$$G = \frac{\sigma_{xy}}{\gamma} \quad (9)$$

The behaviour of the material is frequency dependent and therefore a complex notation is often used. The complex shear modulus as a complex value can be written as:

$$G^* = G' + iG'' \quad (10)$$

The angular frequency dependant complex dynamic viscosity $\eta^*(\omega)$ is defined as:

$$\eta^*(\omega) = \frac{G^*}{i\omega} \quad (11)$$

$$|\eta^*(\omega)| = \frac{|G^*|}{\omega} \quad (12)$$

With:

$$|G^*| = \sqrt{G'^2 + G''^2} \quad (13)$$

The experiments in this work were performed in oscillating shear, with an angular frequency ω . The unit for the angular frequency is shown in the unit rad/s. A rad (radian) is the ratio of an arc to the radius of the corresponding circle. Equally, one rad describes the angle opened by an

arc with the length of the radius of the circle. It is a supplementary unit and can be expressed in SI-Units as:

$$1 \text{ rad} = 1 \frac{1 \text{ m}}{1 \text{ m}} = 1$$

Therefore, in calculations the rad can be omitted and the SI-Unit for the viscosity of the complex viscosity is preserved.

For UHMWPE this amplitude was 1% and for both PP and PEI 5%. The fixed amplitude was used for the second step, which was a frequency sweep from 100 rad/s down to 0.01 rad/s.

Creep recovery experiments in shear were performed with the same set-up as for the frequency sweeps. The deformation was measured at 220 °C under constant shear stress of 500 Pa or 10,000 Pa for a total time of 7,200 s for the creep segment of the measurement cycle. Subsequently, the mechanically applied stress was set to zero. Again over 7,200 s, the recoverable part of the deformation was measured.

Under constant stress, the deformation of the polymer is time dependent and characterised by the creep compliance $J(t)$. While under constant shear stress σ_0 for a time t , the shear deformation $\gamma(t)$ is measured and the creep compliance

$$J(t) = \frac{\gamma(t)}{\sigma_0} \quad (14)$$

results from this. The creep time ends at a set t_{max} and the shear stress is set to zero. The shear deformation recovers to a material and deformation dependent degree over a measured time t' . The recovery time t' is described by $t' = t - t_{max}$ in a continuous creep recovery experiment, because the time t continues after the creep phase. The recovered shear deformation $\gamma_r(t')$ can be divided by the value of the previously applied shear stress to calculate the recovered creep compliance:

$$J_r(t') = \frac{\gamma_r(t')}{\sigma_0} \quad (15)$$

The relation between $J(t)$ and $J_r(t')$ shows how much of the creep deformation can be recovered. More details concerning creep recovery experiments can be found in the reference by Münstedt.^[107]

5.6. Capillary-Flow Porometry

The device “CFP-1500-AEX” by Porous Materials Inc. (Ithaca, USA) was used for capillary flow porometry. The used wetting liquid was Galwick™ with a surface tension of 16 mN/m. The porometry was performed via pressure-step increase method. The pressure was increased in steps as small as 50 mbar, which were held for 10 s. To determine the wet-curve for the membrane, pressures went from 0 bar up to 1 bar for PEI and 2 bar for UHMWPE after the membranes were immersed in Galwick™ for 1 min. After the wetting liquid was blown out of the membrane, the pressure was step-wise reduced from 1 bar (PEI) or 2 bar (UHMWPE) back down to 0 bar to determine the dry-curve for the membrane. This method was chosen due to the pronounced tortuosity and varying diameters of the channels in the porous structure of the samples. A linear pressure increase with a set rate would lead to errors in the measurement. This can be explained through the theory behind capillary flow porometry.

The Young-Laplace equation can be used to describe the pressure difference across the interface of a liquid inside a capillary:

$$\Delta p = \frac{2 \cdot \gamma \cdot \cos\theta}{r} \quad (16)$$

with:

- γ : Surface tension between the liquid and the solid surface
- θ : Contact angle between the liquid and the solid surface
- r : Radius of the capillary

With a small transformation, this equation gives:

$$\Delta p = \frac{4 \cdot \gamma \cdot \cos\theta}{2 \cdot r} \Leftrightarrow \Delta p = \frac{4 \cdot \gamma \cdot \cos\theta}{D} \quad (17)$$

For porometry, Equation (17) is often called “Washburns’s equation”. With a liquid that has fully penetrated the porous structure and wets the surface very well, the contact angle can be assumed as approximately 0 and the equation is simplified to:

$$\Delta p = \frac{4 \cdot \gamma}{D} \quad (18)$$

As the, through a gas applied, external pressure has to be higher than the capillary pressure, Equation (18) shows that this is inversely proportional to the pore diameter by a factor of 4.

This means that a pore with a larger diameter and equal length to another pore will be emptied through the gas flow at a significantly smaller pressure; this is the ideal situation.

Nevertheless, if a linear pressure increase is applied, an increased gas flow rate through an opened pore is calculated to the pressure it was detected at. Imagining two pores of equal diameter but different lengths, if the necessary pressure p_1 that is higher than the capillary pressure is reached, the liquid will begin to be displaced from the pores. Yet both pores take a certain amount of time to be completely emptied.

This is simultaneously happening as the pressure increases linearly. So both pores will be open and therefore cause a detectable increase in gas flow, while the machine has already reached a higher pressure. The increased gas flow will be calculated to the pressure it was detected at. For the shorter pore, this error can be very smaller, but might not be possible to be ignored for the longer pore. In any case, both pores of equal diameter will be detected as pores of different diameters in a purely linear pressure increase mode.

This problem is analogue to a tortuous pore or a pore with greatly varying diameter (**Figure 25**). Even if the irregular pore has the same diameter in the bottleneck as an ideally capillary pore, it might hold a much larger volume of liquid before the bottleneck. The pore will only be detected if the pore has been emptied.

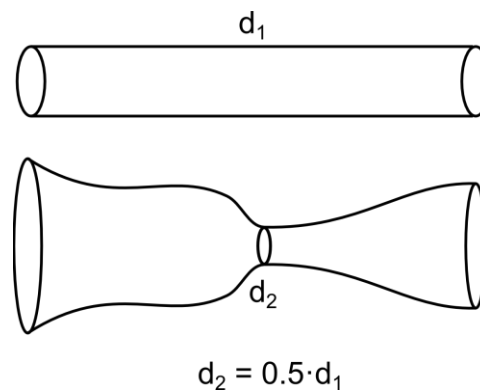


Figure 25: Schematic of 2 capillaries of equal lengths. The top one has a constant diameter, while the bottom one has a varying diameter with one smallest diameter acting as a bottle-neck.

To avoid the problem, a pressure step method or a linear pressure increase with set stability times per increase can be used. Here the pressure is increased in steps and held for a set amount of time. In samples where the exact pore structure is not known or cannot be well defined, these methods give results with smaller errors of the pore diameters, if an appropriate time per step is found.

An important value is the first bubble point, which corresponds to the largest pore diameter. This value is measured first, as the largest pore requires the lowest pressure to blow out the liquid. In contrast, the smallest detected pore diameter requires the largest pressure. The mean flow pore diameter is calculated using the dry-curve of the membrane. Half the slope of the dry curve is used to find the intersection with the wet-curve. This determines the pressure at which half of the maximum possible gas flow through the membrane is achieved.

5.7. Wet-Dry Method

The wet-dry method is a simple method to measure the porosity of an open-porous structure. The dry weight is obtained by simple weighing the sample on a scale. After this step, the sample is immersed in a liquid that effectively wets the material and therefore penetrates the open-porous structure due to capillary forces. This method ignores therefore closed pores. After the immersion time, the sample is weighed again. With the known volume of the samples, the porosity can be calculated with the following formula:

$$\text{Porosity} = \frac{w_2 - w_1}{V \cdot \rho_{\text{Liquid}}} \quad (19)$$

where w_2 is the mass of the wet membrane, w_1 the mass of the dry membrane, V the volume of the membrane and ρ_{Liquid} the density of the used liquid at room temperature. For the experiments, ethanol was used as the liquid, as it effectively wets both polyetherimide and ultra-high molecular weight polyethylene.

5.8. Water Flux Measurements

Water flux measurements were performed using purified Millipore water. The low-pressure dead-end filtration cell GN 10-400 by Berghof (Eningen, Germany) was used. A schematic of the set-up is shown in **Figure 26**.

A cover with a hole with a diameter of 20 mm for PEI and 14 mm for UHMWPE was placed on top of the membrane. A glass cylinder was placed on top of the cover with an O-ring in between as a seal. In the first step, a volume of 420 mL was filled under atmospheric pressure into the glass cylinder. A gas valve on the cell was then opened and the water was permeated at a pressure between 0.2 and 1 bar to stabilize the membrane under flux conditions. Then a second volume of 420 mL was filled into the glass cylinder at atmospheric pressure.

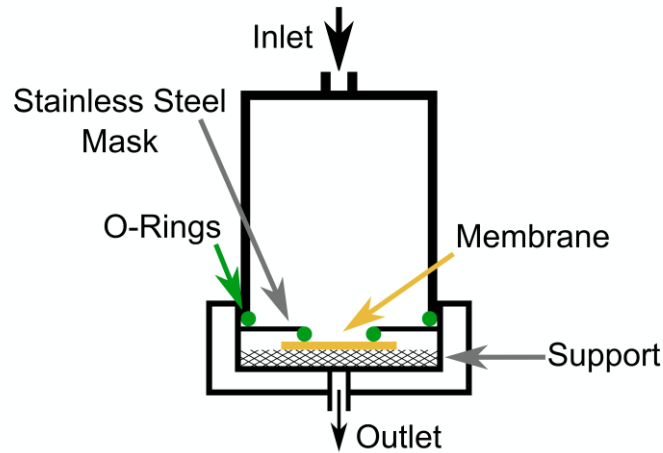


Figure 26: Schematic of the set-up for the water flux measurements using a dead-end filtration cell.

Time measurement was started together with the opening of the gas valve for the measurements pressure that was equal to the pressure in the first step. The time (t) measurement was stopped after a volume of 400 mL (V) had permeated the membrane. The pure water flux J was calculated as follows:

$$J = \frac{\dot{V}}{A} \quad (20)$$

Here A is the permeable surface area which was calculated by using the diameter of the circular hole of the cover and \dot{V} is the volume flow rate. Dividing by the used pressure, the pure water permeability of the porous membrane can be calculated with:

$$P = \frac{J}{\Delta p} \quad (21)$$

Here Δp is the transmembrane pressure that results from the used over pressure and the atmospheric pressure. As an approximation, the pressure of the gas at the valve also is the resulting transmembrane pressure.

5.9. Electrical Conductivity Measurements

Electrical conductivity measurements were performed with two different methods. The method used for the disc shaped porous membranes was the four probe method with four pins in a fixed probing head to measure the electrical sheet resistance. The device for the four-probe method measurements was RM3-AR from Jandel (Linslade, United Kingdom) with a probe spacing of 1 mm. To compensate for the irregularity of the surfaces of the porous membranes, several

points in the centre area of the membranes were measured. The autodetection mode of the device was used to scan through the applied voltage. The autodetection mode automatically scans for linear increases in the sheet resistance to confirm the material as an ohmic resistor. The device scans from 0 mV to 150 mV and can detect a current of 10 nA to 99.99 mA. Extremely low and high values for the given sheet resistance by the device indicated improper contact with the surface and were omitted. The regularly and most often measured value of the measurement was used as the sheet resistance value. The electrical conductivity σ , which is the inverse of the specific electrical resistance ρ , was calculated from the sheet resistance R_s and the thickness of the sample $d_{membrane}$:

$$\sigma = \rho^{-1} = (R_s \cdot d_{membrane})^{-1} \quad (22)$$

Compression moulded and sintered flat rectangular samples were measured using the two probe method with crocodile clamps, using the device 2601A SYSTEM SourceMeter® (Keithley Instruments, Solon, USA) with crocodile clamps, also in direct current. Samples were coated with thin strips approximately 1 cm wide on both sides. The voltage range of the device is from 10 mV to 40 V and with a current range of 100 nA to 100 mA, up to a maximum of 3 A in full power source operation. One crocodile clamp was attached on each silver-coated side respectively. The device was set to measurement of electrical resistance in direct current and kept switched on for one hour before measurement to allow the device to properly heat up. A voltage of 6 V was applied to the samples. In 1 V steps the applied voltage was increased and decreased between 1 V and 10 V to check for a constant electrical resistance and confirm the material as an ohmic resistor.

The electrical conductivity σ was calculated from the measured resistance R of the sample and its dimensions:

$$\sigma = \rho^{-1} = \left(R \cdot \frac{A}{l}\right)^{-1} \quad (23)$$

The temperature dependence of the complex electrical conductivity (AC conductivity) of compression moulded samples was measured using the Novocontrol “Concept 40” broadband dielectric spectrometer, equipped with the Alpha-AN high resolution dielectric analyser and the nitrogen gas temperature controller Novocontrol Quatro Cryosystem (Novocontrol Technologies GmbH, Montabaur, Germany). Samples were prepared through compression moulding, identical to the sample preparation for the rheological analysis. The measurement

could successfully be performed only for UHMWPE/MWCNT because of its very high melt viscosity and elasticity. The viscosities of the melts of PEI/MWCNT and especially PP/MWCNT under the fixation pressure of the electrodes were too low and led to a significant outflow and deformation of the molten samples. This led to unusable measurements.

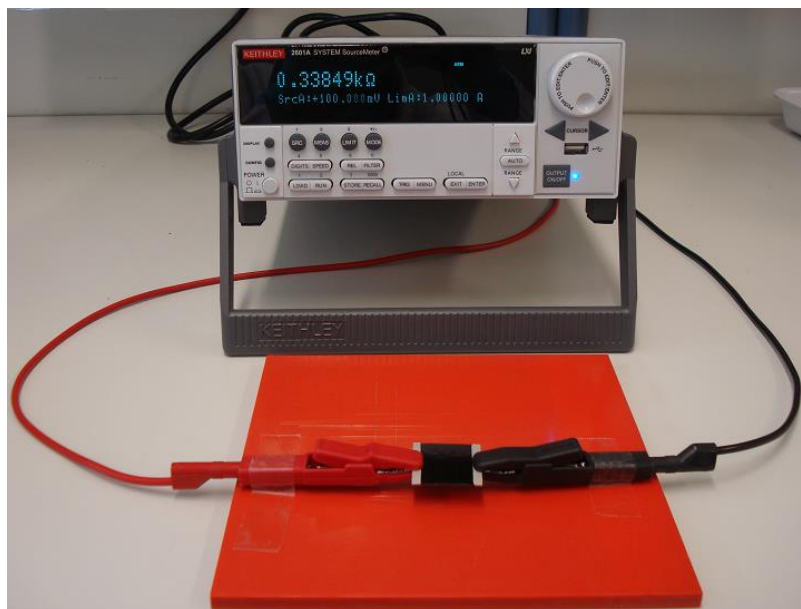


Figure 27: Photograph of the experimental set-up for the two-probe measurements. The sample is covered with conductive silver on two opposite ends and placed between two crocodile clamps.

Samples with MWCNT concentrations of 1.0 wt%, 3.0 wt% and 5.0 wt% were coated with conductive silver and placed between two gold-coated brass electrodes. Both the upper and the lower electrode had a diameter of 40 mm. The measurements were performed in one cycle with one heating step and one cooling step. The heating step was performed from 30 °C to 220 °C in increments of 10 °C, a stabilisation time of 60 s and a stability rate of 0.1 °C/min. The cooling step was performed from 220 °C to 30 °C, also in 10 °C increments and identical stability conditions. The conductivity was investigated in frequency sweep experiments in the frequency range from 10^{-2} to 10^7 Hz. The frequency of 1.78 kHz was arbitrarily chosen for comparison. The conductivity of the samples was found to be mostly independent of the used frequencies, except for the highest frequencies.

5.10. Conductive Atomic Force Microscopy

Conductive atomic force microscopy was performed using a Multimode 8 AFM device (Bruker Corporation, Billerica, USA) in C-AFM mode. Currents between 2 pA to 1 μ A can be detected with this set up. C-AFM imaging was performed in the cross section of ion-milled membranes and compression moulded samples of PEI/MWCNT 3.0 wt% and

UHMWPE/MWCNT 5.0 wt%. The samples were wrapped in a conductive metal foil and placed in a conductive metal sample holder. The sample and probe of the AFM device form an electric circuit. A current source gives the electric output and a current amplifier increases the signal to detect the actual flowing current through the sample.

With C-AFM, MWCNT pathways in the matrix can be confirmed for electrical conductivity and actual shape, as AFM can give a more precise image than SEM in the desired size range.

5.11. Tensile Testing

Tensile testing was performed according to DIN EN ISO 527. A universal testing device Z020 (Zwick Roell GmbH & Co. KG, Ulm, Germany) was used. Traverse speed was set to 1 mm/min for the measurement of the Young's modulus between 0% and 0.25% and to 50 mm/min afterwards until the failure of the sample. For the determination of the Young's modulus, an extensometer device "makroXtens" (Zwick Roell GmbH & Co. KG, Ulm) was used. The sample shape type was Type 5A. Samples were produced through compression moulding. The given values for stress and strain are both nominal.

6. Results and Discussion

6.1. Thermal Analysis

Thermal analysis through TGA and DSC was performed to investigate if the addition of MWCNT leads to any measurable differences and if yes, to what degree. Since sintering was performed as a purely thermal process through heating of the whole material⁶, changes in crystallisation behaviour, thermal stability, melting temperature or glass transition temperature would lead to direct differences in the sintering behaviour and also the resulting sintered porous membranes. For compression moulding, there is a direct relation to shrinking behaviour and melt behaviour.

The initial thermal decomposition temperature $T_{1\%}$ was set as the temperature at which 1% of the material was lost. More common in the literature are 5% and 10%, but a stricter 1% was chosen to be closer to an actual initial decomposition point. A lower percentage was not feasible due to sensitivity of the measurement device. The temperature of maximum degradation rate T_{DR} was the temperature at which the degradation rate as the first derivative of the relative mass over temperature reached its global maximum.

6.1.1. Thermogravimetric Analysis

6.1.1.1. Polyetherimide

Polyetherimide as high performance thermoplastic polymer is well-known for its thermal stability and low amount of smoke development. The TGA measurements of the pristine PEI powder and the decorated powder confirmed this. The key values are listed in **Table 1**. The material is not completely lost from the crucible through pyrolysis, but instead brittle, black and solid foam remains inside.

No significant difference was found for $T_{1\%}$ or T_{DR} . There is a notable trend for $T_{1\%}$ from pristine PEI at 507 °C to PEI/MWCNT 3.0 wt% at 511 °C, with 4 °C this is a small increase. The difference is even smaller for T_{DR} where the materials either show 539 °C or 540 °C.

⁶ Methods such as hot gas convection and microwave could be controlled in a way to only heat the outer parts of the powder particles.

Table 1: Thermal degradation temperatures for varying MWCNT concentrations of PEI. The heating rate was 10 K/min in argon atmosphere.

| Polyetherimide | | |
|---------------------|--|---|
| MWCNT Concentration | Initial Decomposition Temperature $T_{1\%}$ | Temperature of Maximum Degradation Rate T_{DR} |
| [%] | [°C] | [°C] |
| 0 | 507 | 540 |
| 0.2 | 505 | 539 |
| 0.5 | 507 | 539 |
| 1.0 | 510 | 539 |
| 1.5 | 511 | 539 |
| 2.0 | 510 | 540 |
| 2.5 | 511 | 539 |
| 3.0 | 511 | 540 |

Therefore, the addition of MWCNT does not appear to notably change the thermal stability of the composite powder compared to the pristine powder.

6.1.1.2. Ultra-High Molecular Weight Polyethylene

For the TGA measurement of UHMWPE, the process had to be adapted compared to PEI, as was described in Chapter 5.1. It should again be mentioned that the particle filter of the TGA device had to be changed after each measurement to avoid the risk of blocking the gas stream and leading to the failure of the following measurement. It can therefore be assumed that the parts of material, which are taken with the gas stream, are significantly larger than for PEI.

Ultra-high molecular weight polyethylene, just like most PE, is not a polymer suitable for application at high temperatures. Generally a complete or near-complete loss of the measured mass due to pyrolysis was observed for PE. As was expected, UHMWPE is thermally less stable than PEI. The key values are listed in **Table 2**.

Table 2: Thermal degradation temperatures for varying MWCNT concentrations of UHMWPE. The heating rate was 10 K/min in argon atmosphere. No significant differences were found.

| Ultra-High Molecular Weight Polyethylene | | |
|--|--|---|
| MWCNT Concentration | Initial Decomposition Temperature $T_{1\%}$ | Temperature of Maximum Degradation Rate T_{DR} |
| [%] | [°C] | [°C] |
| 0 | 415 | 481 |
| 0.2 | 422 | 484 |
| 0.5 | 411 | 478 |
| 1.0 | 413 | 471 |
| 1.5 | 430 | 484 |
| 2.0 | 430 | 480 |
| 2.5 | 419 | 482 |
| 3.0 | 417 | 473 |
| 5.0 | 413 | 476 |

From the experiments it was found that UHMWPE shows more fluctuations in the two properties, but also shows no direct correlation to the MWCNT concentration. The highest value for $T_{1\%}$ is 430 °C for 1.5 and 2.0 wt%, two of the low quality powders⁷, while the lowest value of 411 °C was found for 0.5 wt%. The material UHMWPE/MWCNT 5.0 wt% with the highest MWCNT concentration shows a lower value of 413 °C for $T_{1\%}$ than pristine UHMWPE at 415 °C. A differently varying and MWCNT concentration independent pattern was found for T_{DR} , where the highest or lowest value of $T_{1\%}$ does not directly correlate to the corresponding value for T_{DR} .

From this it can be concluded that the addition of MWCNT does not show a significant influence on the thermal degradation behaviour of the decorated powder compared to pristine UHMWPE.

⁷ This will be discussed in more detail for with scanning electron micrographs of the powders, but generally only 1.0, 3.0 and 5.0 wt% were found to show effective and sufficiently homogenous decoration of the powder particles

6.1.1.3. Polypropylene

Polypropylene as a polyolefin is comparable to polyethylene in its thermal degradation behaviour. Unlike for UHMWPE, the high mass loss did not lead to any problems with the filter of the TGA device, making frequent filter changes unnecessary. As there was no expected influence of the particle size of the pristine PP, it was only analysed as a mixture of the two particle size contingents. The composite powder was analysed as individually for the particle size contingents due to their expected differences in surface-coverage with MWCNT.

Table 3: Thermal degradation temperatures for varied MWCNT concentrations and particle size of PP. The heating rate was 10 K/min in argon atmosphere.

| Polypropylene | | |
|------------------------|--|---|
| MWCNT Concentration | Initial Decomposition Temperature $T_{1\%}$ | Temperature of Maximum Degradation Rate T_{DR} |
| [%] | [°C] | [°C] |
| 0 | 390 | 458 |
| 5.0 (0.355 – 1.000 mm) | 385 | 467 |
| 5.0 (1.000 – 1.800 mm) | 395 | 469 |

For $T_{1\%}$, no significant difference was found. While pristine PP is at 390 °C, PP/MWCNT 5.0 wt% shows initial decomposition at 385 °C for the smaller powder contingent and 395 °C for the larger one. The values are displayed in **Table 3**.

The difference is larger for T_{DR} . Here the addition of 5.0 wt% MWCNT shows an increase of 9 °C for the small powder 11 °C. This indicates that for PP, the addition of 5.0 wt% MWCNT leads to a change in the thermal degradation behaviour.

6.1.2. Differential Scanning Calorimetry

6.1.2.1. Polyetherimide

The DSC analysis of polyetherimide showed that there was no change of the glass transition temperature for any MWCNT concentration compared to pristine PEI, as is shown in **Table 4**. The deviation of 1 °C for 0.2, 0.5 and 2.0 wt% to the measured 214 °C of pristine PEI are too small to be a material property and are within experimental scatter.

Table 4: Glass transition temperatures for varying MWCNT concentrations of PEI. The heating rate was 10 K/min in nitrogen atmosphere.

| Polyetherimide | |
|---------------------|------------------------------|
| MWCNT Concentration | Glass Transition Temperature |
| [%] | [°C] |
| 0 | 214 |
| 0.2 | 213 |
| 0.5 | 213 |
| 1.0 | 214 |
| 1.5 | 214 |
| 2.0 | 213 |
| 2.5 | 214 |
| 3.0 | 214 |

6.1.2.2. UHMWPE

It was shown in the literature that CNT can act as nucleation sites for crystalline regions in PE and this way decrease crystallinity, with the explanation that crystalline areas always have amorphous areas inside and surrounding them, due to the polymer chain alignments.^[108, 109] With more, smaller nuclei compared to fewer, larger ones, the fraction of amorphous areas also increases. The higher the number of individual crystalline region is, the higher the fraction of amorphous regions surrounding them is. From this influence of the MWCNT decoration on the crystallisation behaviour of the UHMWPE was expected. As **Table 5** shows, this is not the case. The melting temperature is either 133 °C for pristine UHMWPE or 132 °C for UHMWPE/MWCNT independent of concentration, which is not a significant difference. In the first measurement cycle during the heating step, the crystallinity of the materials differs in a notable way. The powder was not turned into a melt during the decoration process. Therefore the crystallinity calculated from the first heating step gives at least some indication of possible differences between the decorated powders. Pristine UHMWPE and the low quality⁸ powder with 2.0 wt% MWCNT show the highest crystallinity of 58%. The other MWCNT

⁸ As mentioned above, low-quality means an ineffective and inhomogeneous coverage of the UHMWPE particles with MWCNT.

concentrations with good or more acceptable quality are between 55% and 51%, showing a lower amount of crystallinity. From this, it would appear that there is an influence of the decoration process depending on the MWCNT concentration. As was mentioned in Chapter 3.4, the powders were not identically prepared. Further, the exact influence of the processing is not known.

Table 5: Melting temperatures and crystallinity values for varying MWCNT concentrations of UHMWPE. The heating rate was 10 K/min in nitrogen atmosphere.

| Ultra-High Molecular Weight Polyethylene | | | | |
|--|---------------------|-------------------------------------|-------------------------------------|--|
| MWCNT Concentration | Melting Temperature | Crystallinity 1 st Cycle | Crystallinity 2 nd Cycle | |
| [%] | [°C] | [%] | [%] | |
| 0 | 133 | 58 | 48 | |
| 0.2 | 132 | 55 | 48 | |
| 0.5 | 132 | 53 | 48 | |
| 1.0 | 132 | 53 | 47 | |
| 1.5 | 132 | 51 | 46 | |
| 2.0 | 132 | 58 | 50 | |
| 2.5 | 133 | 51 | 45 | |
| 3.0 | 132 | 52 | 46 | |
| 5.0 | 132 | 52 | 47 | |

While it was found that the addition of nanoparticles can increase the crystallinity of PE in high energy ball milling, the energy input difference between ball milling and dry mixing is significant.^[110] Additionally, for pristine UHMWPE, high energy ball milling can decrease the percentage of crystallinity.^[111] Due to the significantly lower energy input, an influence of the dry mixing on the crystalline structure of the UHMWPE powder with the addition of MWCNT therefore is unlikely.

The heating step of the second measurement cycle with a full crystallisation in the presence of the MWCNT during the first cooling step gives a different image. The second measurement cycle typically is described as “erasing” the processing history of the measured material, because it is heated and cooled under the DSC controlled conditions. In the second cycle, there is no significant difference between the MWCNT concentrations. Here, 2.0 wt% shows the highest percentage of crystallinity at 50%, while pristine UHMWPE at 48% shows 2% less.

The highest concentration of 5.0 wt% MWCNT shows 1% less than pristine UHMWPE. During all cooling steps the crystallisation temperature was found to be 117 °C independent of MWCNT concentration.

As the MWCNT were not homogeneously distributed over the whole UHMWPE volume, but rather only on the outer shall of the powder particles, their interaction should be limited to a relatively very small fraction of the UHMWPE particle volume. The results from the DSC show that this appears to be the case.

6.1.2.3. PP

The material differences for PP are much smaller than for the other two materials, as only one MWCNT concentration was used, with only a difference in particle size. As for TGA, pristine PP was only analysed as a mixture of the particle sizes because no effects of the particle size were expected for DSC measurements.

Table 6: Melting temperatures and crystallinity values for varying MWCNT concentrations of PP. The heating rate was 10 K/min in nitrogen atmosphere.

| Polypropylene | | | |
|-------------------------|--------------------------|---|---|
| MWCNT Concentration [%] | Melting Temperature [°C] | Crystallinity 1 st Cycle [%] | Crystallinity 2 nd Cycle [%] |
| 0 | 165 | 33.3 | 44.7 |
| 5.0 (Small) | 166 | 34.3 | 43.0 |
| 5.0 (Large) | 168 | 34.3 | 42.1 |

It is shown in **Table 6** that the melting temperature slightly increases from 165 °C for PP to 166 °C for the small powder with 5.0 wt% MWCNT and to 168 °C for the larger powder. It is also shown that the crystallinity of the different powder particles is near identical in the first heating cycle.

The second cycle shows a slightly decreased crystallinity of the pristine PP compared to the small decorated powder and to the large decorated powder. As the particles are significantly larger than they are in the other materials, the decoration with 5.0 wt% MWCNT leads to a significantly higher surface coverage. The larger the particles are, the smaller the surface

volume fraction per weight is. Therefore it is reasonable that the crystallinity decreases and is the smallest for the larger powder particle size contingent.

Polypropylene also shows a significantly different behaviour during the cooling steps, compared to PEI and UHMWPE. For the decorated powders, a second crystallisation peak appears at higher temperatures and overlaps with the crystallisation peak also present in pristine PP. The temperature values are shown **Table 7** with the crystallinity of the material for comparison.

Table 7: Crystallisation temperatures for varying MWCNT concentrations of PP for the second cycle. The heating rate was 10 K/min in nitrogen atmosphere. For PP/MWCNT a second crystallisation peak was found.

| Polypropylene | | | |
|---------------------|--|--|-------------------------------------|
| MWCNT Concentration | 1 st Crystallisation Temperature T _{c1} | 2 nd Crystallization Temperature T _{c2} | Crystallinity 2 nd Cycle |
| [%] | [°C] | [%] | [%] |
| 0 | 113 | - | 44.7 |
| 5.0 (Small) | 113 | 135 | 43.0 |
| 5.0 (Large) | 107 | 131 | 42.1 |

The presence of the second peak shows the formation of a second type of crystalline structure. While the first peak corresponds to the monoclinic α -modification of the crystalline structure, the second one corresponds to the hexagonal β -modification.^[112] Interestingly, the second peak appears in the cooling step of the first and second measurement cycle, but is not visible in the melting peak of the second cycle. This is in good agreement with the slightly reduced crystallinity, as a second crystallisation type also indicates more different crystalline regions and therefore more amorphous regions between them.

6.2. Morphology of Powders

6.2.1. Polyetherimide

The used powder of polyetherimide was Ultem™ 1000P, the commercial non-filled variation of Ultem™ 1000. The powder has a relatively large particle size and with a broad distribution, as can be seen in **Figure 28** and **Figure 29**. The median particle diameter (D50) measured via laser diffraction is 80.13 μm . More than 90% of the particles have a diameter smaller than

206.52 μm (D90) and 10% smaller than 18.33 μm (D10). The cumulative frequency of the particle diameters is shown in **Figure 29**. Most particles are not spherical, but rather elongated in one dimension to varying degrees with some string-like particles in the extreme cases.

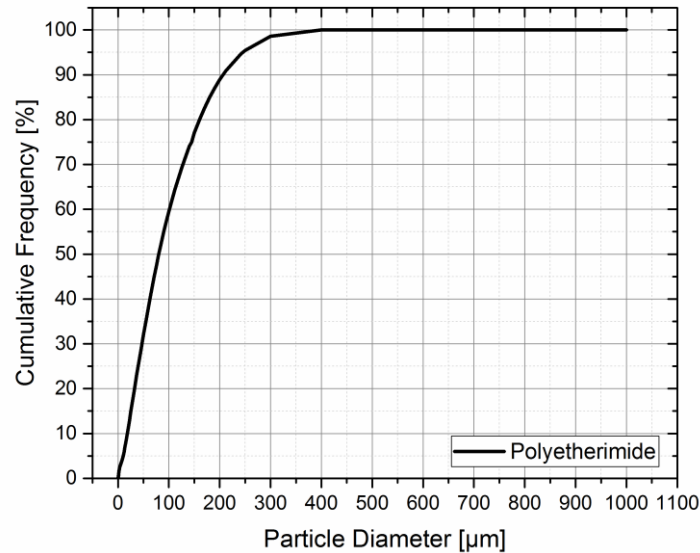


Figure 28: Cumulative frequency of the particle size distribution of the PEI powder. Measurement through laser diffraction was performed by QUANTACHROME GmbH & Co. KG.

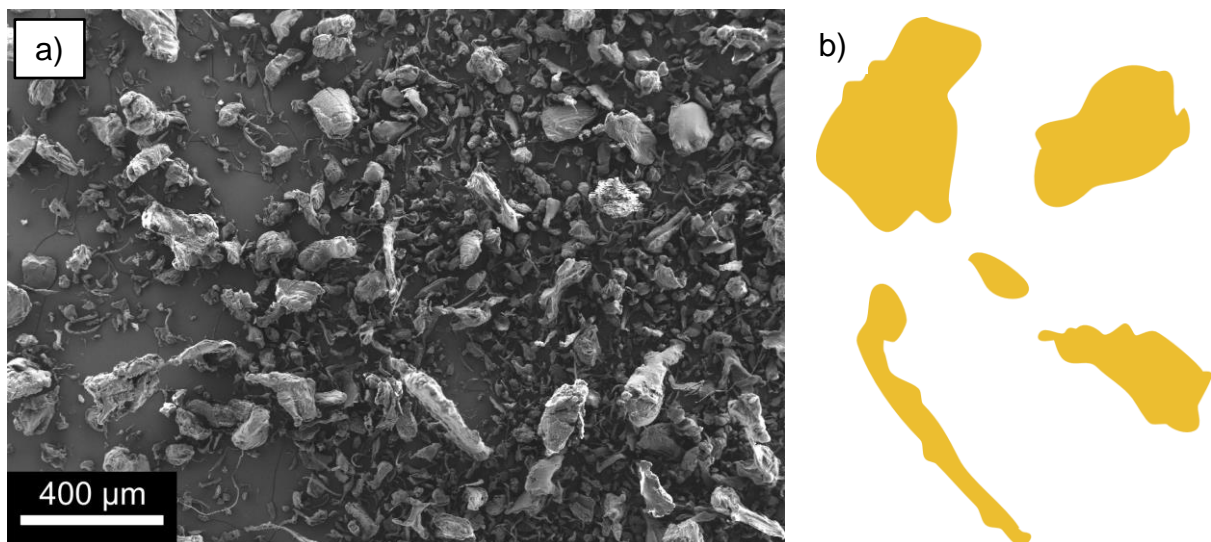


Figure 29: Scanning electron micrograph of the pristine PEI (a) and schematic shapes of particles (b) (not to scale). The powder has a large particle size and high variation in particle shapes. The surfaces of the particles are partially smooth and rugged with cracks and grooves.

A higher magnification in **Figure 30** shows that the surfaces of the powder particles are predominantly not smooth, but rather irregular. Cracks, grooves and gaps can be found on virtually all particles. Overall, the surface has a rugged appearance. The particle shape suggests,

that the polymer was not directly synthesised into the powder, but rather that source polymer material could have been milled using a large scale mill such as a cutting mill or jet mill.

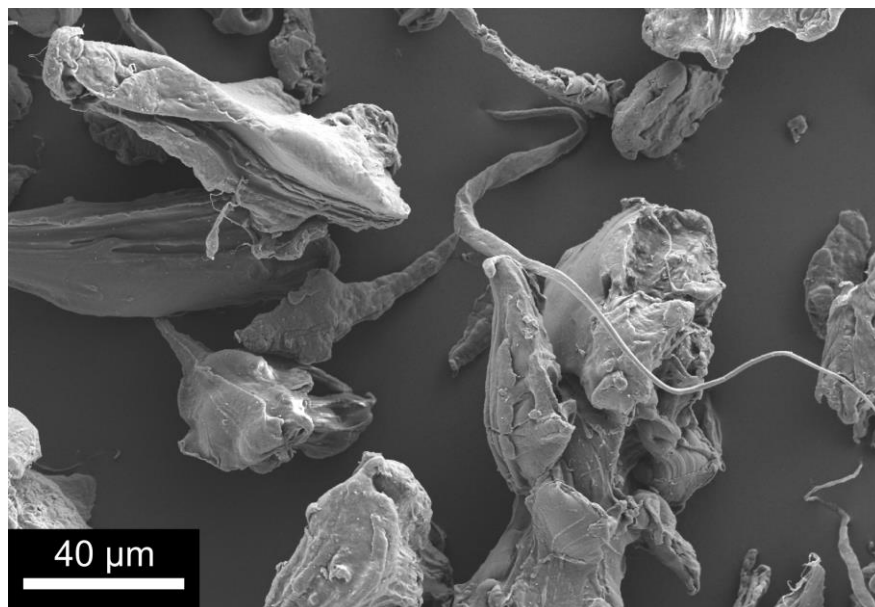


Figure 30: Magnification of PEI powder particles. The irregularities on the surface and large variety of particle shapes are clearly visible.

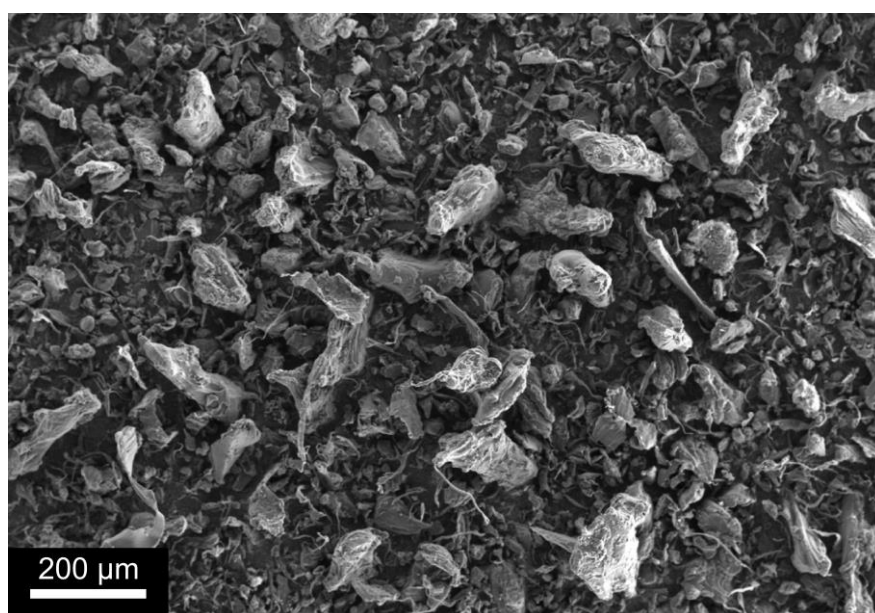


Figure 31: SEM of PEI/MWCNT 2.0 wt%. On a large scale, no differences to the pristine PEI powder are visible.

The powder was decorated in a chemical-free purely mechanical process. As the micrographs from SEM suggest, this mechanical process provides high enough energy to distribute the MWCNT on the particle surfaces and for the largest part avoid pronounced agglomeration of the MWCNT. Yet, the energy input in the process is not high enough to cause any visible

changes in particle sizes or shapes. No visible fractures, cuts, notches or roundings on particles that could have happened during the process were found.

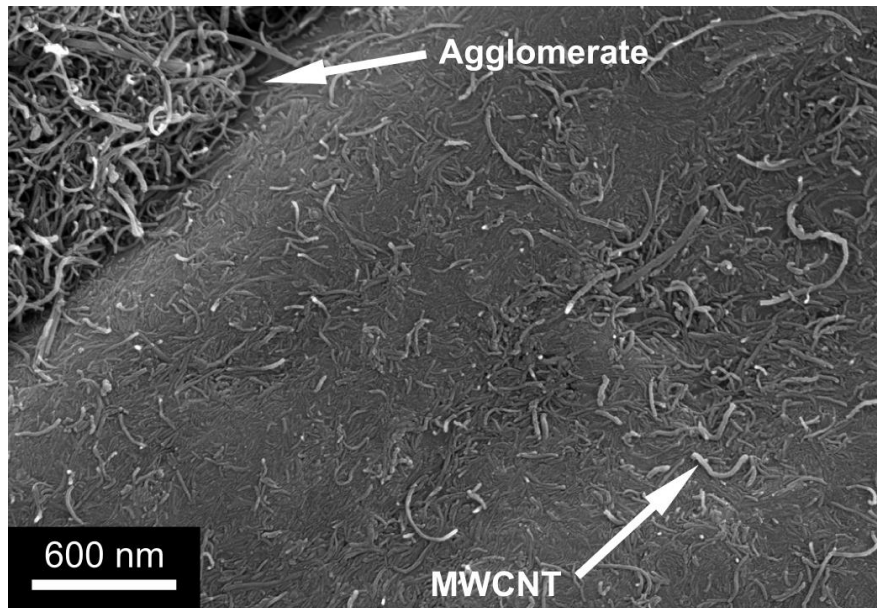


Figure 32: Surface of a powder particle of PEI/MWCNT 3.0 wt%. Most parts of the powder particles are covered by individual MWCNT that are tangentially aligned to the surface that form a network. In the top-left corner a MWCNT agglomerate is visible that formed in a groove on the particle surface.

The decoration process appeared to have effectively covered the surface of all powder particles. The flat parts of the surface were efficiently covered in individual or small groups of MWCNT that are tangentially aligned to the surface (**Figure 32** and **Figure 33**).

These MWCNT form a percolated network on the powder particle surfaces. Some MWCNT were found that were partially oriented away from the surface with typically a length of 130 to 150 nm.

As is the most common problem with MWCNT, agglomerates could not be avoided by the decoration process. But while agglomerates formed, it is important to notice where on the PEI particles they could be found. As could be seen from SEM analysis, most agglomerates can be found in the grooves and gaps of the powder particles (**Figure 32** and **Figure 34**). SEM analysis showed that most agglomerates are around $4.1 \pm 2.0 \mu\text{m}$ in diameter.

The exact agglomeration process of the MWCNT is yet not determined. Two ways seem most possible: The MWCNT could have formed away from the powder particles and the grooves and gaps "caught" smaller agglomerates and formed them into the nest-like agglomerates found in the SEM analysis. The other possibility is that the grooves acted as nucleation sites for the MWCNT by catching and holding them. Both processes could also happen at the same time.

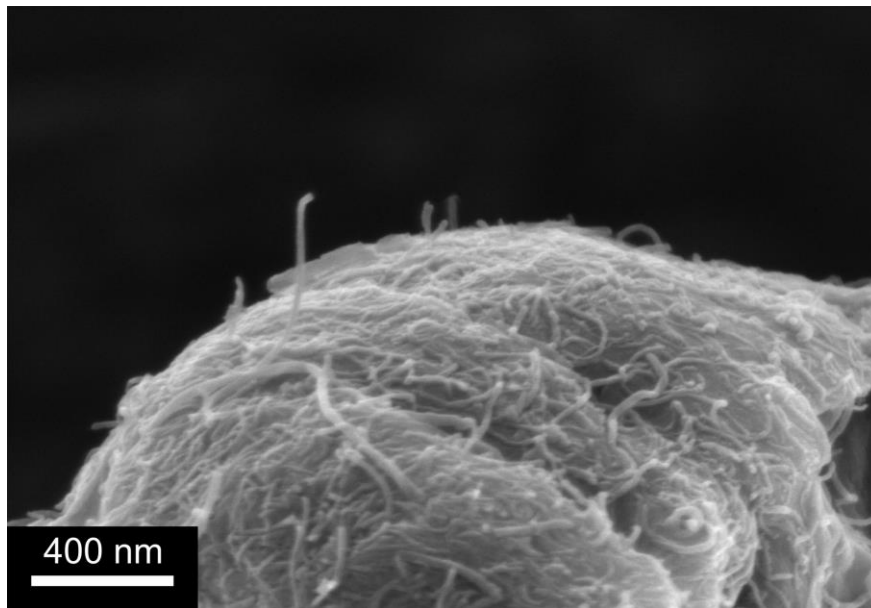


Figure 33: Magnification of the surface of a powder particle in PEI/MWCNT 3.0 wt%. Most particles are clearly tangentially aligned to the surface. Few MWCNT partially reach away from the surface at different angles.

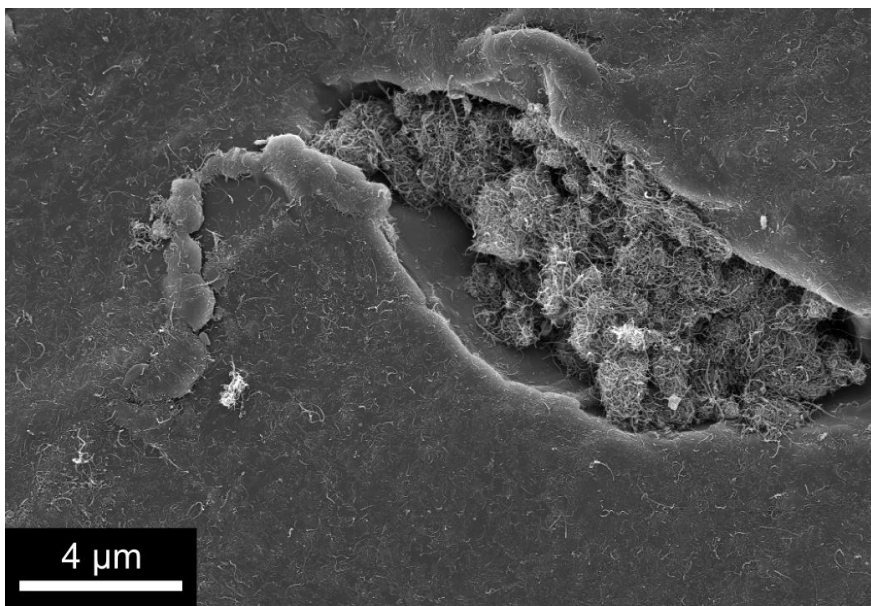


Figure 34: Surface of a powder particle in PEI/MWCNT 1.0 wt% with a groove that acted as a nucleation site for the formation of a MWCNT agglomerates.

Still, the shape of the agglomerate nests in the grooves does not clearly exclude one or the other. In the test powder with 5.0 wt% MWCNT and most particles around 500 μm in diameter, large numbers of agglomerates can be seen on their own, unattached to a particle. But the powder particles are clearly over-saturated with MWCNT (**Figure 35**), as all grooves and gaps appear to be overfilled with MWCNT and are no longer visible. So these free MWCNT could have broken off from the particles after forming on them.

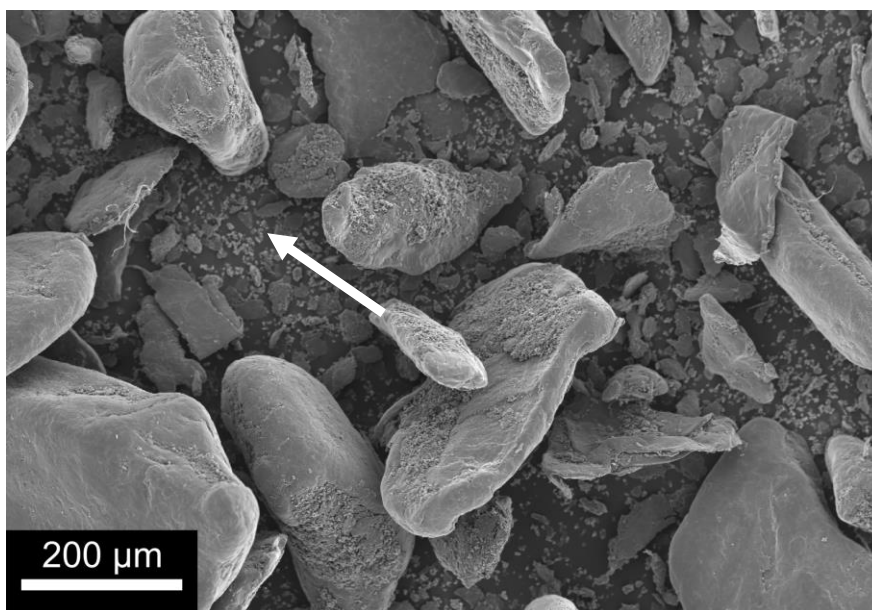


Figure 35: Powder particles of test powder PEI/MWCNT 5.0 wt%. Particles were prepared from Ultem™ 1000 by cut-milling the pellets through a 500 μm mesh. Clearly visible are the large nests of MWCNT on the surface, covering large parts of the surfaces. The smallest, bright particles at the bottom in picture plane are MWCNT agglomerates (arrow).

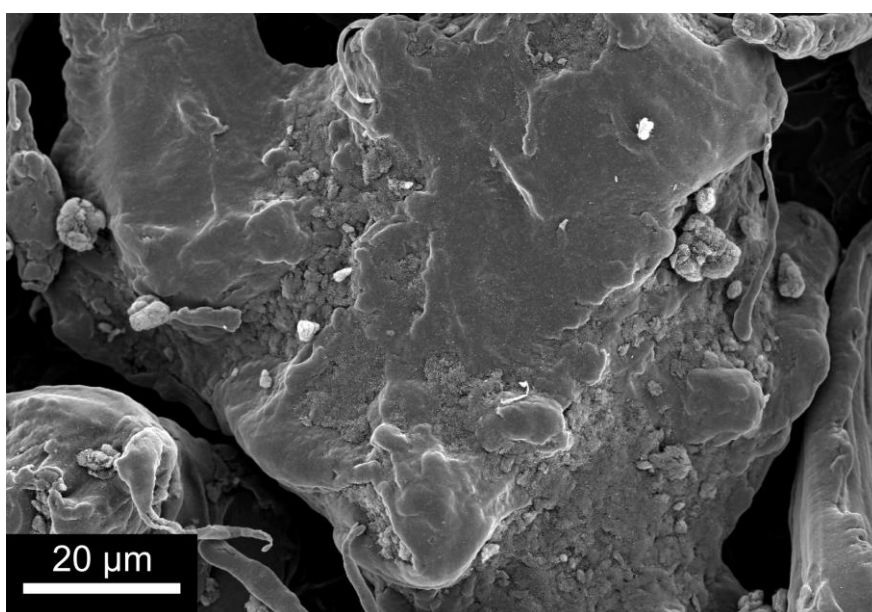


Figure 36: Surface of a powder particle in PEI/MWCNT 3.0 wt% with pronounced grooves and gaps. While the whole smooth surface of the powder particle is covered with tangentially aligned MWCNT, the grooves and gaps are significantly filled with numerous MWCNT agglomerates.

Because the test powder PEI/MWCNT 5.0 wt% had much larger particles than the decorated particles of Ultem™ 1000P, the available surface area was much smaller. With this smaller surface area, the test powder PEI/MWCNT 5.0 wt% was clearly oversaturated with MWCNT. For the largest used MWCNT concentration of 3.0 wt%, no fallen-off MWCNT agglomerates could be found. Therefore, the powder does not appear to be over-saturated with MWCNT.

Still, as can be seen in **Figure 36**, the agglomerate numbers on large particles with large cracks, gaps and grooves are very numerous and the nests can span more than 100 μm in length. As will be discussed further down, this prominence of MWCNT and agglomerates has a significant influence on the sintering behaviour, as they are virtually inert under polymer sintering conditions.

6.2.2. Ultra-High Molecular Weight Polyethylene

The used powder GUR[®] 2126 is a commercially available non-filled powder of ultra-high molecular weight polyethylene. Compared to the commercial powder of PEI, the UHMWPE powder has a relatively small particle size and shape deviation (see **Figure 37** to **Figure 39**). The overall shape is comparable to “popcorn”. The median particle diameter measured via laser diffraction is 35.21 μm (D50). More than 90% of the particles have a diameter smaller than 56.96 μm (D90) and 10% smaller than 15.53 μm (D10).

The powder particle surface is smooth, but shows pronounced gaps and cracks. Round parts protrude from the particles, with variations in size but overall similar in shape to each other. Some particles show stronger irregularities in shape, such as long, thin protrusion or kinks, elongating in one dimension.

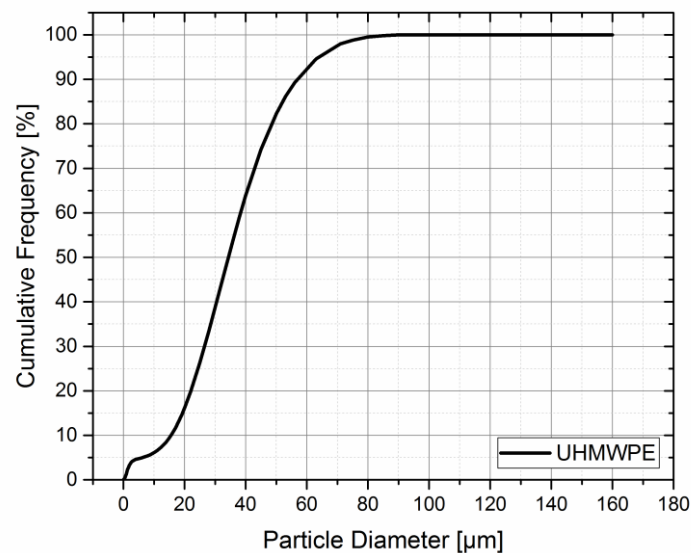


Figure 37: Cumulative frequency of the particle size distribution of the UHMWPE powder. Measurement through laser diffraction was performed by QUANTACHROME GmbH & Co. KG.

Since UHMWPE is highly ductile and difficult to reduce in size with mechanical methods and the particle shape is overall regular, it is very likely that the polymer was synthesized into the

powder shape. This will become relevant in the discussion of the sintered UHMWPE membranes, because the morphology of the material apparently greatly differed from the further processed UHMWPE, at least on the surface.

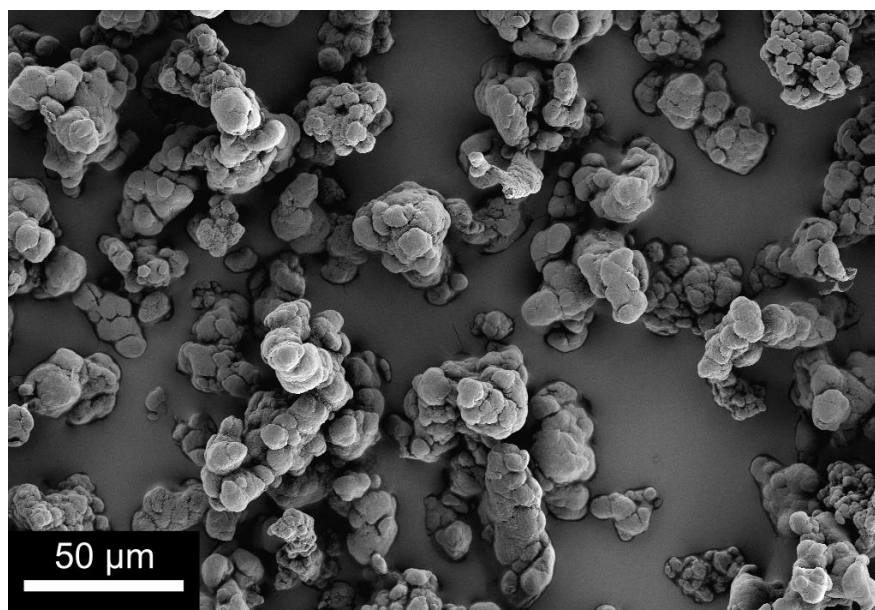


Figure 38: Scanning electron micrograph of the pristine UHMWPE powder. Visible is the relatively small deviation in particle size and shape.

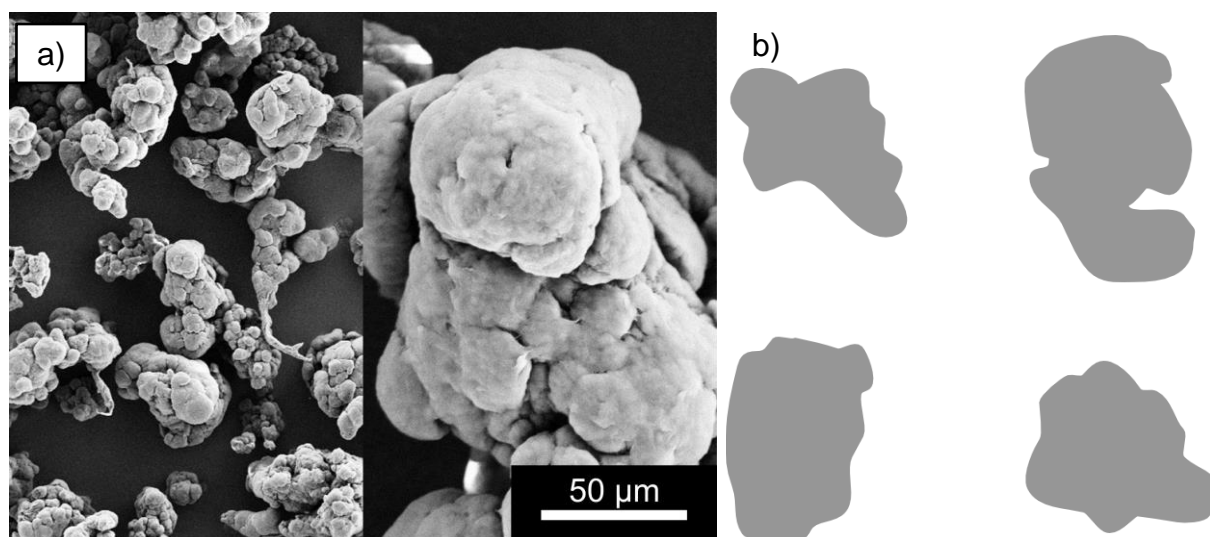


Figure 39: Scanning electron micrograph of the pristine UHMWPE (a) and schematic shapes of particles (b) (not to scale). The powder has a relatively small particle size and relatively small shape variation compared to PEI. The surfaces of the particles are smooth and broken up by cracks and grooves.

UHMWPE is a semi-crystalline thermoplastic polymer with a lamellar crystalline structure.^[96] The absence of such a visible lamellar crystalline structure on the powder particle surfaces is of high interest for the decorated powder particles. Significant reorganisation of the UHMWPE chains into the lamellar crystalline structure on the surface might result in displacements of MWCNT. This will be further discussed in the morphology of the sintered UHMWPE and UHMWPE/MWCNT membranes and the conductivity measurements.

Compared to PEI, the decoration process stood before two new challenges. One was the much smaller average particle size with a significantly different shape, the other the material itself. UHMWPE is semi-crystalline, significantly softer than the amorphous PEI and also has a lower density.

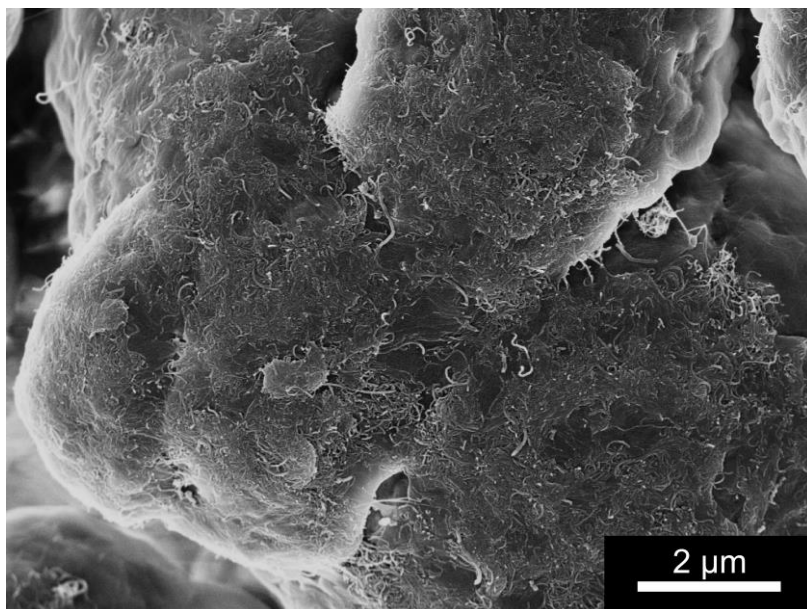


Figure 40: Surface of a particle of UHMWPE/MWCNT 1.0 wt%. The outside-faced smooth parts of the surface are decorated with tangentially aligned individual MWCNT that form a network. The inner parts of the surface in the cracks and grooves is only partially covered with MWCNT, parts closer to the particle centre are not decorated.

Overall, the decoration process was successful in covering surfaces of the UHMWPE powder particles with individual MWCNT at the MWCNT concentrations 1.0 wt%, 2.0 wt%, 3.0 wt% and 5.0 wt%. For these concentrations, a significant amount of MWCNT is tangentially aligned to the surface and spans smaller gaps on the particle surfaces, but the much smaller gaps and grooves on UHMWE particles appear to be much harder to cover for the decoration process. As can be seen in **Figure 40**, the gap in the upper right corner of the powder particle in UHMWPE/MWCNT 1.0 wt% appears to be mostly pristine, with only very few silhouettes, that could be isolated MWCNT.

For reasons that remain still unknown, the decoration process is strongly ineffective for the MWCNT concentrations lower than 1.0 wt% and between 1.5 wt% and 2.5 wt%. Details will be discussed further below in the discussion of the results of the electrical conductivity measurements. As can be seen in **Figure 41** for UHMWPE/MWCNT 2.0 wt%, the decoration process appears to no longer fully cover the powder particles with MWCNT. Instead, surfaces mostly show small areas covered with MWCNT and relatively fewer individual MWCNT that do not form an effective network. Instead, a large amount of MWCNT appears to have agglomerated on its own and without being attached to a particle. These agglomerates can be seen with the naked eye, but do not appear in prepared SEM samples, as they do not effectively attach to the tacky sample holder surface.

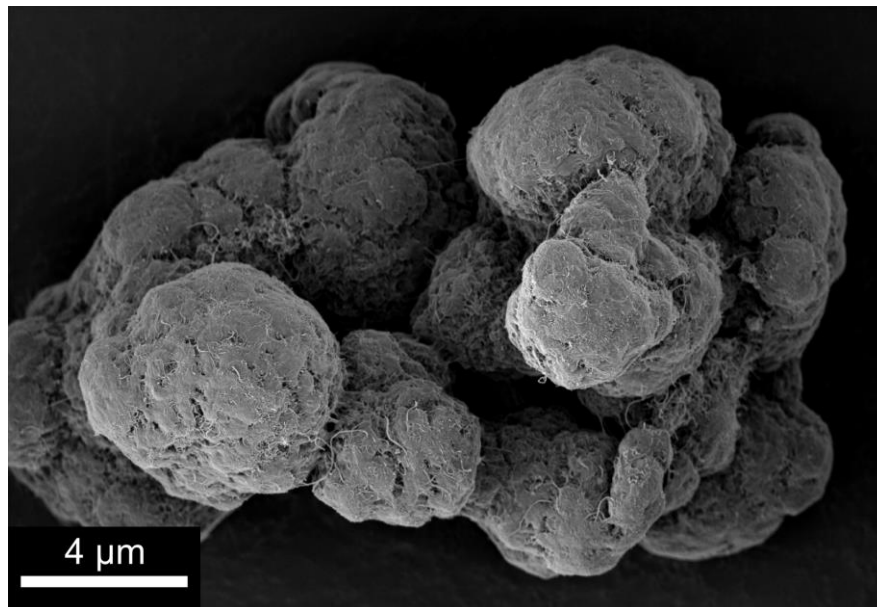


Figure 41: Magnification of a powder particle of UHMWPE/MWCNT 2.0 wt%. The decoration process appears to be ineffective in fully covering the particle with MWCNT and create a percolated network of tangentially aligned MWCNT on the surface.

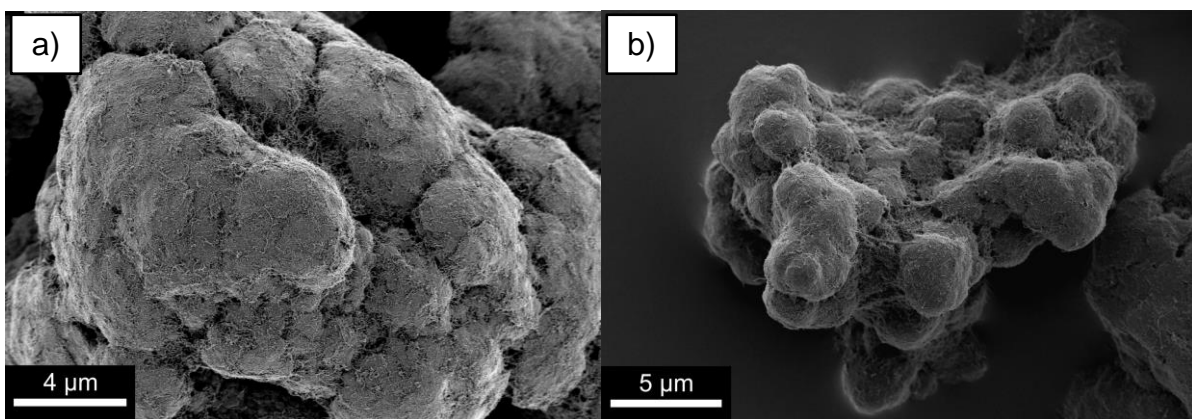


Figure 42: Magnifications of particles of UHMWPE/MWCNT 5.0 wt%. These particles appear to be very well covered in MWCNT, with many MWCNT spanning across the gaps on the powder particles.

At higher concentrations, the decoration of the particle surfaces apparently starts to compete with the agglomeration process again. For UHMWPE/MWCNT 5.0 wt%, **Figure 42** shows the very dense coverage of the particle surfaces with MWCNT. Few parts of the surfaces are at least not partially covered with MWCNT that are connected to the overall percolated network of MWCNT. The covering with MWCNT also spans over the gaps and grooves of the particles, giving the decorated particles a kind of “webbed” look.

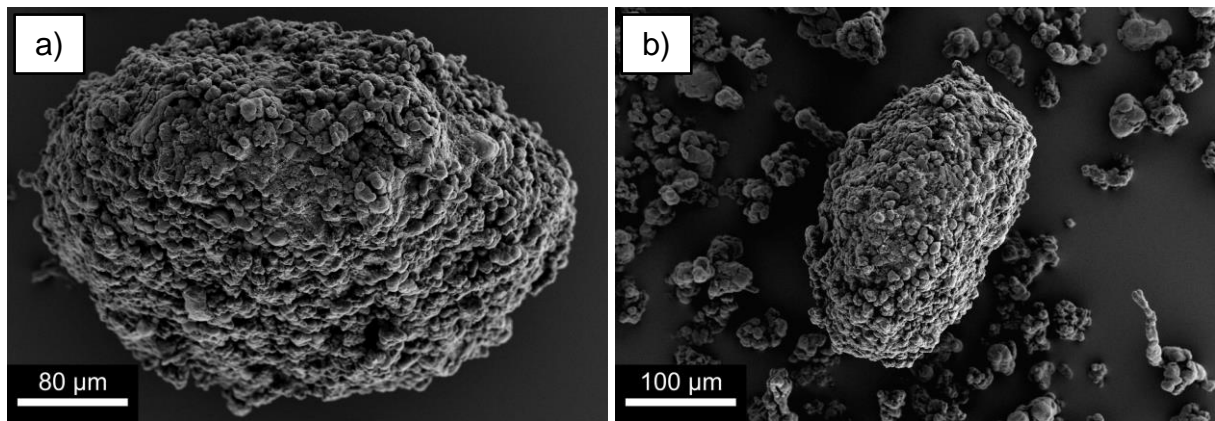


Figure 43: Micrographs of UHMWPE-MWCNT bundles in the decorated powder of UHMWPE/MWCNT 5.0 wt%. Powder particles and MWCNT apparently can form a bundle that binds an unknown amount of MWCNT, which then are no longer available for an even distribution on the particle surfaces.

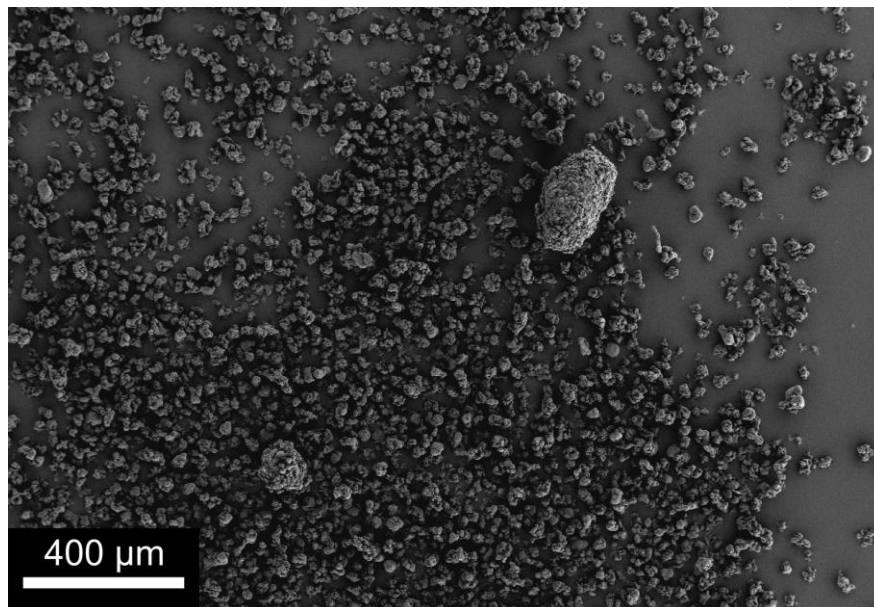


Figure 44: Lower magnification of the powder of UHMWPE/MWCNT 5.0 wt%. This micrograph illustrates that the cluster particles are relatively numerous compared to the individual, non-clustered decorated powder particles.

But, the number of MWCNT agglomerates is visibly increased between 1.0 wt%, 3.0 wt% and 5.0 wt%, which again do not attach to the tacky sample holder for the powder. Nevertheless, for UHMWPE/MWCNT 5.0 wt% clusters of UHMWPE particles and MWCNT (see **Figure 43**) agglomerates could be found, as they more readily attached.

These clusters are significantly larger than the original powder particles in any given dimension. The outside appears to be predominantly made up out of highly MWCNT-covered UHMWPE powder particles. In-between these attached particles, advances of MWCNT agglomerates of strongly varying dimensions stick out.

It is shown in **Figure 44** that the clusters are clearly much larger than the individual powder particles. It can also be seen that these clusters apparently are not very numerous. Still, because of their overall size and composition they, like MWCNT agglomerates, have to be considered for all discussions of results from experiments. This was not such a concern for polyetherimide, which is a large factor in the decorated powders for setting them apart in terms of MWCNT-induced property changes.

6.2.3. Polypropylene

The used powder Moplen[®] HF 500 H is a commercially available non-filled powder of polypropylene. Compared to PEI and UHMWPE, this powder has a larger particle size. Polypropylene was chosen as a supplementary polymer for compression moulding and only used with the highest feasible MWCNT concentration of 5.0 wt%, which from preliminary tests was the most promising concentration with low concern for loose MWCNT in the powder.

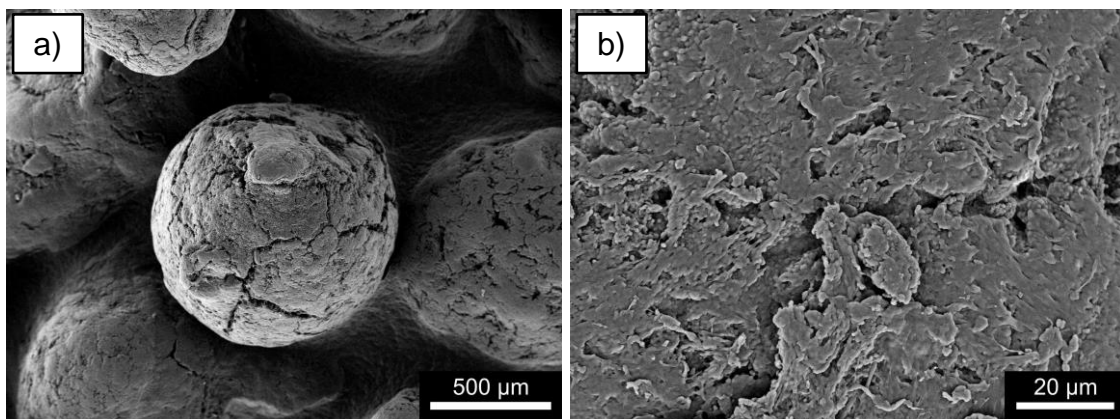


Figure 45: Scanning electron micrograph of a polypropylene particle (a). The particles are generally spherical in shape with long cracks along the surface. The surface (b) is rugged and irregular with relatively small grooves and gaps.

The particle shape is generally spherical with relatively small amounts of irregularities (see **Figure 45**), such as elongations from the surface, incomplete fusion between two particles and grooves on the surface.

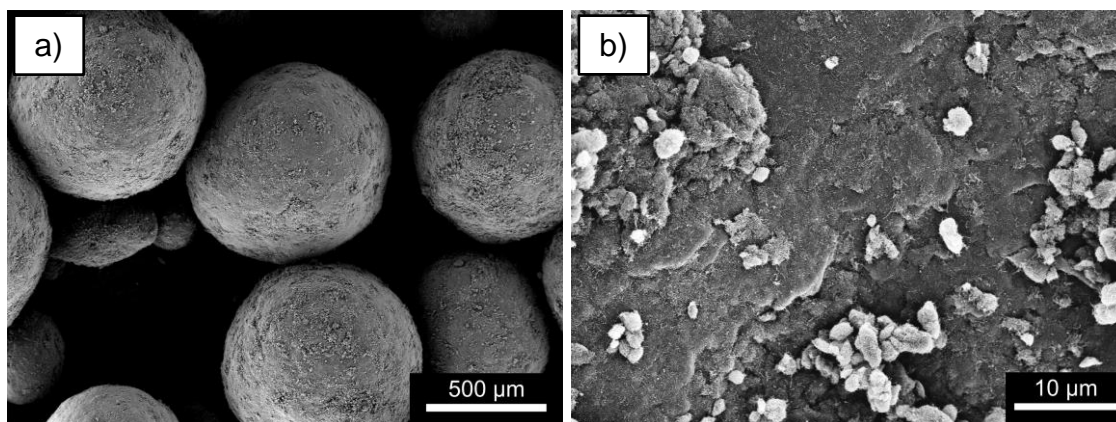


Figure 46: Scanning electron micrograph of the polypropylene powder particles decorated with 5.0 wt% MWCNT (a). The gaps that were visible in the pristine powder are no longer visible. The rugged surface also has been smoothed (b). Small agglomerates around 5 μm are visible as individual entities or more often in nest. The particle surface appears to be fully covered with individual MWCNT that are tangentially aligned to the surface and the aforementioned agglomerates.

Compared to the pristine powder particles, the decorated powders surfaces appear to be overall smoother at lower magnifications. The noticeable cracks are not visible anymore. They appear to have been at least partially and close to the surface filled by MWCNT and agglomerates of MWCNT. Even though a relatively large number of MWCNT filled the gaps, the majority appear to be tangentially aligned as individual nanotubes or attached to the surface in agglomerates of around 5 μm in diameter and nests thereof.

6.2.4. Summary for Morphology of Powders

The decoration process worked effectively for the PP and PEI powder. For UHMWPE, there is a noticeable amount of agglomerates, apparently MWCNT-void surface parts and lack of bound agglomerates to the powder particles in varying degrees, depending on the powder. Overall, UHMWPE/MWCNT 1.0 wt% appears to have the best balance between MWCNT bound to the surface and free agglomerates, making it the prime benefactor of the MWCNT decoration.

The comparison of the scanning electron micrographs of PP/MWCNT, PEI/MWCNT and UHMWPE/MWCNT, allow for the assumption that at least for these chosen materials, the particle size appears to be of noticeable importance, less so than the shape. The reason for this is not yet known. At least the following hypothesis can be given: The powder particles for PEI and PP could be large enough to bind large numbers of MWCNT tangentially to their surface

before a competitive formation of MWCNT agglomerates can gain the upper hand. Formed MWCNT agglomerates then are small and around 5 μm in diameter, which is efficiently small compared to the powder particles. These agglomerates can then attach to the irregularities on the large powder particles. Additionally, the mass of the large powder particles could work against MWCNT formations by breaking up forming larger agglomerates during the mixing process, analogue to a ball-milling process. The UHMWPE particles lack the diameter, mass and size of surface irregularities compared to the other powders, which under the given hypothesis would then result in the visible problems of the decorated powder.

Yet for this, a further and more focused investigation is necessary to discover the actual mechanisms behind the powder decoration process and MWCNT agglomerate formation in the decorated powders.

6.3. Rheology of Polymers and Composites

The rheological analysis of the polymer and composites were performed to acquire information about the properties of the respective melts. It is known from the literature, that the addition of MWCNT changes the rheological behaviour and viscosity of polymer/MWCNT composites.^[113, 114] The measured curves served as guidelines. The exact influence on the coalescence and densification during sintering and compression moulding cannot be exactly concluded from these results, because the distribution of the MWCNT and their influence on the matrix in the powder form and the compression moulded samples for rheology respectively can be assumed to be different. In shear rheology with plate-plate geometry, the whole sample is put through shear deformation, with a non-homogenous strain distribution in the measured sample. Since the deformation is kept in the linear-viscoelastic range for the respective polymer, a good estimation to the material is given. The rheological analysis enables qualitative information to the interpretation of the sintering behaviour and more directly allows for insight in the interpretation of the compression moulding of the composites.

Results for PEI and PEI/MWCNT are displayed as master curves calculated through the time-temperature superposition principle to the reference temperature of 300 °C. The shift of the curves acquires a larger frequency range than from 10^{-2} to 10^2 rad/s, because the measured curves at a given temperature are distinctly different in their shapes. In a master curve, the angular frequency is written as $a_T\omega$ to show that a shift was performed through the horizontal shift factor a_T . For PP and PP/MWCNT, master curves were calculated but showed only a slight increase to the frequency range, due to their strong similarity to each other.

The results for UHMWPE and UHMWPE/MWCNT are displayed as the measured frequency sweeps at the given processing temperature. UHMWPE and PP are semi-crystalline polymers with glass transition temperatures well below the melting temperature. The curves at the individual measured temperatures differ only slightly from each other between temperatures, resulting in only very small frequency shifts for a master curve.

6.3.1. Polyetherimide and Composites

For the rheological analysis of pristine PEI and MWCNT concentrations of 1.0 wt%, 2.0 wt% and 3.0 wt% were chosen to represent the influence of the MWCNT on the composites. Measurements were performed as frequency sweeps from the highest frequency of 10^2 rad/s to the lowest of 10^{-2} rad/s with an amplitude of 5% and at temperatures 240 °C, 260 °C, 280 °C, 300 °C and 320 °C. The results were used to create a master curve with reference temperature 300 °C, using the software LSSHIFT.

Polyetherimide shows the typical behaviour of a thermoplastic amorphous homopolymer with a solid-like behaviour with a higher G' at higher frequencies and a fluid-like behaviour with a higher G'' at lower frequencies. The cross-over of the curves is at 87 rad/s for pristine PEI, 81 rad/s for PEI/MWCNT 1.0 wt%, 73 rad/s for PEI/MWCNT 2.0 wt% and 47 rad/s for PEI/MWCNT 3.0 wt%. This means that the more elastic solid-like behaviour of the melts is shifted to lower frequencies with increasing MWCNT concentration. The rubbery region, where G' shows a plateau, is in the frequency range from the cross-over frequency to approximately 10^4 rad/s for the pristine PEI. For PEI/MWCNT, no rubbery region is visible as only the slope of the curve of G' decreased. At higher frequencies to the highest accessible frequencies, the material behaviour shifts to the glassy regime.

The shear moduli G' and G'' almost reach slopes of 2 and 1 respectively for pristine PEI at lower frequencies. These slopes relate to the terminal behaviour of the Maxwell model. At this region, the disentanglement of the chains and the chain diffusion become fast enough relative to the measurement time to allow for a liquid-like behaviour of the fluid melt, while still retaining viscoelastic properties.

The addition of MWCNT increases the overall values for G' and G'' of the whole frequency range, with the highest increase for G' at lower frequencies. The increase of G' is caused by the elastic deformation of the MWCNT and their interaction with the polymer matrix as well as by inter-MWCNT interactions.

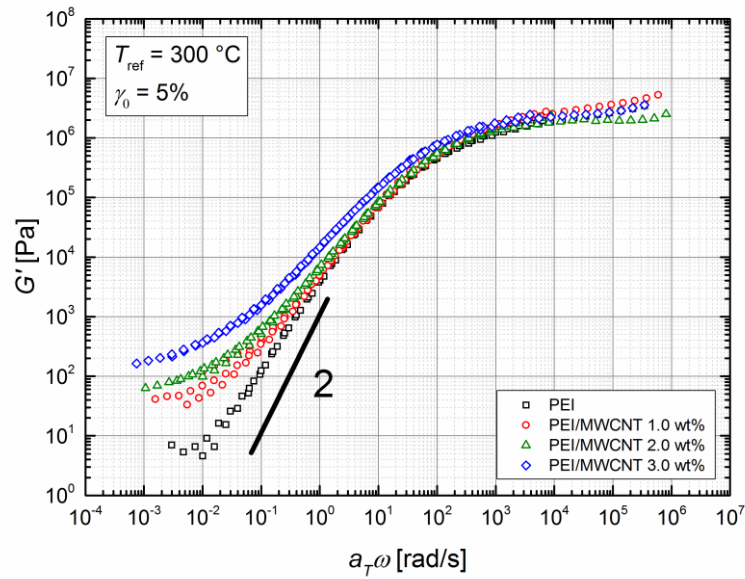


Figure 47: Master curves of the storage modulus G' for pristine polyetherimide, PEI/MWCNT 1.0 wt%, PEI/MWCNT 2.0 wt% and PEI/MWCNT 3.0 wt% composites. The increase of the storage modulus at low frequencies is pronounced due to the stronger influence of the MWCNT at lower frequencies. The reference temperature was 300 °C.

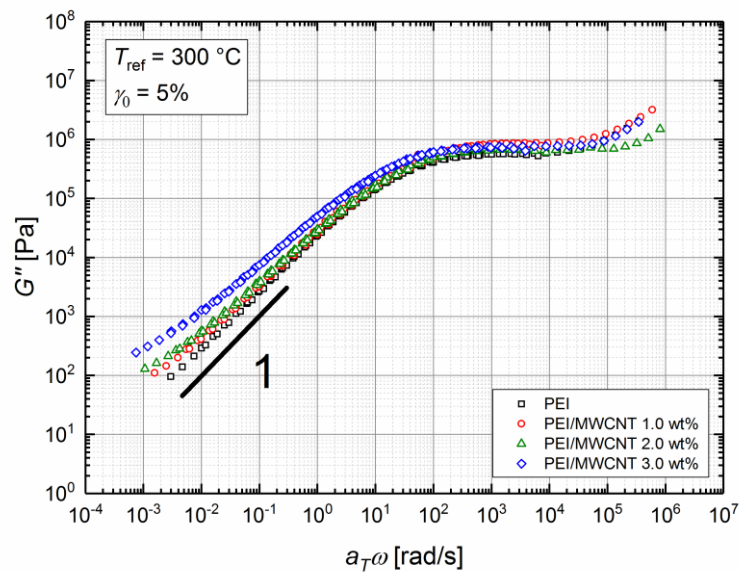


Figure 48: Master curves of the loss modulus G'' for pristine polyetherimide, PEI/MWCNT 1.0 wt%, PEI/MWCNT 2.0 wt% and PEI/MWCNT 3.0 wt% composites. The overall increase of the loss modulus is less pronounced than for G' . The reference temperature was 300 °C.

The increase of G'' results from the spatially non-uniform velocity field around the MWCNT and the resulting inner friction, which is caused by the addition of the MWCNT. At higher angular frequencies, the properties of the PEI matrix dominate the behaviour of the composite, resulting in marginally higher values for PEI/MWCNT and no notable difference relating to the MWCNT concentration.

The zero-shear viscosity for pristine PEI at the reference temperature of 300 °C is around 29000 Pa s. In the covered frequency range, it is not clear if a true plateau value was found. At the lowest frequencies, a small indication of a possible further increase can be seen. For PEI/MWCNT no zero-shear viscosity could be found as there is no measured maximum plateau value of the absolute value of the complex viscosity. Further, instead of a plateau as seen for pristine PEI, the composite materials reach a nearly linearly increasing viscosity on the double-logarithmic scale at the lower frequencies.

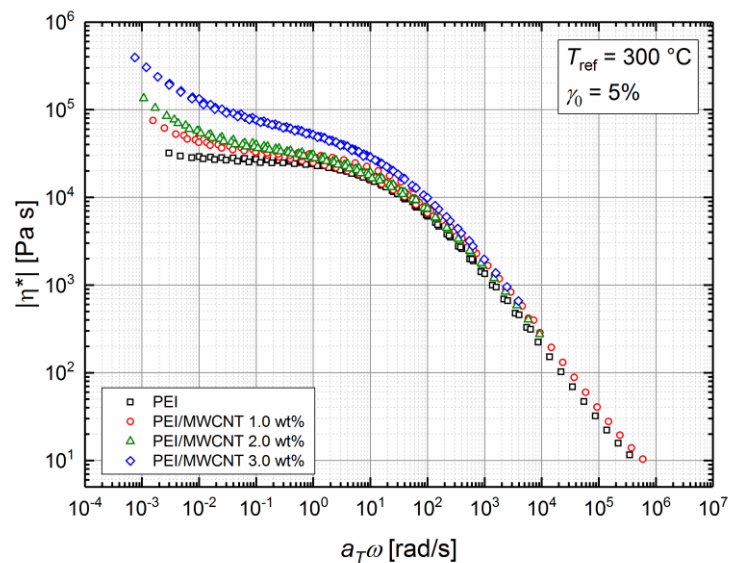


Figure 49: Master curves of the absolute value of the complex viscosity of pristine PEI, PEI/MWCNT 1.0 wt%, PEI/MWCNT 2.0 wt% and PEI/MWCNT 3.0 wt%. Corresponding to the changes in G' and G'' due to the MWCNT influence, the viscosity and curve shape is significantly increased and changed at lower frequencies.

The addition of MWCNT to polyetherimide led to a shift to a more solid-like behaviour at lower frequencies and a notable increase in viscosity. Both will alter the sintering and compression moulding behaviour of the composite material compared to the pristine polymer.

6.3.2. Ultra-High Molecular Weight Polyethylene and Composites

For the rheological analysis of pristine UHMWPE and MWCNT concentrations of 1.0 wt%, 3.0 wt% and 5.0 wt% were chosen to represent the influence of the MWCNT on the composites. Measurements were performed as frequency sweeps from the highest frequency of 10² rad/s to the lowest of 10⁻² rad/s with an amplitude of 1% and at the temperature 220 °C.

The results of the frequency sweeps for the storage modulus G' are shown in **Figure 50** and for the loss modulus G'' in **Figure 51**. UMWPE is a semi-crystalline homopolymer with a very high molecular weight. The results for G' correspond to the entanglement plateau. With

increasing angular frequency the storage modulus also increases moderately over the whole measured frequency range. Further, the loss modulus G'' is smaller than G' over the whole frequency range.

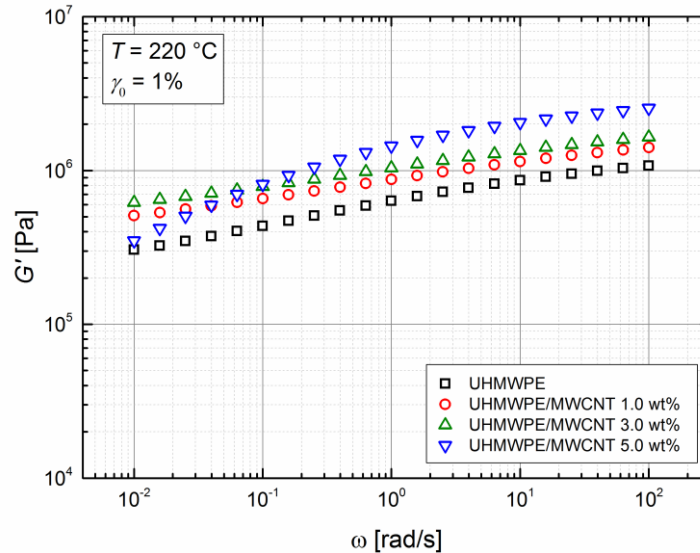


Figure 50: Curves of the storage modulus G' of pristine UHMWPE, UHMWPE/MWCNT 1.0 wt%, UHMWPE/MWCNT 3.0 wt% and UHMWPE/MWCNT 5.0 wt% composites. The storage modulus increases with increasing MWCNT concentration, while the behaviour at 5.0 wt% strongly differs. The measurement temperature was 220 °C.

Therefore the UHMWPE melt behaves solid-like in the measured range. With the addition of 1.0 wt% of MWCNT, both G' and G'' are increased over the whole measured frequency range. For UHMWPE/MWCNT 1.0 wt% the slope of G' decreases less at lower frequencies compared to pristine UHMWPE, while the curve of G'' comparably shows a decreased curvature.

The same effect was found for UHMWPE/MWCNT 3.0 wt%, with a significant increase compared to the pristine UHMWPE and with a notably smaller increase compared to UHMWPE/MWCNT 1.0 wt%. The MWCNT concentration of 5.0 wt% shows a peculiar behaviour compared to the other MWCNT concentrations and pristine UHMWPE. The values of G' and G'' are increased between 1 rad/s and 100 rad/s compared to the less increased values for 1.0 wt% and 3.0 wt%. Yet, at frequencies lower than 1 rad/s there is an unexpected behaviour in form G' being lower and G'' being higher than expected from 1.0 wt% and 3.0 wt%.

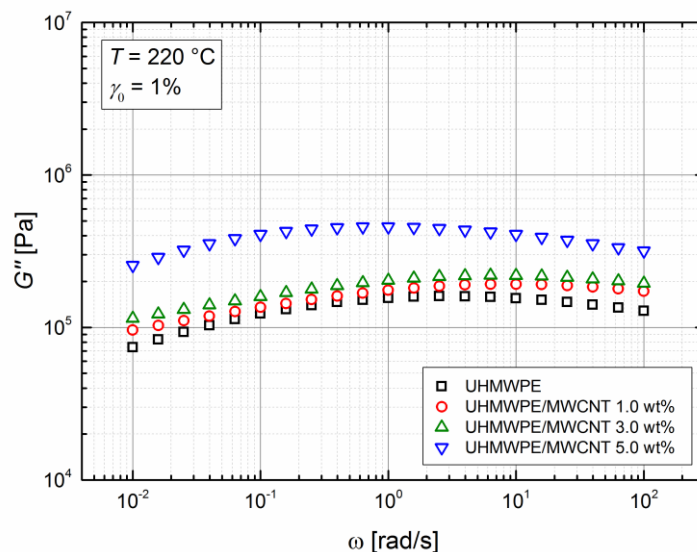


Figure 51: Curves of the loss modulus G'' of pristine UHMWPE, UHMWPE/MWCNT 1.0 wt%, UHMWPE/MWCNT 3.0 wt% and UHMWPE/MWCNT 5.0 wt% composites. The loss modulus increases with increasing MWCNT concentration to different degrees, depending on the angular frequency. The measurement temperature was 220 °C.

Below 1 rad/s there is a notable decrease for G' with it becoming increasingly lower than for 1.0 wt% and 3.0 wt% with decreasing angular frequency. At 0.063 rad/s G' for 5.0 wt% is lower than for 3.0 wt%, at 0.025 rad/s lower than for 1.0 wt% and at 0.01 rad/s the value is close to the value of pristine UHMWPE. For G'' the values are significantly increased over the whole frequency range with a shift of the peak to lower frequencies, compared to the other MWCNT concentrations and the pristine UHMWPE. The peak is at 0.631 rad/s for 5.0 wt%, at 6.31 rad/s for 3.0 wt%, at 10 rad/s for 1.0 wt% and 2.512 rad/s for pristine UHMWPE. The peak is the maximum value of G'' and corresponds to the maximum of the dissipative energy loss during the dynamic deformation. The shift to a lower frequency indicates that a slower dissipative process has a stronger influence compared to the other MWCNT concentrations or pristine UHMWPE.

A possible explanation is the use of a non-volatile liquid for the decoration process of the powder at 5.0 wt% MWCNT by the project partner FutureCarbon GmbH. At higher frequencies, the elastic properties of both the UHMWPE matrix and the added MWCNT dominate the behaviour, while at lower frequencies a plasticizing influence of the non-volatile liquid could lead to the increase of the viscous characteristics of the melt.

The absolute value of the complex viscosity is shown in **Figure 52** and shows the extremely high viscosity of the UHMWPE melt. Overall the magnitude of the complex viscosity of UHMWPE is increased by the addition of MWCNT, with a smaller increase from 1.0 wt% to

3.0 wt%, than from pristine UHMWPE to 1.0 wt%. Only at frequencies below 0.1 rad/s there is a further increase with 5.0 wt% that is also the largest increase in viscosity. Between 0.1 rad/s and 0.01 rad/s, the viscosity becomes lower than for 3.0 wt% and also 1.0 wt%.

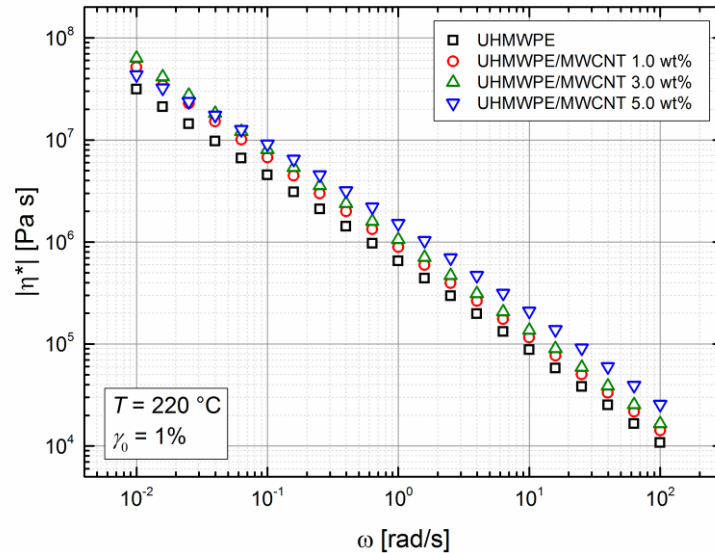


Figure 52: Curves of the absolute value of the complex viscosity of pristine UHMWPE, UHMWPE/MWCNT 1.0 wt%, UHMWPE/MWCNT 2.0 wt% and UHMWPE/MWCNT 3.0 wt%. Corresponding to the changes in G' and G'' due to the MWCNT influence, the viscosity and curve shape is increased.

The linear increase for pristine UHMWPE, the composites with 1.0 wt% and 3.0 wt% and the near-linear increase of the complex viscosity for the composite with 5.0 wt% on the double-logarithmic scale are caused by the very high relaxation times of the highly entangled molecules of the UHMWPE matrix melt. Analogue to G' and G'' , the slope of the increase of the complex viscosity decreases with decreasing angular frequency.

Due to its ultra-high molecular weight and the resulting strong entanglement of the polymer chains, the melt predominantly behaves like an elastic solid. This is also noticeable in the lack of a cross-over frequency of G' and G'' for the measured materials in the measured frequency range. The melt shows a rubbery behaviour even at lower frequencies and the samples mostly preserved their shape after removal from the rheometer. The overall increase in G' and therefore elastic properties is explainable by the elastic properties of the MWCNT, their interaction with the UHMWPE matrix and MWCNT-MWCNT interactions. Additional viscous MWCNT-MWCNT and MWCNT-polymer interactions through friction result in the small increase of G'' for UHMWPE/MWCNT compared to pristine UHMWPE.

For further analysis of the solid-like UHMWPE melt, creep recovery experiments were performed for 7,200 s at a creep stress of 500 Pa and 10,000 Pa respectively. Again in shear

with the same configuration as for the oscillating shear rheology. Creep recovery experiments allow for the determination of the flow behaviour at constant stress in particular at large times. Because of the ultra-high molecular weight of UHMWPE the chosen measurement time was not as usual larger than the average retardation time of the polymer chains, as this would have taken a substantial amount of time, but instead 7,200 s for both the loading phase and the recovery phase. The chosen time of 7,200 s is the used sintering time and therefore sufficiently allows for an estimation of the influence of creep on the sintering behaviour. The results are shown in **Figure 53**.

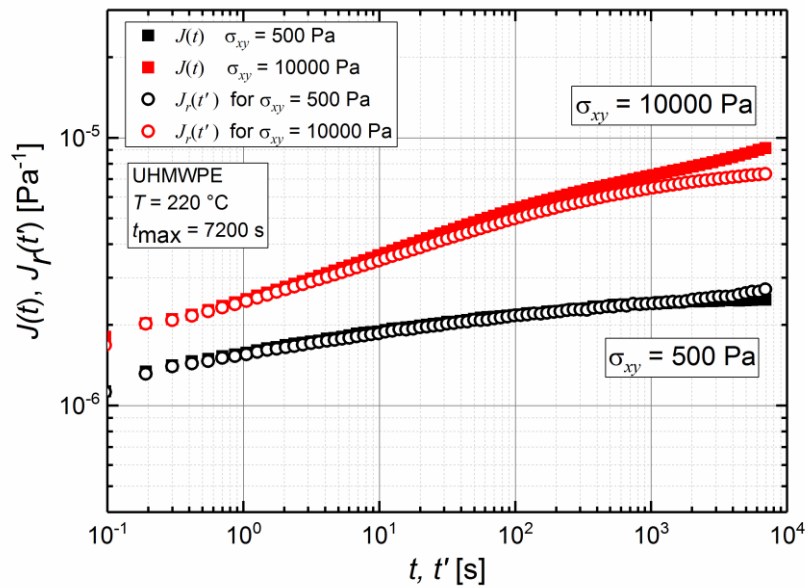


Figure 53: Creep compliance $J(t)$ and recovered creep compliance $J_r(t')$ in shear for pristine UHMWPE as a function of time t and recovery time $t' = t - t_{\max}$ respectively. The creep stresses were 500 Pa and 10,000 Pa, respectively with a creep time $t_{\max} = 7,200$ s and a measurement temperature of 220 °C.

The first experiment was performed with a loading stress of 500 Pa. Upon loading with 500 Pa, an instantaneous shear strain of around 0.06% is measured. Over the whole measurement time of 7,200 s for the loading phase, an approximately linear behaviour on a double-logarithmic scale for the creep compliance $J(t)$ and therefore the increase of the shear strain is observed. The final strain at 7,200 s was roughly doubled at 0.13%. At the end of the recovery phase, the recovered creep compliance $J_r(t')$ for 500 Pa shows no significant difference to $J(t)$. Increasing the shear stress to 10,000 Pa, a notably higher instantaneous shear strain of 2.5% was measured. At t_{\max} , the final strain was significantly higher at 9.23%. The curve shape of $J(t)$ for the creep shear stress of 10,000 Pa is slightly different from the curve shape of $J(t)$ at 500 Pa, which indicates a nonlinear response. For the smaller times up to 100 s, no significant differences between $J(t)$ and $J_r(t')$ were found. For times above 100 s up to 7,200 s, a slight difference between the curves of $J(t)$ and $J_r(t')$ can be seen, with only a notable difference around 7,200 s.

Because the curve shapes of $J(t)$ and $J_r(t')$ only show no differences for 500 Pa and only small differences for 10,000 Pa, the deformation was predominantly elastic. As the values for $J(t)$ and $J_r(t')$ for 500 Pa are very similar after t_{max} , the deformation can be assumed to be fully recoverable. For the applied creep stress of 10,000 Pa a slightly smaller value at t_{max} for $J_r(t')$ compared to $J(t)$ implies at least a small amount of irreversible deformation.

Therefore, it can also be assumed that the Laplace pressure, which is associated with the curvature of the molten particles and sintering bridges during coalescence, needs to exceed 10,000 Pa to induce a notable amount of creep deformation of the molten UHMWPE matrix during the sintering time of 7,200 s.

6.3.3. Polypropylene and Composites

Rheological analysis of pristine PP and MWCNT concentration of 5.0 wt% for the smaller particle contingent and the larger one were performed. Measurements were performed as frequency sweeps from the highest frequency of 10^2 rad/s to the smallest of 10^{-2} rad/s, with an amplitude of 5% and at temperatures 170 °C, 190 °C and 210 °C. The results were then shifted into a master curve with reference temperature 190 °C, using the software LSSHIFT.

Polypropylene as a semi-crystalline polyolefin is similar to UHMWPE in that the curve shape does not deviate notably from one temperature to another. Overall no significant changes in the curve shape are visible. For the larger powder contingent of PP/MWCNT 5.0 wt% at around 0.05 rad/s a slight decrease in the slope of the storage modulus G' is visible, without an equivalent for the loss modulus G'' . This is even less pronounced for the smaller powder contingent of PP/MWCNT 5.0 wt%.

While the curve shape is not changed with the addition of 5.0 wt% MWCNT, the overall values of G' and G'' are increased compared to the pristine PP. For pristine PP, the cross-over frequency was found to be around 7.5 rad/s, while for the smaller contingent of PP/MWCNT 5.0 wt% it was around 4.3 rad/s, and around 5.5 rad/s for the larger one. The shift of the solid-like behaviour to lower frequencies through the addition of MWCNT therefore is very small.

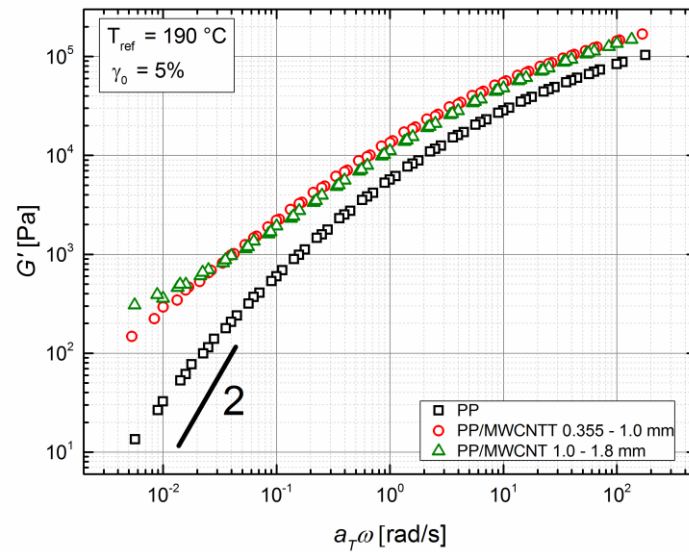


Figure 54: Master curve of the storage modulus G' for pristine PP and PP/MWCNT 5.0 wt% in two different size contingents. The elastic modulus is notably increased with the addition of the MWCNT concentration. The reference temperature was 190 °C.

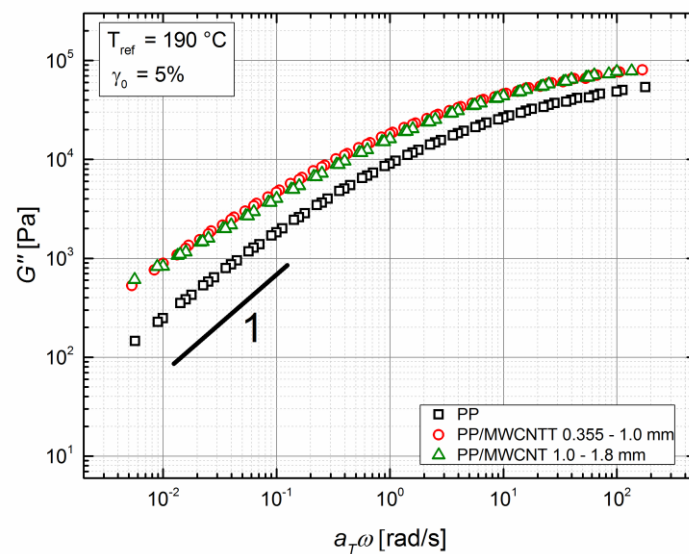


Figure 55: Master curve of the loss modulus G'' for pristine PP and PP/MWCNT 5.0 wt% in two different size contingents. The loss modulus is notably increased with the addition of the MWCNT concentration. The reference temperature was 190 °C.

At the lowest frequencies the curve for G' nearly reaches a slope of 2 and for G'' a slope of 1 on the double-logarithmic scale, which indicates a trend to a terminal flow regime. The slopes are closer to 2 and 1 respectively for pristine PP, compared to PP/MWCNT, which is comparable to the effect observed for PEI/MWCNT even though significantly less pronounced. While also not significantly pronounced, G' is slightly more increased compared to G'' for PP/MWCNT compared to pristine PP.

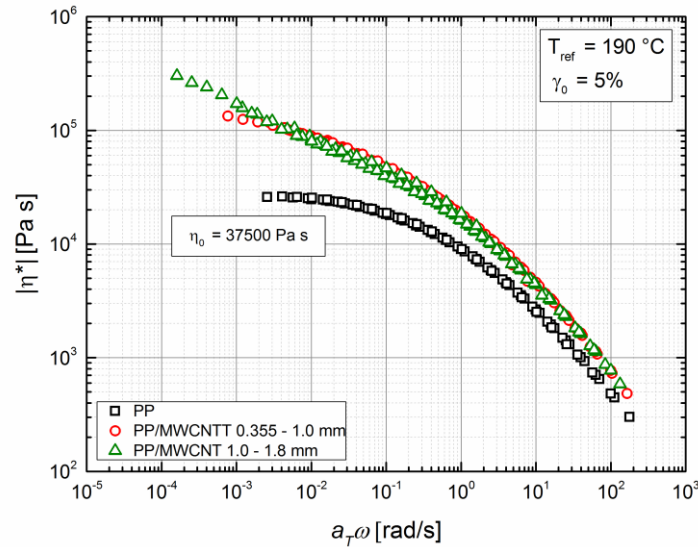


Figure 56: Master curves of the absolute value of the complex viscosity of pristine PP, and PP/MWCNT 5.0 wt% for both the small and the large contingent. Corresponding to the changes in G' and G'' due to the MWCNT influence, the viscosity and curve shape is significantly increased and changed at lower frequencies.

The absolute value of the complex viscosity is shown in **Figure 56**. Pristine PP shows Newtonian flow behaviour at lower frequencies. From the mid-range of the frequency to the low-range, the slope of the viscosity curve decreases until it reaches a viscosity plateau at the lowest measured frequencies. This viscosity plateau corresponds to the zero-shear viscosity η_0 of 26,000 Pa s. For PP/MWCNT 5.0 wt%, no Newtonian flow behaviour was found. Instead, the elastic MWCNT in the matrix hinder the flow of the polymer chains. This leads to a higher viscosity at lower frequencies and no plateau was reached for PP/MWCNT.

The addition of MWCNT to polypropylene led to a relatively small shift to a more solid-like behaviour at lower frequencies with a significant increase in viscosity. As was mentioned for polyetherimide, both can be expected to alter the sintering and compression moulding behaviour of the composite material compared to the pristine polymer.

6.4. Sintering and Morphology of Sintered Membranes

Due to restrictions regarding the polymer powder particle size and shape variations, and also their interaction with the available substrates, the optical microscopy analysis of the sintering of the powder particles remains qualitative. The observations give insight into the sintering behaviour of the used powders, but a confident quantitative analysis of the complete fusion was limited. In the PEI and PEI/MWCNT powders, the powder particles are too different in sizes and shapes to allow for precise results. UHMWPE had the very high tendency to strongly wet

the available substrate of different materials, i.e. glass and PEEK-foil. For maximum visibility, the glass substrate was chosen. The wetting of the glass with the UHMWPE melt overlaps at a certain observed time with the fusion of the powder particles and results in a singular drop of UHMWPE with a very small contact angle.

Nevertheless, the observations allow for a qualitative comparison between UHMWPE and PEI and also between the pristine powders and the decorated ones. The fusion of two powder particles was recorded in video format.

6.4.1. Sintering of PEI and PEI/MWCNT Powder

Two relatively round powder particles of pristine PEI with a diameter of roughly 40 μm are placed in contact together, as can be seen in **Figure 57**. The contact between the two powder particles is through two small round protrusions from the left particle to a round part of the right one.

The time was measured after the particles were visibly above the glass transition temperature and in the molten state, as could be seen by a sharp transition to a more transparent appearance. When the two powder particles are heated above the glass transition, they became more transparent and quickly begin to round and the protrusion of both particles retract through viscous flow. In 40 seconds, the retraction of protrusion at the bottom into the powder particle is finished and only the upper one remains as a sintering bridge. In the first 40 seconds, it increases in diameter and growth continues further. After 100 seconds, the particles no longer possess protrusions and the diameter of the sintering bridge has roughly reached half the diameter of the left particle. After 160 seconds, the diameter of the bridge is identical to the diameter of the left particle.

From here on, further fusion happens through notable viscous flow and shift of both particles towards the sintering bridge. After 6 min, the particles fully fused together, but still have a relatively irregular shape. The new particle experiences continuing viscous flow to continue rounding to minimize the surface area. After 11 min, no further rounding of the powder particle was visible until the end of the experiment at 25 min. The change of the dimensionless neck radius for the larger of the two particles over time can be seen in **Figure 58**.

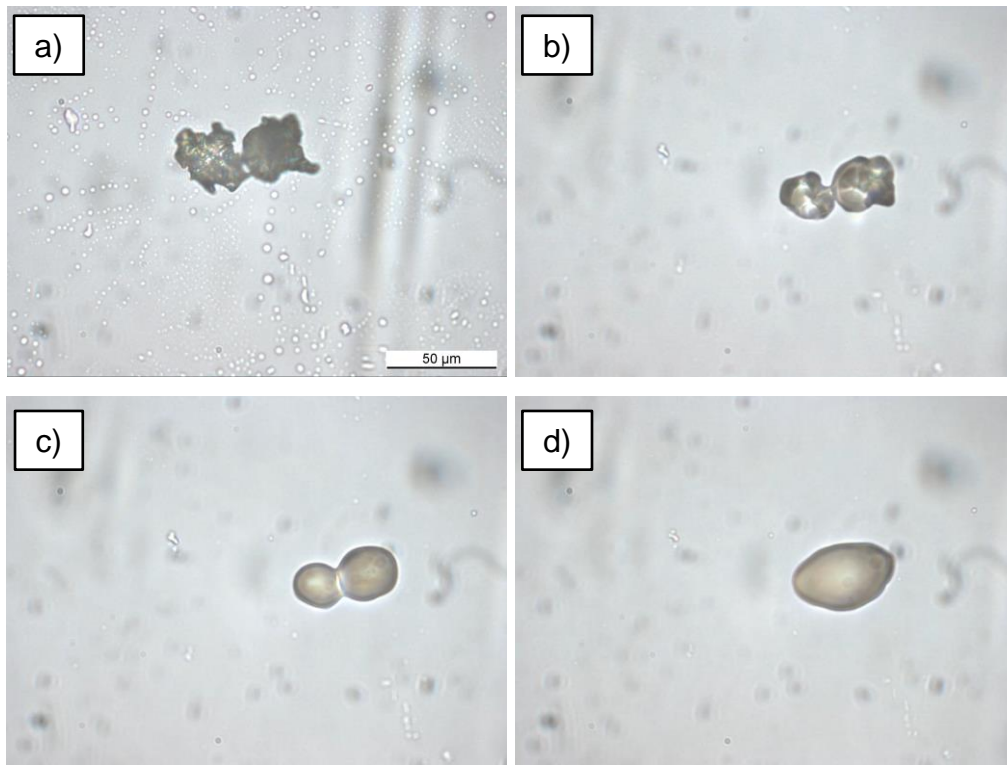


Figure 57: Sintering of two particles of PEI at 300 °C. The particles have two small contact areas before the glass transition and coalescence (a). Both particles round in the melt (b) and the contact areas turn into one sintering bridge. With continuing sintering, the diameter of the sintering bridge increases (c). After the sintering time of 25 min, the two particles are completely fused together, but do not attain a spherical shape (d).

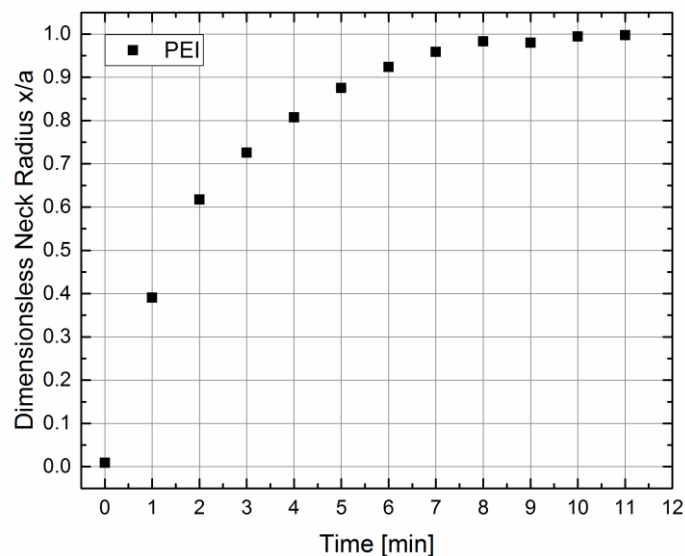


Figure 58: Increase of the dimensionless neck radius of two PEI particles over the sintering time at 300 °C. The curve shape is qualitatively typical for the sintering of two particles.^[73, 77, 78, 81, 84]

Qualitatively, the curve shows the more common shape for a sintering process, be it polymer, metal or ceramic. The initial part of the neck growth is very fast, but continuously slows down over time, as the Laplace pressure decreases. The dimensionless neck radius grows in 1 min to

0.4 and is already over 0.9 after 6 min. The material achieves complete coalescence at the before mentioned 11 min mark and did not spread on the glass substrate.

At the chosen sintering time, PEI as an amorphous polymer with high melt viscosity shows a relatively high growth rate for the dimensionless neck radius of two particles in contact. While this cannot give full insight into the actual sintering of the porous structure of the membranes, it gives a good qualitative explanation for the effectiveness of the chosen sintering parameters.

In the second step for polyetherimide, two powder particles of PEI/MWCNT 3.0 wt% were pushed together, as can be seen in **Figure 59**. The left one is relatively round, while the other one has an irregular shape. The MWCNT-decoration is visible in form of darker particles and black spots, which resemble the MWCNT agglomerates from the SEM analysis. The contact between the two particles is a single contact area. During the heating, this contact point turns into a sintering bridge. The powder particles notably do not round and therefore contract as much as the pristine PEI.

The rounding is reduced, to the effect that after 10 min the irregular shape of the right particle is still recognizable. After 15 min, the round protrusion of the larger particles is moved towards the centre, while the diameter of the sintering bridge further increases. The growth of the sintering bridge predominantly happens through viscous flow from the smaller particle. After 25 min, a further fusion of the particles is no longer visible.

The sintering behaviour clearly differs from pristine PEI. Indeed, if the growth of the dimensionless neck radius of the round part of the larger particle for PEI/MWCNT 3.0 wt% from **Figure 60** is compared to pristine PEI in **Figure 58**, a rather good qualitative comparison is possible. As was mentioned in the experimental section, irregularities in the individual points of the curve result from the manual measurement method.

Just as with pristine PEI, the initial neck growth is rapid, when the driving force is at its peak. But in comparison, the ongoing growth rate is significantly slower with additionally a slower decrease in growth rate of time and neck radius value. When then two PEI particles finished the sintering process around 11 min, the value of the dimensionless neck radius for PEI/MWCNT 3.0 wt% is only around 0.55.

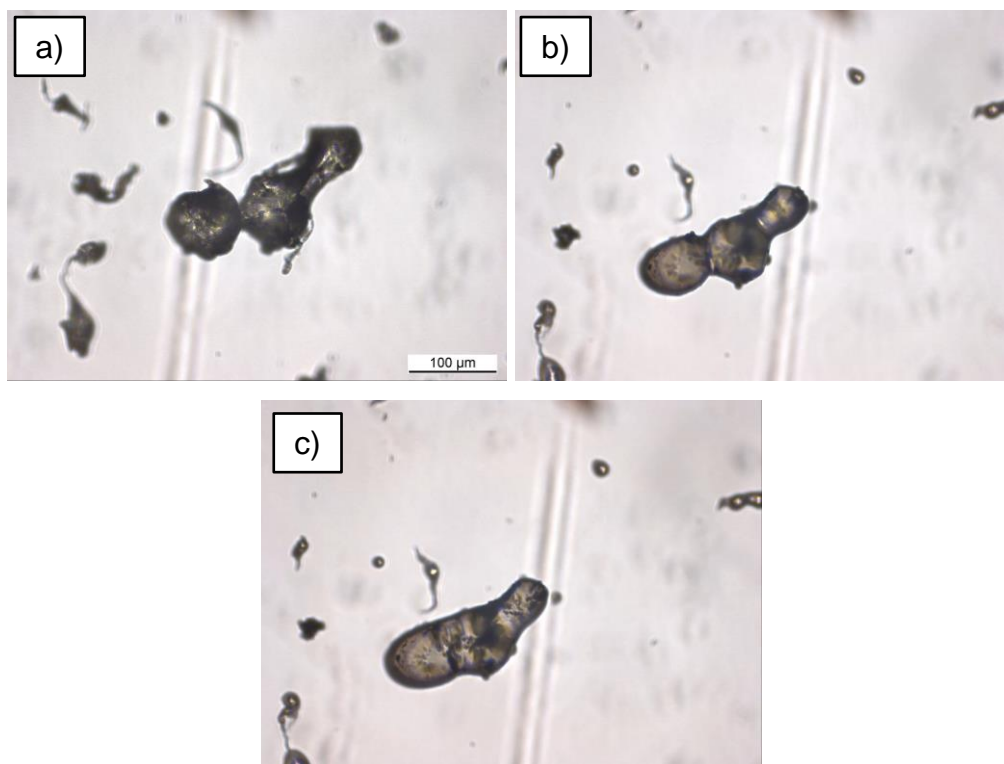


Figure 59: Sintering of two decorated particles of PEI/MWCNT 3.0 wt%. The particles have one contact area before the glass transition and fusion (top left). Both particles round in the melt (top right) and the contact area turns into a sintering bridge. After the sintering time of 25 min (middle bottom), the particles have fused together.

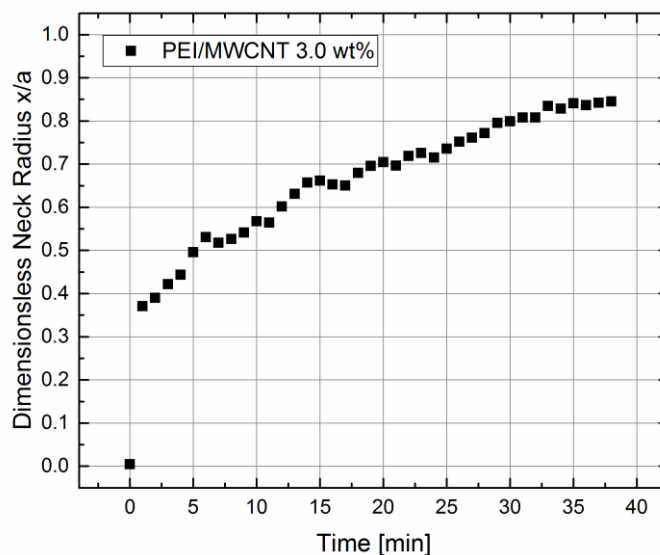


Figure 60: Increase of the dimensionless neck radius of two PEI/MWCNT 3.0 wt% particles over the sintering time at 300 °C. The curve shape is typical for the sintering of two particles together. The deviations in the curve shape result from the manual measuring of the neck and particle diameter for each time.

Due to technical limitations at the used temperature of 300 °C, the sintering experiment was stopped at 38 min. Parts of the heating table had become too warm and around this time, the sintering rate was so low, that a precise neck radius measurement had become exceedingly difficult. From this, it can be concluded that the sintering process would likely not allow for a dimensionless neck radius value of 1.0, as at 0.85 the sintering rate was very low. Additionally in the middle bottom image of **Figure 59**, it can be seen that the neck diameter is close to the diameter of the smaller part from the smaller former particle to the left of it. It is to be expected that the surface tension and therefore driving force for the sintering process is possibly too small for a notable progression of the sintering process.

The addition of the MWCNT significantly changes the viscous flow behaviour of the powder particles and resulting from that, the fusion of the powder particles. As was discussed in the results of the rheological behaviour, the storage modulus and therefore solid-like behaviour at low deformation rates is increased for PEI/MWCNT 3.0 wt%. The shape of the powder particles does not quickly round above the glass transition temperature, as was the case for pristine PEI and their overall shift due to the rounding is highly reduced. The significantly reduced rounding tendency is further illustrated in **Figure 61**.

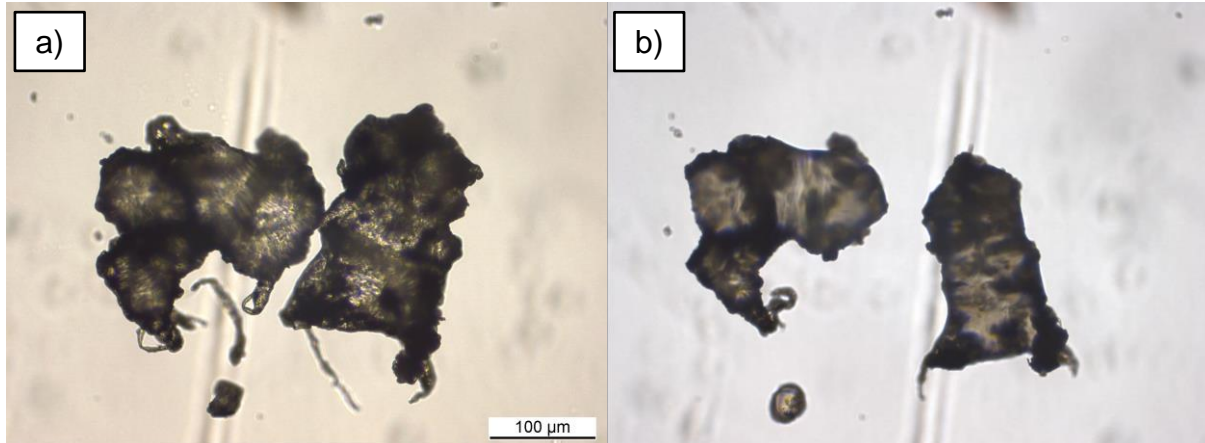


Figure 61: Illustration of unsuccessful sintering of two powder particles in PEI/MWCNT 3.0 wt%. The right particle shifted its position before the glass transition (left) due to retraction of its two string-like protrusions at the bottom above the glass transition (right). The small contact between the two could not form a sintering bridge. The pictures show the significantly reduced rounding of the decorated powder particles above the glass transition temperature. They do not form sphere-like drops like pristine PEI.

The growth of the sintering bridge is analogue to pristine PEI. The fusion continues until the diameter of the sintering bridge is nearly the same as the diameter of the neighbouring areas of the two former particles. At this point, the driving force of the fusion is no longer large enough to induce further viscous material flow. Additionally, the reduction of the surface energy is at this point also not high enough to induce more viscous flow for further rounding of the fused

particle. The Laplace pressure is apparently not high enough to overcome the resistance of the shear modulus and continue the viscous flow, which is increased through the MWCNT, as was found from the rheological analysis in chapter 6.3.1 for lower frequencies.

6.4.2. Sintering of UHMWPE and UHMWPE/MWCNT Powder

The viscosity and shear modulus of the pristine UHMWPE and UHMWPE/MWCNT melts are significantly higher than for PEI and PEI/MWCNT up to 3.0 wt%. It was therefore expected that the fusion of the powder particles would be much slower. While this was observed, it was also observed that UHMWPE, unlike PEI, wets the glass substrate with a very low contact angle. The fusion of the powder particles therefore could only be observed to a certain time, before the wetting of the glass completely obscured the powder particle fusion. Use of different available substrates resulted in the same problem.

Two powder particles of typical shape were individually chosen and put together. Care was taken to orient the powder particles in such a way, that their contact to the glass substrate was minimal. The contact between the two particles is at one point by two round protrusions, one for each particle. The powder particles are transparent with an opaque dark grey hue below the melting temperature. They became more transparent above the melting temperature and showed pronounced uneven diversion of the light from the bottom, due to their irregular shape.

The significantly higher viscosity for UHMWPE results in no rapid rounding or shifting of the powder particles in the melt state. This results in the sintering bridge forming at the original contact point without changes in distance or orientation of the particles to each other. Formation of the sintering bridge is fast and the shape of the bridge is nearly indistinguishable from the original contact area.

Over the range of 24 min, the fusion slowly progresses through viscous flow of the UHMWPE with onsets of particle rounding. After the observed sintering time of 24 min, the particle shapes quickly changed and it appeared as if the fusion rate suddenly accelerated. At this point, the wetting of the glass substrate by the UHMWPE had progressed so far, that the majority of the viscous material flow happened through the spreading of the UHMWPE melt across the glass substrate surface.

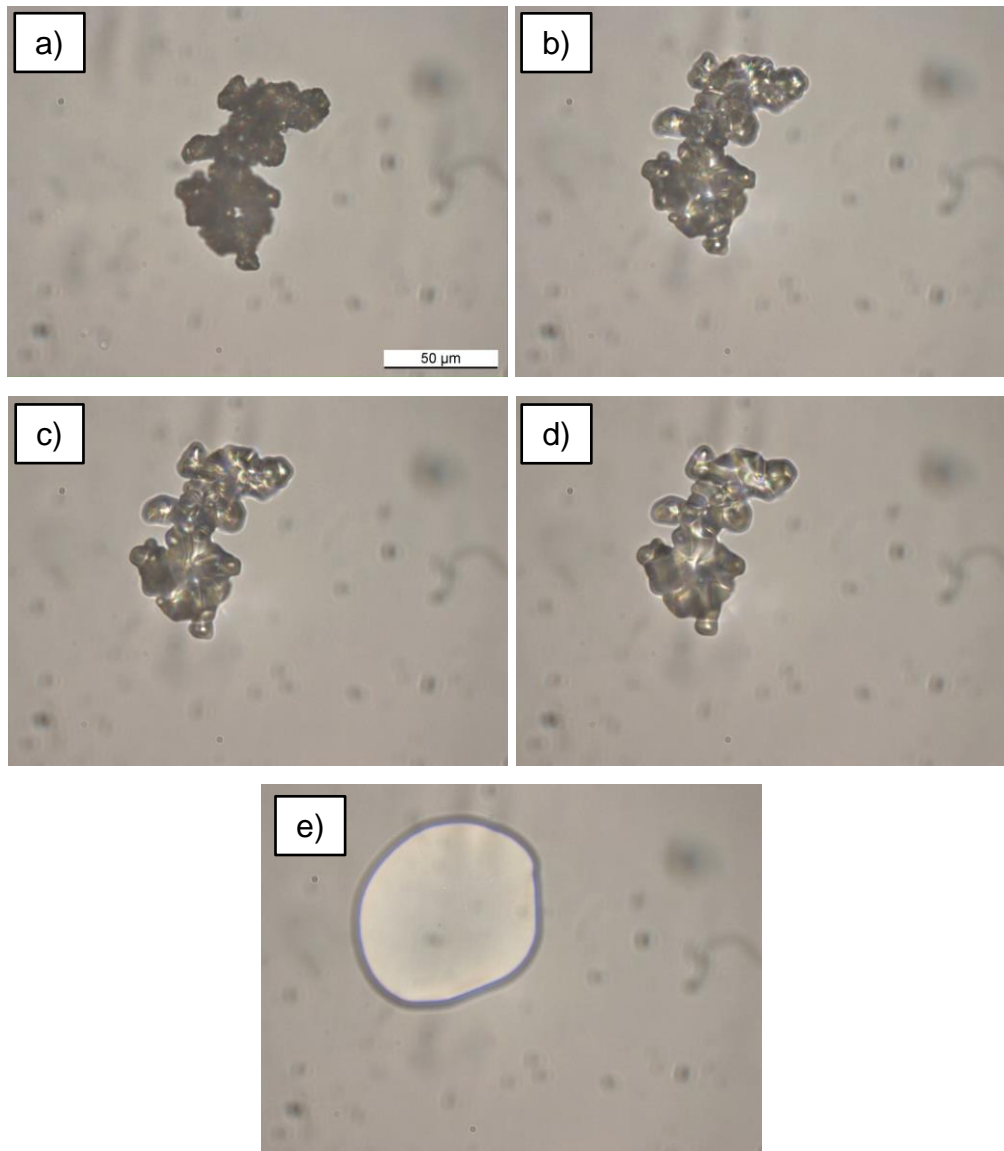


Figure 62: Sintering of two particles of UHMWPE. The particles have one contact area before the glass transition and fusion begins (a). Both particles become more transparent after melting (b). The contact area turns into a sintering bridge during fusion. The fusion continues for 18 min (c) to (d), when the UHMWPE quickly wets the glass substrate with a very small contact angle (e).

The minimisation of the surface energy of the molten particles through wetting of the glass clearly outpaces the fusion of the two separate particles into a single, larger one. Coalescence in this experiment is therefore highly driven by the wetting behaviour of UHMWPE to the glass substrate. As estimated from the rheological results, the fusion rate is significantly lower than for PEI. As will be discussed in for the results of the morphological analysis through SEM of the sintered UHMWPE membranes, the observed fusion rate matches the observations from the sintering experiments for the membranes. While the initial fusion to form a sintering bridge through small-scale material flow is rapid, the continuous fusion through larger scale material flow is extremely slower. Therefore, only a nearly flat line could be observed for the dimensionless neck radius, which can be seen in **Figure 63**. Due to the particle shape and rapid

fusion, no value of 0 for the dimensionless neck radius was confidently identifiable and therefore set to around 0.55 for the time 0 min.

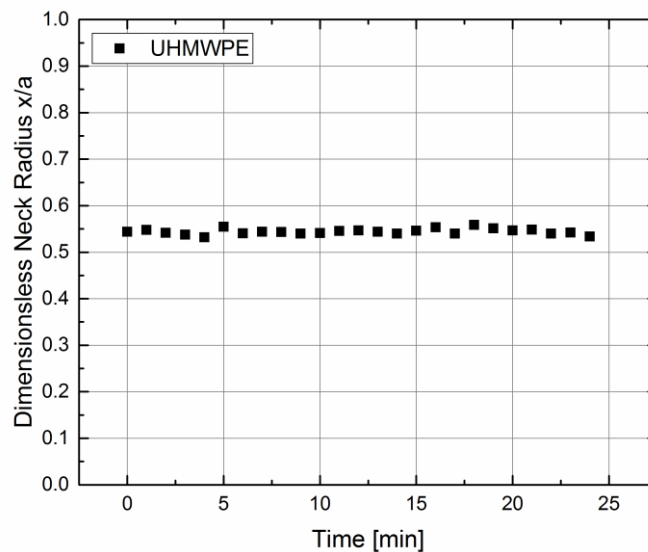


Figure 63: Dimensionless neck radius of two UHMWPE particles over the sintering time at 220 °C. The flat curve shape is not typical for the sintering of two particles together. The curve ends at the point where the wetting of the glass substrates disrupts the measurement. The deviations in the curve shape result from the manual measuring of the neck and particle diameter for each time.

The decorated material of UHMWPE/MWCNT 5.0 wt% behaved very similarly to pristine UHMWPE, while the addition of the MWCNT caused some notable differences that do not clearly show a difference in the sintering rate to UHMWPE. Still, they give indications for the differences in the sintered membranes of UHMWPE/MWCNT, which will be discussed in Chapter 6.4.5. The chosen two particles were less irregular in shape with less prominent protrusions. They were placed together in such a way that they had a continuous contact area where small protrusions were in good contact with each other. It was observed through the optical microscope how the particles were clearly black in varying intensity.

The melting of the particles was visible through parts of the powder particles, as they became suddenly more transparent. For the whole sintering time of 41 min, in which the UHMWPE matrix did not yet wet the glass substrate, no pronounced fusion was visible (see **Figure 64**). When the UHMWPE matrix started to spread across the glass substrate surface, a “core” was left behind where the MWCNT as black parts were left behind. This “core” is close in shape to the two original particles put together. It appears therefore, that the MWCNT change the spreading behaviour of the material, leading to a reduced effect compared to pristine UHMWPE, especially in the “core” area.

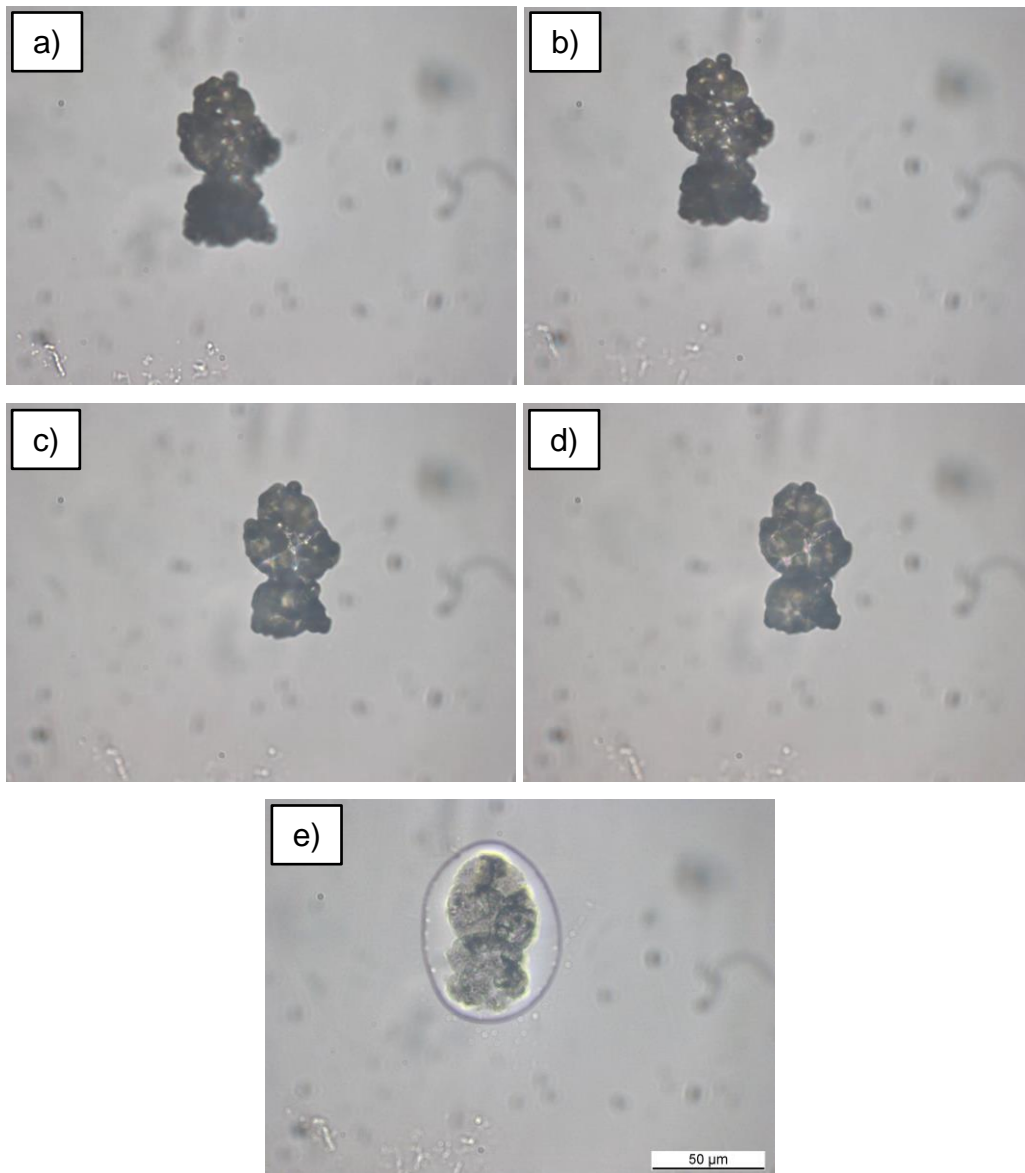


Figure 64: Sintering of two decorated particles of UHMWPE/MWCNT 5.0 wt%. The particles have two contact areas with a small gap between them before the glass transition and fusion begins (a). Both particles become slightly more transparent after melting (b). The contact area turns into a sintering bridge during fusion. The fusion continues for 32 min (c) to d). Shortly after the UHMWPE matrix quickly wets the glass substrate with a very small contact angle (e), leaving a dark “core” with the MWCNT in the middle while spreading out.

Again, due to the particle shape and rapid initial fusion, no clear value of zero could be confidently identified for the dimensionless neck radius (see **Figure 65**). Therefore it was set to around 0.58 at the time 0 min. Identical to pristine UHMWPE, no definitive change in the dimensionless neck radius could be observed up to 41 min after which the UHMWPE matrix spreads across the glass substrate surface, which happened later than for pristine UHMWPE with 24 min.

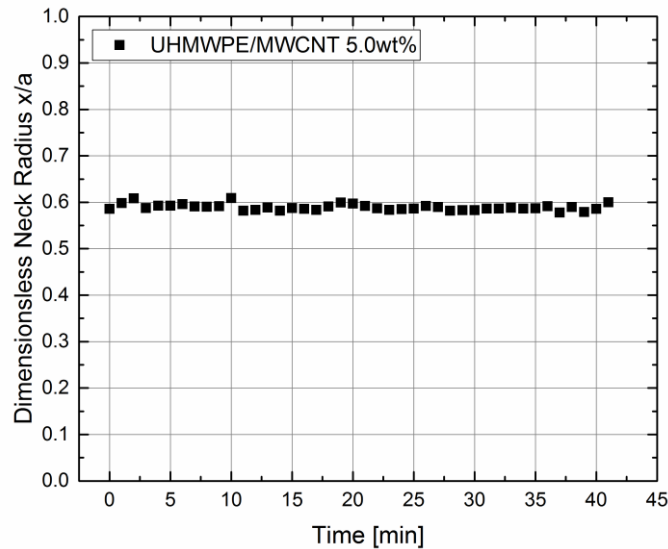


Figure 65: Dimensionless neck radius of two UHMWPE/MWCNT 5.0 wt% particles over the sintering time at 220 °C. The flat curve shape is not typical for the sintering of two particles together. The curve ends at the point where the wetting of the glass substrates disrupts the measurement. The deviations in the curve shape result from the manual measuring of the neck and particle diameter for each time.

The MWCNT therefore hinder the wetting of the glass with the UHMWPE and additionally leave a “core” behind where not further spreading was possible with the matrix. The addition of 5.0 wt% MWCNT increased the elastic properties and viscosity of the melt, as was discussed in Chapter 6.3.2. Even though the effect at lower frequencies is significantly lower than at higher ones, with part of the UHMWPE spread across the glass surface and out of the MWCNT-containing part of the particle, the left-behind “core” can be assumed to have a further increased MWCNT concentration and lower concentration of the non-volatile liquid. This could make the “core” stable and resist deformation due to the wetting behaviour of the UHMWPE matrix.

Overall, the very high melt viscosity of the matrix has the largest influence on the sintering behaviour, while the addition of the MWCNT alters the behaviour without complete changes.

6.4.3. Sintering of Polyetherimide Membranes

The scanning electron micrographs of the sintered samples of pristine polyetherimide show a porous structure caused by the pronounced fusion of the powder particles during the sintering process. As was explained in Chapter 4.2.1, the sintering time for pristine PEI and PEI/MWCNT up to 1.5 wt% was 15 min, while the sintering time for PEI/MWCNT with concentrations higher than 2.0 wt% was increased to 24 min.

The original shape of the particles can be still recognized in the significantly rounded and partially fused particles. Especially smaller particles show a pronounced tendency to strongly fuse with larger particles. The sintering of polyetherimide resulted in a relatively irregular structure. This was caused by the large particle size and shape variation and the random stacking and compression of the powder particles during the green body production. Additionally, the sintering neck growth is dependent on the quantity of contacts and the contact angle to neighbouring particles. This leads to large differences in the fusion rates between different particles. The scanning electron micrographs of the surface give an insight into the material flow and particle deformation. In **Figure 66** and **Figure 67**, the surface of a sintered PEI membrane is shown.

The sintering bridges between particles are clearly visible. Due to their shape, it is not clear which ones were formed by two particles fusing together or which ones resulted from a smaller particle in contact between two larger particles. Distance between two larger particles might be an indication, but it can also be assumed that the drag of the polymer melt flow causes displacement of the molten particles. Generally, it appears that the larger pores formed around larger particles, while clusters of smaller particles mostly fuse partially together and generate zones of smaller pores.

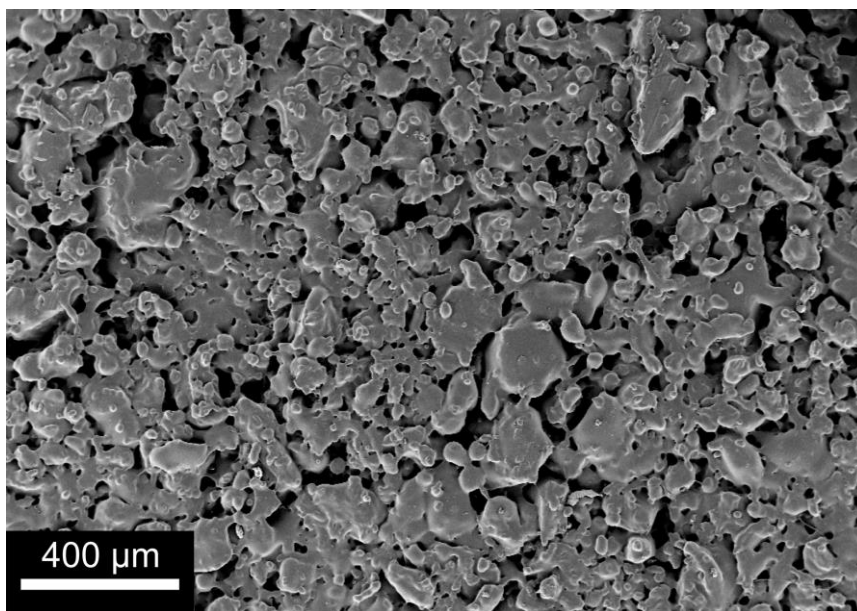


Figure 66: Surface of a sintered polyetherimide membrane surface. The sintering bridges between fusing particles are recognizable. Pore structure and shape vary due to the shapes and diameters of the particles around them. The material surface is significantly smoother than for the pristine powder particles.

It should be mentioned again, that conventional sintering of powder particles usually does not generate membranes with a distinct separation layer on a surface. Rather, they result in depth-

filters with a winding tortuous pore channel structure, characterised by bottleneck pores. The tortuous structure itself is not necessarily limited in its filtration performance by the smallest diameters in the pore channels. The complicated structure increases in filtration performance with an increasing number of trapped particles inside the pores. This is analogue to the formation of a filtration cake, that itself can have a smaller diameter cut-off than the membrane below.

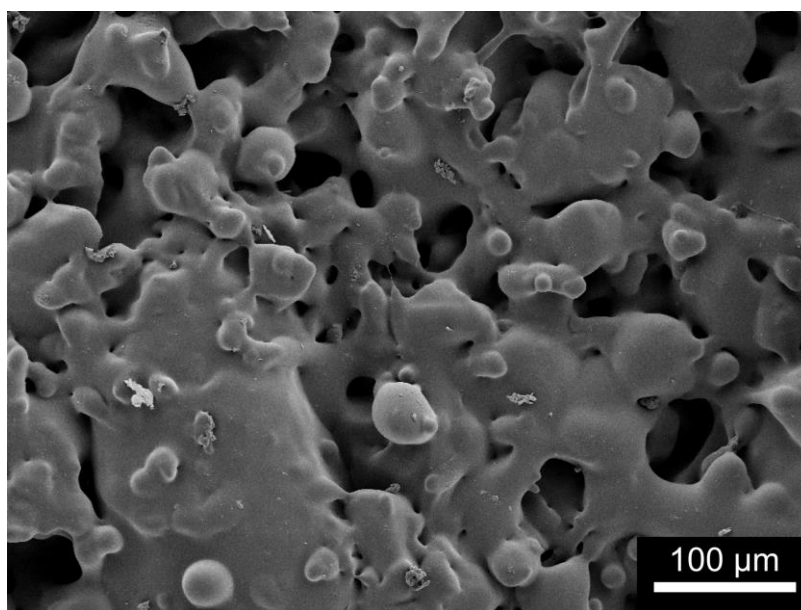


Figure 67: Magnification of the surface of sintered PEI membrane. Partially fused particles are visible, especially in the lower left of the micrograph. Also visible are the sintering bridges between former individual particles, some relatively thick, others are more sting-like.

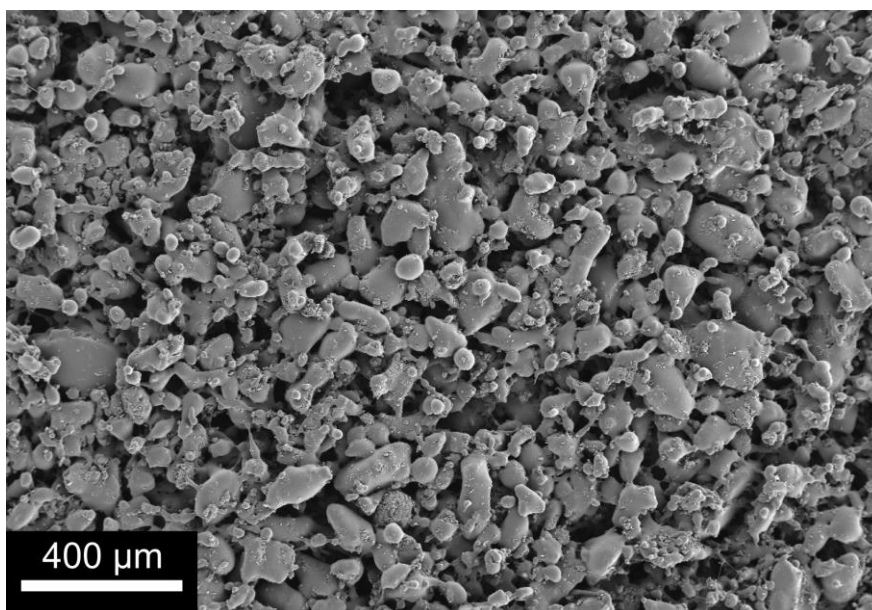


Figure 68: Surface of sintered PEI/MWCNT 1.0 wt%. While the sintering of the decorated particles is considerable, it overall appears to be much less developed compared to pristine PEI. Most individual particle shapes can still be confidently identified.

With the addition of MWCNT, the sintering behaviour is noticeably changed. It can be seen in **Figure 68** for PEI/MWCNT 1.0 wt% that the melt flow behaviour apparently differed greatly from the pristine PEI. The original particle shapes are better preserved and fusion between particles is not as pronounced. The same can be seen for PEI/MWCNT 2.0 wt% and PEI/MWCNT 3.0 wt% in **Figure 69**.

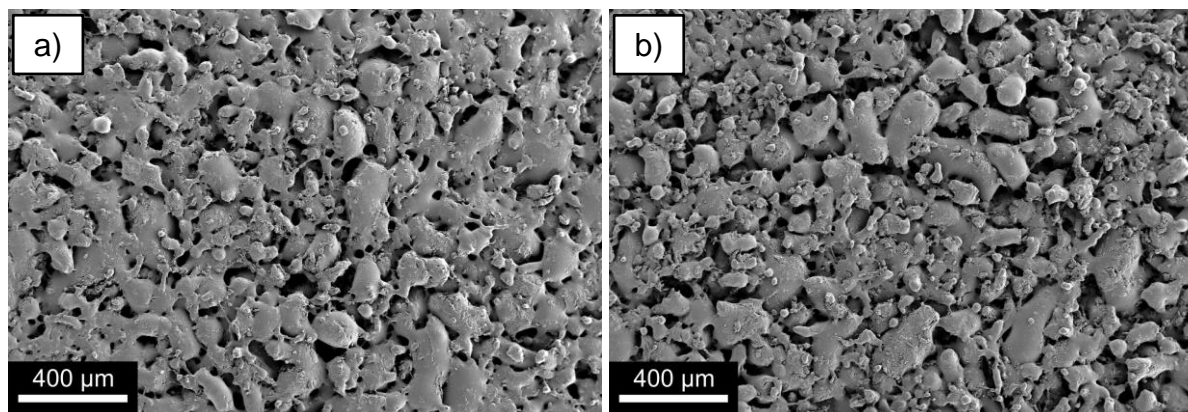


Figure 69: Surface of sintered PEI/MWCNT 2.0 wt% (left) and 3.0 wt% (right). The sintering time was increased compared to concentrations below 2.0 wt%.

The magnification of the PEI/MWCNT 3.0 wt% surface in **Figure 70** show the overall less pronounced fusion of the powder particles and also that the surface of the powder particles appear rougher due to partially sunken in MWCNT agglomerates. As will be discussed in more details for the cross section: The surface appears still smoother compared to the powder particles as the individual MWCNT have sunken under the matrix surface during the sintering process.

Even though the sintering times were increased from 15 min to 24 min, the structure on the surface shares its characteristics with PEI/MWCNT 1.0 wt%. Overall particles have noticeably rounded during the sintering process and partially fused together forming less well developed sintering bridges. Instead the fusion between particles with a high contact surface area appears to have been greatly favoured over viscous material flow along formed sintering bridges.

In the cross section, small magnifications show that the porous structure generally is highly tortuous with an apparent high connectivity between pores. Due to the large particle size distribution, pore diameters are far from uniform and show a very large diameter size distribution along the thickness of the membrane. As can be seen in **Figure 71**, differences are visible between pristine PEI and PEI/MWCNT 3.0 wt%, which was sintered for the longer sintering time of 24 min. The thickness of the membranes was decreased to around 0.8 mm instead of the 1.0 mm for PEI and PEI/MWCNT up to 1.5 wt% MWCNT. This manifests as a

denser packing of the membrane. The pore channels are more difficult to make out in the SEM micrographs, but are still noticeable.

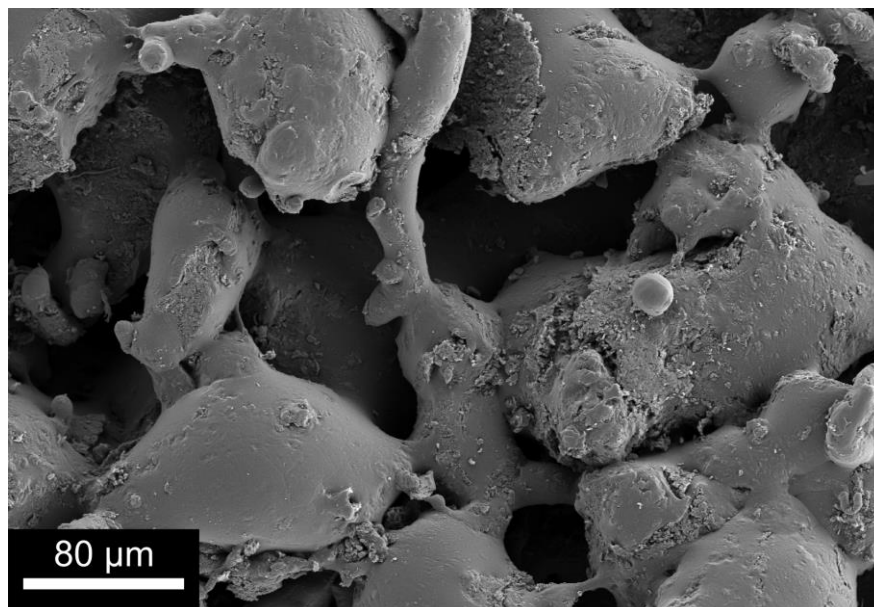


Figure 70: Magnification of the surface of sintered PEI/MWCNT 3.0 wt%. Differences in sintering behaviour are visible in comparison with **Figure 67**. Fusion of individual particles appears to be less pronounced compared to pristine PEI with sharper distinction between sintering bridges, fusion sites and the particles.

Due to the noticeable difference in the sintering behaviour, PEI/MWCNT 1.0 wt% shares more similarities in shapes in cross section with PEI/MWCNT 3.0 wt%, yet the thickness is the same as for pristine PEI. An explanation for these similarities is that the less pronounced fusion results in lower amount of drag.

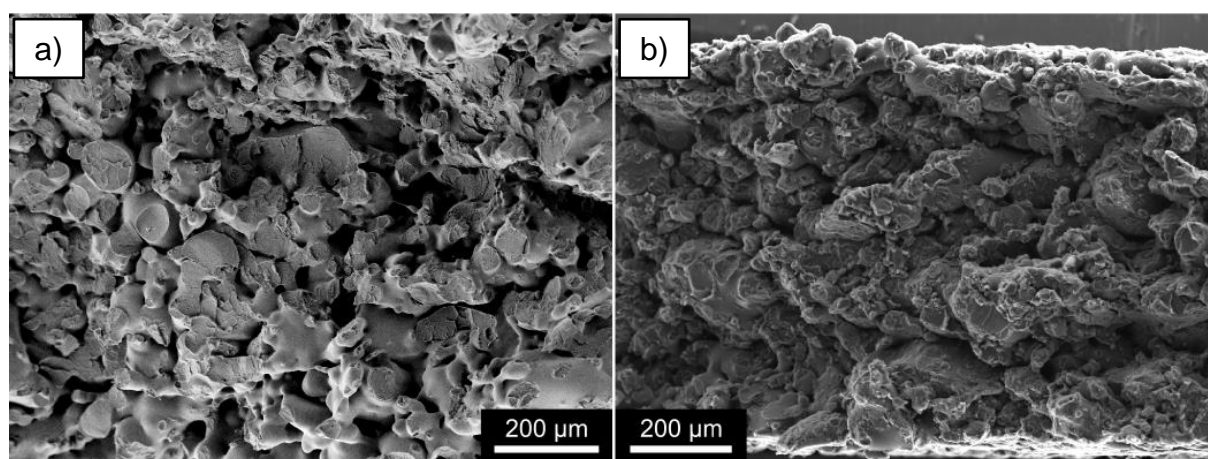


Figure 71: Cross section of (a) polyetherimide and (b) PEI/MWCNT 3.0 wt%. As sintered membranes, they show a relatively low porosity. Porosity and pore shape are dictated by the used particle shape and size. Samples were prepared by fracturing under cryogenic conditions (-196 °C).

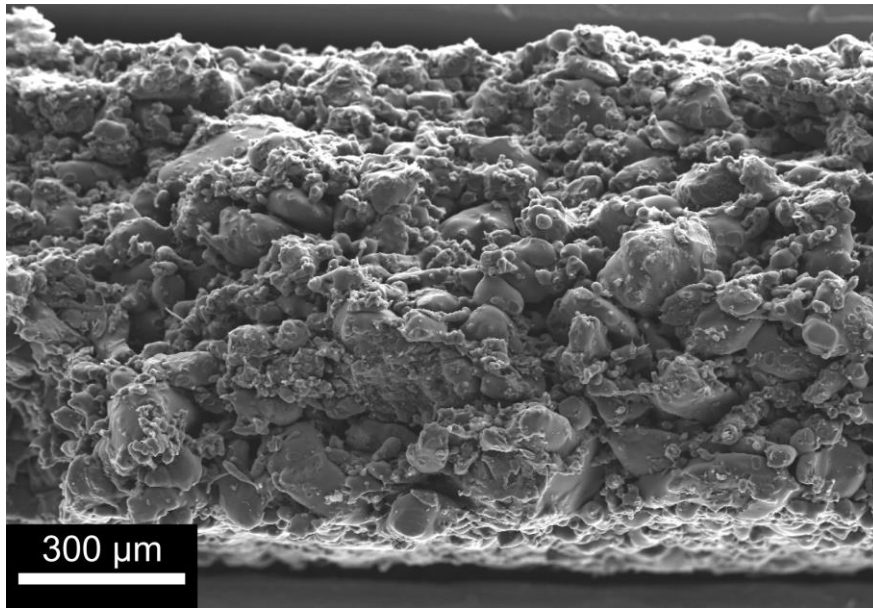


Figure 72: Cross section of PEI/MWCNT 1.0 wt%. The overall structure looks more similar to pristine PEI than PEI/MWCNT 3.0 wt%. This results from the identical sintering parameters to PEI.

With less drag, the smaller particles or particles that are exposed to strong fusion are less susceptible to shifting and moving which might create less large void like pores in the membrane.

As mentioned above, the surfaces of the particles have noticeably smoothed and rounded, especially for pristine PEI. Of higher importance is for PEI/MWCNT that the MWCNT have a strong tendency to sink under the polymer surface during the sintering. Individual MWCNT are fully enveloped by the matrix and sink so deep under the surface that they are only partially visible under the surface as a soft shimmer. In some places, larger groups of non-agglomerated MWCNT shine more strongly under the surface and can partially stick out of the polymer matrix. This can be seen in **Figure 73**, where also one agglomerate illustrates that agglomerates in general only partially sink under the surface for the given sintering times. The agglomerates are partially penetrated by the polymer melt and apparently simultaneously dragged under the surface. The SEM micrographs show that only few agglomerates are strongly penetrated by the polymer melt and for the most part sunken under the surface.

Especially large agglomerates preferably stay for the most part out of the polymer matrix and appear to be only anchored. Therefore, the individual non-agglomerated MWCNT are enveloped and strongly bound to the polymer matrix, while still close enough to the surface to provide an electrical contact. MWCNT agglomerates are anchored to the matrix, but still large numbers of the agglomerated MWCNT are only bound to the membrane through MWCNT entanglement and therefore physical bonding.

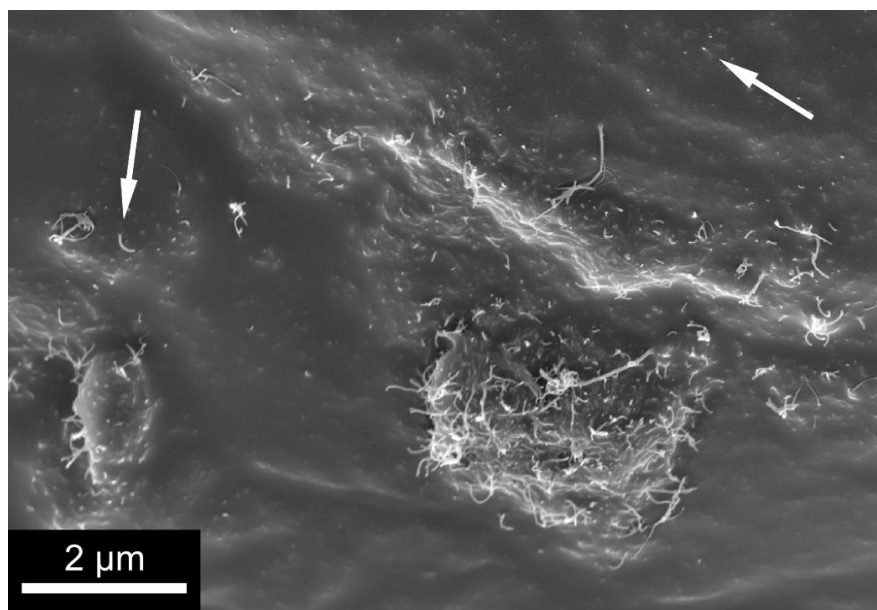


Figure 73: Magnification of a surface inside the cross section of a PEI/MWCNT 1.0 wt% membrane. Individual MWCNT have sunken under the polymer matrix surface during sintering and are shining through the surface (arrows) or partially sticking out. MWCNT agglomerates appear to only partially sink into the matrix, while being partially penetrated by it.

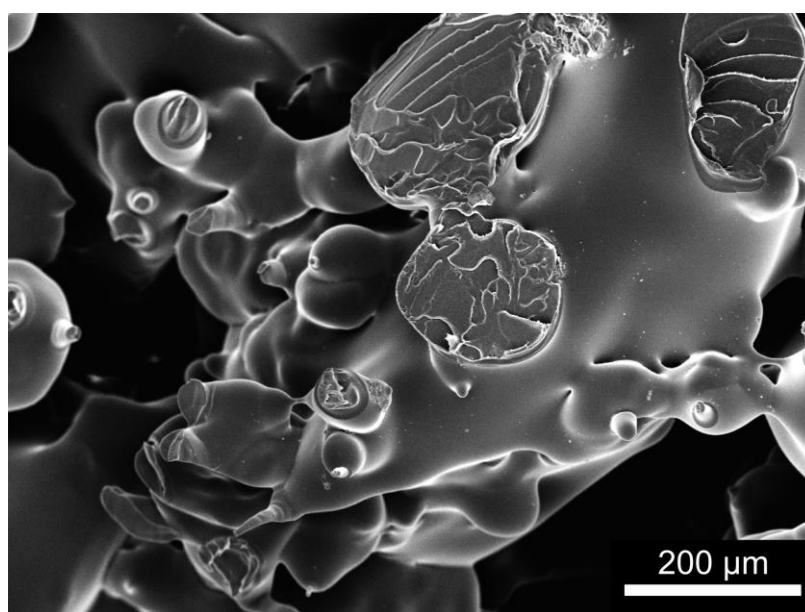


Figure 74: Magnification of the cross section of a sintered PEI membrane. The fractures predominantly happen at the sintering bridges and fusion sites between particles.

Because the samples for analysis of the cross section were prepared via cryogenic fracturing, a large number of different fracture sites were visible. In the case of pristine PEI, the fractures predominantly occurred at sintering bridges and fusion sites between particles. These areas provide weak spots, as they generally have a lower thickness than the particles between them. The fracture sites show a typical fracturing behaviour for an amorphous polymer at cryogenic

conditions. Fracture sites are mostly arrangements of relatively flat areas with parts between them where the material was pulled out from the fracture plane, as can be seen in **Figure 74**.

Analogue to the fracturing behaviour of the sintered PEI membranes, the fracture sites in PEI/MWCNT are also located in the sintering bridges and fusion sites between particles. What distinguishes the composite membranes from the pristine ones is the specific fracture area in the sintering bridges and fusion sites. For the pristine PEI, i.e. the fracture cannot exactly be identified at a specific weak point such as the smallest diameter, curvature of the sintering bridge or irregular shape. However, for the composites the fractures appears to particularly happen at the MWCNT-MWCNT contact areas. This means at the areas where the MWCNT covered surface of one particle fused with another one. The contact of the covered surfaces generates the MWCNT network in the composite but also a localised MWCNT concentration. The interaction of the relatively densely packed MWCNT with the matrix between and around them leads to areas of significantly increased brittleness compared to the MWCNT-free matrix. This was indicated in the rheological analysis of PEI and PEI/MWCNT of different concentrations and in the increased tendency of PEI/MWCNT with MWCNT concentrations of 2.0 wt% and above to break during demoulding and handling if sintering times were not increase from 15 to 24 min. Examples of the fracture sites can be seen in **Figure 75** - **Figure 77**.

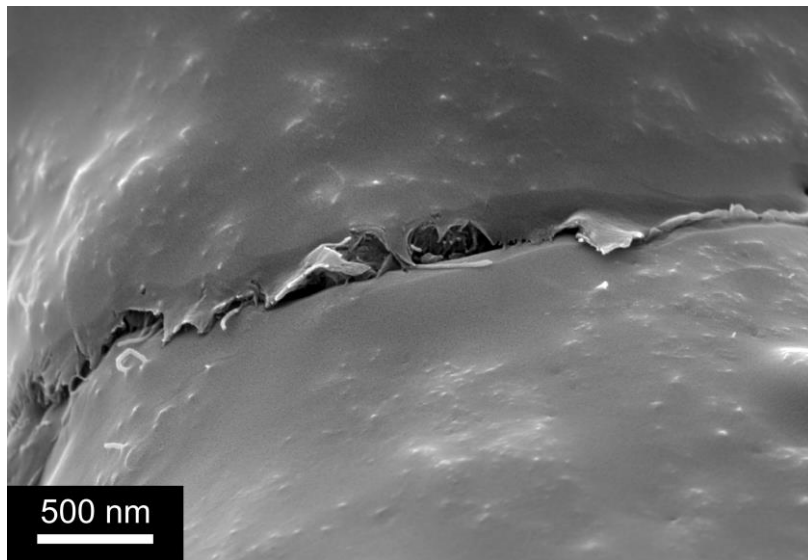


Figure 75: Magnification of a partial fracture site in the sintered membrane of PEI/MWCNT 2.0 wt%. Clearly visible are the MWCNT shimmering through the PEI surface. In the partial fracture, the strong presence of MWCNT is illustrated by them being visible in the crack and shaping the “lips” of the fracture on the outside.

Apart from the MWCNT shining through and partially sticking out from the surface shown in **Figure 75**, a partial fracture can be seen in the middle of the micrograph. The visible inside of

the fracture is filled with MWCNT and the edges of the fracture are shaped by MWCNT, resulting in a crease with visible MWCNT sticking out. An example for a fracture at a fusion site can be seen in **Figure 76**. The round craters resulted from particles that were significantly smaller than the larger particle in the background. They were partially pulled into the larger particle due to drag and simultaneously rounded because of the surface tension of the polymer melt.

The fracture site resulting from the fusion site as the weak part in the connection between the particles was the contact area between the MWCNT covered surfaces of the particles. The fracture site shows a more pronounced roughness than for pristine PEI, caused by the presence of the MWCNT. Large MWCNT concentrations lead to an increased brittleness of a polymer-MWCNT composite. While the MWCNT concentration in the overall composite is not very large, local concentration of the MWCNT in the segregated network can be expected to significantly change the mechanical behaviour in these areas to a more brittle behaviour. This results in the sintering bridges and fusion sites to act as the brittle weak spot. As can be seen in **Figure 77**, fracture sites are for the most part characterised by a rougher fracture surface. The thin string-like cylinders can be identified as the MWCNT because of their uniform appearance compared to the pulled out parts of the PEI matrix.

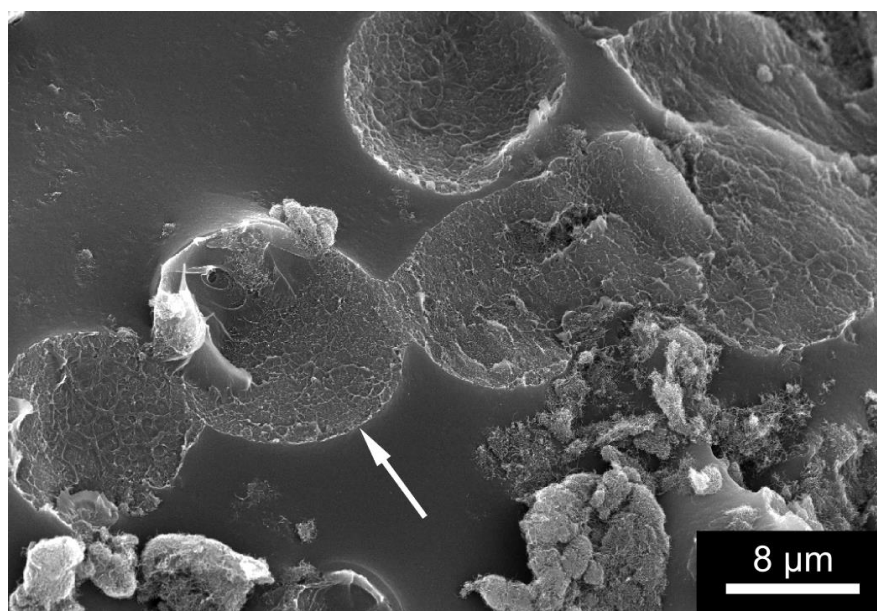


Figure 76: Cross section of a PEI/MWCNT 1.0 wt% membrane. Round, rugged areas (arrow) resulted from smaller, spherical particles that broke off during sample preparation. MWCNT agglomerates are visible in the lower parts of the micrograph. The surface around these areas is smoother than the used powder particles.

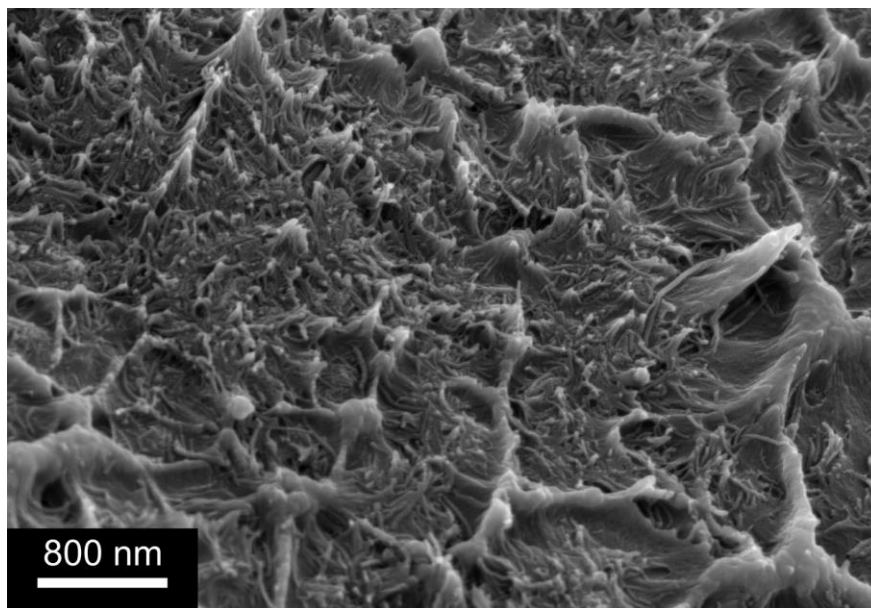


Figure 77: Magnification of a fracture site in PEI/MWCNT 1.0 wt%. The roughness between the web-like pulled out polyetherimide results from partially exposed MWCNT which are visible as string-like cylinders.

The predicted MWCNT network structure in the sintered polymer membranes became visible in some fracture sites of the cross section. One such part of the network can be seen in **Figure 78**. This micrograph was taken at a fracture site that appeared to have been at the fusion region of three particles. This is also indicated by the triangle-like MWCNT bundle in the top middle-left part of the micrograph. Here the MWCNT were pushed together during the viscous material flow of the three particles. The line of MWCNT in the horizontal middle of the micrograph is from the fusion of a larger particle with the other two. While the exact shape of the MWCNT network is distorted due to the breaking behaviour of the composite and the PEI matrix, the indicated MWCNT distribution and the measured conductivity values made the assumption of a network structure reasonable.

To confirm the presence of such a network of MWCNT, a sample of PEI/MWCNT 3.0 wt% was chosen for preparation of a SEM analysis of the cross section via ion milling. The observable cross section would then be no longer an array of fracture sites, but a smooth, clean cut straight through, which is highly advantageous for SEM investigations of the MWCNT network. However, this method is highly time intensive and therefore had to be limited to samples with a high chance of success for the network analysis.

With PEI/MWCNT 3.0 wt%, this sample was chosen and as can be seen in **Figure 79**, the MWCNT became clearly visible using backscatter electron contrast (BSE). As the used MWCNT were synthesised using an iron catalyst, in BSE the remaining iron can be distinguished from the matrix with BSE contrast being more sensitive to material contrasts.

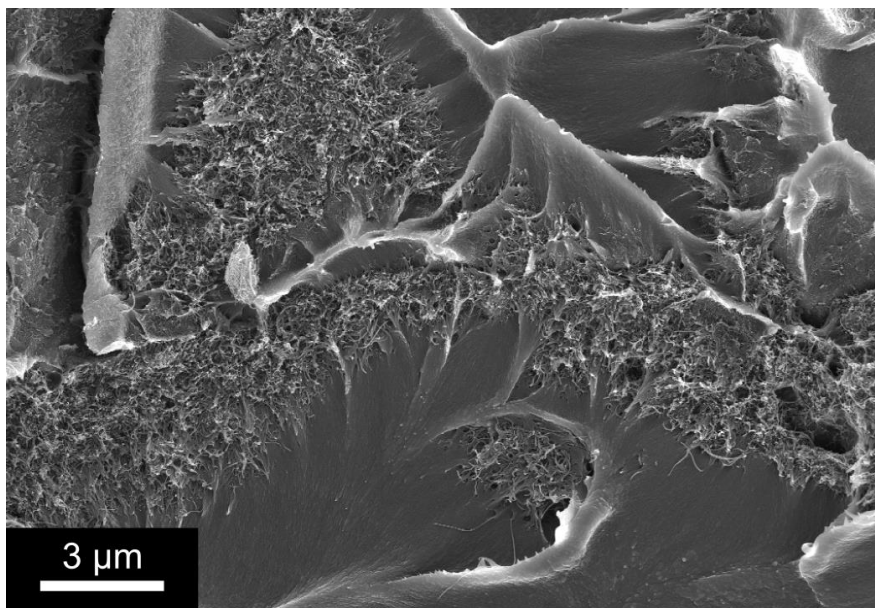


Figure 78: Fracture site in the cross section of PEI/MWCNT 3.0 wt%. The fracture happened at a fusion point between three decorated particles. The rough, fuzzy areas are MWCNT in a network, surrounded and partially penetrated by the polymer matrix.

As can be seen in the micrograph, the individual MWCNT that were tangentially aligned to the surfaces of the unsintered powder particles resulted in thin lines inside the matrix. Agglomerates resulted in bundles, connected by the thin lines.

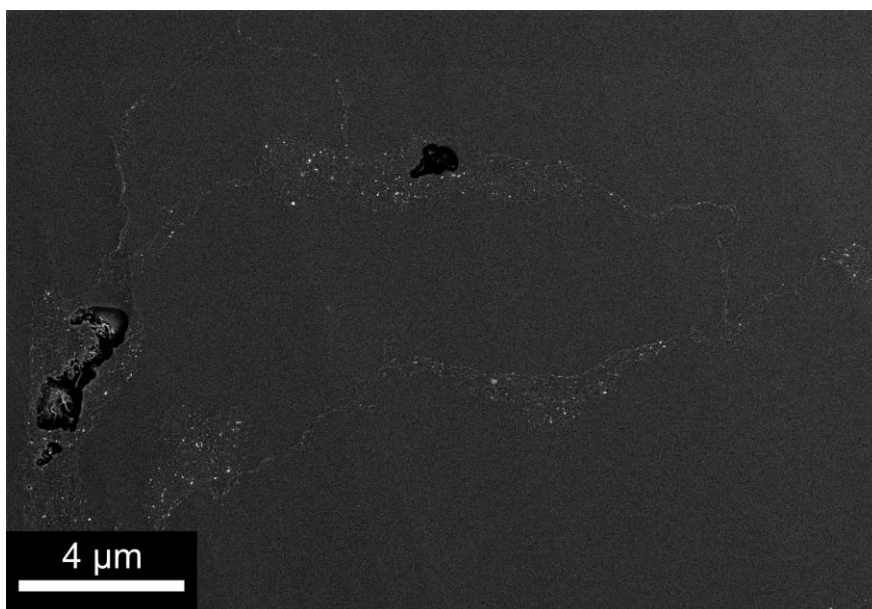


Figure 79: MWCNT network visible in the cross section of a PEI/MWCNT 3.0 wt% membrane. The network was made visible by preparing the sample via ion beam cutting and using electron back scattering contrast. The thin lines are small paths of non-agglomerated MWCNT, while thicker line parts are agglomerates or nests of smaller agglomerates. The shape of the network in the middle resembles a shape found in the decorated powder.

In the middle, a larger former particle can be made out. In the top left corner, a smaller particle was completely surrounded by the matrix in this plane. **Figure 80** shows a different area with

a similar view, here with both BSE and SE contrast. In the bottom right an agglomerate of MWCNT that was penetrated by the PEI matrix is visible. The pathways for the sintered membrane appear to be continuous and well developed. Because the sample was cut with an ion beam, the cross section is flat. The three dimensional structure of the MWCNT cannot be fully deduced from this, because it is not known what the membrane looks like in the plane away and into the image.

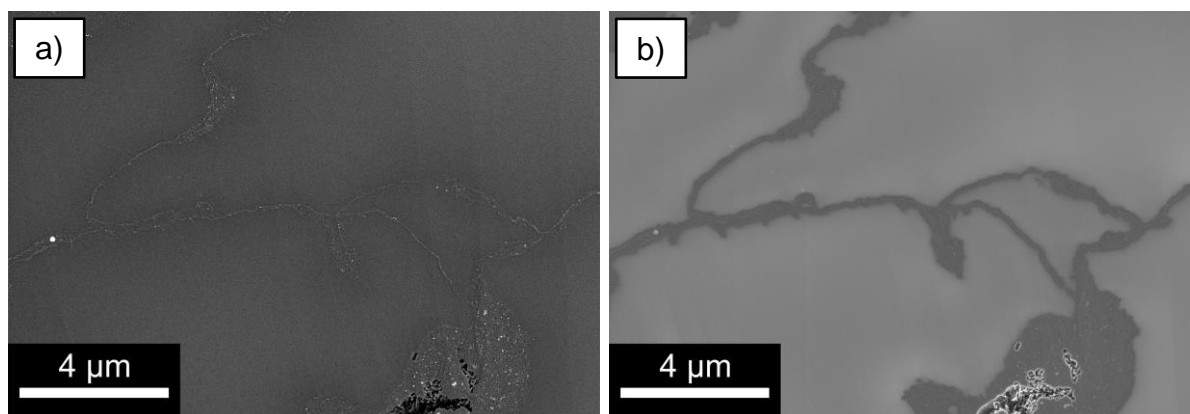


Figure 80: MWCNT network visible in the cross section of a PEI/MWCNT 3.0 wt% membrane. The network was made visible by preparing the sample via ion beam cutting. On the left side, the network is visible in a mixed signal of BSE and SE contrast. The brightest spots are remaining parts of the iron catalyst on the MWCNT. The right micrograph shows the same area in SE contrast.

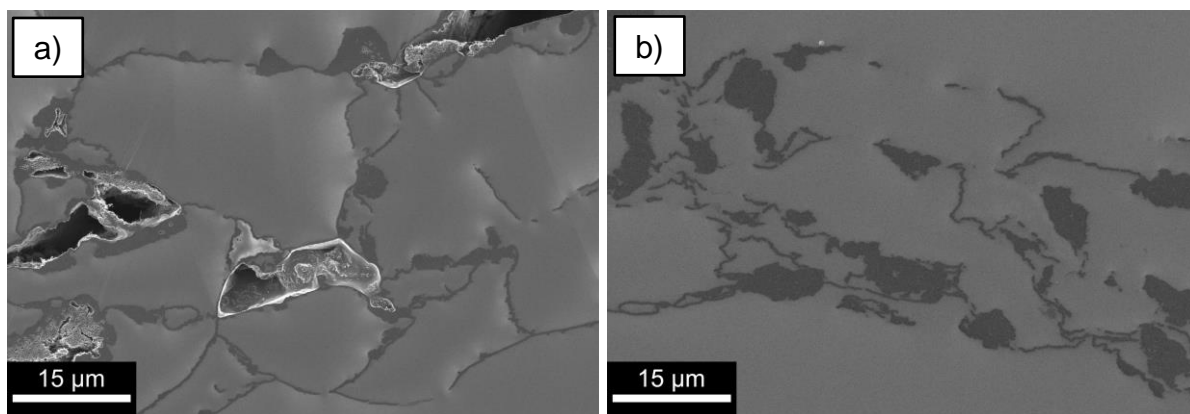


Figure 81: SEM micrographs of the cross sections of ion milled of PEI/MWCNT 3.0 wt% samples. Both images show SE contrast micrographs. The left micrograph (a) is from a porous sintered membrane, the right (b) from a compression moulded dense sample.

For comparison a compression moulded sample of PEI/MWCNT 3.0 wt% was also ion-milled and the side-by-side comparison with the sintered sample is shown in **Figure 81**. It is clearly visible that the MWCNT network for the sintered sample appears to be significantly better connected. Many of the paths for the compression moulded sample are either interrupted or dead-ends. Further, most of the agglomerates, which predominantly are on the outside of the

powder particles, appear to be significantly less connected in the cut plane to the MWCNT network.

In comparison, the sintered sample shows also some interrupted pathways, but overall the gaps between them are smaller and MWCNT agglomerates are generally connected to the MWCNT network. Even if for the compression moulded sample the paths continue outside of the cut plane, the lack of a path in the cut plane means a reduced number of MWCNT for the conductive path.

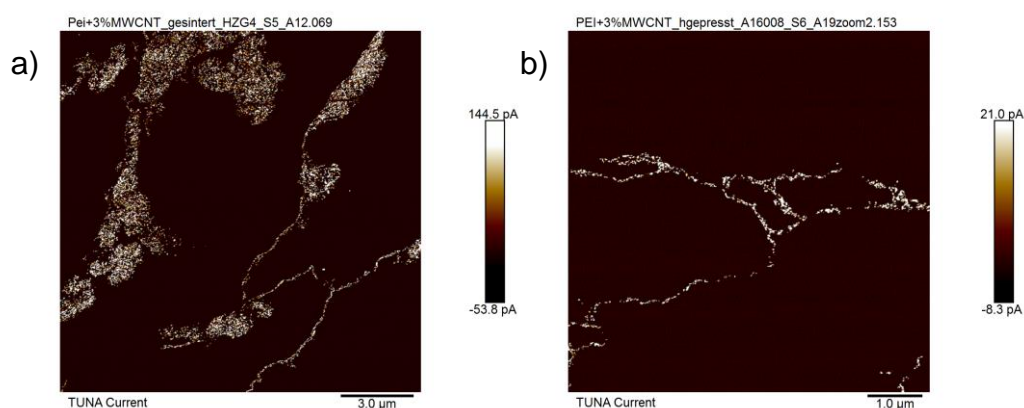


Figure 82: C-AFM image of a region of PEI/MWCNT 3.0 wt%. The left image (a) shows a region of a sintered porous membrane, the right image (b) a region of a compression moulded sample.

To qualitatively prove that the pictured MWCNT network is indeed conductive and visible paths are not strongly interrupted through nano-scaled isolation by the PEI matrix, C-AFM was performed to gain insight. With C-AFM the visibility of the MWCNT in the SEM micrographs can be shown to also result from their electrical conductivity and not only through a different interaction between sample and electron beam. In **Figure 82**, the conductivity of the pathways is shown for both the sintered sample and the compression moulded one.

The results will be again discussed in comparison with the results for electrical conductivity in Chapter 6.8.1.

6.4.4. Summary for Sintered PEI and PEI/MWCNT Membranes

Polyetherimide as an amorphous polymer was expected to show low displacement of the MWCNT due to low amounts of shear or lack of significant local morphology changes during the fusion of the particles. The melting of the powder particles resulted in a pronounced rounding and smoothening of the surface, strongly noticeable for pristine PEI. The addition of MWCNT to the surface led to a significant local concentration and also led to a significant

change in mechanical and rheological behaviour of the decorated powder particle surfaces. Therefore the particle still showed a noticeable rounding of the particles but also a lowered overall deformation of the particle shape. Pristine PEI powder particles appeared on the surface and in the cross section to have been exposed to a larger degree of viscous flow and drag, leading to pronounced sintering bridges and fusion of particles. Especially fusion sites show a very strong progression of fusion. Compared to this, PEI/MWCNT still shows strong sintering bridges and well progressed particle fusion, but to a noticeably lower degree than pristine PEI does. Additionally, the strongly localised MWCNT change the mechanical properties in the contact areas between MWCNT-covered surfaces of the former particles to be significantly more brittle. This leads to these MWCNT contact areas to act as weak spots, resulting in fractures happening in these specific areas in the sintering bridges and fusion sites. For pristine PEI, the sintering bridges and fusion sites are also notable weak spots, because they have a smaller cross section than the particles between them, leading to a larger mechanical stress. However, fractures do not have a characteristic spot or area where they happen in the sintering bridges or at fusion sites.

The ion-milled cross section of PEI/MWCNT 3.0 wt% in SEM and C-AFM confirmed the proposed formation of the MWCNT network through the fusion of the MWCNT-covered particle surfaces with very low shear during viscous material flow. The network shows a network formed by the individual MWCNT as thin lines of conductive pathways through the matrix. Agglomerates and bundles of them form local clusters of MWCNT that are, depending on their size, either fully enveloped and penetrated by the PEI matrix or partially penetrated and therefore “anchored” into the matrix. Individual MWCNT sink under the matrix surface and shimmer through the surface in SEM. Only some of them partially stick out from the surface in very few spots.

6.4.5. UHMWPE

The sintering parameters of the UHMWPE and UHMWPE/MWCNT membranes were identical, as the fusion of the particles happened sufficiently to allow for handleable samples. All samples were flexible and supple. This allows for a direct comparison between MWCNT concentrations. As the particle size and shape variation of the UHMWPE powder was significantly smaller than for PEI, the powder could be handled with different techniques. One investigated technique was the rolling of the powder under a compressive force between two sheets of PEEK foil. The flowability of the powder was low enough to allow for very thin, compressed sheets of the non-sintered powder that could resist minor impacts through tapping.

Through sintering, membranes as thin as 80 μm could be produced. Nevertheless, the addition of MWCNT at a concentration as small as 0.5 wt% already increased the flowability of the powder to such a level, that the rolling technique was rendered unusable. The powder did not fold on itself, but rather slipped and was pressed from between the PEEK sheets as individual powder particles. From these observations, the sintering technique was adapted to allow for the same approach of the UHMWPE powders, independent of MWCNT concentration.

The surface of a sintered membrane from pristine UHMWPE can be seen in **Figure 83**. Because the UHMWPE particles are smaller than for PEI, the surface pore size generally is also smaller. The relatively small difference in particle size and shape also produces a more homogenous shape of the membrane surface.

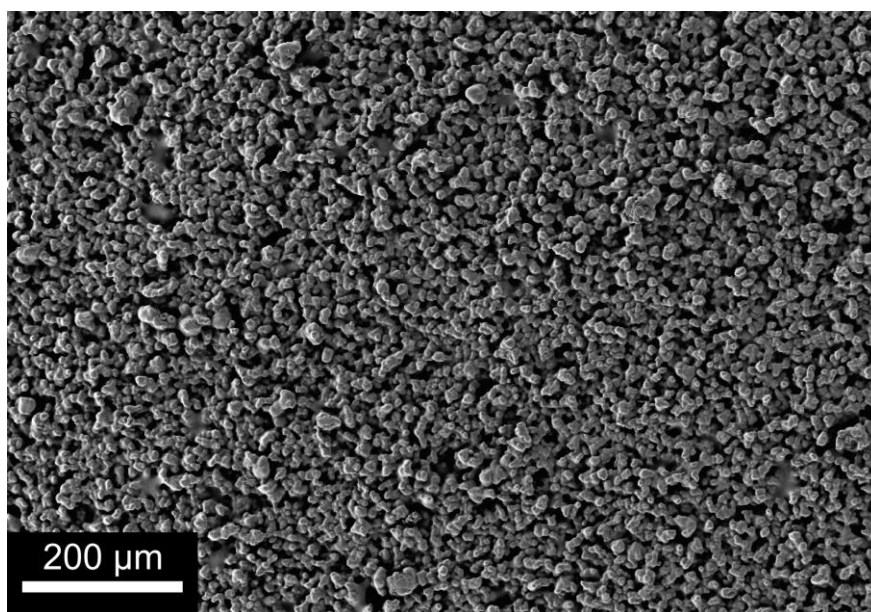


Figure 83: Surface of a sintered UHMWPE membrane at 220 °C for 2 h.

As was discussed in the observation of the sintering behaviour of two pristine UHMWPE particles through optical microscopy, **Figure 84** confirms the observation for more complex powder systems and sintering conditions. A porous membrane can be sintered at a relatively low temperature of 170 °C and 19 min. In the comparison, the surface porosity and pore size is visibly decreased for the membrane sintered at 220 °C for 2 h. The observation from the optical microscopy, that initial fusion is rapid and further viscous flow is slow, holds true in the more complex particle and heating arrangement for the membranes.

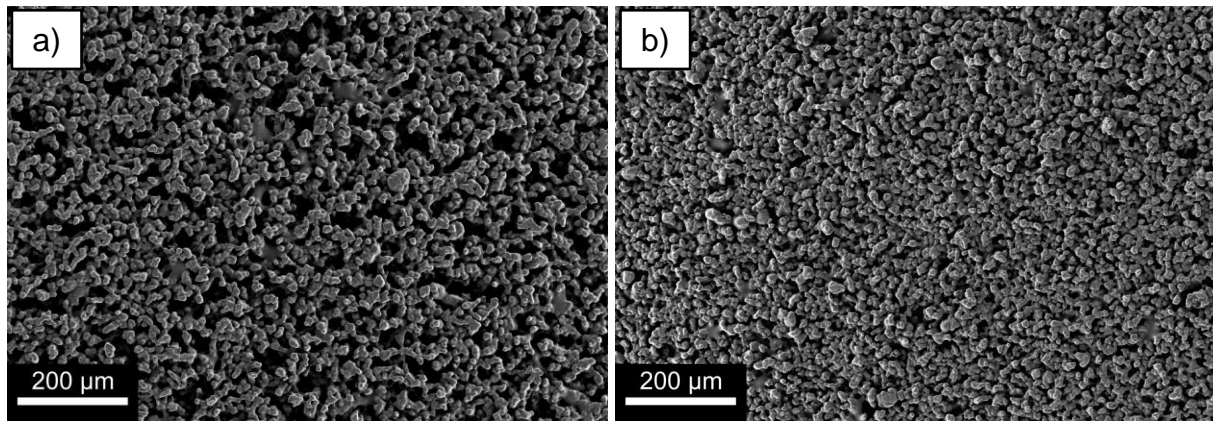


Figure 84: Comparison of the surface of an 80 μm thin membrane (a) of UHMWPE that was sintered for 19 min at 170 $^{\circ}\text{C}$, compared to (b) the membrane sintered at 220 $^{\circ}\text{C}$ for 2 h.

The magnification of the surface in **Figure 85** illustrates the pronounced fusion of the particles. Sintering bridges are strongly developed to a point where a certain distinction of former particles can no longer be made. A notable rounding to a smoother spherical shape of the former particles cannot be observed in comparison with the powder particles before sintering. As the results from the rheological analysis suggest, the tension in the surface of the polymer melt was therefore not strong enough to induce the necessary material flow for a pronounced rounding. Additionally, it appears that viscous flow and therefore drag played a significantly smaller role than for PEI. The shapes of the sintering bridges and the pores indicate that the fusion happens more or less equally in all contact directions. There are no significantly larger particles in the used powder and therefore single particles that dominate during the sintering. This does not mean that the amount of viscous material flow is negligible, as it is the mechanism behind the fusion of the particles. A few sintering bridges clearly show that viscous material flow influences the sintering process, as can be seen in **Figure 85**, where some bridges are clearly thinned out in their middle.

Notably, the gaps and cracks present on the powder particles before the sintering are no longer visible, indicating that these smaller scale movements were possible together with the particle fusion.

As the UHMWPE shows a well progressed particle fusion and the particle rounding during the sintering progress appears to have not played a significant role, the pore shape can be assumed to directly result from the powder particle stacking in the green body and the viscous material flow induced by the fusion process of the particles.

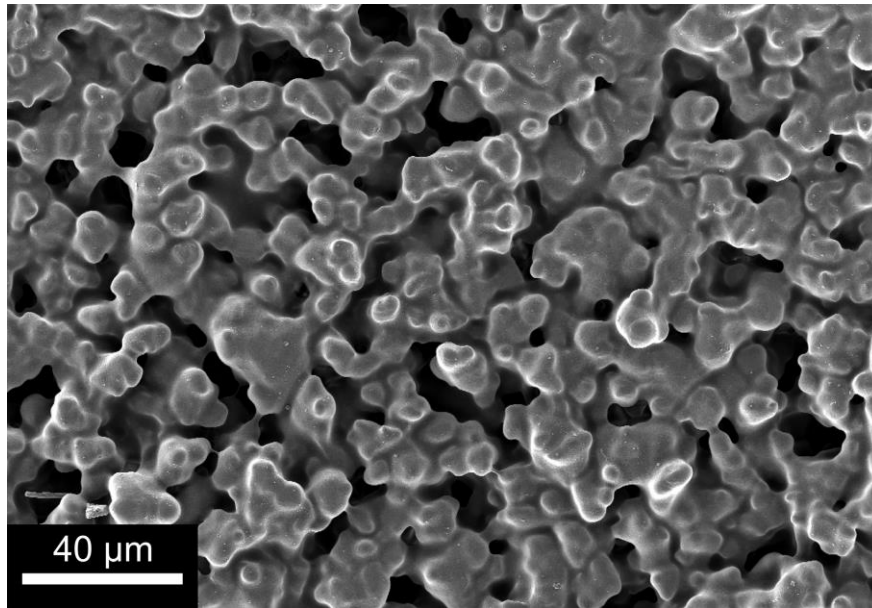


Figure 85: Magnification of the surface of a sintered UHMWPE membrane. Visible is the pronounced fusion of the UHMWPE particles and the resulting sintering bridged between them. Pore size and shape result from the neighbouring particle shapes and sizes, and the resulting flow drag during the fusion.

A larger magnification can be seen in **Figure 86** which shows the material surface itself. The image of the material is significantly changed compared to the pristine powder particles before the sintering. The surface no longer appears to be smooth, but rather shows a string-like profile. These strings are the crystalline lamellae which can usually be found in UHMWPE. The heating and cooling during the sintering allowed for a display on the surface. As the results from DSC showed, the crystallinity of the initial powder particles (1st DSC run) is higher than for the molten and cooled material (2nd DSC run). This indicates that the production of the powder particles likely has smoothed the surfaces and not lowered the overall crystallinity.

The cross section of the UHMWPE membrane shows a similar image to the surface with thick sintering bridges and well-progressed fusion sites. The fusion of the powder particles with the well progressed development of the sintering bridges and fusion sites gives many fracture sites a roughly elliptical shape. From what can be seen from SEM micrographs, the elliptical shape is a result of the fusion of different particles and the fusion of the round protrusions on the particles with each other, resulting in the extension in one dimension. As the fusion of the round protrusions and the particles both are in many cases involved in the same sintering bridge, they act as weak spots together for fracturing. At significantly shorter sintering times and lower temperature, the onset of the progression from nearly circular sintering bridges to elliptical ones can be seen, here shown by **Figure 88**.

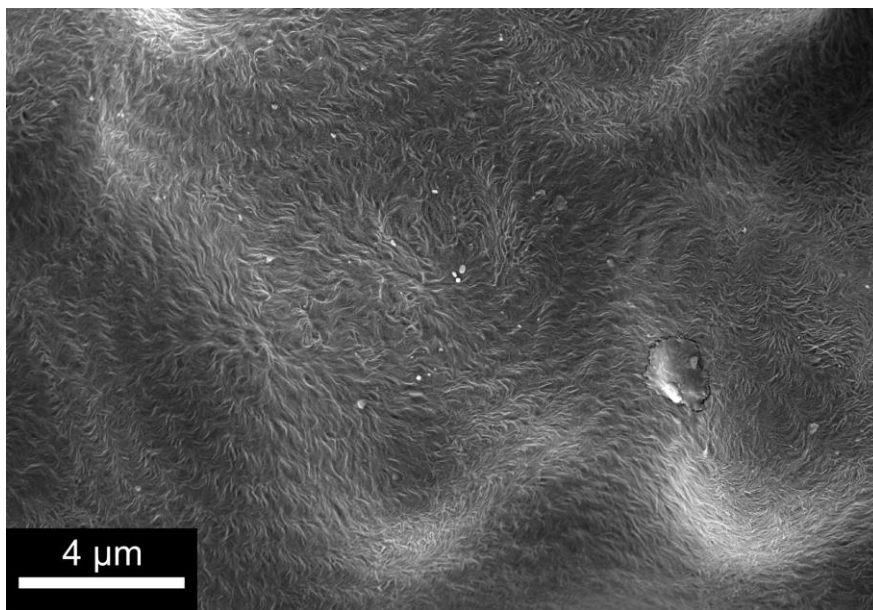


Figure 86: Magnification of the surface of a former UHMWPE particle in the membrane. Significant is the difference in the visible surface morphology compared to the original powder particles. Wave-like shapes resulted from a recrystallization into a lamellar crystalline structure during the cooling after the sintering.

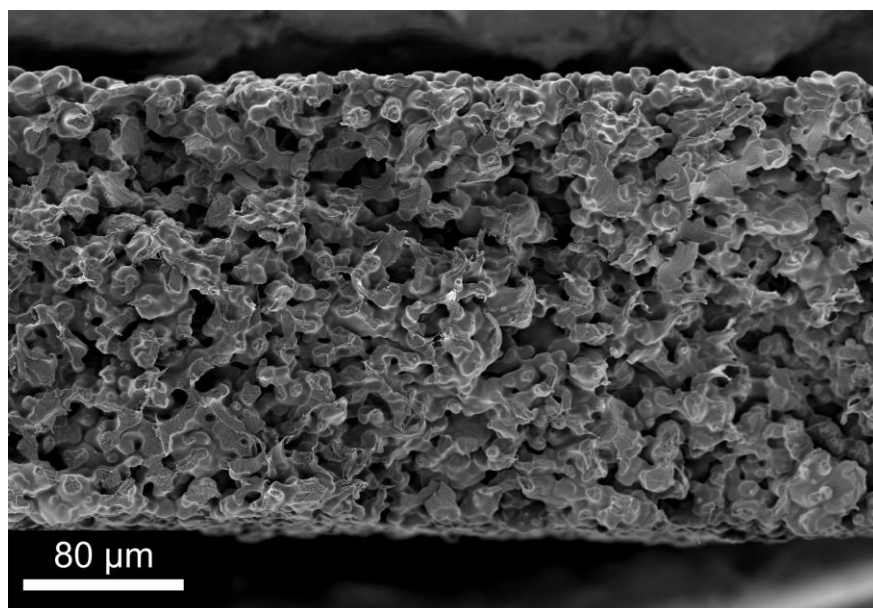


Figure 87: Cross section of a sintered UHMWPE membrane. A tortuous pore structure, typical for sintered membranes, through the whole membrane is visible.

Identical to the differences in surface structure and porosity as was discussed for **Figure 84**, a sintered porous structure is visible for the thinner membrane sintered at 170 °C for 19 min and for thicker one at 220 °C for 2 h in **Figure 89**. The initial fusion rate is rapid and also causes significant sintering bridges between the particles over the whole thickness. Compared to the images of the porous surfaces, the difference are harder to see in the cross section, caused by the irregular path of fracture plane through the sample.

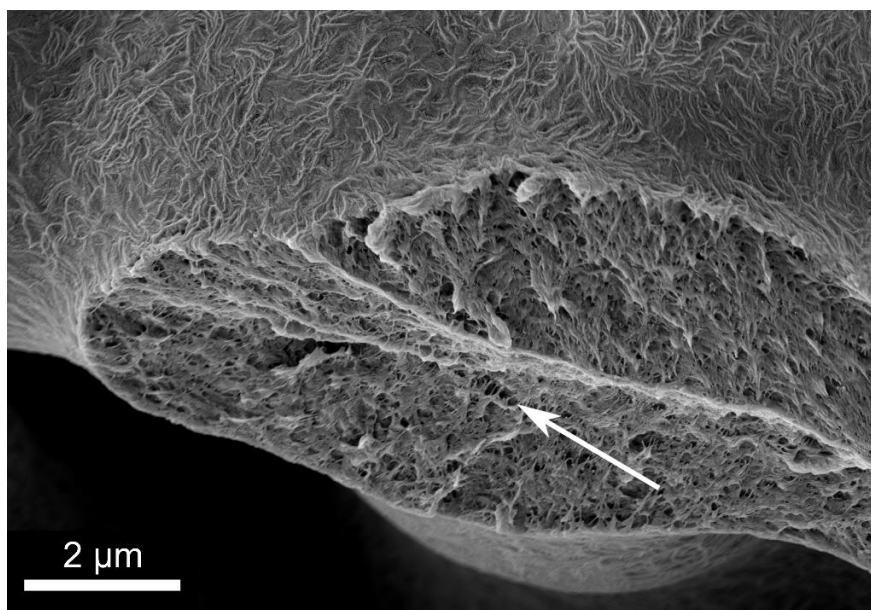


Figure 88: Magnification of a fracture site in the cross section of a sintered UHMWPE membrane. The structure of the fracture shows small pores and a relatively string-like ruptured matrix.

The bridges in the right image are more developed and show elliptical fracture surfaces, while they are less developed with circular fracture surfaces in the left image.

The results from the rheological analysis show that UHMWPE melt has a very high melt viscosity at low deformation rates. As the dimensionless neck radius x/r quickly increases, the driving force behind the fusion quickly decreases.

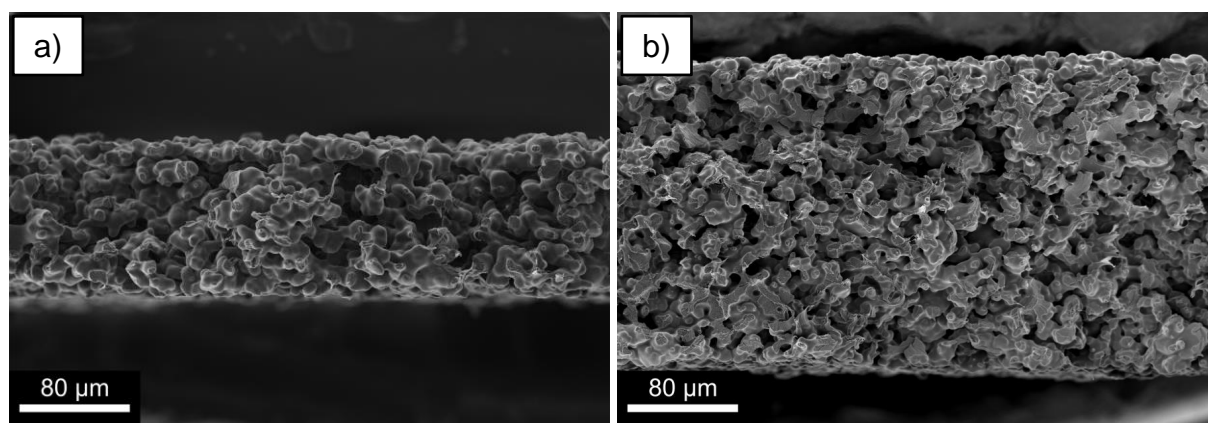


Figure 89: Comparison of the cross section of an 80 μm thin membrane (a) of UHMWPE that was sintered for 19 min at 170 °C, compared to (b) the membrane sintered at 220 °C for 2 h.

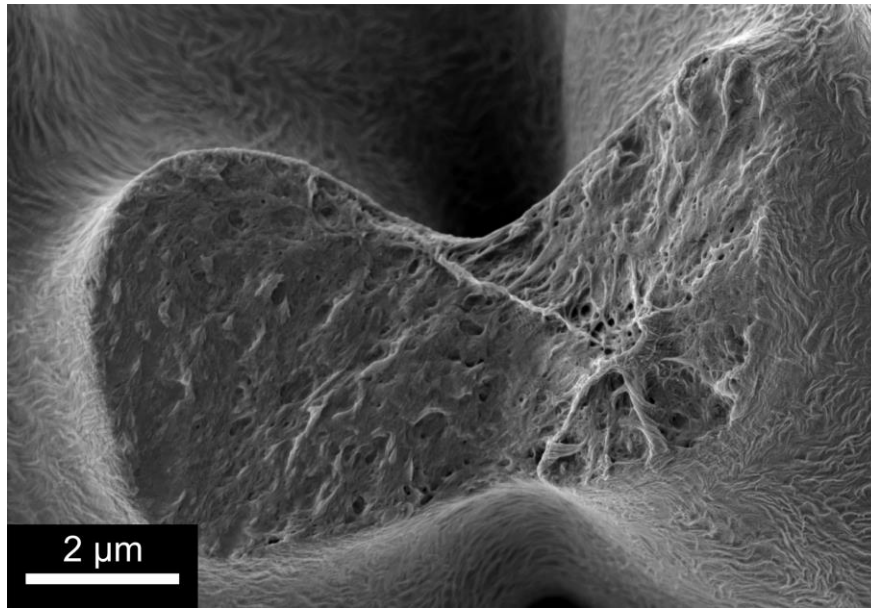


Figure 90: Magnification in a fracture site in an UHMWPE membrane, sintered at 180 °C for 11 min. Apparently fusion happened between two directions, one in plane of the image between left and right and one perpendicular to the image plane, giving the fracture site a shape reminiscent of the number “8”.

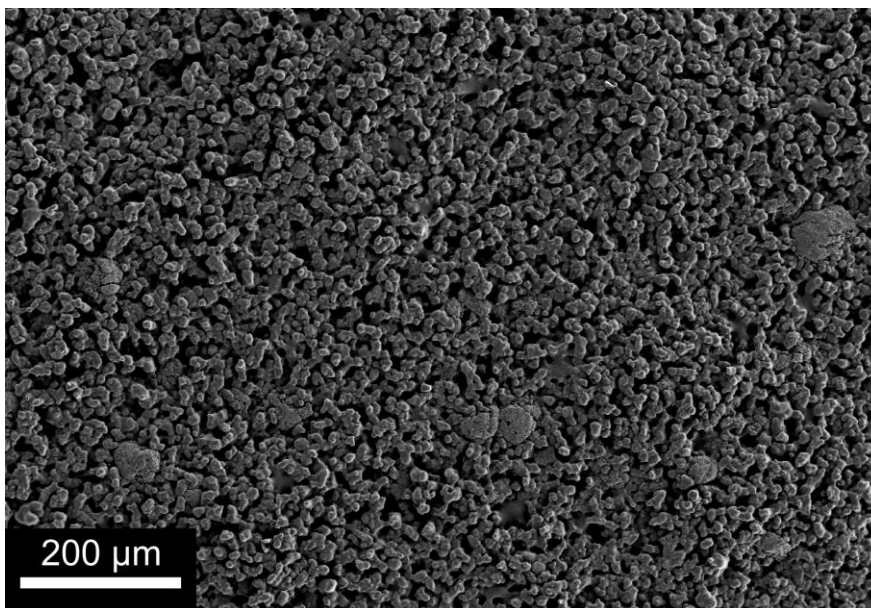


Figure 91: Surface of sintered membrane of UHMWPE/MWCNT 3.0 wt%. Overall the image is the same as for pristine UHMWPE, with the exception of the clearly visible MWCNT agglomerates. These agglomerates were also present in the powder of UHMWPE/MWCNT 3.0 wt% and did not result from the sintering process.

While a significant influence of the MWCNT could be observed in SEM micrographs for PEI/MWCNT, the same is only partially true for UHMWPE/MWCNT. The overall shape of the pores, sintering bridges and fusion sites is generally the same as for pristine UHMWPE. The clearly visible MWCNT agglomerates recognisable in **Figure 91** stand out. Rarely the MWCNT are recognisable as shimmering lines under the surface and for the most part, when they partially stick out from the surface.

The quality⁹ of a sintered membrane strongly depends on the quality of the used powder, especially for the used composite powder with MWCNT decorated powder particles. As was mentioned above, the distribution of the MWCNT on the powder particles of UHMWPE was less successful than for PEI, as the size of agglomerates was significantly smaller in PEI on the absolute scale and also relative to the powder particle dimensions. While the MWCNT agglomerates in PEI/MWCNT were either strongly enveloped or notably partially penetrated, this is not the case for UHMWPE/MWCNT. The very large agglomerates apparently are only penetrated to a small depth and the largest part of them remains pure MWCNT. For the higher MWCNT concentrations of 3.0 wt% (see **Figure 92**) and 5.0 wt%, and also the low-quality powder of 1.5 wt% to 2.5 wt%, extremely large agglomerates were found. They sometimes reach diameters well above 100 μm , which is roughly a fifth of the membrane thickness.

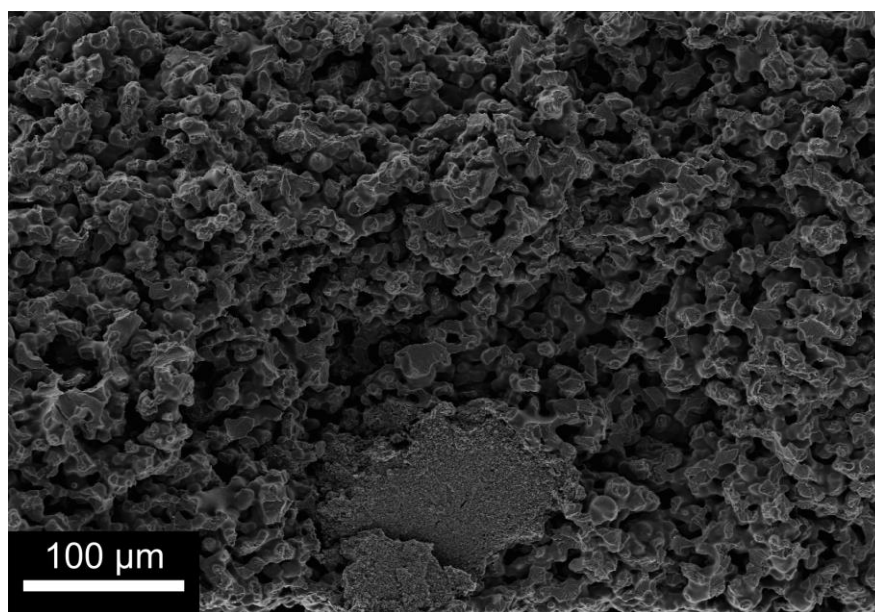


Figure 92: Cross section of a sintered UHMWPE/MWCNT 3.0 wt% membrane. A tortuous pore structure as for UHMWPE can be seen. In the bottom centre is a large agglomerate of MWCNT visible.

Nevertheless, apart from the MWCNT agglomerates, handling and processing of UHMWPE/MWCNT could be performed identical to UHMWPE. The sintered samples of UHMWPE/MWCNT were all flexible and easy to handle. Even though the MWCNT have a notable influence on G' and G'' at low angular frequencies, this does not have a clearly visible influence on the morphology of the membranes. Apart from the rheological behaviour, the

⁹ In terms of amount of agglomerates.

UHMWPE matrix also shows an apparent identical image to the pristine material of the surface after crystallisation.

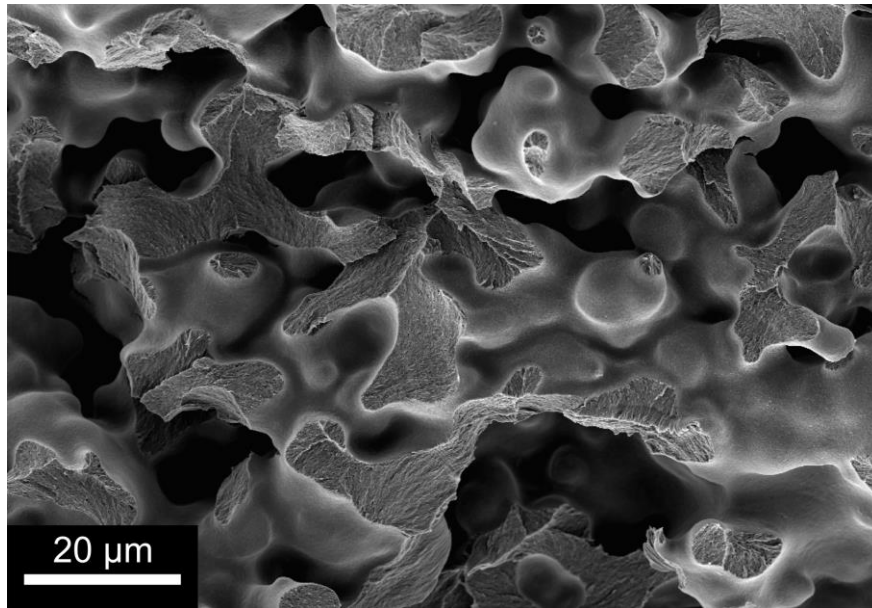


Figure 93: Magnification of the cross section of a sintered UHMWPE membrane. The deviation of the pore sizes and channel structure can be seen. Fracture sites are typically elongated and resemble the shapes of the sintering bridges, indicating that they are the expected weak spots of the membrane structure.

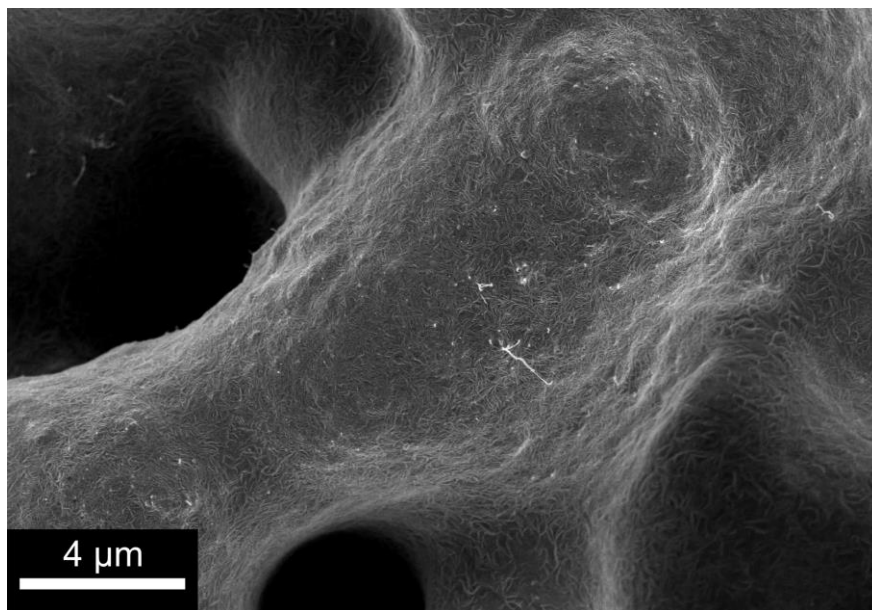


Figure 94: Magnification of a sintering bridge between particles in the cross section of UHMWPE/MWCNT 1.0 wt%. MWCNT have sunken under the matrix surface with only a few MWCNT being visible due to them partially sticking out from the surface.

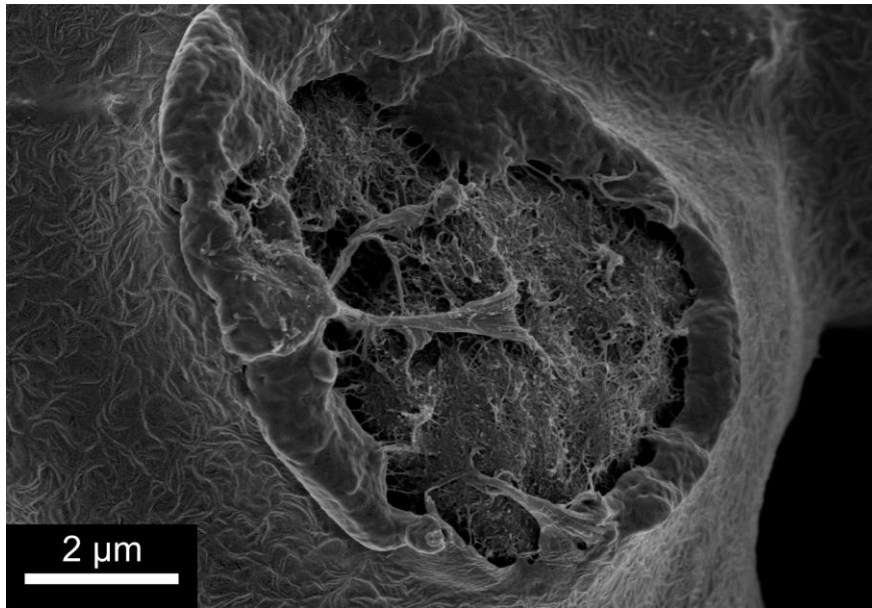


Figure 95: Magnification of a fracture site in the cross section of UHMWPE/MWCNT 5.0 wt%. An enveloped MWCNT agglomerate acted as a weak spot in the connection of two fusing particles.

From the SEM micrographs alone it is uncertain if the crystallisation and therefore the rapid increase in density during the cooling in the sintering process causes deformations in the sintered structure. Yet, the significant change in the surface morphology of the material has strong implications for the MWCNT network. The MWCNT are located on the smooth surfaces of the powder particles. During sintering, the MWCNT sunk under the surface of the polymer matrix, analogue to PEI.

It can be assumed that the sinking itself does not cause significant disruptions in the MWCNT network. But as the matrix melt starts to crystallise into the lamellar crystal structure, a possible disruption of the MWCNT may occur. Scanning electron micrographs do not allow for an analysis of this, because the MWCNT for the largest parts of the membranes are not visible under the surface. Measurements of the conductivity depending on the temperature will be discussed in Chapter 6.8.2, where indeed a disruptive effect of the crystallization was found.

To better investigate the structure of the MWCNT, a sintered sample of UHMWPE/MWCNT 5.0 wt% was cut through ion-milling. This resulted in a flat cut through the cross section of the membrane. The MWCNT network is clearly visible for both BSE and SE contrast in **Figure 96**. In both cases the MWCNT are visible as either brighter parts (BSE) or darker parts (SE).

With a flat cut, the pathways of MWCNT in the network become visible and show an apparently well connected network. As can be seen with both images in **Figure 96**, the MWCNT are mostly

positioned near the material surface (right image), but in some areas (left image) they are present in an apparent deeper part of the UHMWPE matrix. Two things have to be kept in mind. Firstly, the UHMWPE powder particles are relatively irregular in shape with their “popcorn-like” structure. Round protrusions are present on virtually all particles. Secondly, the cut is straight through the cross section. How the network looks like in the plane away and into the image is not known. Therefore, paths of MWCNT that are apparently deeper in the matrix may very well be closer to an edge than it appears.

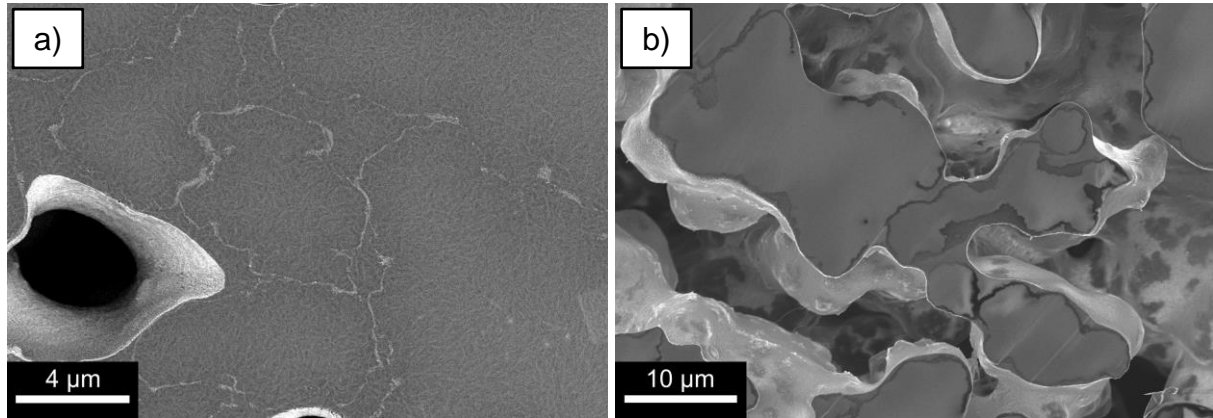


Figure 96: MWCNT network visible in the cross section of a UHMWPE/MWCNT 5.0 wt% membrane. The network was made visible by preparing the sample via ion beam cutting. On the left side, the network is visible in a mixed signal of BSE and SE contrast. The brightest spots are remaining parts of the iron catalyst on the MWCNT. The right image shows a different area in SE contrast, here the MWCNT are visible as darker lines.

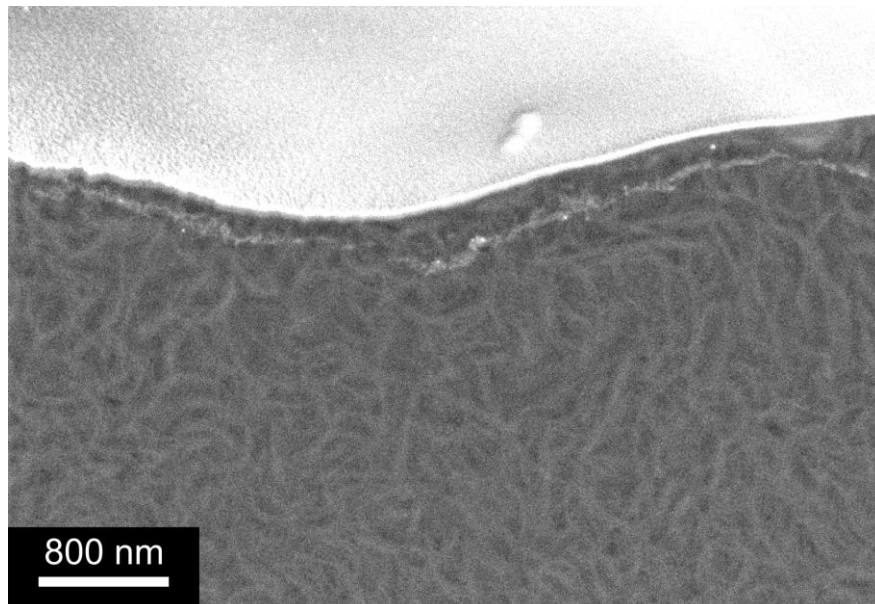


Figure 97: Magnification of a MWCNT path that had sunken under the material surface during the sintering of UHMWPE/MWCNT 5.0 wt%.

From the images, it is clearly visible that the MWCNT are in a very well segregated network, which resulted in the good conductivity of the sintered membrane. Thicker parts, as can be seen,

for example, in the bottom left corner of the left image in **Figure 96** are small MWCNT agglomerates that are already present in the decorated powder. It is also visible that the individual MWCNT sink under the surface during the sintering, which is magnified in **Figure 97**.

For comparison, a compression moulded sample of UHMWPE/MWCNT 5.0 wt% was also ion-milled. A side-by-side comparison with the sintered sample is shown in **Figure 98**. At the same magnification, it is clearly visible that the MWCNT network for the compression moulded sample appears to be significantly denser and better connected.

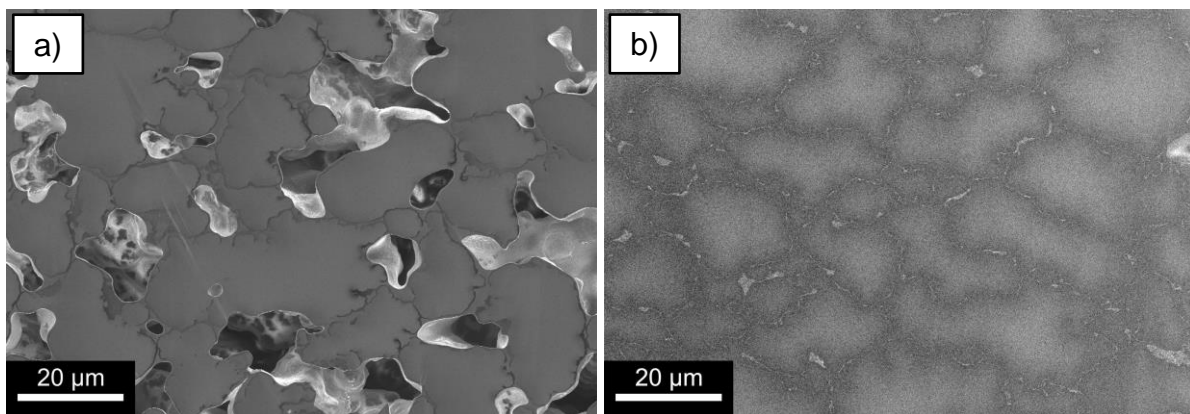


Figure 98: SEM micrographs of the cross sections of ion milled of UHMWPE/MWCNT 5.0 wt% samples. The left image is in SE contrast, the right one in BSE contrast. The left micrograph is in SE contrast from a porous sintered membrane, the right in a mixed signal of BSE and SE contrast from a compression moulded dense sample.

This is the opposite of what was observed for PEI/MWCNT 3.0 wt%. This is probably a result of the significantly higher viscosity of UHMWPE/MWCNT 5.0 wt% and a higher elastic property of the composite melt. During the compression part of the compression moulding, the original powder particle shape and therefore MWCNT distribution is better conserved, leading to a better developed network.

Analogous to PEI/MWCNT, to prove qualitatively that the pictured MWCNT network is indeed conductive through its pathways and the contrasting effect is not a different interaction between sample and electron beam, conductive AFM was performed for supportive results. In **Figure 99**, the conductivity of the pathways is shown for both the sintered sample and the compression moulded one.

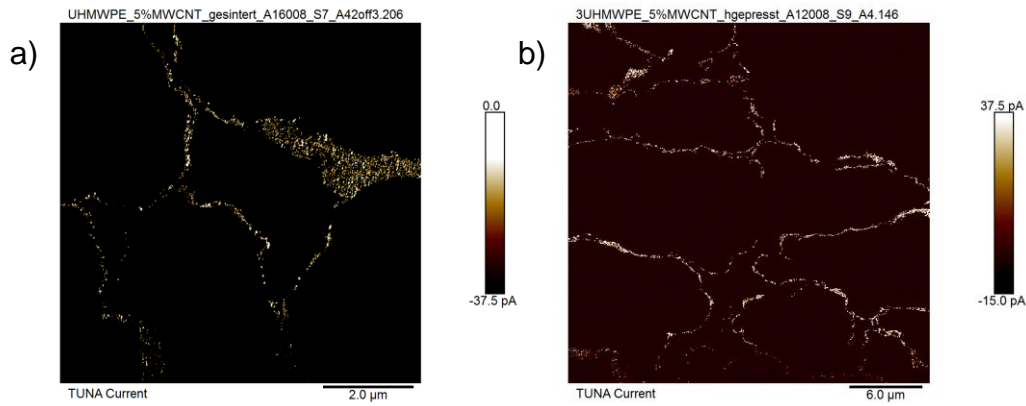


Figure 99: C-AFM image of regions of UHMWPE/MWCNT 5.0 wt%. The left image (a) shows a region of a sintered porous membrane, the right image (b) a region of a compression moulded sample.

6.4.6. Summary for the UHMWPE and UHMWPE/MWCNT membranes

Ultra-high molecular weight polyethylene is a semi-crystalline polymer with a pronounced lamellar crystalline structure. While PEI showed in the scanning electron micrographs indications of the expected low displacement of the MWCNT in the finished membrane, things appear to be different for UHMWPE. The surface of the powder particles before sintering is considerably smoother than for the sintered membranes. In comparison, the lamellar crystalline structure is clearly visible on the material surfaces in the sintered membranes, but not in the powder. This gives implications for the formation of the MWCNT network, as the MWCNT were found to sink under the polymer surface during the sintering. The MWCNT are not clearly shimmering through the surface as was the case for PEI, but rather only are visible at a few selected spots. This could mean that the MWCNT more easily sink under the UHMWPE surface as polyethylene and MWCNT are more similar in their material composition than MWCNT and PEI, or that the crystallisation of the UHMWPE in the cooling step of the sintering causes the MWCNT to be not visible. This could have happened either through further shifting the MWCNT into the matrix or covering them through the similarity of the pronounced string-like appearance of the lamellae on the surface.

Unlike for PEI, the presence of the MWCNT does not appear to drastically change the sintering behaviour. The sintered membranes of UHMWPE and UHMWPE/MWCNT of any concentration show no clearly visible differences from the SEM micrographs in their general morphology. The decorated powder particles do not preserve their shape as strongly as was the case for PEI/MWCNT compared to the pristine polymer. Fusion of the particles through sintering bridges and direct fusion sites is very well developed. Individual particle shapes can no longer be clearly distinguished in most cases.

Fractures in the membrane also show no direct correlation to strong MWCNT presence through fusion of two decorated surfaces. The fractures happened at different points of the sintering bridges and fusion sites, not predominantly at the MWCNT-MWCNT contact points of the two surfaces of the particles in contact before the sintering. Still, the presence of smaller MWCNT agglomerates at the fusion sites or the sintering bridges apparently leads to brittle weak point that act as origin points for fractures, at least at cryogenic conditions.

The ion-milled cross section of UHMWPE/MWCNT 5.0 wt% illustrates the formed conductive network of the MWCNT inside the UHMWPE matrix. From the micrographs, it can be seen that the network overall appears to be continuous. Due to the shape of the original particles and the MWCNT distribution on them, it is likely that not all apparent dead-ends are in fact ends in the pathways. The path in the uncut matrix may have continued out of the visible plane from the cut sample.

6.5. Wet-Dry Method for Determination of Porosity

The wet-dry method using ethanol was used to determine the porosity of the sintered membranes for PEI and UHMWPE. Penetration of the open porous structure of the membranes was fast because the pore sizes were relatively large. Ethanol wets both PEI and UHMWPE efficiently and does not dissolve the materials.

6.5.1. Polyetherimide

The measurement results for PEI and PEI/MWCNT membranes show a direct correlation between sintering time and porosity, as can be seen in **Figure 100**. For PEI/MWCNT with MWCNT concentrations higher than 1.5 wt%, the sintering time was increased from 15 min to 24 min. While the porosity of PEI and PEI/MWCNT with less than 2.0 wt% ranges between 25% and 30%, for PEI/MWCNT with 2.0 wt% and higher concentrations it is around 20%. For the membranes with the sintering time of 15 min, no direct correlation between MWCNT concentration and porosity was found. For example, PEI/MWCNT 0.5 wt% shows a lower porosity than pristine PEI, while 1.5 wt% is about the same as for pristine PEI, but with a lower standard deviation. The membranes with the sintering time of 24 min overall have a lower porosity and do not significantly deviate from each other. The values of all membranes are in the range that can be expected for sintered membranes.

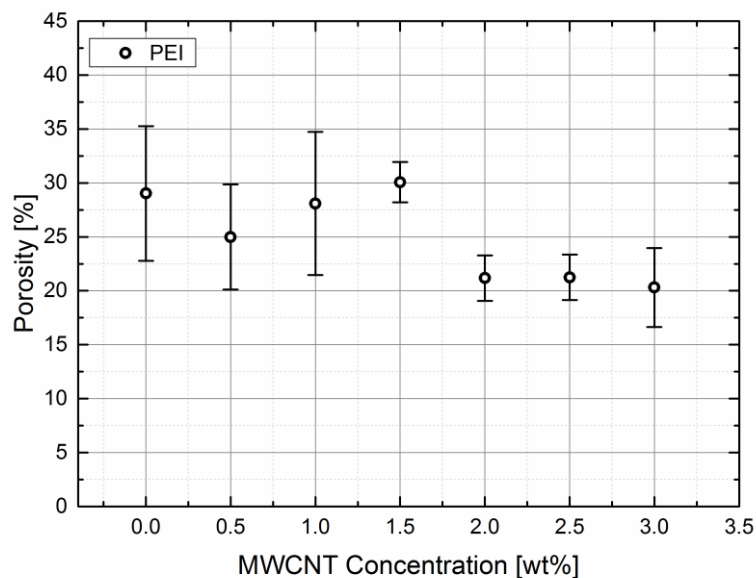


Figure 100: Porosity of PEI and PEI/MWCNT membranes as determined by the wet-dry method. No significant difference between pristine PEI and MWCNT concentrations up to 1.5 wt% were found. For UHMWPE/MWCNT with MWCNT concentrations from 2.0 wt%, a noticeable drop in porosity is visible. Longer sintering times were used for 2.0 wt% and higher concentrations.

From the results of the rheological analysis, it was expected to see a significant difference in the porosity of membranes with MWCNT for the same sintering parameters, which was not found. Even though the addition of MWCNT noticeably changes the rheological behaviour at lower frequencies, this does not appear to directly influence the porosity. A possible explanation for this can be the random nature of the stacking of the powder particles in the green body and the morphology change from the compressed green body to the sintered membrane. Pristine PEI appears to have higher viscous flow and drag than PEI/MWCNT of any MWCNT concentration, as was seen via SEM (see **Figure 67** to **Figure 70**). Viscous flow and the resulting drag change the porous structure and can open up gaps, while closing others, depending on the particle orientation to each other and the contact points. The powder particles of PEI/MWCNT showed a less pronounced viscous flow and therefore can be assumed to deviate less from the structure originally present in the green body. This appears to result in similar porosities for the same sintering times.

6.5.2. Ultra-High Molecular Weight Polyethylene

The porosity of the UHMWPE and UHMWPE/MWCNT membranes is in the range of pristine PEI and PEI/MWCNT with less than 2.0 wt% MWCNT. While there is no significant difference between UHMWPE and UHMWPE/MWCNT membranes, a few points stand out. Firstly, there is a small increase in the median porosity from UHMWPE to UHMWPE/MWCNT 0.2 wt% and again to UHMWPE/MWCNT 0.5 wt%. While not significant, this could indicate a small change in the sintering behaviour through the addition of MWCNT. With further increasing MWCNT concentration, porosity shows no further increases with two exceptions. First is UHMWPE/MWCNT 2.5 wt%, where the mean porosity is visibly higher than for 2.0 wt% or 3.0 wt%. The second exception is UHMWPE/MWCNT 5.0 wt%. The mean value is not the notable point, but rather the increased standard deviation. Of all the MWCNT concentrations for UHMWPE, 5.0 wt% is the powder with the highest surface-covering with MWCNT and amount of agglomerates. This apparently caused the powder to be the least consistent with sintering and porous structure formation, possibly with a strong influence of the clusters of MWCNT agglomerates and powder particles. Those clusters appear from the SEM analysis to be highly packed and could very likely be impenetrable for liquids.

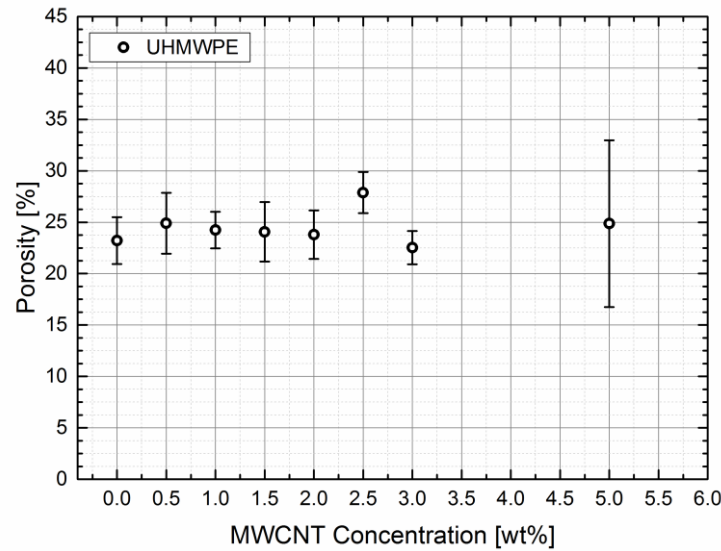


Figure 101: Porosity of UHMWPE and UHMWPE/MWCNT membranes as determined by the wet-dry method. No significant difference between pristine UHMWPE and MWCNT concentrations up to 5.0 wt% were found. For UHMWPE/MWCNT 5.0 wt%, the deviation between samples is visibly increased.

6.6. Porometry

For the analysis of the porous structure through porometry, the three most important values are the first bubble point diameter¹⁰, the smallest detected diameter and the mean flow pore diameter¹¹. Capillary flow porometry only detects the smallest diameter of a continuous pore channel or channel network at a set pressure. The comparison of these values should suffice for additional insight into the different membrane morphologies, depending on the MWCNT concentration. For polyetherimide, they also relate to the two different used sintering parameters.

A more in-depth comparison of individual membranes with a complete pore size distribution would not be feasible because the pore size distributions greatly differ in their exact make-up. Conventional sintering of membranes automatically leads to a certain degree fluctuations in the membrane morphology, due to the particle stacking and shifting during the sintering process.

¹⁰ As described in Chapter 5.6: The first bubble point corresponds to the largest detected pore diameter

¹¹ The mean flow pore diameter is the diameter at which 50% of the gas flow through the dry membrane is achieved

6.6.1. Polyetherimide Membranes

The mean flow pore diameter in **Figure 102** shows overall a declining trend with increasing MWCNT concentration. The change from pristine PEI at around 16.25 μm down to around 5 μm for PEI/MWCNT 3.0 wt% is an effect of the addition of the MWCNT and the increased sintering time. Independent of the sintering times, a decrease of the mean pore flow diameter with increasing MWCNT concentration is visible. While the measurement of the porosity showed that there are two distinguishable groups, separated by the different sintering parameters, this is not the case for the mean pore flow diameter. As was discussed in the analysis of the rheological properties, the sintering behaviour and the morphology of the sintered membranes, the addition of MWCNT leads to a lower tendency of the powder particles to round and show overall viscous flow. This is in good correlation with the trend for the mean pore flow diameter. Because the powder is already highly compressed in the green body, a relatively low value of porosity and pore diameter for the geometry of the compacted powder can be assumed. With a relatively large amount of particle rounding and viscous material flow during sintering, material may preferentially flow in one direction to perform coalescence. If there is a preferred viscous flow direction, other contact points may be underdeveloped initially, leading to some pores to grow and other to shrink. From the mean pore flow diameter, it is shown that the shift of the material during sintering can cause a larger mean pore flow diameter while keeping a relatively constant porosity. The addition of MWCNT therefore directly causes a change in morphology while keeping the dimensions and the porosity of the sintered membrane comparable between MWCNT concentrations of identical sintering parameters.

In comparison to the porosity, indications of a comparable trend can be seen in **Figure 103** for the first bubble point¹² and smallest detected pore diameter¹³. While the porosity does not differ significantly between pristine PEI and MWCNT concentration up to 1.5 wt% (see **Figure 100**), the less porous concentrations of 0.5 wt% and 1.0 wt% show smaller first bubble point and larger smallest detected pore diameter values, with 1.5 wt% being the exception.

¹² It has to be mentioned again, that the first bubble point is the largest singular pore diameter per measured membrane. Usually this is a single pore or a very small number of pores in the same detection tolerance.

¹³ Analogous to the first bubble point diameter, this value is a generally for the singular smallest detectable pore diameter or a small number of pores in the same detection tolerance

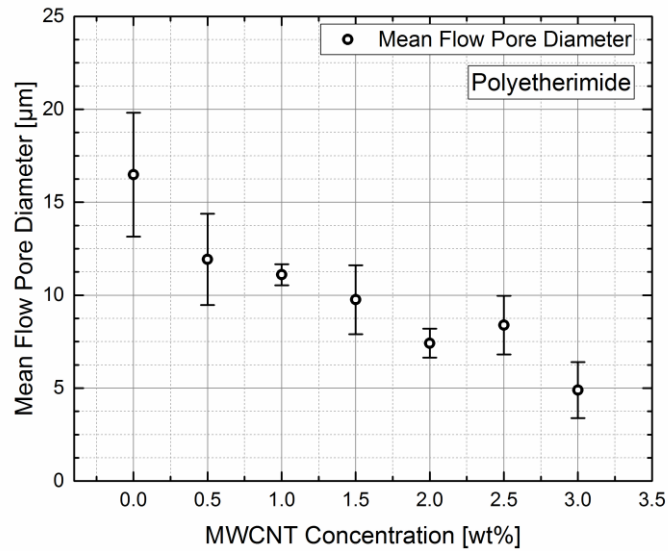


Figure 102: Mean flow pore diameter of PEI and PEI/MWCNT membranes.

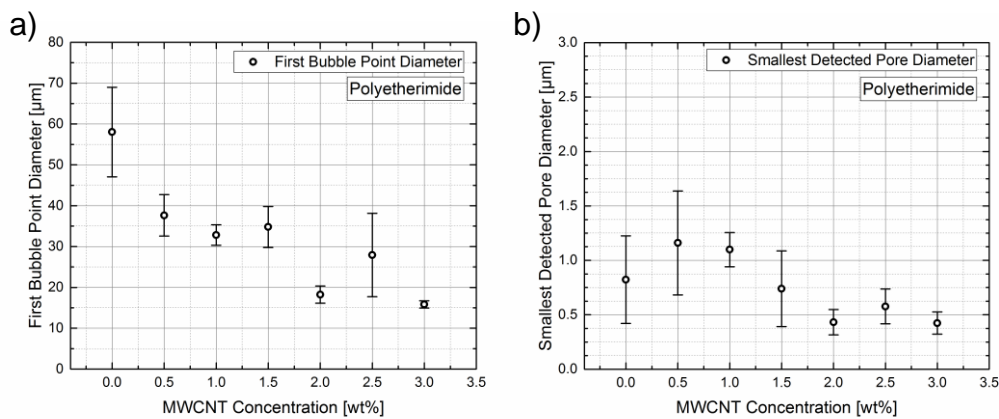


Figure 103: First bubble point diameter for largest detected pore diameter (a) and smallest detected pore diameter (b) for PEI and PEI/MWCNT membranes.

As was expected from the large particle size and shape deviation of the commercial PEI powder, the first bubble point and smallest detected pore diameter value are very different from the mean pore flow diameter. This is less pronounced for the higher MWCNT concentrations from 2.0 wt% to 3.0 wt%, for which the overall porosity was lower and nearly identical to each other. The lower fusion rate, the lower tendency for particle rounding and the overall reduced porosity most likely are the main contributors to the smaller deviation between the mean flow pore diameter and the first bubble point and smallest detected pore diameter. The composite powders therefore apparently sintered in a more homogenous manner to a smaller porosity with additionally smaller pore size diameter variation. On the contrary, the lower MWCNT concentrations from 0.2 wt% to 1.5 wt% and the pristine PEI seem to sinter increasingly inhomogeneous with decreasing MWCNT concentration. Therefore, while the addition of

MWCNT indeed hinders the sintering process and decreases the coalescence and densification rate, it allows for a better control of the pore structure with increased time.

6.6.2. Ultra-High Molecular Weight Polyethylene Membranes

For UHMWPE, the sintering parameters were kept identical for all MWCNT concentrations. Therefore, any difference in the detected pore diameters is a direct influence of only the MWCNT and their distribution on the powder particles on the sintering behaviour. The differences of the quality were expected to then cause differences between the decorated powders.

While no difference was observable in the direct observation through optical microscopes, the porosity measurement indicated that in the more complex real sintering condition for the membrane, the MWCNT concentration has some influence, even though not linearly with the MWCNT concentration. Instead, the porosity follows a rather unintuitive trend (see **Figure 101**). This also applies for the mean pore flow diameter. While the significance of the difference between the MWCNT concentrations is limited for pristine to 3.0 wt% and to 5.0 wt% due to the large standard deviations, some apparent trends can be seen.

The mean pore diameter appears to show some increase with increasing MWCNT concentration, although not in a significant manner and not linearly, caused by the large differences in the quality of the decorated powders. The MWCNT concentrations from 0.5 wt% to 3.0 wt% show no significant differences. In comparison, pristine UHMWPE shows a smaller mean value and standard deviation and the concentration of 5.0 wt% is higher than the other concentrations, possibly due to the large agglomerates and clusters that are most significant for this MWCNT concentration.

The other MWCNT concentrations, 0.5 wt% without a measurable electrical conductivity with conventional methods and 1.5 wt% to 2.5 wt% with a significantly lower powder quality, do not fit this trend, as can be expected. The inhomogeneous distribution and notable presence of large agglomerates in the powder influence the morphology of the porous membrane negatively. As mentioned above, agglomerates act as barriers for the sintering process, hindering the sintering process.

The first bubble point and smallest detected pore diameter do not give a clear addition to the indications from the mean flow pore diameter. Especially for the first bubble point, relatively insignificant fluctuations are predominant between the MWCNT concentrations, expect for

2.0 wt% and 5.0 wt%. Here the agglomerate presence is a prime candidate for the cause of the larger mean value of the first bubble point diameter and the significantly larger standard deviations.

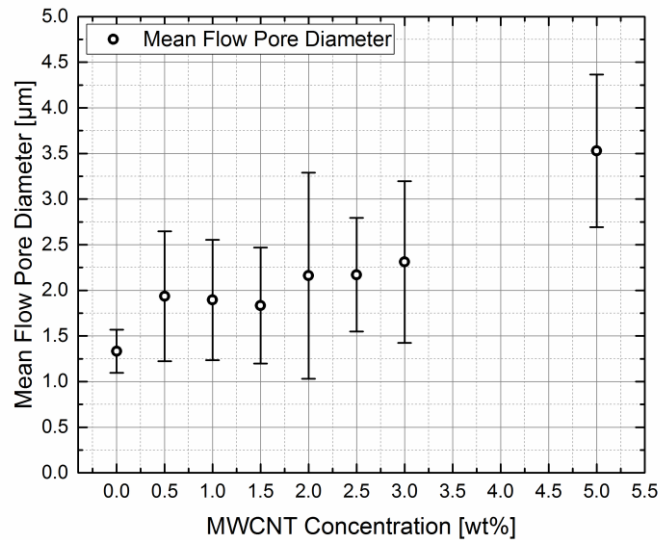


Figure 104: Mean flow pore diameter of UHMWPE and UHMWPE/MWCNT membranes.

For the smallest detected pore diameter, no significant differences were found, except for the standard deviation. The standard deviations are generally too high to allow for an adequate comparison of the mean values. Overall it can be said that the smallest detected pore diameter is comparable between the concentrations.

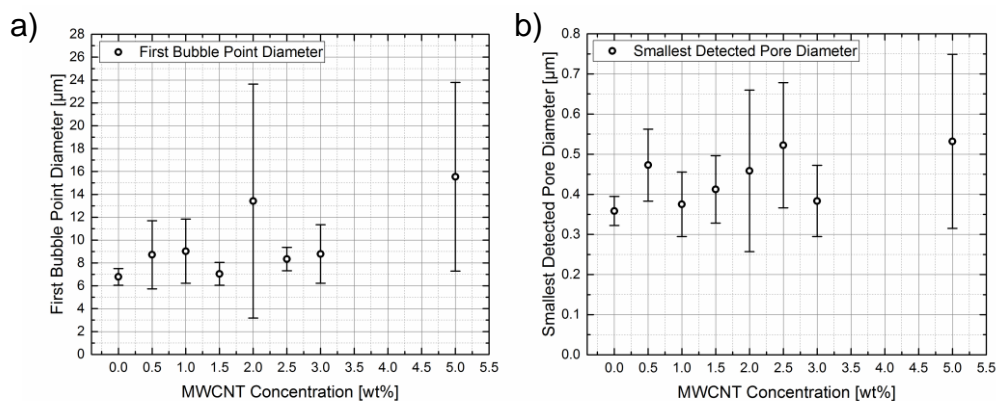


Figure 105: First bubble point diameter for largest detected pore diameter (top) and smallest detected pore diameter (bottom) for UHMWPE and UHMWPE/MWCNT membranes.

Unlike for PEI, the increasing MWCNT concentration does not allow for a better-controlled morphology. Instead, with the good quality powders of the MWCNT concentrations of 1.0 wt% and 3.0 wt%, it can be seen that the mean pore flow diameter may differ only slightly between the concentrations. Additionally, the first bubble point diameter and smallest detected pore

diameter show comparable values to pristine UHMWPE, but have a larger standard deviation. From this, it can be concluded that the addition of MWCNT indeed causes a decrease in morphology quality and control. This is more pronounced for the MWCNT concentrations with lower powder quality, such as 1.5 wt% to 2.5 wt%, for which agglomerates and inhomogeneous MWCNT distribution, in general, contribute to the problem.

6.7. Pure Water Membrane Permeability

6.7.1. Polyetherimide

Pure water flux experiments of PEI and PEI/MWCNT showed that the pure water permeability of the disc-shaped membranes significantly varies. The volume flow of the pure water differed so greatly between the membranes that the used pressure had to be adapted to allow for comparable measurements. No accurate measurement of pristine PEI could have been performed at 1 bar, while 150 mbar were not enough to pass the water through the membrane with 3.0 wt% MWCNT.

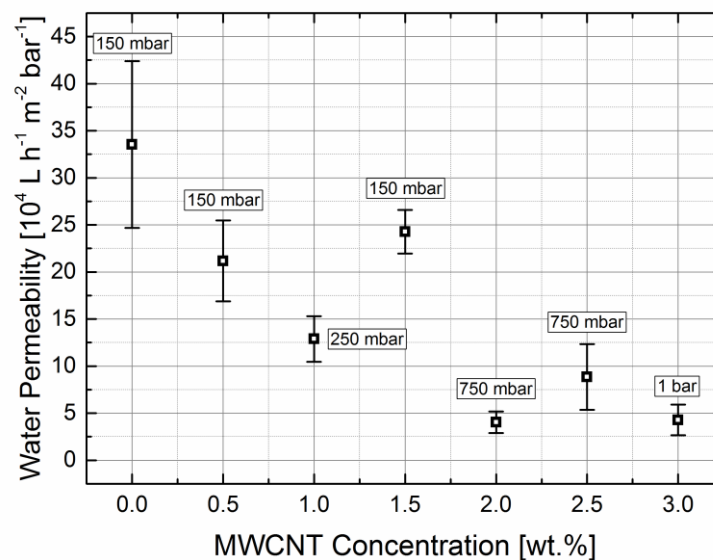


Figure 106: Pure water permeability of PEI and PEI/MWCNT membranes. The transmembrane pressure had to be varied, because the flux greatly varied between samples.

All membranes show high pure water permeability in the range that can be expected of sintered membranes. Even though the membranes are relatively thick with 0.8 mm to 1.0 mm, the pores are large enough to allow for high pure water permeability values.

Even though the SEM analysis revealed that the decorated powder particles tend to keep their original shape more while rounding and fusing together, the flux experiments (**Figure 106**) show a peculiar behaviour.

From the pristine PEI membranes up to a MWCNT concentration of 1.5 wt%, where the sintering parameters were identical, the pristine PEI membranes showed the highest pure water permeability with the highest deviation between the samples. With the addition of MWCNT, the permeability of the membranes with the concentration of 0.5 wt% is reduced with a smaller standard deviation. This trend continues for 1.0 wt% with an even lower permeability and smaller standard deviation. The MWCNT concentration of 1.5 wt% was the highest with the used sintering time of overall 15 min and shows a permeability comparable to 0.5 wt%. This could be an indication for a threshold of MWCNT concentration where the pore structure is larger to allow for a higher flow rate of the pure water. Up to 1.0 wt%, the permeability goes down, possibly because of a change in pore morphology due to reduced viscous material flow and drag.

With the increase of the sintering time to 24 min for MWCNT concentrations higher than 1.5 wt%, a notable drop in pure water permeability was found. Transmembrane pressure had to be increased to 750 mbar and 1 bar respectively, to produce a comparable volume flow through the membranes. As was shown from the SEM analysis, porometry and the porosity measurement, the open-porous channels are significantly reduced compared to the smaller MWCNT concentrations and the pristine PEI membrane.

Fluctuations in the values of the pure water permeability of samples of the same MWCNT concentration are part of the nature of the performed sintering process. As was mentioned before, the stacking of the powder particles and the deformation and viscous material flow during the sintering, are random.

To investigate the stability of the sintered membranes, which means the stability of the MWCNT in the polymer matrix, water flux experiments were performed for three PEI/MWCNT 3.0 wt% membranes for 40 cycles. For each cycle, the same volume of water was used. Sporadically, small amounts of pure water were added to keep the volume that could be measured as permeate at 400 mL. The filtration conditions were kept identically to the water flux measurements before. For each membrane, the electrical conductivity was measured before and after performing the full 40 cycles. If any notable changes in these properties would occur, it could be assumed that large numbers of MWCNT would be flushed out of the membrane.

Theoretically, they should agglomerate in the permeated water and become visible as black particles. The detection of individual MWCNT or very small quantities is not a simple task and necessary equipment was not available. Yet, as SEM micrographs indicated, individual MWCNT should have sunken under the matrix surface. Agglomerates, which are partially sticking out from the matrix, are the prime candidates to be flushed out. As there are large numbers of them, if they could be flushed out, they should become visible and changes in electrical conductivity should be measured. The MWCNT concentration of 3.0 wt% was chosen as it was the highest concentration available for PEI with the highest number of anchored agglomerates.

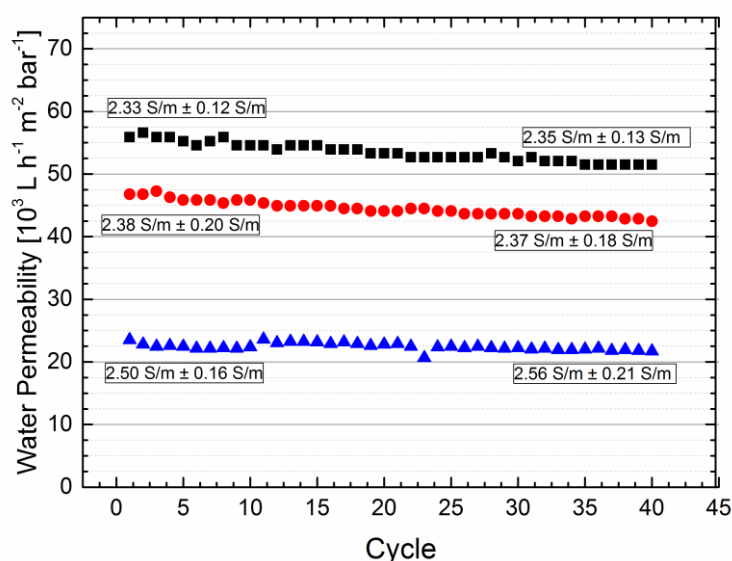


Figure 107: Flux stability for three different membranes of PEI/MWCNT 3.0 wt%. Shown is the electrical conductivity of the samples before and after the 40 flux cycles.

As can be seen in **Figure 107**, the electrical conductivity did not change in the range of measurement accuracy; no significant changes in the pure permeability were measured, either. The two membranes with the higher permeability show a slight decline with ongoing cycles, but no visible difference was found for the one with the lowest permeability. The small decrease could have happened due to swelling of the membranes or small degrees of fouling. While care was taken to avoid contaminations of the pure water, the repeated opening and refilling of the test cells could have introduced dust particles and such into the membranes.

The results show, that the membranes appear to be stable. No loss of large numbers of MWCNT was detected.

6.7.2. Ultra-High Molecular Weight Polyethylene

The sintering conditions for UHMWPE and UHMWPE/MWCNT could be kept identical, independent of the MWCNT concentration. Correspondingly, all measurements could be performed at identical parameters. The transmembrane pressure was kept at 1 bar for all measurements. The pure water permeability of the UHMWPE and UHMWPE/MWCNT membranes are shown in **Figure 108**. No clear trend is visible over the whole range of MWCNT concentrations. The permeability values are generally smaller than for polyetherimide, but not by much. As was shown above through porometry and porosity measurements, the membranes for UHMWPE are comparable in porosity, but have significantly smaller pores. The pore size plays an important role in the permeability, leading to the smaller pure water permeability for UHMWPE. Also, the UHMWPE membranes are with 500 μm much thinner than for PEI with 1000 μm and 800 μm respectively.

Noteworthy is the reverse trend in permeability for the MWCNT concentrations 0 wt% to 1.0 wt%, compared to PEI. The permeability increases correspondingly to the increased pore sizes. The presence of the MWCNT on the surfaces does not significantly change the rounding and viscous flow of the powder particles for UHMWPE. The lack of significant rounding was shown in the discussion of the SEM investigation of the membrane morphology. The shear rheological analysis showed the relatively small influence of the MWCNT on the UHMWPE matrix, compared to PEI. Still, the influence of the MWCNT on the powder particles is large enough to hinder the fusion of the powder particles in UHMWPE/MWCNT, compared to pristine UHMWPE. The SEM analysis also showed that drag due to viscous material flow plays a significantly smaller role in UHMWPE, compared to PEI. This hindered fusion and basically, the unchanged rounding behaviour of the molten particles leads to larger pores. Pristine UHMWPE, with the least hindrance in fusion and not MWCNT or MWCNT agglomerates possess the smallest mean permeability and smallest standard deviation.

Above 1.0 wt%, the permeability drops back down to values comparable to 0.5 wt% with higher standard deviations. The permeability values of the powders with MWCNT concentrations of 1.5 wt% to 2.5 wt% should be closer to UHMWPE/MWCNT 0.5 wt%, as the decoration process here is not as efficient and parts of powder particles or whole particles are devoid of MWCNT.

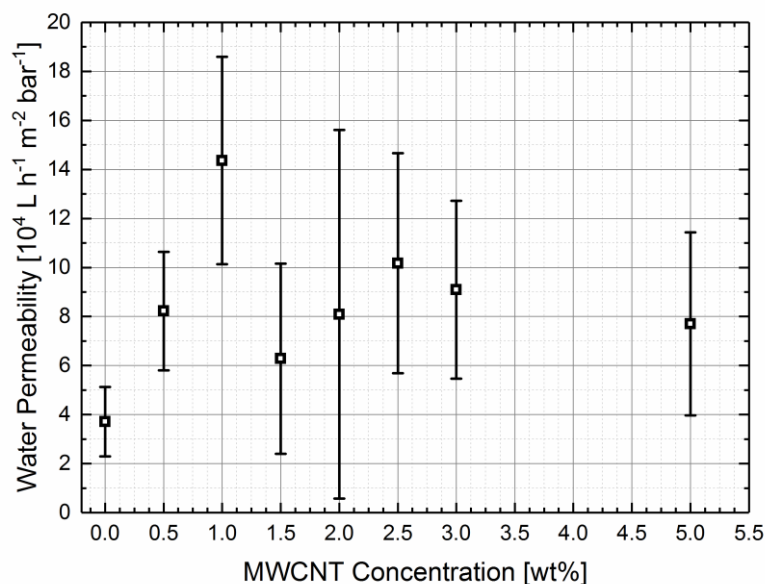


Figure 108: Pure water permeability of UHMWPE and UHMWPE/MWCNT membranes. The transmembrane pressure for all samples was 1 bar.

The most likely reason for the increased standard deviations is the increased presence and size of MWCNT agglomerates. At the used pressure of 1 bar, the agglomerates out of pure MWCNT and the clusters out of MWCNT and powder particles should not be penetrated by pure water, as MWCNT are highly hydrophobic.

The agglomerates are also most likely the reason, why the mean permeability of UHMWPE/MWCNT 3.0 wt% and 5.0 wt% is below the values of 1.0 wt%. The increased MWCNT concentration on the surfaces of the powder particles hindered the fusion more than for 1.0 wt%, leading to larger pores. The generally larger pores should allow for an increased water flux. Nevertheless, the number of MWCNT agglomerates is still increased compared to 1.0 wt%, leading to sections of the membranes that are blocked for the water flux. The MWCNT concentrations of 1.5 wt% and 2.5 wt% show higher standard deviations for the permeability and also a more random distribution in MWCNT agglomerate number and size in SEM micrographs.

As can be seen in **Figure 109**, the electrical conductivity did not change in the range of measurement accuracy. Unlike for PEI/MWCNT 3.0 wt%, there are notable differences in the permeability value for UHMWPE/MWCNT 5.0 wt%. The largest drop for UHMWPE/MWCNT 5.0 wt% is 15.5%, while it was 9.4% for PEI/MWCNT 3.0 wt%. Because the pores are smaller than for PEI/MWCNT 3.0 wt%, unavoidable small amounts of contaminations would show a larger influence.

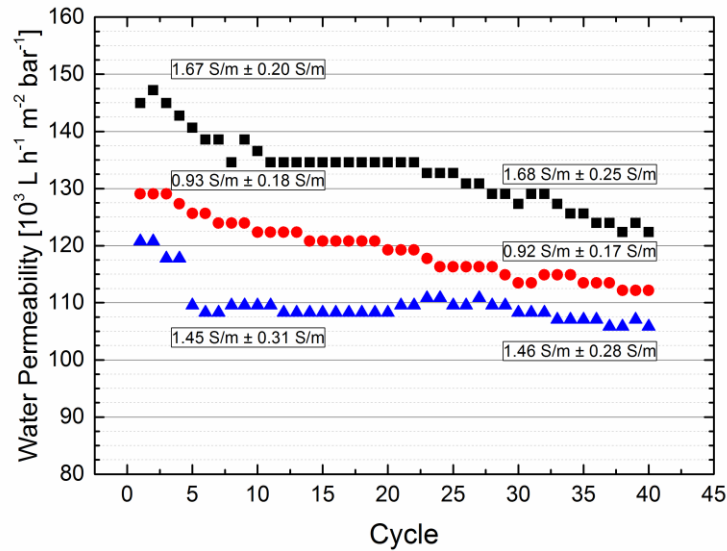


Figure 109: Flux stability for three different membranes of UHMWPE/MWCNT 5.0 wt%. Shown is the electrical conductivity of the samples before and after the 40 flux cycles.

As mentioned for PEI/MWCNT 3.0 wt%, the repeated opening of the measuring cell and refilling of the cycled water could introduce dust particles and other materials into the membrane. Additionally, since UHMWPE is much softer than PEI, a small amount of mechanical relaxation under the pressure of the membrane fixation inside the cell might lead to a small decrease in permeable volume.

Overall, the conductivity value is stable, indicating that no large amounts of MWCNT escaped from the membrane. Further, no visible amounts of MWCNT were found in the repeatedly used pure water as the permeate.

6.8. Electrical Conductivity

6.8.1. Polyetherimide

The polyetherimide powder particles decorated with MWCNT proved to be efficient in resulting in electrically conductive membranes as can be seen in **Figure 110**. As was expected from the use of the decorated powder particles, the percolation threshold apparently is below 0.2 wt%. As was seen from the SEM analysis, the MWCNT are predominantly aligned in a network structure inside the PEI matrix. Resulting from this network, the jump in electrical conductivity from 0.2 wt% at 0.0003 S/m to 0.5 wt% and 0.005 S/m is significant. The strong increase from 0.2 wt% to 0.5 wt% corresponds to the high initial increase in conductivity due

to significant increases in contact points between MWCNT during further percolation into a more developed network.

The further increase from 0.5 wt% to 1.0 wt% and 0.02 S/m is also significant. The increase in conductivity persists through further increases in the MWCNT concentration up to the highest sinterable MWCNT concentration of 3.0 wt%. It apparently follows a linear increase with a slope of 0.95 on a logarithmic scale in the investigated range of MWCNT concentrations.

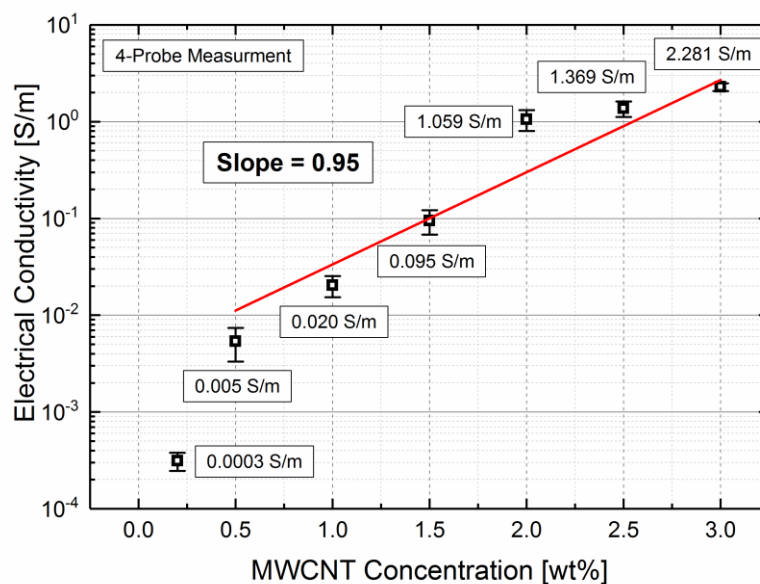


Figure 110: Electrical conductivity of PEI/MWCNT depending on the MWCNT concentration. Overall the increase in conductivity approximately follows an exponential increase in the measurement range

Apart from the SEM micrographs, these results illustrate that the MWCNT are located in a network and with increasing MWCNT concentration the inter-MWCNT contacts and median thickness of conductive pathways through the membrane increase significantly. The low shear stress of the small-scale viscous material flow preserved the MWCNT network from the compressed green body and also further increased the inter-MWCNT contacts at the particle contact sites. This happens through the fusion of the particles, which pushes more MWCNT in the sintering bridges and fusion sites together.

At this point, it can be mentioned that while the sintered membranes are porous structures, it should not necessarily be assumed that the porosity has a significant effect on the electrical conductivity. An effect of porosity on the electrical conductivity of a sample is well known for conductive materials such as silver and copper. But in these cases, the whole material is electrically conductive. In a composite material with a conductive filler material and an electrical isolator as the matrix, the distribution of the conductive filler is the only important

parameter for the conductivity. Parts of the isolating matrix missing between conductive pathways in the matrix does not account for a loss in conductivity as long as the conductive pathways are similar.

As can be seen from the graph, while the overall trend from 0.5 wt% to 3.0 wt% is an increase with the slope 0.95 on a double-logarithmic scale, the MWCNT concentration of 2.0 wt% is with 1.059 S/m notably higher than the expected values of around 0.3 S/m of the fitted function. Exactly at 2.0 wt% the longer sintering times were applied, resulting in a more pronounced jump in electrical conductivity. The effect is not directly a decrease in porosity, but rather the simultaneously occurring growth of the diameters of sintering bridges and fusion sites, which leads to further increased inter-MWCNT contacts. The effect of this is slightly lower for 2.5 wt% and 3.0 wt%, where inter-MWCNT contacts at sintering bridges are already higher due to the higher MWCNT concentration. This puts the jump for 2.0 wt% into perspective as the exception from the rule, because 2.5 wt% and 3.0 wt% agree well with the fitted function.

In **Figure 111** the values of the sintered porous membranes are compared to the conductivity values of the compression moulded samples and rectangular sintered plates. The sintered plates are not porous. For the compression moulded and sintered rectangular samples, no measurement of the conductivity could be performed for 0.2 wt% and 0.5 wt%, because the electrical resistance of the samples was too high for the measurement device. Additionally, the two first test concentrations 2.0 wt% and 5.0 wt% with the cut-milled powder with a particle size of around 500 μm was included, as they could be compression moulded but not sintered. With their larger diameter and MWCNT concentration, they provide additional information. The concentration of 2.0 wt% for the sintered rectangular samples is not included as no material was left at this point.

The sintered rectangular samples at MWCNT concentrations of 1.0 wt% and 1.5 wt% show a higher conductivity than the sintered membranes, while 2.5 wt% and 3.0 wt% are in good agreement with each other. From this, it seems that lower MWCNT concentrations are more sensitive to the processing than higher one, at least for the sintering. A possible explanation for the higher conductivity of the sintered rectangular samples of 1.0 wt% and 1.5 wt% is the simpler sintering process.

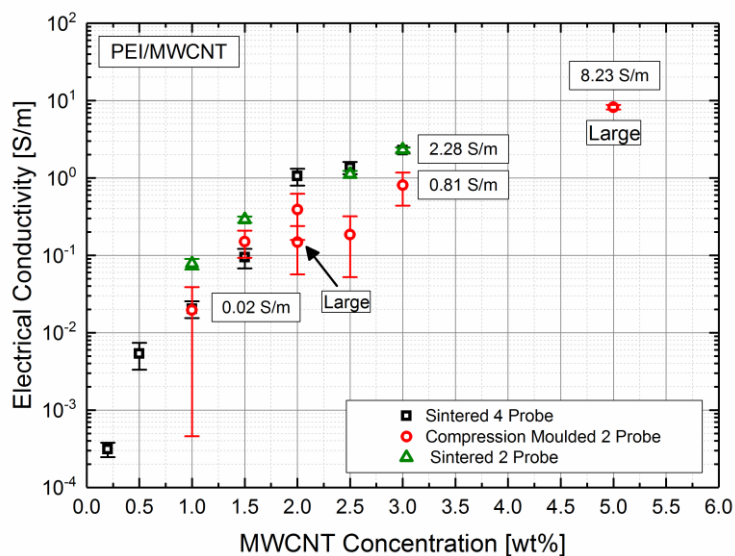


Figure III: Comparison of the electrical conductivity of sintered membranes to compression moulded plates. Sintered membranes were measured via four-probe method, compression moulded plates via two-probe method and sintered plates via two-probe method.

The membranes went through three different steps, while the rectangular samples only through one. While the membrane sintering process allowed for sufficient control for the production of a porous structure, it may cause small disruptions for the powder during the process, either leading to an overall less conductive network or a porous structure with less developed inter-particle MWCNT contact. With higher MWCNT concentrations and particle surface coverage, the decorated powder would be less susceptible to disruptions and therefore the MWCNT concentrations of 2.5 wt% and 3.0 wt% have more similar conductivity values.

Compression moulding puts a larger amount of shear on the material than pressureless sintering. Therefore, it is not unreasonable that for 0.2 wt% and 0.5 wt% no conductivity could be measured, but 1.0 wt% is at a comparable value to the sintered sample, even if so with a significant standard deviation. The standard deviation of the compression moulded sample is the largest of all samples for 1.0 wt%. This implies that for smaller MWCNT concentrations, the MWCNT percolation is more sensitive to the induced shear stress. This was also observed in the formation of isolating sample surfaces for all MWCNT concentrations, if compression moulding was not performed with minimal shear flow of the material.

With further increasing MWCNT concentration, 1.5 wt% is slightly higher at 0.151 S/m compared to the sintered sample at 0.095 S/m. From 2.0 wt% to 3.0 wt%, the conductivity values of the compression moulded samples are below those of the sintered ones and show larger standard deviations. Further, the larger powder of 2.0 wt% produces a less conductive

compression moulded samples compared to the smaller ones. This could be explained by a smaller number of possible pathways due to the reduced number of particle surfaces with the larger powder at the same mass. At the MWCNT concentration 2.0 wt%, the thickness of these pathways is not high enough to resist the loss of inter-MWCNT contacts due to the applied shear. Overall, for concentrations of 0.2 wt% to 3.0 wt%, sintering is the more efficient process to produce electrically conductive samples with a much better reproducibility, due to the significant lower shear stresses during the process.

As was mentioned in the discussion of the scanning electron micrographs, a notable visual difference was found between porous sintered and dense compression moulded PEI/MWCNT 3.0 wt%. This was shown in **Figure 81**. The conductive network for the sintered PEI/MWCNT 3.0 wt% is clearly more cohesive, while it is more interrupted and irregular for the compression moulded sample. The stronger shear forces during compression moulding in the melt apparently disrupted the network sufficiently to result in a lower conductivity value at higher MWCNT concentrations. The individual grains of the powder can be identified in the sintered sample while the original shapes are obscured for the compression moulded one. This further shows the disruptive effect of the shear forces during compression moulding.

One notable exception was found. The large powder with 5.0 wt% produces through compression moulding the most conductive samples at 8.23 S/m at a small standard deviation of 0.57 S/m. This is a significant jump from 3.0 wt% at 0.81 S/m for compression moulded and around 2.3 S/m for the sintered samples. Because the 5.0 wt% powder is the most strongly MWCNT-covered one, the formation of a dense MWCNT network is much more likely. Additionally, with the highest MWCNT concentration, the highest melt viscosity can be assumed, compensating for the applied shear forces. As mentioned above, this is not only an effect of particle surface coverage by the MWCNT, as was found for 2.0 wt%, but possibly a MWCNT concentration threshold for this to occur. As no other larger powder of PEI was investigated, it can only be assumed to be somewhere between 2.0 wt% and 5.0 wt% for 500 μm powder.

To illustrate the conductivity of a sintered membrane of PEI/MWCNT 3.0 wt% and compression moulded PEI/MWCNT 5.0 wt%, electrolysis of water was performed, which is shown in **Figure 112**. At an applied voltage of 10 V¹⁴, a clearly visible bubble formation occurs

¹⁴ 10 V was chosen for illustrative purposes. Electrolysis of water could also be performed with lower voltages, but did not render meaningful photographs, due to the lower bubble formation rate.

at the membrane and the compression moulded disc. Electrolysis of water is one of the suggested possible cleaning mechanisms of electrically conductive membranes.

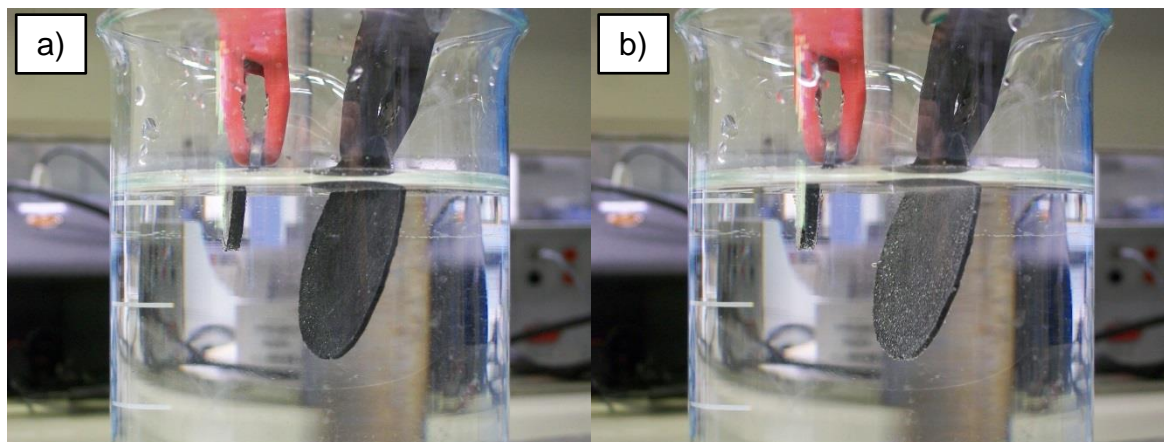


Figure 112: Demonstration of effect of applied voltage to sintered membrane of PEI/MWCNT 3.0 wt%. For the demonstration, the sintered membrane is placed in water and a compression moulded disc of PEI/MWCNT 5.0 wt% faces the membrane. Before the voltage is applied (a) no bubble formation happens at the membrane. When a demonstration voltage of 10 V is applied (b) bubble formation happens at both the disc and the membrane. Bubbles come from the surface, inside and opposite surface of the membrane, caused by electrolysis of the water.

As an addition, a very simple qualitative experiment was performed to show the cleaning effect through electrolysis of water and therefore bubble formation from the membrane. A yeast suspension was produced from 7 g of yeast and 1000 mL pure water. The yeast was left to grow for 24 h at 41 °C to disperse and consume any existing nutrients in the water. Since the goal was to completely block the pores of the membranes, the actual weight percentage of yeast was not necessary to be known. First, the clean membrane was measured for the non-fouled water flux value. Then a volume of 410 mL yeast suspension was used to foul a membrane of PEI/MWCNT 2.5 wt%¹⁵ at a pressure of 1 bar. After around 200 mL of permeate, the flux was no longer measureable in a sufficient time frame, as no water drop formation was observable at the outlet of the filtration cell. The membrane was therefore assumed to be fully blocked and a dense filtration cake had formed on the membrane. Because the pore size of PEI/MWCNT 2.5 wt% is relatively large and the used pressure high, the permeate showed turbidity visible to the eye.

¹⁵ PEI/MWCNT 2.5 wt% was used, because this qualitative experiment was performed at the latest stage of this work and no usable PEI/MWCNT 3.0 wt% remained.

Table 8: Water flux for illustrative anti-fouling experiment of a PEI/MWCNT 2.5 wt%. Shown are the water flux value before the fouling, after the cleaning and the percentage of the recovered water flux.

| Water Flux PEI/MWCNT 2.5 wt% Membrane | | | |
|---------------------------------------|--------------------------------------|--------------------------------------|----------------------|
| Non-Fouled | Fouled/Blocked | Cleaned | Recovered Water Flux |
| [L m ⁻² h ⁻¹] | [L m ⁻² h ⁻¹] | [L m ⁻² h ⁻¹] | [%] |
| 95,493 | ≈ 0 | 61,115 | 64 |

After the fouling of the membrane, the filtration cell was disassembled and the membrane was carefully suspended by a crocodile clamp at the non-fouled outer area of the membrane in an empty beaker glass. A compression moulded plate of PEI/MWCNT 5.0 wt% was placed on the opposite side the membrane. Regular water was filled up to the point where the filtration cake was immersed in the water, but the crocodile clamps were still dry. The assembly looked similar to the one in **Figure 112**. The fouled membrane was left in the water for 3 h to see if only the hydration of the filtration cake and gravity would remove the filtration cake. After 3 h, the filtration cake remained on the membrane and no visible amounts of yeast had deposited at the bottom of the beaker glass. A voltage of 10 V was applied for 1.5 min. During the first 20 s the bubble formation was visible and the filtration cake shortly afterwards detached from the membrane. A turbid stream of yeast flowed from the membrane for a few seconds after the detached filtration cake. After the 1.5 min elapsed, the now cleaned membrane was put back into the filtration cell and pure water flux was measured. As is shown in **Table 8**, 60% of the original flux could be recovered after full blocking of the membrane.

While this experiment is by no means well controlled or useable for any strong statement, it still shows to some degree, that the produced conductive membrane shows potential.

6.8.2. Ultra-High Molecular Weight Polyethylene

The electrical conductivity of prepared UHMWPE/MWCNT samples does not behave like PEI/MWCNT with increasing MWCNT concentration. As can be seen **Figure 113**, the electrical conductivity values do not behave in an expected way. Three distinct points stand out for the measured values. Firstly, the conductivity value at 1.0 wt% is an order of magnitude higher than for PEI/MWCNT. Secondly, there is a significant “dip” in the curve around 2.0 wt%. And thirdly, the increase in conductivity between 1.0 wt%, 3.0 wt% and 5.0 wt% is significantly lower than for PEI/MWCNT.

The electrical conductivity for UHMWPE/MWCNT with the concentration of 1.0 wt% is notably high with 0.47 S/m, which is significantly higher than the 0.02 S/m for PEI/MWCNT 1.0 wt%. This means that the decorated powder particles at this MWCNT concentration for UHMWPE are more effective than for PEI. A possible explanation for this is the difference in particle diameter and shape. As was shown in the discussion of the results from the SEM analysis of the decorated powder particles, UHMWPE/MWCNT does not show the same level of surface-bound agglomerates as PEI/MWCNT. This is because of the lack in size for UHMWPE, leading to very few proper spots on the powder particles to allow for agglomerates to attach themselves or form in, like for PEI/MWCNT. Additionally, the amount of MWCNT agglomerates was lower than for higher concentrations. Therefore, most MWCNT likely are individually bound to the UHMWPE powder particles.

The observed agglomerates and missing MWCNT from the particle surfaces were significant for UHMWPE/MWCNT with MWCNT concentrations between 1.5 wt% and 2.5 wt%. While it was not possible to confidently distinguish the quality of the decorated powder particles from the SEM analysis alone, the measured conductivity values allow for a more refined categorisation.

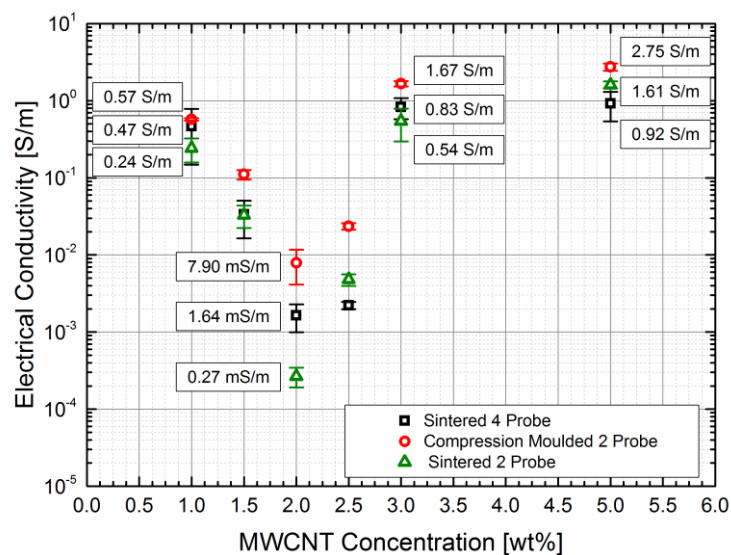


Figure 113: Electrical conductivity of UHMWPE/MWCNT depending on the MWCNT concentration. Concentrations below 1.0 wt% are not visible because their resistance was too high for measurement. Significant is the drop in conductivity between 1.0 wt% and 3.0 wt%.

As can be seen from **Figure 113** the quality of the powder with 1.5 wt% MWCNT is less than for 1.0 wt%, 2.0 wt% has the lowest quality with the lowest conductivity and from 2.5 wt% the quality is again increasing. Even though the conductivity of UHMWPE/MWCNT 3.0 wt% is

higher than for UHMWPE/MWCNT 1.0 wt%, it is important to note the significantly smaller degree of increase in conductivity compared to PEI/MWCNT. In PEI/MWCNT the increase from 1.0 wt% to 3.0 wt% for the sintered membranes is by a factor of 114.02, while it is only a factor of 1.78 for UHMWPE/MWCNT.

Combined with the SEM analysis, it is reasonable to assume that in the decoration process for UHMWPE the processes of surface decoration with individual tangentially aligned MWCNT is competing with the formation of MWCNT agglomerates away from the powder particles. This process most likely happens at any MWCNT concentration. Conductivity values for UHMWPE/MWCNT with the concentration of 0.2 wt% and 0.5 wt% could not be measured with the available conventional measuring devices independent of the processing method, because the conductivity was too low.

At 1.0 wt%, the competing processes apparently reach such a level that, independent of the agglomerates, the MWCNT still are sufficiently covering the powder particles to form an efficient conductive network. From 1.0 wt%, the formation of agglomerates apparently overtakes the decoration of the powder particles, as was observed in SEM and the lowered conductivity values. The observed peak of the dominance of the agglomeration formation over the decoration is at 2.0 wt%, where a high number of poorly decorated surfaces were seen in SEM micrographs and the conductivity is at its lowest measured point. The conductivity again significantly increases with 2.5 wt% up to 3.0 wt%. From here, the increase in conductivity for the sintered membranes is very small, even though the powder particles for UHMWPE/MWCNT 5.0 wt% appear to be covered more significantly with MWCNT than for UHMWPE/MWCNT 3.0 wt%.

Except for the MWCNT concentrations of 2.5 wt% and 5.0 wt%, the rectangular sintered samples are less conductive than the sintered membranes. As both sample types only went through one continuous sintering step, this indicates a better conductive network for the membranes for the other concentrations, which was possibly caused a beneficial effect through the better compression of the green body compared to the less densely compressed powder in the mould.

Interestingly, the compression moulded samples of UHMWPE/MWCNT are more conductive than the sintered ones. This is reversed compared to PEI/MWCNT. As the sintering rate is significantly slower and the sintering time correspondingly significantly higher, the sinking of the MWCNT into the matrix and coalescence of the particles overlap differently. The sinking

happens faster compared to the coalescence, compared to PEI, possibly hindering the MWCNT from one particle to acquire a sufficient contact with the MWCNT of another particle. Also, the coverage of the UHMWPE particles is more “patchy” than for PEI, meaning that the sintering bridges might form at spots of low MWCNT surface coverage.

The conductive pathways between the particles are then defective. The scanning electron micrographs of the ion-milled cross section gave indications for this, as was shown in **Figure 98**. The MWCNT paths are more often further away from the material surface than was visible for PEI/MWCNT. The cloud-like shape of the network sections resulted most likely from the “popcorn-like” UHMWPE particles. In many places dead-ends and interruptions in the paths are visible. In contrast, the pathways appear to be more continuous and dense for the compression moulded samples. Through compression moulding, the molten particles are forced to fuse through the externally applied pressure. The time scale is much smaller and happens over all parts of the particle surfaces, negating the possible problems for the pressureless sintering process.

The overall still unsatisfying increase of the conductivity with the MWCNT which is also present for the compression moulded samples therefore is an effect of the powder particle decoration quality and the semi-crystalline UHMWPE matrix, for which PEI as an amorphous polymer is more effective.

To investigate the influence of melting and crystallisation of the UHMWPE on the MWCNT network and the electrical conductivity, the real part of the complex electrical conductivity σ' was measured over a temperature range from 30 °C to 220 °C in a measurement cycle with a heating and a cooling step. The results are shown in **Figure 114**.

An increase in conductivity can be observed for all MWCNT concentrations up to a certain temperature below the melting point. For UHMWPE/MWCNT 1.0 wt% and 3.0 wt% the local maximum is reached at around 100 °C while for 5.0 wt% this is around 90 °C. A pronounced drop in conductivity is visible at 125 °C, after the melting of the UMWPE matrix.

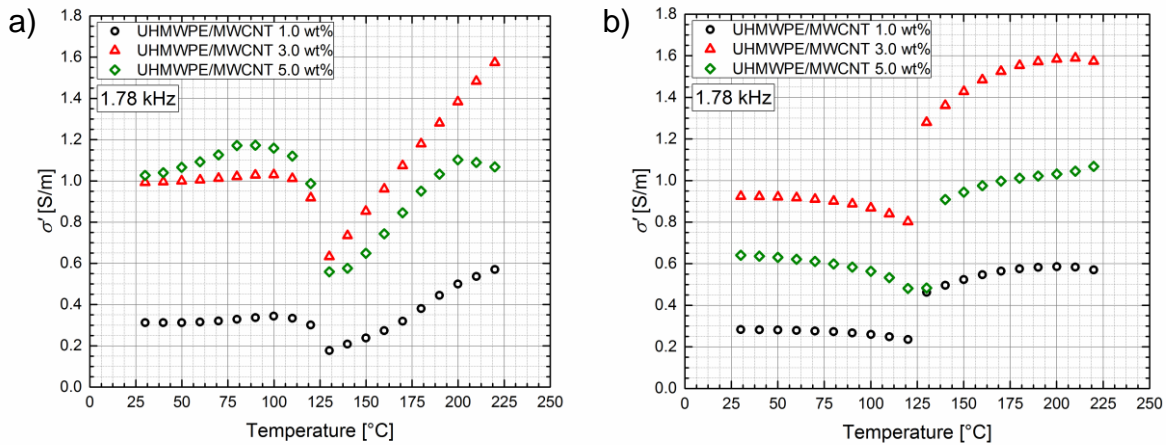


Figure 114: Real part of the complex conductivity σ' at a frequency of 1.78 kHz for compression moulded UHMWPE samples with MWCNT concentrations of 1.0 wt%, 3.0 wt% and 5.0 wt%, (a) heating interval from 30 °C up to 220 °C (b) cooling interval from 220 °C down to 30 °C.

This drop is the most pronounced for 5.0 wt%, for which the conductivity in the melt is dropped below 3.0 wt%. After the drop, the conductivity increases in almost linearly with the temperature, with a second smaller drop after 200 °C for 5.0 wt%. During the cooling step, the conductivity decreases in a non-linear way, with a small increase of the conductivity of 1.0 wt% at 200 °C with a maximum of 0.59 S/m and 3.0 wt% at 210 °C with 1.59 S/m. For 5.0 wt% the conductivity decreases monotonically with an inflection point at 180 °C. The samples crystallize around 125 °C, visible through the sudden drop in conductivity. After the crystallisation, the conductivity increases monotonically for all measured concentrations until 30 °C is reached. At 30 °C the new conductivity values are 0.28 S/m for 1.0 wt%, 0.93 S/m for 3.0 wt% and 0.64 S/m for 5.0 wt%. This is a relatively small decrease for 1.0 wt% and 3.0 wt%, but a significant decrease for 5.0 wt%.

For both the heating and cooling curves, the sudden change of the electrical conductivity at the melting and crystallisation temperature range around 125 °C can be attributed to the rapid morphology change of the crystalline regions to and from the amorphous melt. UHMWPE/MWCNT shows the peculiar behaviour that a significantly higher conductivity value of the melt at 220 °C is measured compared to the initial conductivity at 30 °C, but the new conductivity after a full cycle at 30 °C is decreased. The morphology change apparently causes a disruption in the MWCNT network. This is especially significant for 5.0 wt%, with a drastic decrease in conductivity, even though a more disruption-resistant MWCNT network would be assumed at the highest MWCNT concentration. The recovery of the conductivity after the crystallisation with decreasing temperature most likely happens through the thermal

shrinkage of the composite, bringing the MWCNT again in a denser contact during the decrease of the spatial distances between them.

The measurement shows that the conductivity of the compression moulded samples is not at its maximum for the MWCNT concentration after the sample preparation. It was also shown that the crystallisation behaviour of the matrix significantly disrupts the MWCNT network which can lead to a decrease in inter-MWCNT contacts and overall conductivity.

6.8.3. Polypropylene

For polypropylene only two different particle size contingents were used, both with the same MWCNT concentration of 5.0 wt%. The difference between them was the particle size and therefore the surface coverage of the particles. The results are shown in **Figure 115**.

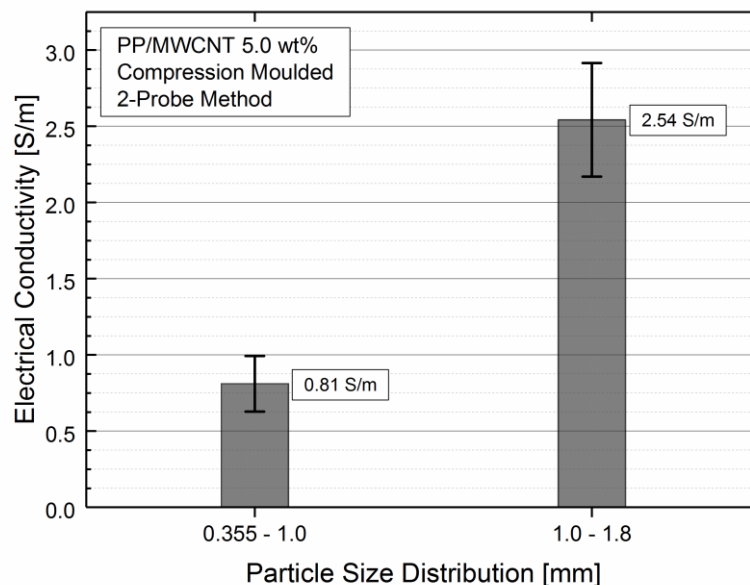


Figure 115: Electrical conductivity for PP/MWCNT 5.0 wt%. The powder was split into two particle size distribution. The larger particles show a significantly higher electrical conductivity for the compression moulded samples.

The larger contingent with particles of 1.000 – 1.800 mm shows a notably larger conductivity than the smaller one with particles of 0.355 – 1.000 mm. Because neither MWCNT concentration nor different preparation method has to be taken into account, the increased conductivity is a direct consequence of the particle size and therefore surface coverage. Because the powders were prepared by FutureCarbon GmbH with the same amount of material and MWCNT weight concentration, the larger powder provided a smaller surface area for the MWCNT decoration than the smaller one. This higher coverage directly translated to a higher

conductivity and therefore quality of the conductive MWCNT network. This corresponds well with the observation for PEI/MWCNT 5.0 wt% with particles around 0.5 μm .

Therefore, from PP/MWCNT 5.0 wt% it can be directly concluded that a higher surface concentration of the power particles with MWCNT, leading to most likely fewer but thicker MWCNT pathways in the conductive network, is more effective than a lower surface concentration with a larger number of thinner pathways. The thicker pathways apparently are less susceptible to disruptions during the compression moulding process.

6.9. Tensile Testing

It is important to state that the compression moulding was performed using flat “flash type moulds”. This type of mould excels in flexibility for laboratory applications, as it can be used in small scale with hand-powered flat presses and the mould themselves are cheap to produce and maintain. The main drawback of this type of mould is the large flash, impossible to fully reproduce flow of the material and, a relatively low grade of sample consistency, which is intrinsic for compression moulding. For tensile testing, this can be compensated for polymers by compression moulding large scale plates and cutting out the samples. For soft polymers with MWCNT, punch-cutting can be performed otherwise a saw machine is commonly used. As the used materials were either high-performance polymers in the case of UHMWPE and PEI, or combined with MWCNT, a sawing technique was not performed due to the limits of the available facility and safety concerns for the emission of MWCNT into breathable air. Therefore, a certain amount of variation and lack in quality of the samples is intrinsic to the preparation method and unavoidable. Still, effort was put into keeping the compression moulding process as close as possible to sintering under pressure with minimised material flow and flash development.

6.9.1. Polyetherimide

Tensile testing was performed for pristine PEI and PEI/MWCNT with concentrations of 0.5 wt% to 3.0 wt% in increments of 0.5 wt%. Representative curves are shown in **Figure 116**. All measured curves that were used for analysis can be found in **Figure 128 to 134**.

For the compression moulded samples of PEI, an anomaly in the curve was found for all samples. Between 0% and 0.25% of strain with a traverse speed of 1 mm/min, the slope of the curve is higher than after 0.25% at 50 mm/min. This resulted in inflated values for the Young's modulus above 5,000 MPa. The cause for this anomaly is unclear. In contrast, injection

moulded samples of Ultem™ 1000 provided expected results of a Young's modulus around 3,300 MPa, no notable change in slope and an elongation at break of around 31%. Also, no change in slope was found for UHMWPE or other materials tested on the device during the same time period. To compensate for this, the Young's modulus was calculated between 0.3% and 0.5%. While not the optimal range, it still provides reasonable values.

The addition of MWCNT through the decoration of the polymer powder particles showed a significant influence on the mechanical performance of the prepared samples. The first trial of samples was performed with the MWCNT concentrations of 1.0 wt%, 2.0 wt% and 3.0 wt%. Afterwards samples were prepared for 0.5 wt%, 1.5 wt% and 2.5 wt%. No significant improvements of the mechanical properties were observed, as can be seen from **Figure 116**, **Figure 117** and **Table 9**. Compared to pristine PEI, only a small increase of the Young's modulus in the range of was found. The smallest increase was 2.4% for 2.0 wt% and the largest 10.0% for 2.5 wt%.

The ultimate tensile strength and elongation at break were reduced through the addition of MWCNT. Observation of the fractured samples showed that nearly all samples had a visible cavity in the fracture site. Due to its size, it is unlikely to result from agglomerates, because no agglomerates of this magnitude were found in the microscopy analysis of the powders and sintered membranes.

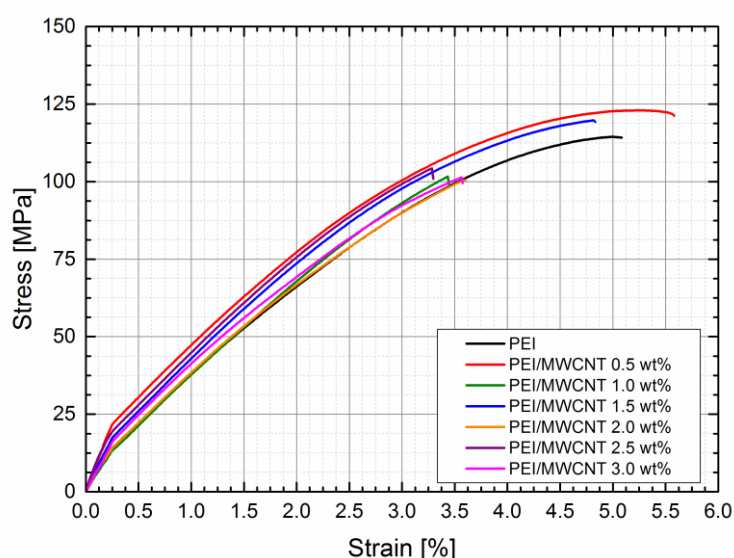


Figure 116: Representative stress-strain curves under uniaxial loading for compression moulded PEI and PEI/MWCNT composites of varied MWCNT concentrations. Maximum elongation, ultimate tensile strength and stress at break are reduced with the addition of MWCNT, nearly independent of concentration.

Due to limitations in the available amount of material, a second series with the same concentrations was not possible. Sample preparation was therefore adapted and tested for 0.5 wt%, 1.5 wt% and 2.5 wt%. The adaptation was relatively small. The filling of the decorated powder into the mould was slightly changed. The powder was now filled in four steps into the mould, supported by a manual levelling with a steel plate on top after each filling step. This levelling successfully eliminated the appearance of the cavities from the fracture sites, but led to only minor improved elongation at break. Compared to the other MWCNT concentrations, only 0.5 wt% and 1.5 wt% showed a small improvement in the elongation at break. No difference was found for 2.5 wt% in comparison to 2.0 wt% and 3.0 wt%.

Pristine PEI served as the reference for comparison. The compression moulded samples generally break without pronounced neck formation. Only one sample visibly went through a small degree of neck formation, the other samples broke at the onset.



Figure 117: Photographs of the broken samples for tensile testing of PEI and PEI/MWCNT with 1.0 wt%, 2.0 wt% and 3.0 wt%. All samples showed brittle fracturing behaviour with a few samples breaking at two points.

The compression moulded samples show an overall low elongation at break. PEI is an amorphous high performance polymer and injection moulded samples show a relatively high ability for neck formation. Typically, the injection moulded samples can reach an elongation at break of around 40%. Injection moulding mixes the molten material and partially aligns the polymer chains preferably in direction of the tensile stress, which results in better developed cohesion compared to compression moulding. Compression moulding, especially with a flash type mould as used in this work, does not provide the alignment and less cohesion in the areas of low shear flow. This results in comparably more brittle samples. Additionally, the same level of reproducibility possible with automated injection moulding was not available for the manual compression moulding. The result is a relatively high deviation between samples.

Table 9: Mechanical properties of PEI and PEI/MWCNT composites depending on the MWCNT concentration, measured through tensile testing under uniaxial loading. The measurement temperature was 23 °C.

| MWCNT concentration [wt%] | Young's Modulus (0.3 – 0.5%) [MPa] | Elongation at Break [%] | Ultimate Tensile Strength [MPa] | Tensile Stress at Break [MPa] |
|---------------------------|------------------------------------|-------------------------|---------------------------------|-------------------------------|
| 0 | 3157.0 ± 83.8 | 4.8 ± 0.3 | 111.0 ± 3.7 | 103.0 ± 12.6 |
| 0.5 | 3367.5 ± 66.1 | 4.7 ± 0.7 | 115.6 ± 6.3 | 114.0 ± 5.3 |
| 1.0 | 3333.9 ± 146.9 | 3.6 ± 0.4 | 104.3 ± 11.1 | 104.3 ± 11.1 |
| 1.5 | 3361.2 ± 77.9 | 4.5 ± 0.7 | 116.0 ± 6.4 | 116.0 ± 5.3 |
| 2.0 | 3231.8 ± 110.8 | 3.3 ± 0.4 | 92.8 ± 11.7 | 92.8 ± 11.7 |
| 2.5 | 3473.0 ± 56.3 | 2.8 ± 0.8 | 93.2 ± 16.8 | 93.2 ± 16.8 |
| 3.0 | 3394.7 ± 72.4 | 2.9 ± 0.8 | 89.6 ± 15.4 | 89.6 ± 15.4 |

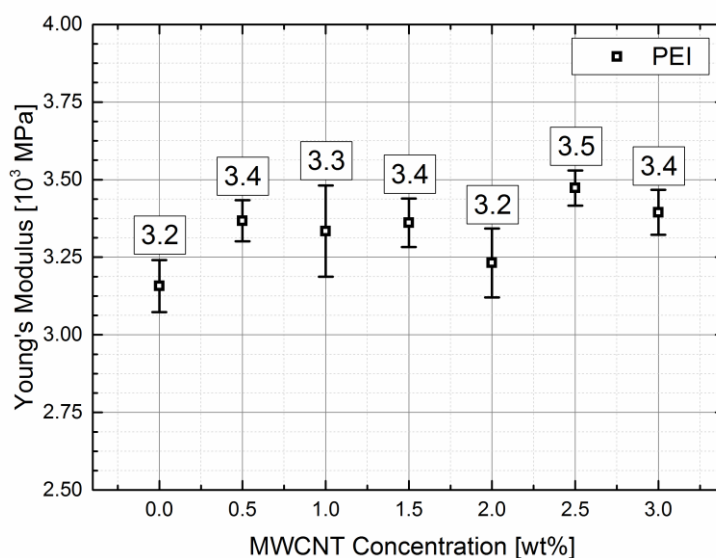


Figure 118: Young's modulus of pristine PEI and PEI/MWCNT. The MWCNT concentrations of 0.5, 1.5 and 2.5 wt% show notably higher Young's moduli than the other concentrations.

Comparing the representative curves in **Figure 116**, it can be seen that they can be distinguished into two groups: Pristine PEI, 0.5 wt% and 1.5 wt% with the higher elongation at break and 1.0 wt%, 2.0 wt%, 2.5 wt% and 3.0 wt% in the third group. The trends between the MWCNT concentrations are visualised in **Figure 118** to **Figure 121**.

The fracture sites of 0.5 wt%, 1.5 wt% and 2.5 wt% did not show cavities. For 0.5 wt% 1.5 wt%, this could explain why the elongation at break is comparable to pristine PEI. On the other hand, 2.5 wt% does not show any notable differences.

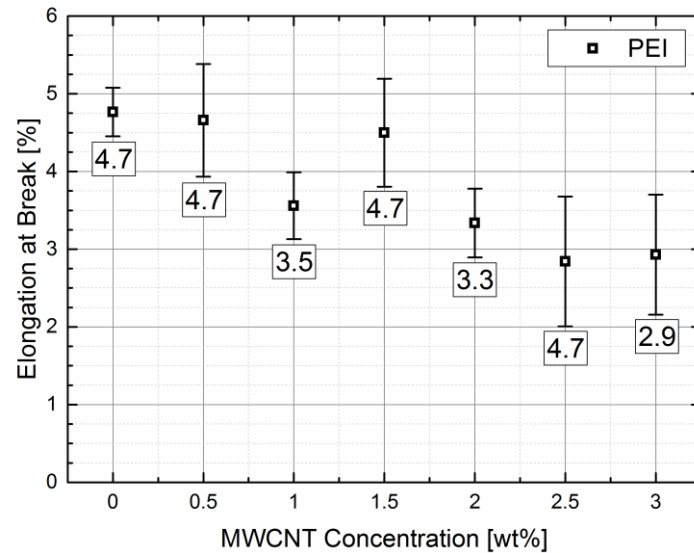


Figure 119: Elongation at break of pristine PEI and PEI/MWCNT. The MWCNT concentrations 1.0, 2.0, 2.5 and 3.0 wt% showed slightly smaller average values than the other concentrations.

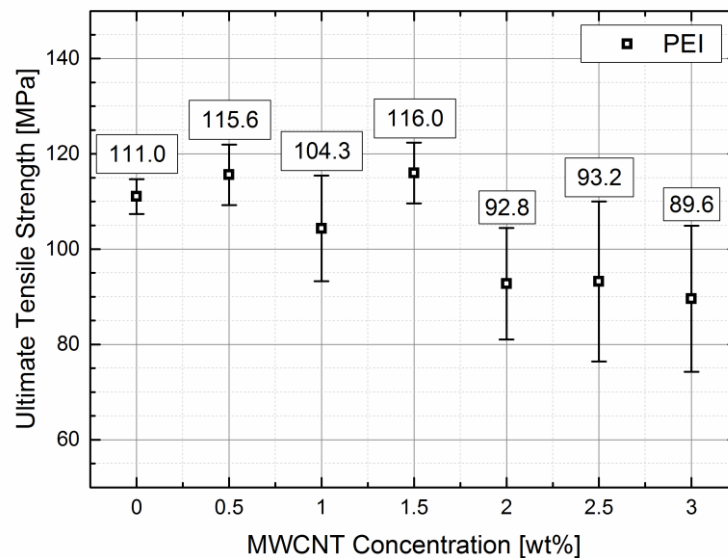


Figure 120: Ultimate tensile strength of PEI and PEI/MWCNT. While no significant difference is visible, a slight trend towards decreasing ultimate tensile strength with increasing MWCNT concentration is indicated. Additionally, variation within the samples of a given MWCNT concentration increases with concentration.

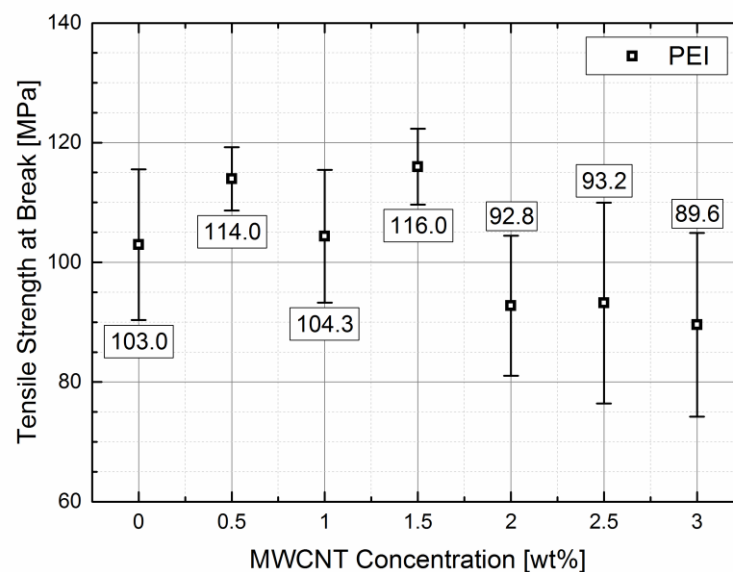


Figure 121: Tensile strength at break for pristine PEI and PEI/MWCNT. The values for PEI/MWCNT are identical to the ultimate tensile strength at fracture of the samples happened at this point, except for pristine PEI and 0.5 wt%. Samples for pristine PEI and 0.5 wt% showed onset of neck formation during deformation.

The addition of MWCNT did not lead to improvements of the mechanical properties of the composite material compared to pristine PEI, with the exception of the increase of the Young's modulus in the range of 2.4% to 10%. At a MWCNT concentration of 0.5 wt%, the material is already more susceptible to defects from the compression moulding than pristine PEI. Higher amount of care in the filling of the mould had to be taken to avoid defects in form of cavities. Nevertheless, the small defects did not lower the mechanical properties of the samples in a major way compared to the defect-free samples, with the exception of a slightly reduced elongation at break for MWCNT concentrations below 2.0 wt%. Above this concentration, no differences were notable.

6.9.2. Ultra-High Molecular Weight Polyethylene

UHMWPE with its large variation in the composite powder quality and therefore MWCNT distributions was expected to show large deviations between the MWCNT concentrations and the samples of each MWCNT concentration. The mechanical properties were analysed for compression moulded samples to have reproducible sample shapes with no pore or density deviations. These deviations would strongly change the mechanical strength and make a comparison between different MWCNT concentrations difficult, because they could not easily be distinguished from the effect of higher numbers of MWCNT. It should be noted for the concentrations of 2.5 wt% and above, that it was not possible to use a truly representative curve for **Figure 122**. The deviation in deformation behaviour was too extreme, as can also be seen from **Figure 124** to **Figure 127** by the larger standard deviations relative to the mean values. All measured curves can also be found in the appendix.

Compression moulding of the samples was significantly easier than for PEI and PEI/MWCNT. The smaller powder particles and lower mechanical stiffness of UHMWPE allowed for better filling of the mould and compression of the powder, eliminating problems of cavities or weak viscous fusion of the molten particles.

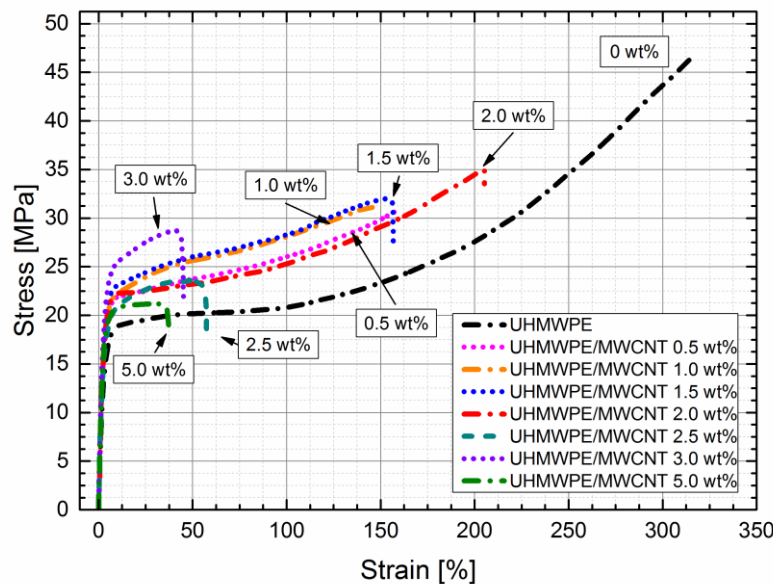


Figure 122: Representative Stress-strain curves under uniaxial loading for compression moulded UHMWPE and UHMWPE/MWCNT composites of varied MWCNT concentrations. Maximum elongation, ultimate tensile strength and stress at break are generally reduced with increasing MWCNT concentration. Exceptions are 1.5 wt% and 2.0 wt%, where the powder decoration is more imperfect and the properties are more similar to pristine UHMWPE compared to the nearby concentrations respectively.

As is illustrated in **Figure 122**, the powder quality indeed heavily influences the shape of the stress-strain curves. The mechanical properties are significantly changed, depending on the MWCNT concentration and distribution, which is also visible in **Figure 123**.

The compression moulded samples for UHMWPE show the very pronounced property of UHMWPE for very large elongation with a high strain percentage, which for the representative curve is above 300%. The average elongation at break for pristine UHMWPE was 285.7%. The values of the important mechanical properties with standard deviations can be found in **Table 10**. UHMWPE possesses a strong ability to strain harden, caused by the alignment of the UHMWPE chains in the stress direction during the plastic deformation. The alignment of the chains increases the resistance of the material against the plastic deformation. The strain hardening continues until the stress is too high and the sample breaks with fracture typical for ductile materials. Because of the strain hardening until fracture, ultimate tensile strength and tensile stress at break are identical for pristine UHMWPE.

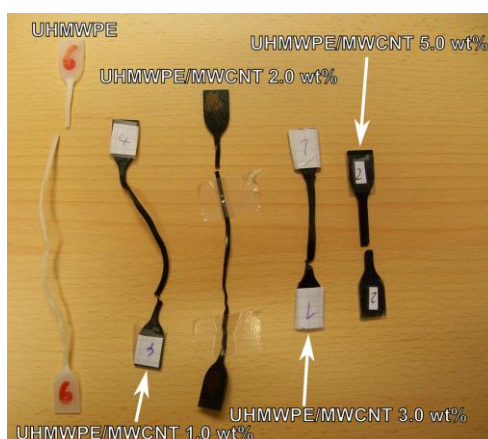


Figure 123: Photographs of the broken samples for tensile testing of UHMWPE and UHMWPE/MWCNT with 1.0 wt%, 2.0 wt%, 3.0 wt% and 5.0 wt%. The samples showed increasingly brittle fracturing behaviour with increasing MWCNT concentration.

At the lower MWCNT concentrations of 0.5 wt% and 1.0 wt%, the mechanical properties are changed significantly. For 0.5 wt%, no change in the Young's modulus was found, but elongation at break and ultimate tensile stress were notably reduced, resulting from a reduced capability for strain hardening. Comparing the representative curves, the curve for electrically conductive concentration of 1.0 wt% exhibits a significantly higher Young's modulus and also higher stress values up to the fracture elongation of 150%, but also lacks in strain hardening. While a certain amount of strain hardening can be observed as increasing stress until fracture, the overall ability is significantly lowered. This is the influence of the elastic properties of the

stiff MWCNT inside the matrix. They increase the Young's modulus through elastic interaction between the MWCNT and the matrix.

Table 10: Mechanical properties of UHMWPE and UHMWPE/MWCNT composites depending on the MWCNT concentration, measured through tensile testing under uniaxial loading. The measurement temperature was 23 °C.

| MWCNT concentration [wt%] | Young's Modulus [MPa] | Elongation at Break [%] | Ultimate Tensile Strength [MPa] | Tensile Stress at Break [MPa] |
|------------------------------|--------------------------|----------------------------|------------------------------------|----------------------------------|
| 0 | 646.7 ± 77.9 | 285.7 ± 30.4 | 42.5 ± 3.6 | 42.5 ± 3.6 |
| 0.5 | 674.1 ± 42.0 | 160.1 ± 24.6 | 29.2 ± 3.7 | 29.0 ± 3.6 |
| 1.0 | 1075.4 ± 53.4 | 150.2 ± 11.5 | 29.5 ± 2.6 | 26.9 ± 5.2 |
| 1.5 | 1096.7 ± 122.8 | 158.4 ± 12.8 | 31.2 ± 1.2 | 27.8 ± 1.7 |
| 2.0 | 678.0 ± 101.1 | 189.8 ± 16.8 | 33.0 ± 2.4 | 33.0 ± 2.4 |
| 2.5 | 1070.2 ± 200.5 | 51.5 ± 16.5 | 23.1 ± 1.1 | 23.8 ± 3.0 |
| 3.0 | 1180.9 ± 83.9 | 63.5 ± 25.4 | 29.3 ± 2.3 | 23.9 ± 3.0 |
| 5.0 | 659.9 ± 118.7 | 48.5 ± 12.0 | 20.5 ± 2.0 | 16.9 ± 4.4 |

As the MWCNT take part of the stress, the much higher Young's modulus of the MWCNT increases the modulus of the composite to 1075 MPa for 1.0 wt%, compared to the 646.7 MPa of the pristine UHMWPE. Nevertheless, MWCNT are incapable of any large scale ductile deformation behaviour and further act as obstacles for the chain alignment as they restrict UHMWPE chain movement through their interaction.

As the MWCNT are spatially non-uniformly distributed inside the matrix, the conductive pathways are significantly more brittle than the majority of the composite volume, which is the pristine UHMWPE. Local fractures or ruptures lead to extreme local stress increases, which then lead to further fracturing. This is why the addition of 0.5 wt% and 1.0 wt% already nearly halves the elongation at break for the composite, compared to the pristine UHMWPE.

Even though UHMWPE/MWCNT 1.5 wt% shows a significantly lower electrical conductivity than 1.0 wt%, the mechanical properties are overall very similar. From the measurements of the electrical conductivity and SEM analysis of the decorated powder particles, it was concluded

that the added MWCNT concentration of 1.5 wt% is not as homogeneously distributed as for 1.0 wt%, with a higher number of agglomerates and non-decorated powder particle surfaces. Yet, while the lack of effectiveness of the MWCNT decoration for 1.5 wt% reduces the number and quality of effective conductive pathways in the finished composite, the MWCNT distribution still influences the mechanical properties similar to 1.0 wt%. This indicates that the distribution is comparable, but the inter-MWCNT contact in the network is lacking.

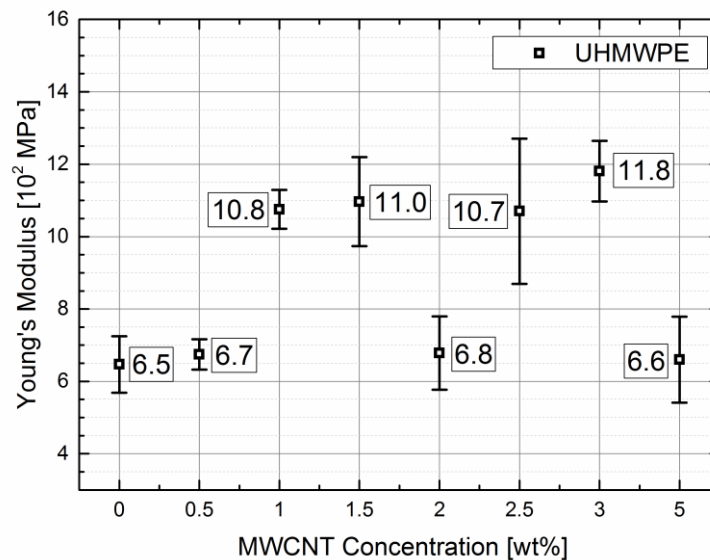


Figure 124: Young's modulus of pristine UHMWPE and UHMWPE/MWCNT. The value is significantly increased for 1.0, 1.5 and 3.0 wt%. No statistical significance was found for 2.0 wt% and 5.0 wt%.

The MWCNT concentration of 2.0 wt% is the least effective and efficient in the decoration process. The electrical conductivity is the lowest of all measurable concentrations and the number of large-scale agglomerates is significant. This explains why the curve shape is the most similar to pristine UHMWPE and the Young's modulus is nearly identical.

The influence of the MWCNT manifests in the mechanical properties as a reduced capability for plastic deformation. Instead, the elastic limit and the stress during plastic deformation are higher, because the plastic deformation is hindered and requires more energy up to the fracture. The fracture happens at a lower strain, caused by the hindrance of the plastic deformation, including hindered chain alignment and therefore strain-hardening.

With a further increased MWCNT concentration of 2.5 wt%, the mechanical properties have changed significantly. The composite shows a strongly decreased elongation at break with a largely decreased capability for plastic deformation. Further, the required stress for the plastic deformation until fracture is on the level of 2.0 wt%. The MWCNT distribution in a network

should be more pronounced, because the electrical conductivity is one order of magnitude higher for 2.5 wt%, but it can also be assumed that at the same time the number and size of MWCNT agglomerates is increased.

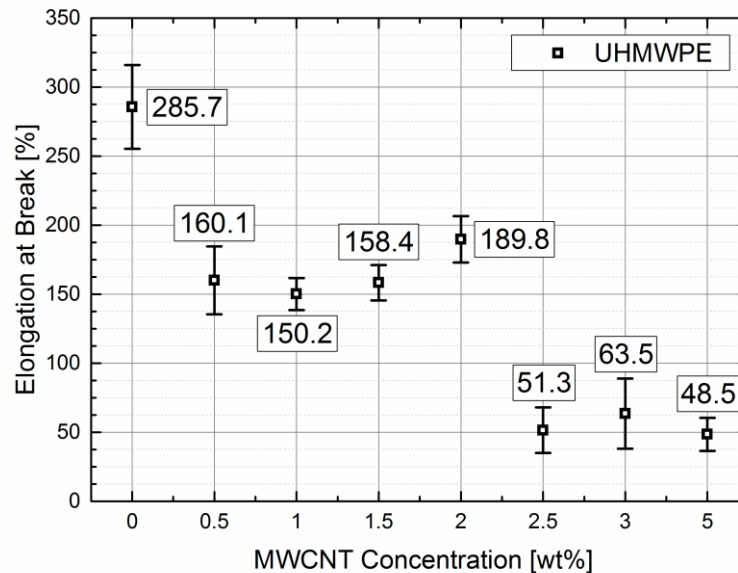


Figure 125: Elongation at break of pristine UHMWPE and UHMWPE/MWCNT. The value is significantly higher for pristine UHMWPE compared to any MWCNT concentration. Generally, an increase of MWCNT with effective concentration leads to a decreasing ability of the composite for plastic deformation, as 1.0, 3.0 and 5.0 wt% show. Less effective decoration leads higher elongation values, as more of the matrix is less influenced by the MWCNT concentration.

This trend would be the same as for 3.0 wt% and 5.0 wt%, in which a much higher electrical conductivity was found, but also numerous agglomerates that can be in the order of 100 μm large. The MWCNT agglomerates are relatively loose bundles, comparable to a fine non-woven, which means that their mechanical strength is very low compared to the polymer matrix or individual MWCNT. Their size is significant compared to the dimension of the samples of 2 mm thickness and 4 mm width. This means they can act as local weak spots with a wide ranging influence in the cross section of the tensile testing sample. The failure of the composites around the MWCNT agglomerates would explain the significantly reduced elongation at break for 2.5 wt% and higher.

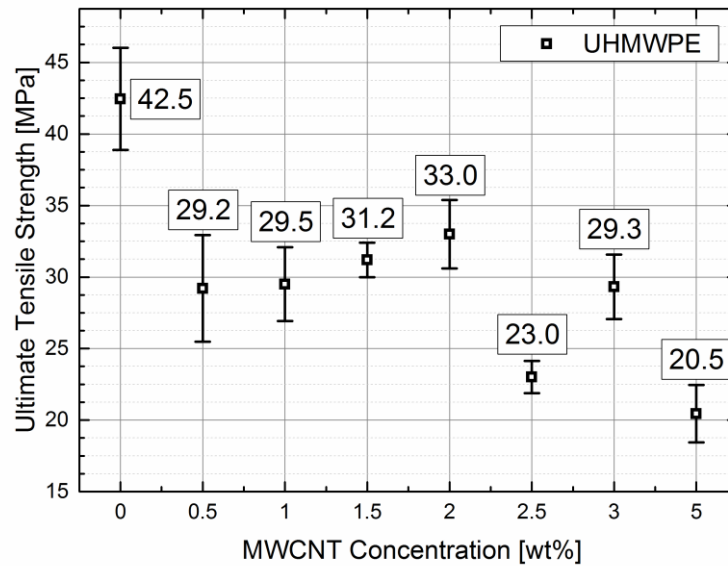


Figure 126: Ultimate tensile strength for pristine UHMWPE and UHMWPE/MWCNT. The values are generally lower for UHMWPE/MWCNT, as MWCNT limit the capability of the polymer matrix for strain hardening and additionally for some samples lead to a slight necking before fracture. The necking leads to a slightly lower stress value at fracture compared to UHMWPE, which elongates significantly and ruptures without noticeable necking.

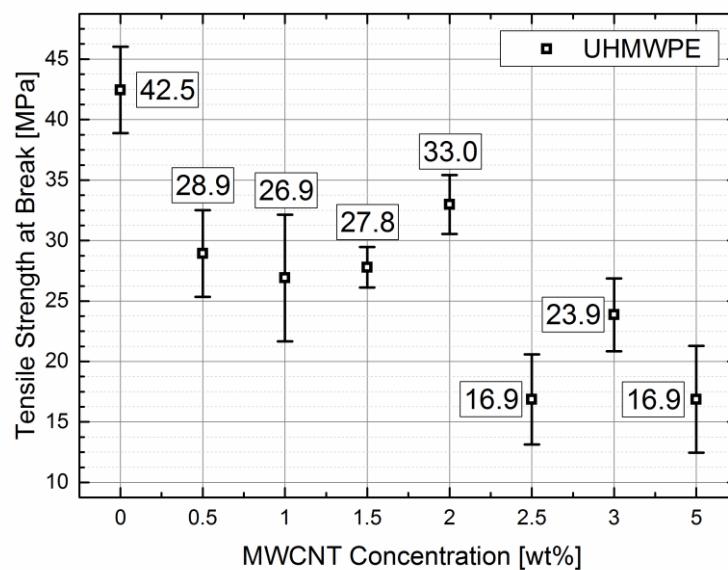


Figure 127: Tensile strength at break for pristine UHMWPE and UHMWPE/MWCNT. The behaviour depending on the MWCNT concentration is analogue to the ultimate tensile strength (**Figure 126**) with slightly different values for some MWCNT concentrations, as some samples showed neck formation and broke at lower stress values than the ultimate tensile strength.

The MWCNT concentration at 5.0 wt% is separated in one property from 2.5 wt% and 3.0 wt%, because the Young's modulus is at the level of pristine UHMWPE and UHMWPE/MWCNT 2.0 wt%. The concentration of 5.0 wt% shows the highest electrical conductivity, most decorated powder particles in SEM and the lowest elongation at break. It can therefore not be assumed, that the Young's modulus of UHMWPE matrix dominates the

elastic range. Rather it is more likely that the number and size of MWCNT agglomerates is counteracting the elastic interactions of the individual MWCNT, decreasing the Young's modulus to a comparable value.

It is clearly visible from the graphs **Figure 124** to **Figure 127** that the samples are separated into two groups for the Young's modulus and three groups for the other properties. As mentioned above, the addition of MWCNT increases the elastic properties of the composite, while the large agglomerate presence in 2.0 wt% and 5.0 wt% does not lead to an increased Young's modulus.

Further, with MWCNT concentrations between 1.0 wt% and 2.0 wt% the elongation at break, ultimate tensile strength and tensile strength at break are reduced comparatively. Additionally, 3.0 wt% is in the same group, except for elongation at break. The better distribution of the MWCNT in the powder and therefore matrix for 3.0 wt% allow for higher necessary stresses to break the sample, but do not increase the maximum possible elongation. Ultimate tensile strength and tensile strength at break are even further reduced for 2.5 wt% and 5.0 wt%, as the MWCNT concentration is increased but also less well distributed than for 3.0 wt%. Larger numbers of agglomerates do not allow for more resistance of the material against the tensile force near the maximum elongation.

As expected, UHMWPE shows a significant capability of strain hardening and elongation until fracture. With the addition of MWCNT in the efficient MWCNT concentrations of 1.0 wt% and 3.0 wt%, the Young's modulus is significantly increased at the cost of a lower value for elongation at break, lower ultimate tensile strength and lower tensile strength at fracture, caused by the reduced capability for strain hardening. The addition of MWCNT was therefore found to strengthen the initial elastic resistance against an external force, but also reduces the capability for plastic deformation and polymer chain alignment for strain hardening. From the measurements, 5.0 wt% it was found to be an insufficient concentration for the mechanical properties, even though it provides the highest electrical conductivity values.

7. Summary

A segregated network of multi-walled carbon nanotubes (MWCNT) spanning a polymer matrix offers the most promising approach for high electrical conductivity values combined with an efficient use of MWCNT concentrations.

The aim of this work was to investigate the production of electrically conductive composites with a segregated MWCNT network through the use of MWCNT decorated polymer powder particles. The focus was on open-porous samples with appropriate characteristics for microfiltration membranes, produced through pressureless sintering. Compression moulding was also performed to produce non-porous composites and additionally investigate the influence of the processing methods on the formation and quality of the resulting MWCNT network.

The decorated powder was received from the project partner FutureCarbon GmbH and processed at the Institute of Polymer Research of Helmholtz-Zentrum Geesthacht. Decorated powders with MWCNT concentrations of 0.2 wt% to 3.0 wt% were investigated for polyetherimide (PEI) with the addition of results for a first-phase, larger test powder at 5.0 wt%. Ultra-high molecular weight polyethylene (UHMWPE) with MWCNT concentrations of 0.2 wt% up to 5.0 wt% was processed and analysed. For polypropylene (PP), only the concentration of 5.0 wt% was used for two different particle size contingents.

The polymers varied in material properties and powder particle sizes and shapes. Investigations on the received decorated powders showed that the results of the decoration process appear to strongly depend on the powder properties. The effectiveness of the decoration process is characterised by the surface-coverage of the powder particles with MWCNT and the amount, size and localisation of MWCNT agglomerates. Results from scanning electron microscope (SEM) investigations showed that the different powders were decorated with varying effectiveness, depending on their specific characteristics. The hard amorphous polyetherimide was effectively decorated for all concentrations, while the smaller, less dense and softer UHMWPE showed an unexpected, strong dependency of the effectiveness of the powder particle decoration on the MWCNT concentration. The also soft polypropylene was effectively decorated with MWCNT, due to its larger powder particle diameters.

MWCNT agglomerates were numerous for polyetherimide, but they were relatively small compared to the powder particles, located in cracks and grooves and attached to the powder

particles. The same was observed for polypropylene, with the MWCNT being attached to the powder particles predominantly at irregularities of the surface structure. The surface of the UHMWPE particles also showed prominent grooves and gaps, but the MWCNT agglomerates did not form predominantly at the powder particles, but rather away from them as unbound agglomerates, comparable to or much larger than the powder particles in size, depending on the MWCNT concentration. A competitive process between surface-coverage by individual MWCNT on the powder particles and the formation of agglomerates away from the particle surfaces was assumed from the observation of the decorated powders through SEM investigations.

The applied pressureless sintering process was developed to accompany the changed sintering behaviour of the decorated powder for polyetherimide. The process was also adapted for UHMWPE and the decorated powder. The challenge was to provide enough driving force to the fusion process of the powder particles and to keep the cohesion of the green body intact during the thermal expansion of powder particles, while also allowing for enough control to acquire an open porous structure. Simpler sintering processes were found to produce samples with fractures or defects with the decorated powders.

In contrast, compression moulding could be performed for all powders without adaptations of the process itself and only through adaptations in applied external pressure, temperature and time.

The effectiveness of the decoration process and therefore powder quality proved to be a strong influence on the electrical and mechanical properties of the processed composite material. The electrical conductivity of PEI/MWCNT showed a predictable dependency on the MWCNT concentration with significantly increasing values with increasing concentration. For PP, it was found that the larger powder particles provided the highest electrical conductivity value, due to them possessing less surface area per weight compared to the smaller particles. At the same MWCNT concentration of 5.0 wt%, the surface concentration was therefore higher for the larger powder particle contingent of PP. From the results for PP and PEI, it was found that a larger surface coverage directly lead to a higher electrical conductivity value. Because of this, a better developed MWCNT network can be assumed.

This explains the strong deviation in electrical conductivity values between the MWCNT concentrations for UHMWPE. While 1.0 wt%, 3.0 wt% and 5.0 wt% showed a significant coverage of the powder particles surfaces in scanning electron micrographs, 0.2 wt%, 0.5 wt%

and 1.5 wt% to 2.5 wt% showed particles with fully non-covered or only partially covered parts of their surface. These powders therefore show significantly lower conductivity values compared to the powders with 1.0 wt%, 3.0 wt% and 5.0 wt% MWCNT.

The sintered membranes for PEI and UHMWPE showed water-permeable, open-porous structures. Analysis of the pore sizes through capillary flow porometry showed that the mean flow pore diameter for pristine PEI and for PEI/MWCNT up to a MWCNT concentration of 1.5 wt% was above ($> 10 \mu\text{m}$) the values expected for microfiltration membranes, while 2.0 wt% to 3.0 wt% were in an appropriate diameter range ($< 10 \mu\text{m}$). Because of their smaller particle diameter, UHMWPE and UHMWPE/MWCNT showed the smallest mean pore flow diameters between 1 and 4 μm . The pure water permeability was in a very high value range between 40,000 (pristine UHMWPE) and 400,000 $\text{L h}^{-1} \text{m}^{-2} \text{bar}^{-1}$ (pristine PEI with the largest pores).

For PEI and UHMWPE, differences in the electrical conductivity of sintered samples compared to compression moulded ones were found. For UHMWPE, the compression moulded samples were generally more conductive with the highest value of up to 2.75 S/m for 5.0 wt%, while the sintered samples reached a maximum of 1.61 S/m . In comparison, the sintered samples for PEI were generally more conductive than the compression moulded ones with one exception. The sintered samples reached 2.28 S/m at the maximum sinterable concentration of 3.0 wt%, while the compression moulded ones at 3.0 wt% reached 0.81 S/m . The exception was 5.0 wt% with the test powder with larger particle diameters around 500 μm . This powder could not be sintered but be compression moulded and achieved 8.23 S/m , which is significantly larger than for any other used material in this work. Relative to the other materials, PP at a MWCNT concentration of 5.0 wt% reached 2.54 S/m with the larger particle contingent. The smaller contingent was measured at 0.81 S/m .

Indications for the difference in the MWCNT network quality were investigated through ion-milling of representative samples to acquire a flat cut through the samples and investigate the cross sections with SEM and C-AFM. As expected from the electrical conductivity values, the MWCNT network shows better development in the compression moulded sample of UHMWPE/MWCNT 5.0 wt% than in the sintered one. The inverse case was found for PEI/MWCNT 3.0 wt%.

Differences in the mechanical properties of compression moulded samples was directly related to the MWCNT concentration and powder decoration quality. A higher concentration with good

decoration quality led to a stiffer composite with higher Young's modulus and reduced elongation at break.

From the comparison of the sintered samples to the compression moulded ones and between the different used powder particles, it was found that a high surface concentration and homogeneous surface coverage, together with a high melt viscosity, is desired for high conductivity values for compression moulded samples. For open porous membranes, smaller powder particles with high surface coverage but moderate melt viscosity are preferable. Additionally, an amorphous polymer is preferred to avoid influences of the crystallisation of the polymer matrix on the MWCNT network.

It was shown that the sintering and compression moulding of MWCNT-decorated polymer powder particles can produce composites with very high electrical conductivity values. The electrical conductivity results from a segregated MWCNT network distributed through the polymer matrix.

8. Outlook

The main focus of this work was the production of sintered membranes and the general processing of the decorated material through sintering and compression moulding. A large fraction of the effort was the sintering of the porous membranes, as the aim was a solvent-free processing, which excluded binding agents. A new approach had to be found for the production of flat membranes from a dry powder. The development time for the sintering limited the amount of time available for performable membrane characterisations and more sophisticated morphology approaches such as asymmetric particle diameter stacking. Further, the analysis of the anti-fouling properties requires dedicated experimental set-ups with enough adaptability for the different membrane dimensions.

Future research can therefore directly use the presented method and membrane types to characterise their filtration and/or anti-fouling performance. Because the produced membranes are depth-filters, an unconventional approach would be necessary. As depth-filters can filter material through surface adsorption, a charged membrane surface could enhance this effect. Hypothetically, the UHMWPE/MWCNT membranes could filter out certain bacteria such as *Escherichia coli* and the filtration performance may be enhanced by presenting an appropriately charged surface that attracts the bacteria. The filtered bacteria could then also be deactivated by destroying their membrane through electrochemical oxidation of their membrane, performed by a sufficiently positively charged membrane surface in water. This would be analogous to what Vecitis et al found for the depth-filtration of viruses at smaller pore scales, where an applied voltage improved the filtration performance for viruses and simultaneously deactivated them.^[9] This would prevent the formation of a biofilm inside of the membrane. It may also be possible to attract smaller particles with a high enough zeta potential to the appropriately charged membrane walls.

The decorated powder could also be combined with even smaller particles to decrease the permeable diameters in the pore channels. This concept is already widely used for filtration modules with activated carbon. A combination with activated carbon could also enhance the filtration performance and still preserve the properties associated with the electrical conductivity.

A change of the membrane geometry from a flat membrane towards a thicker cylindrical geometry would increase the filtration performance. With the achieved pore diameters and very high flux values, this approach would be feasible.

The research concerning electrically conductive membranes or filtration assemblies is still an emerging field of research with interesting possibilities and promising initial results. Because of possibilities to effectively combat fouling and biofouling, more approaches to diversify the material combinations, filler distributions and membrane/filter geometries are still desired.

9. Zusammenfassung

Ein gesondertes Netzwerk aus mehrwandigen Kohlenstoffnanoröhren (MWCNT), das durch eine Polymermatrix verläuft, stellt den vielversprechendsten Ansatz dar, um hohe elektrische Leitfähigkeiten verbunden mit effizienter Nutzung der MWCNT-Konzentration zu erreichen.

Das Ziel dieser Arbeit war die Untersuchung der Nutzung von MWCNT-dekorierten polymeren Pulverpartikeln zu Herstellung von elektrisch leitfähigen Kompositen mit einem gesonderten MWCNT-Netzwerk. Der Schwerpunkt lag auf offenporigen Proben, die durch druckloses Sintern hergestellt wurden, mit angemessenen Eigenschaften für Mikrofiltrationsmembranen. Ebenfalls durchgeführt wurde Formpressen, um porenfreie Komposite herzustellen und zusätzlich den Einfluss der Herstellungsmethode auf die Formierung und Qualität des resultierenden MWCNT-Netzwerkes zu untersuchen.

Das dekorierte Pulver wurde vom Projektpartner FutureCarbon GmbH erhalten und am Institut für Polymerforschung des Helmholtz-Zentrum Geesthacht verarbeitet. Dekorierte Pulver mit MWCNT-Konzentrationen zwischen 0,2 Gew.-% und 3,0 Gew.-% wurden für Polyetherimid (PEI) untersucht, ergänzt mit zusätzlichen Ergebnissen eines größeren Testpulvers mit 5,0 Gew.-% aus der ersten Phase. Ultra-hochmolekulares Polyethylen (UHMWPE) mit MWCNT-Konzentrationen zwischen 0,2 Gew.-% und 5,0 Gew.-% wurden verarbeitet und analysiert. Nur die Konzentration von 5,0 Gew.-% MWCNT wurde für zwei verschiedenen Größenkontingente von Polypropylen (PP) verwendet.

Die Polymere unterschieden sich in ihren Materialeigenschaften, Pulverpartikelgrößen und –formen. Untersuchungen an dem erhaltenen dekorierten Pulver zeigten, dass die Ergebnisse des Dekorationsprozesses stark von den Pulvereigenschaften abhängig zu sein schienen. Die Effektivität des Dekorationsprozesses zeichnet sich anhand der Oberflächenbedeckung der Pulverpartikel mit MWCNT und durch die Anzahl, Größe und Platzierung der MWCNT-Agglomerate aus. Ergebnisse aus rasterelektronenmikroskopischen Untersuchungen zeigten, dass die verschiedenen Pulver, abhängig von ihren spezifischen Eigenschaften, mit abweichender Effektivität dekoriert waren. Das harte, amorphe Polyetherimid war für alle MWCNT-Konzentrationen effektiv dekoriert worden, wohingegen das kleinere, weniger dichte und weichere UHMWPE eine unerwartete, starke Abhängigkeit der Effektivität der Pulverdekoration von der MWCNT-Konzentration zeigte. Das ebenfalls weiche Polypropylen war, aufgrund seiner größeren Partikeldurchmesser, effektiv dekoriert worden

MWCNT-Agglomerate waren zahlreich für Polyetherimid, aber in Relation zu den Pulverpartikeln klein, lokalisiert in Rissen und Furchen und an den Pulverpartikeln haftend. Das gleiche wurde für Polypropylen beobachtet, mit einer bevorzugten Lokalisierung der MWCNT an Unregelmäßigkeiten auf der Oberflächenstruktur. Die Oberfläche der UHMWPE-Partikel zeigten ebenfalls deutliche Furchen und Kluften, jedoch formten sich die MWCNT-Agglomerate nicht bevorzugt an den Pulverpartikeln, sondern stattdessen abseits von ihnen und als ungebundene Agglomerate, die, abhängig von der MWCNT-Konzentration in ihrer Größe vergleichbar oder deutlich größer waren als die Pulverpartikel. Ein konkurrierender Vorgang zwischen der Oberflächenbedeckung der Pulverpartikel durch individuelle MWCNT und der Formierung von Agglomeraten abseits der Pulverpartikel wurde aufgrund der Untersuchungen der dekorierten Pulver mittels Rasterelektronenmikroskop (SEM) angenommen.

Der angewendete drucklose Sinterprozess wurde entwickelt um dem veränderten Sinterverhalten des dekorierten Polyetherimidpulvers gerecht zu werden. Der Prozess wurde ebenfalls angepasst für UHMWPE und dessen dekorierten Pulvers. Die Herausforderung lag darin, genug treibende Kraft in den Verschmelzungsprozess der Pulverpartikel einzubringen und die Kohäsion des Grünkörpers während der thermischen Ausdehnung der Pulverpartikel intakt zu halten, sowie gleichzeitig ausreichende Kontrolle für die Erzeugung einer offenporigen Struktur zu erlauben.

Im Gegensatz hierzu konnte Formpressen für alle Pulver, ohne Anpassungen am Prozess selbst und nur durch Anpassungen des angewendeten externen Drucks, der Temperatur und der Zeit durchgeführt werden.

Die Effektivität des Dekorationsprozesses und somit der Pulverqualität stellte sich als starker Einfluss auf die elektrischen und mechanischen Eigenschaften der hergestellten Komposite heraus. Die elektrische Leitfähigkeit von PEI/MWCNT zeigte eine vorhersehbare Abhängigkeit von der MWCNT-Konzentration mit signifikant ansteigenden Werten mit ansteigender Konzentration. Für PP zeigte sich, dass die die größeren Pulverpartikel, aufgrund ihrer im Vergleich zu den kleineren Partikel geringeren Oberfläche pro Gewicht, die höchsten Werte der elektrischen Leitfähigkeit aufwiesen. Bei der gleichen MWCNT-Konzentration von 5,0 Gew.-% war somit die Oberflächenkonzentration des größeren Pulverpartikelkontingentes von PP höher. Aus den Ergebnissen für PEI und PP stellte sich heraus, dass eine höhere Oberflächenbedeckung direkt verbunden ist mit einer höheren elektrischen Leitfähigkeit. Deshalb kann ein besser ausgebildetes MWCNT-Netzwerk angenommen werden.

Dies erklärt die starken Abweichungen der Werte der elektrischen Leitfähigkeit zwischen den MWCNTN-Konzentrationen für UHMWPE. Während 1,0 Gew.-%, 3,0 Gew.-% und 5,0 Gew.-% eine deutliche Oberflächenbedeckung der Pulverpartikel zeigten, zeigten 0,2 Gew.-%, 0,5 Gew.-% und 1,5 Gew.-% bis 2,5 Gew.-% Partikel mit vollständig unbedeckten oder nur teilweise bedeckten Abschnitten auf den Oberflächen. Daher zeigten diese Pulver signifikant geringere elektrische Leitfähigkeitswerte als die Pulver mit 1,0 Gew.-%, 3,0 Gew.-% und 5,0 Gew.-% MWCNT.

Die gesinterten Membranen aus PEI und UHMWPE wiesen wasserdurchlässige, offenporige Strukturen auf. Die Analyse der Porengrößen mittels Kapillar-Flüssigkeits-Porometrie zeigte, dass der Durchmesser der mittleren Strömung für reines PEI und für PEI/MWCNT bis zu einer MWCNT-Konzentration von 1,5 Gew.-% über den Werten lag ($> 10 \mu\text{m}$), die von einer Mikrofiltrationsmembran erwartet werden, während 2,0 Gew.-% bis 3,0 Gew.-% in einem angemessenen Durchmesserbereich lagen ($< 10 \mu\text{m}$). Aufgrund ihrer kleineren Partikeldurchmesser zeigten UHMWPE und UHMWPE/MWCNT die kleinsten Durchmesser der mittleren Strömung mit Werten zwischen 1 und 4 μm . Die Permeabilität für reines Wasser lag in sehr hohen Wertebereichen zwischen 40.000 (reines UHMWPE) und 400.000 $\text{L h}^{-1} \text{m}^{-2} \text{bar}^{-1}$ (reines PEI).

Für PEI und UHMWPE wurden Unterschiede in der elektrischen Leitfähigkeit zwischen gesinterten und formgepressten Probekörpern festgestellt. Für UHMWPE waren die formgepressten Probekörper generell leitfähiger und mit bis zu 2,75 S/m bei 5,0 Gew.-%, während die gesinterten Proben maximal 1,61 S/m erreichten. Im Vergleich waren die gesinterten Probekörper für PEI generell leitfähiger als die formgepressten. Die gesinterten Probekörper erreichten bis zu 2,28 S/m bei der höchsten sinterbaren Konzentration von 3,0 Gew.-%, während die formgepressten Probekörper bei 3,0 Gew.-% 0,81 S/m erreichten. Die Ausnahme stellte das Testpulver mit 5,0 Gew.-% und Partikeldurchmessern um 500 μm dar. Dieses Pulver konnte nicht gesintert, jedoch formgepresst werden und erreichte 8,23 S/m, was signifikant höher ist als für jedes andere verwendete Pulver in dieser Arbeit. Im Vergleich zu den anderen Materialien erreichte PP mit 5,0 Gew.-% MWCNT einen Wert von 2,54 S/M mit dem größeren Pulverpartikelkontingent. Für das kleinere Kontingent wurde 0,81 S/m gemessen.

Die Anzeichen der Unterschiede der Qualität der MWCNT-Netzwerke wurde untersucht mittels Ionenätzung repräsentativer Probekörper um flache Schnitte durch die Probekörper zu erhalten und die Querschnittsflächen mittels SEM und Strom-Spannungs-Mikroskopie (C-AFM) zu untersuchen. Wie aus den Werten der elektrischen Leitfähigkeit erwartet wurde,

zeigte der formgepresste Probekörper für UHMWPE mit 5,0 Gew.-% eine bessere Ausbildung als der gesinterte. Der umgekehrte Fall wurde für PEI/MWCNT 3,0 Gew.-% festgestellt.

Der Einfluss der MWCNT auf die unterschiedlichen mechanischen Eigenschaften von formgepressten Probekörpern war direkt verbunden mit der MWCNT-Konzentration und der Qualität der Pulverdekorierung. Eine höhere Konzentration mit guter Dekorationsqualität führte zu einem steiferen Komposit mit höherem Elastizitätsmodul und verringerter Bruchdehnung.

Aus dem Vergleich zwischen den gesinterten und den formgepressten Probekörpern, sowie zwischen den unterschiedlichen Pulverpartikeln, wurde festgestellt, dass eine hohe Oberflächenkonzentration und homogene Oberflächenbedeckung, verbunden mit hoher Schmelzviskosität, vorteilhaft sind für hohe Leitfähigkeitswerten von formgepressten Probekörpern. Für offenporige Membranen sind kleinere Pulverpartikel mit hoher Oberflächenbedeckung und moderaterer Schmelzviskosität vorteilhaft. Zusätzlich sind amorphe Polymere vorteilhaft um den Einfluss der Kristallisation der Polymermatrix zu vermeiden.

Es wurde gezeigt, dass das Sintern und Formpressen von MWCNT-dekorierten Polymerpulverpartikeln Komposite mit sehr hohen elektrischen Leitfähigkeitswerten herstellen kann. Die elektrische Leitfähigkeit resultierte aus dem segregierten MWCNT-Netzwerk, das verteilt in der Polymermatrix vorliegt.

10. Acknowledgements

I would like to thank Prof. Dr. Volker Abetz for his support, the discussions we had and the kind supervision of my time as his PhD student. I also thank him for being the first evaluator of this thesis.

I thank Prof. Dr. Gerrit A. Luinstra for kindly agreeing to invest the time to be the second evaluator of this thesis.

I would also like to thank PD Dr. Ulrich A. Handge for his supervision as head of the department of material characterisation and processing, and the scientific discussions we had.

I am thankful to FutureCarbon GmbH, especially Dr. Ortrud Aschenbrenner and Juliane Kerwitz for providing and working on the decorated powder, as well as their contribution during the research project.

The financial support of the Arbeitsgemeinschaft industrieller Forschungsvereinigungen "Otto von Guericke" e.V. (AiF) is gratefully acknowledged (project number KF2176906WZ2).

I am grateful to Dr. Rainer Walkenhorst and Dr. Christian Ohm (Celanese Ticona GmbH) for providing the UHMWPE GUR[®] 2126, as well as to Dr. Dieter Langenfelder (LyondellBasell) for kindly providing the polypropylene Moplen[®] HF 500 H.

I thank Dr. Prokopios Georgopoulos for his friendship and support. The talks about work and other topics in a fresh, unrestrained way adorned the hard times and elevated the good ones.

My special gratitude goes to Dr. Maryam Radjabian who through her kind nature and curious mind always had time for interesting discussions about nearly any topic during break time and outside of work. From her I learned to be more patient, kind and overall to remember the aspiration to try and be a better person. The astounding supply of saffron and formed friendship will forever be appreciated.

Nils Müller has my thanks for his friendship in a resonating way which even these days in terms of a modern perspective on culture and humorous outlook is rarely found.

Clarissa Abetz I thank for her SEM measurements that were prominent for this work, her self-motivated input for improvements, offered suggestions and discussions.

Nina Beckmann is to be thanked for the joyous, cooperative and educational time we spent during her time as a master student.

To my family and friends from Saarland I will forever be grateful for their kindness and care about me.

Miepje and Benny as special beings with unconditional kindheartedness and offer of joy and comfort cannot be thanked enough.

I also thank Joachim Koll, Ivonne Ternes, Kristian Buhr, Daniel Tiemann, Zhenzhen Zhang and Anke-Lisa Metze for their support and overall good times.

11. Appendix

11.1. Results Tensile Testing

11.1.1. Polyetherimide

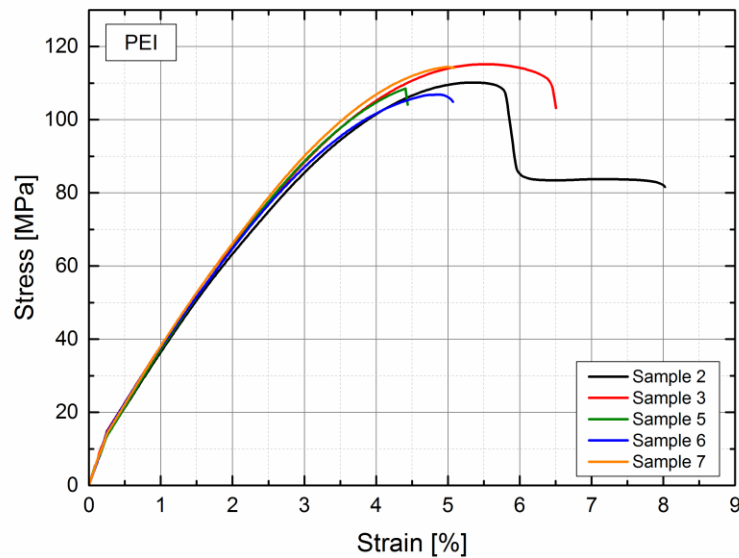


Figure 128: Stress-strain curves for all used measurements with listed PEI samples. Number gaps result from excluding faulty samples that were omitted due largely deviating results with visible defects after fracture. Sample 2 and 3 show a visible stress decrease during small neck formation. Other samples break at the onset of neck formation.

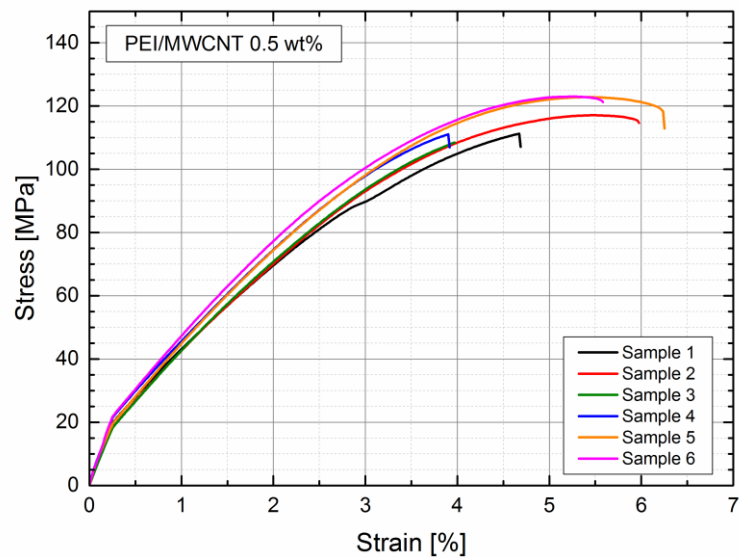


Figure 129: Stress-strain curves for all used measurements with listed PEI/MWCNT 0.5 wt% samples. Samples 2, 5 and 6 showed the onset of small neck formation.

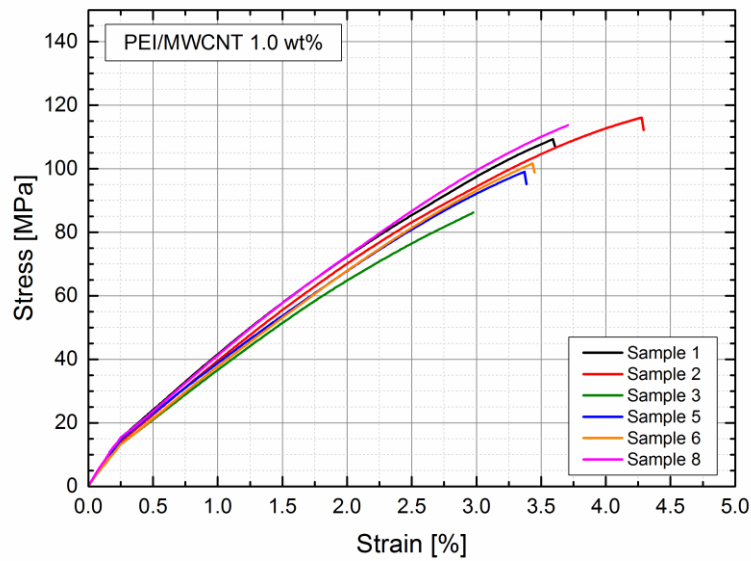


Figure 130: Stress-strain curves for all used measurements with listed PEI/MWCNT 1.0 wt% samples. Number gaps result from excluding faulty samples that were omitted due largely deviating results with visible defects after fracture. No samples show a necking region and show brittle behaviour.

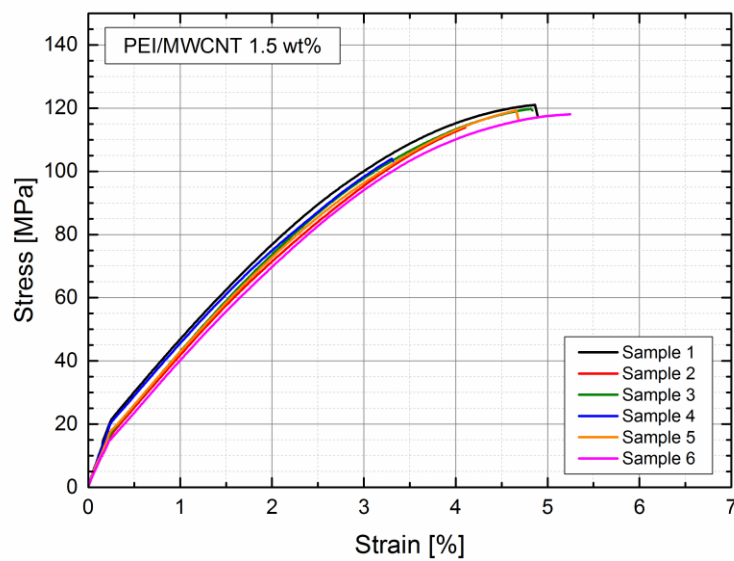


Figure 131: Stress-strain curves for all used measurements with listed PEI/MWCNT 1.5 wt% samples.

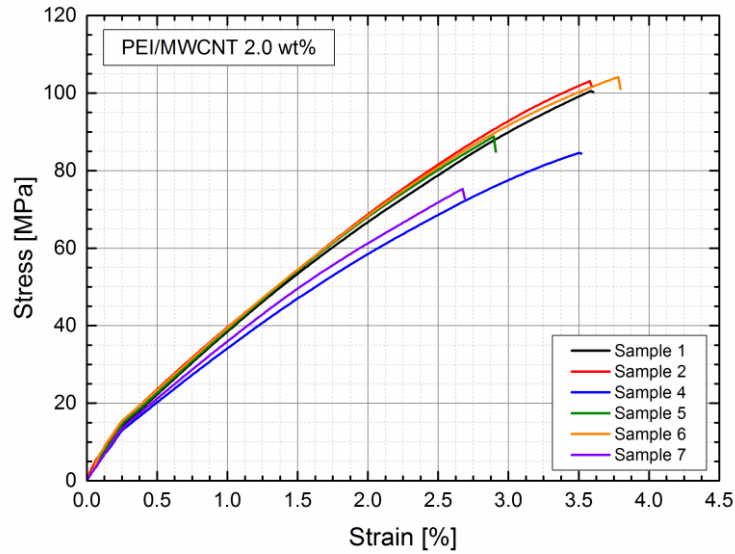


Figure 132: Stress-strain curves for all used measurements with listed PEI/MWCNT 2.0 wt% samples. Number gaps result from excluding faulty samples that were omitted due to largely deviating results with visible defects after fracture. No samples show a necking region and show brittle behaviour with a visible deviation between samples.

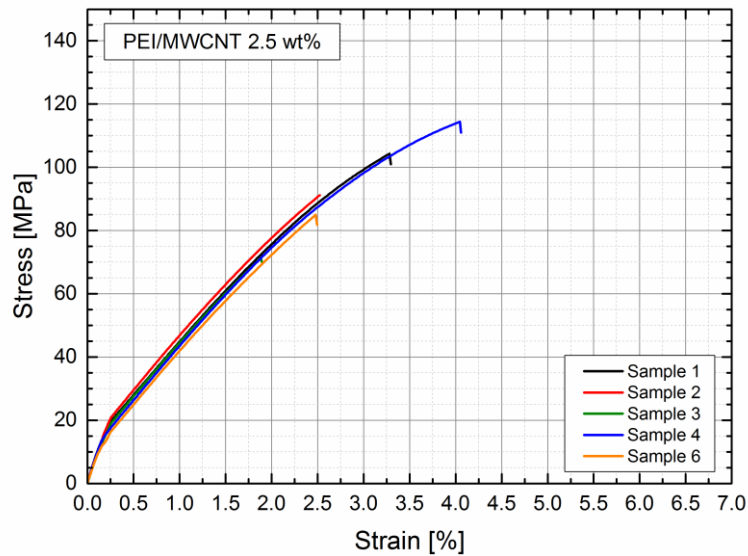


Figure 133: Stress-strain curves for all used measurements with listed PEI/MWCNT 2.5 wt% samples. Samples 2, 5 and 6 showed the onset of small neck formation.

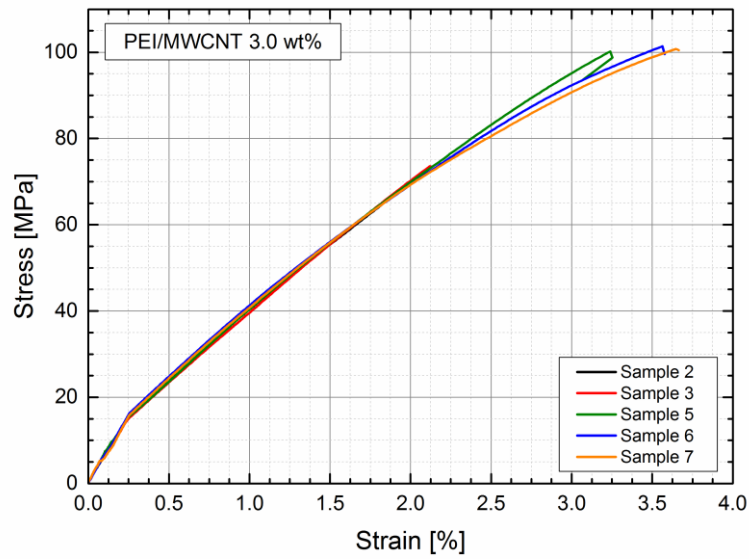


Figure 134: Stress-strain curves for all used measurements with listed PEI/MWCNT 3.0 wt% samples. Number gaps result from excluding faulty samples that were omitted due largely deviating results with visible defects after fracture. No samples show a necking region and show brittle behaviour with a visible deviation between samples.

11.1.2. Ultra-High Molecular Weight Polyethylene

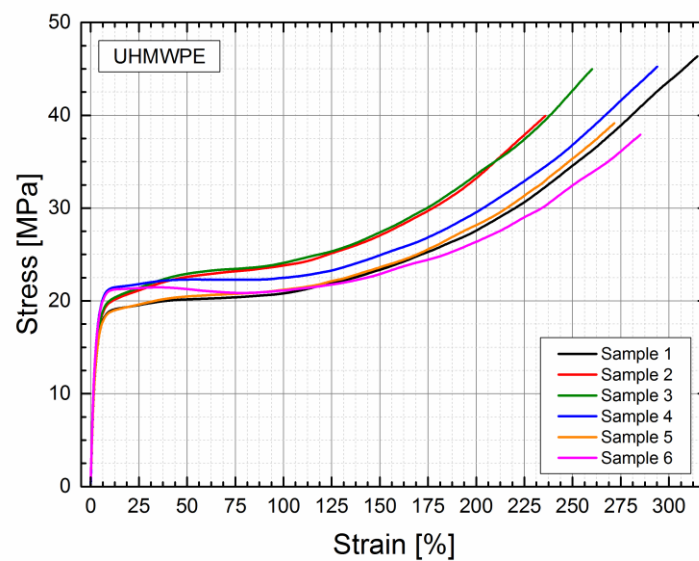


Figure 135: Stress-strain curves for all used measurements with listed UHMWPE samples. Samples show typical plastic deformation and strain hardening behaviour of UHMWPE.

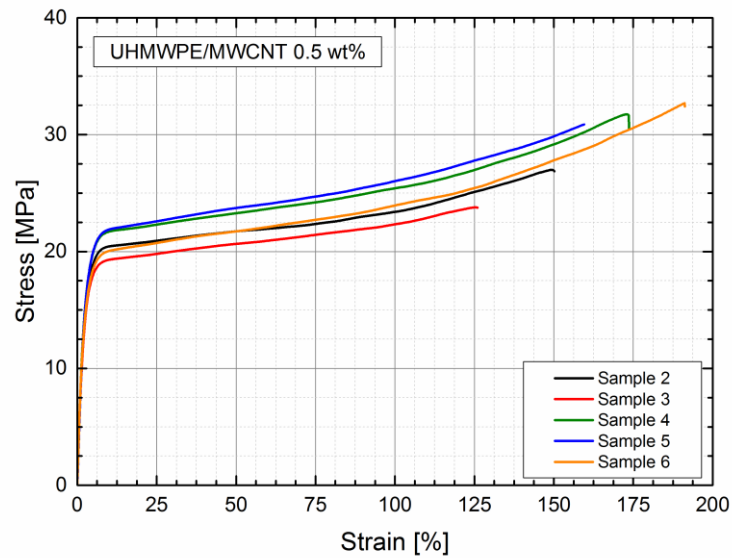


Figure 136: Stress-strain curves for all used measurements with listed UHMWPE/MWCNT 0.5 wt% samples. The addition of 0.5 wt% MWCNT results in a lowered capacity of the composite for plastic deformation. The strain-hardening region is significantly reduced compared to pristine UHMWPE.

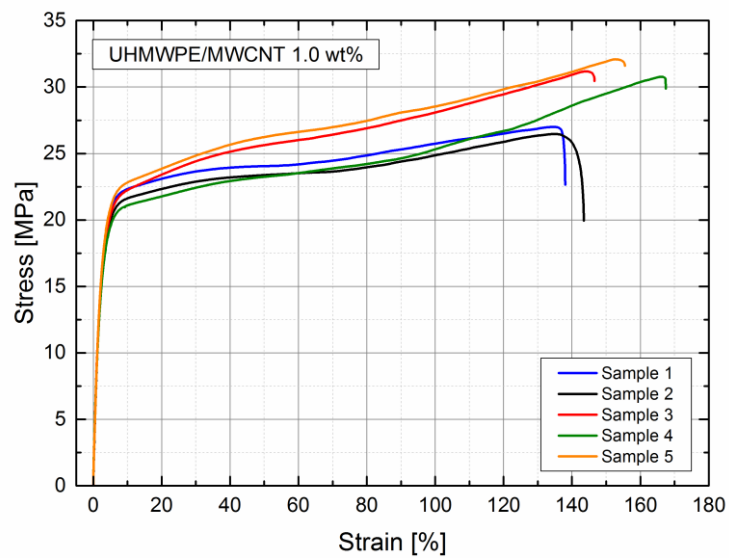


Figure 137: Stress-strain curves for all used measurements with listed UHMWPE/MWCNT 1.0 wt% samples. The addition of 1.0 wt% MWCNT results in a lowered capacity of the composite for plastic deformation. The strain-hardening region is significantly reduced compared to pristine UHMWPE.

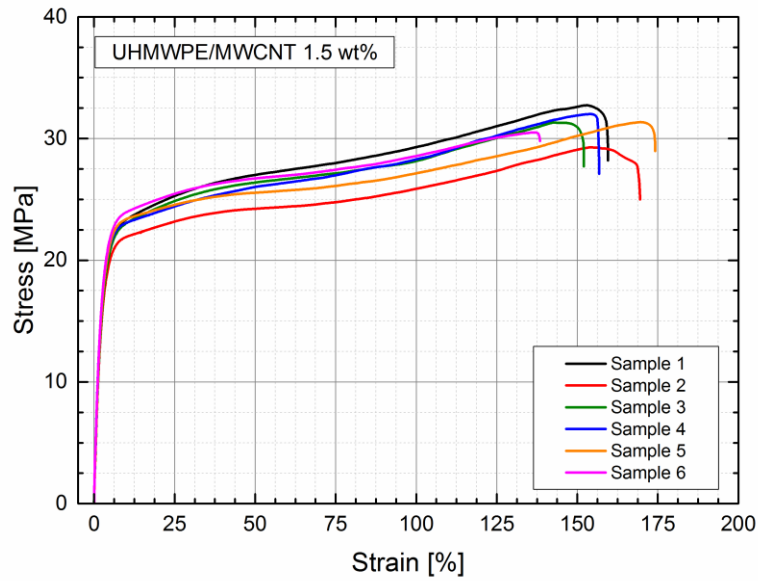


Figure 138: Stress-strain curves for all used measurements with listed UHMWPE/MWCNT 1.5 wt% samples. The plastic deformation and strain-hardening are reduced with significant similarity to UHMWPE/MWCNT 1.0 wt%.

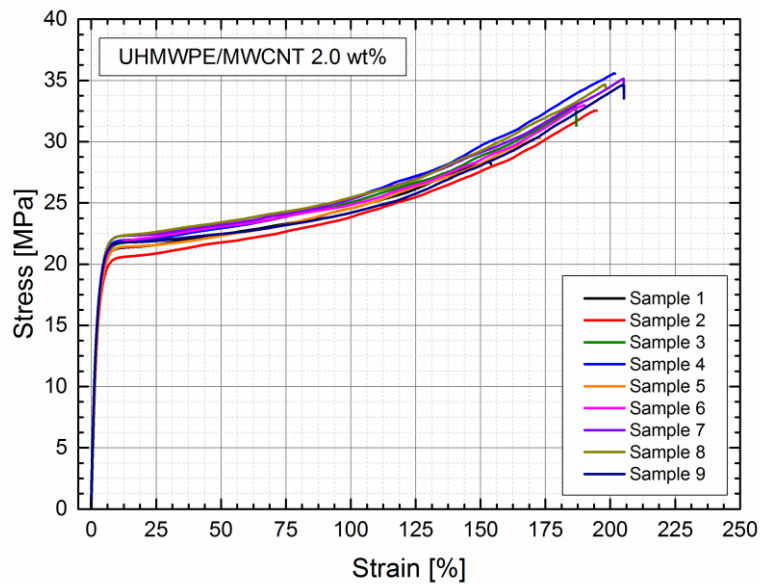


Figure 139: Stress-strain curves for all used measurements with listed UHMWPE/MWCNT 2.0 wt% samples. The samples show a significant similarity to pristine UHMWPE in terms of deformation and strain-hardening, compared to the other MWCNT concentrations. The reason for this is a greatly reduced covering of the compression moulded powder with MWCNT, as was shown with electric conductivity measurement and scanning electron micrographs.

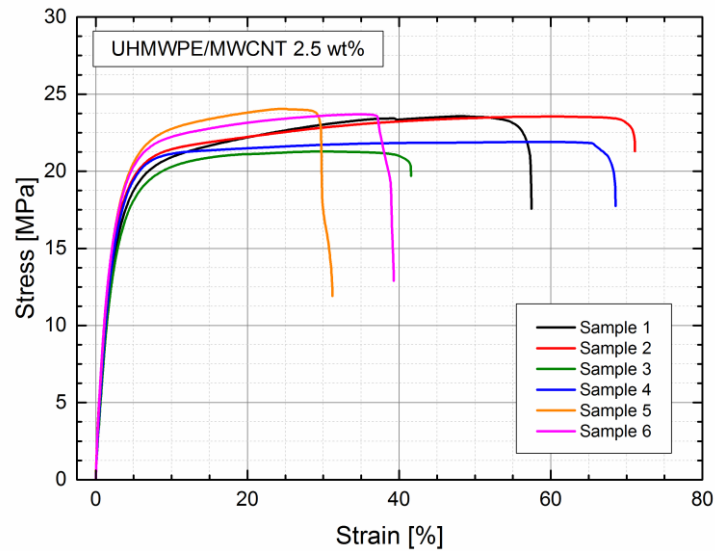


Figure 140: Stress-strain curves for all used measurements with listed UHMWPE/MWCNT 2.5 wt% samples. Compared to 2.0 wt%, here the influence of the MWCNT is significant. Large deviations between samples, a significantly reduced plastic deformation and a lack of strain-hardening can be seen. The deviation in the samples most likely results from fluctuations due to more pronounced MWCNT agglomerates in the decorated powder.

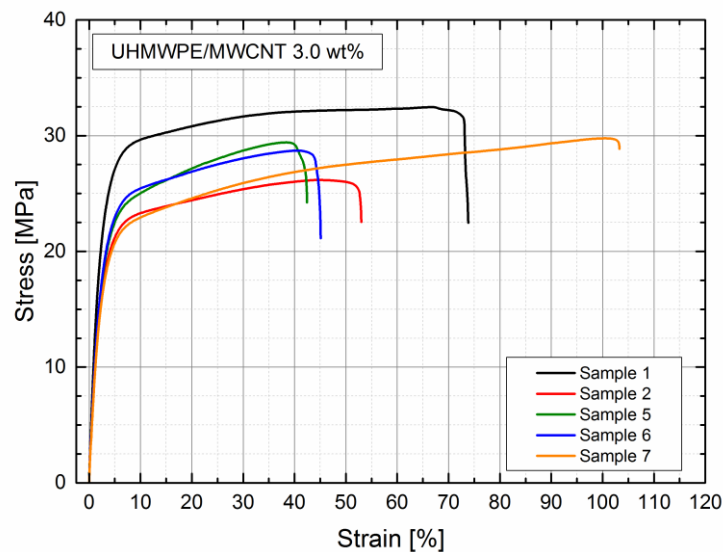


Figure 141: Stress-strain curves for all used measurements with listed UHMWPE/MWCNT 3.0 wt% samples. At this MWCNT concentration, large deviations between samples and a significantly reduced plastic deformation become visible. The deviation in the samples most likely results from fluctuations due to more pronounced MWCNT agglomerates in the decorated powder.

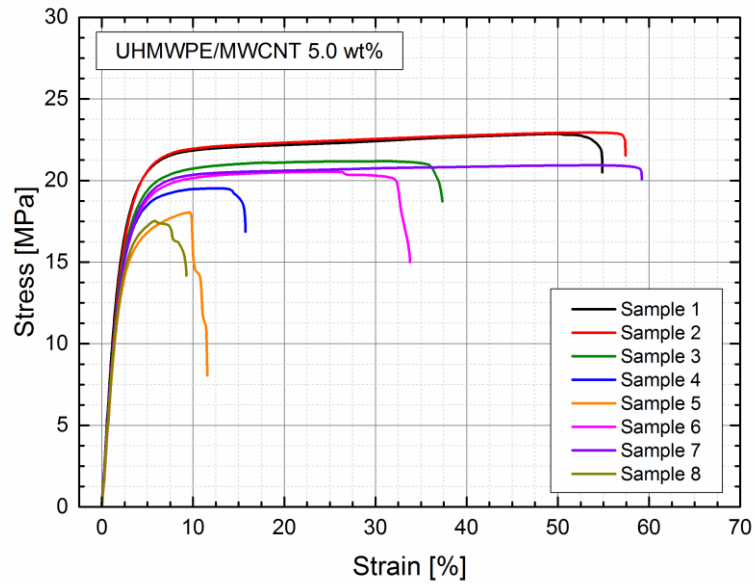


Figure 142: Stress-strain curves for all used measurements with listed UHMWPE/MWCNT 5.0 wt% samples. At this MWCNT concentration, significant deviations between samples and an immensely reduced plastic deformation become visible. At these MWCNT concentrations, strong particle coverage and agglomerates influence the mechanical behaviour.

12. References

- [1] United States Geological Survey, "Earth's Water Distribution", 2016.
- [2] V. K. Thakur, S. I. Voicu, *Carbohydrate Polymers* **2016**, *146*, 148.
- [3] R. W. Baker, "*Membrane Technology*", Wiley Online Library, 2000.
- [4] I. Koyuncu, R. Sengur, T. Turken, S. Guclu, M. Pasaoglu, A. Basile, A. Rastogi, *Advances in Membrane Technologies for Water Treatment: Materials, Processes and Applications* **2015**, 83.
- [5] M. E. Ersahin, H. Ozgun, R. K. Dereli, I. Ozturk, K. Roest, J. B. van Lier, *Bioresource Technology* **2012**, *122*, 196.
- [6] T. Nguyen, F. A. Roddick, L. Fan, *Membranes* **2012**, *2*, 804.
- [7] World Health Organization, "Fact Sheets - Antimicrobial Resistance ", 2016.
- [8] B. Zhu, X. Xia, N. Xia, S. Zhang, X. Guo, *Environmental Science & Technology* **2014**, *48*, 4086.
- [9] C. D. Vecitis, M. H. Schnoor, M. S. Rahaman, J. D. Schiffman, M. Elimelech, *Environmental Science & Technology* **2011**, *45*, 3672.
- [10] P. v Zumbusch, W. Kulcke, G. Brunner, *Journal of Membrane Science* **1998**, *142*, 75.
- [11] L. Liu, J. Liu, B. Gao, F. Yang, S. Chellam, *Journal of Membrane Science* **2012**, *394*, 202.
- [12] E. Celik, H. Park, H. Choi, H. Choi, *Water Research* **2011**, *45*, 274.
- [13] Z. Spitalsky, D. Tasis, K. Papagelis, C. Galiotis, *Progress in Polymer Science* **2010**, *35*, 357.
- [14] J. Mulder, "*Basic Principles of Membrane Technology*", Springer Science & Business Media, 2012.
- [15] W. Li, C. Kiser, Q. Richard, "Development of a filter cake permeability test methodology", in *American Filtration & Separations Society 2005 International Conferences & Exposition*, 2006, p. 6/57.
- [16] Y. Wu, Z. Yan, P. Wang, P. Luo, Y. Lin, *Journal of Applied Polymer Science* **2016**, *133*.
- [17] P. Bacchin, M. Meireles, P. Aimar, *Desalination* **2002**, *145*, 139.
- [18] H. Darcy, "*Les fontaines publiques de la ville de Dijon: Exposition et application*", Victor Dalmont, 1856.
- [19] T. Melin, R. Rautenbach, "*Membranverfahren: Grundlagen der Modul-und Anlagenauslegung*", Springer-Verlag, Berlin, 2007.
- [20] Y. Zhang, Y. Zhao, H. Chu, B. Dong, X. Zhou, *Chinese Science Bulletin* **2014**, *59*, 247.
- [21] T. Yang, B. Qiao, G.-C. Li, Q.-Y. Yang, *Desalination* **2015**, *363*, 134.

- [22] M. Padaki, R. S. Murali, M. Abdullah, N. Misdan, A. Moslehyani, M. Kassim, N. Hilal, A. Ismail, *Desalination* **2015**, 357, 197.
- [23] J. Dasgupta, J. Sikder, S. Chakraborty, S. Curcio, E. Drioli, *Journal of Environmental Management* **2015**, 147, 55.
- [24] K. Kimura, K. Tanaka, Y. Watanabe, *Water Research* **2014**, 49, 434.
- [25] J.-Y. Lee, C. Y. Tang, F. Huo, *Scientific Reports* **2014**, 4.
- [26] R. J. Gohari, E. Halakoo, W. J. Lau, M. A. Kassim, T. Matsuura, A. F. Ismail, *RSC Advances* **2014**, 4, 17587.
- [27] J. Prince, S. Bhuvana, K. Boodhoo, V. Anbharasi, G. Singh, *Journal of Membrane Science* **2014**, 454, 538.
- [28] X. Shi, G. Tal, N. P. Hankins, V. Gitis, *Journal of Water Process Engineering* **2014**, 1, 121.
- [29] W. Guo, H.-H. Ngo, J. Li, *Bioresource Technology* **2012**, 122, 27.
- [30] M.-W. Wan, F. Reguyal, C. Futralan, H.-L. Yang, C.-C. Kan, *Environmental Technology* **2013**, 34, 2929.
- [31] S. R. Gonzalez-Avila, F. Prabowo, A. Kumar, C.-D. Ohl, *Journal of Membrane Science* **2012**, 415, 776.
- [32] F. Carlesso, G. Zin, S. M. d. Souza, M. D. Luccio, A. A. d. Souza, J. V. Oliveira, *Environmental Technology* **2016**, 37, 952.
- [33] R. Vardanega, M. V. Tres, M. A. Mazutti, H. Treichel, D. de Oliveira, M. Di Luccio, J. V. Oliveira, *Bioprocess and Biosystems Engineering* **2013**, 36, 1087.
- [34] R. Hofmann, C. Posten, *Chemical Engineering Science* **2003**, 58, 3847.
- [35] R. Hofmann, T. K ppler, C. Posten, *Separation and Purification Technology* **2006**, 51, 303.
- [36] M. H.-O. Rashid, S. Q. Pham, L. J. Sweetman, L. J. Alcock, A. Wise, L. D. Nghiem, G. Triani, M. in het Panhuis, S. F. Ralph, *Journal of Membrane Science* **2014**, 456, 175.
- [37] L. F. Dum e, K. Sears, J. Sch utz, N. Finn, C. Huynh, S. Hawkins, M. Duke, S. Gray, *Journal of Membrane Science* **2010**, 351, 36.
- [38] L. Dum e, V. Germain, K. Sears, J. Sch utz, N. Finn, M. Duke, S. Cerneaux, D. Cornu, S. Gray, *Journal of Membrane Science* **2011**, 376, 241.
- [39] A. V. Dudchenko, J. Rolf, K. Russell, W. Duan, D. Jassby, *Journal of Membrane Science* **2014**, 468, 1.
- [40] C.-F. de Lannoy, D. Jassby, D. Davis, M. Wiesner, *Journal of Membrane Science* **2012**, 415, 718.
- [41] R. Hashaikeh, B. S. Lalia, V. Kochkodan, N. Hilal, *Journal of Membrane Science* **2014**, 471, 149.
- [42] Q. Zhang, C. D. Vecitis, *Journal of Membrane Science* **2014**, 459, 143.

- [43] W. Hu, S. Chen, Z. Yang, L. Liu, H. Wang, *The Journal of Physical Chemistry B* **2011**, *115*, 8453.
- [44] J. Huang, Z. Wang, J. Zhang, X. Zhang, J. Ma, Z. Wu, *Scientific reports* **2015**, *5*.
- [45] C. Gao, Z. Guo, J.-H. Liu, X.-J. Huang, *Nanoscale* **2012**, *4*, 1948.
- [46] P. J. F. Harris, "*Carbon Nanotube Science: Synthesis, Properties and Applications*", Cambridge university press, 2009.
- [47] S. Bellucci, *physica status solidi (c)* **2005**, *2*, 34.
- [48] M.-F. Yu, B. S. Files, S. Arepalli, R. S. Ruoff, *Physical Review Letters* **2000**, *84*, 5552.
- [49] M.-F. Yu, O. Lourie, M. J. Dyer, K. Moloni, T. F. Kelly, R. S. Ruoff, *Science* **2000**, *287*, 637.
- [50] D. Qian, G. J. Wagner, W. K. Liu, M.-F. Yu, R. S. Ruoff, *Applied Mechanics Reviews* **2002**, *55*, 495.
- [51] M. Kumar, Y. Ando, "*Carbon Nanotube Synthesis and Growth Mechanism*", INTECH Open Access Publisher, 2011.
- [52] J. Kong, C. Zhou, A. Morpurgo, H. Soh, C. Quate, C. Marcus, H. Dai, *Applied Physics A* **1999**, *69*, 305.
- [53] M. F. De Volder, S. H. Tawfick, R. H. Baughman, A. J. Hart, *Science* **2013**, *339*, 535.
- [54] R. K. A. Al-Rub, A. I. Ashour, B. M. Tyson, *Construction and Building Materials* **2012**, *35*, 647.
- [55] J. Guo, Y. Liu, R. Prada-Silvy, Y. Tan, S. Azad, B. Krause, P. Pötschke, B. P. Grady, *Journal of Polymer Science Part B: Polymer Physics* **2014**, *52*, 73.
- [56] P. Zhou, X. Yang, L. He, Z. Hao, W. Luo, B. Xiong, X. Xu, C. Niu, M. Yan, L. Mai, *Applied Physics Letters* **2015**, *106*, 111908.
- [57] G. Mittal, V. Dhand, K. Y. Rhee, S.-J. Park, W. R. Lee, *Journal of Industrial and Engineering Chemistry* **2015**, *21*, 11.
- [58] S. U. Khan, J. R. Pothnis, J.-K. Kim, *Composites Part A: Applied Science and Manufacturing* **2013**, *49*, 26.
- [59] S.-k. Hong, D. Kim, S. Lee, B.-W. Kim, P. Theilmann, S.-H. Park, *Composites Part A: Applied Science and Manufacturing* **2015**, *77*, 142.
- [60] N. G. Sahoo, S. Rana, J. W. Cho, L. Li, S. H. Chan, *Progress in Polymer Science* **2010**, *35*, 837.
- [61] V. Choudhary, B. Singh, R. Mathur, "*Syntheses and Applications of Carbon Nanotubes and their Composites*", InTech, 2013, p. 978.
- [62] W. Bauhofer, J. Z. Kovacs, *Composites Science and Technology* **2009**, *69*, 1486.
- [63] I. Alig, P. Pötschke, D. Lellinger, T. Skipa, S. Pegel, G. R. Kasaliwal, T. Villmow, *Polymer* **2012**, *53*, 4.
- [64] R. Rahman, P. Servati, *Nanotechnology* **2012**, *23*, 055703.

- [65] H. Pang, L. Xu, D.-X. Yan, Z.-M. Li, *Progress in Polymer Science* **2014**, *39*, 1908.
- [66] C. Yu, Y. S. Kim, D. Kim, J. C. Grunlan, *Nano Letters* **2008**, *8*, 4428.
- [67] Y. Zhan, M. Lavorgna, G. Buonocore, H. Xia, *Journal of Materials Chemistry* **2012**, *22*, 10464.
- [68] I. Jurewicz, P. Worajittiphon, A. A. King, P. J. Sellin, J. L. Keddie, A. B. Dalton, *The Journal of Physical Chemistry B* **2011**, *115*, 6395.
- [69] J.-F. Feller, J. Lu, K. Zhang, B. Kumar, M. Castro, N. Gatt, H. Choi, *Journal of Materials Chemistry* **2011**, *21*, 4142.
- [70] H. Pang, Y.-Y. Piao, C.-H. Cui, Y. Bao, J. Lei, G.-P. Yuan, C.-L. Zhang, *Journal of Polymer Research* **2013**, *20*, 1.
- [71] A. Mierczynska, M. Mayne-L'Hermite, G. Boiteux, J. Jeszka, *Journal of Applied Polymer Science* **2007**, *105*, 158.
- [72] G. Gorrasi, M. Sarno, A. Di Bartolomeo, D. Sannino, P. Ciambelli, V. Vittoria, *Journal of Polymer Science Part B: Polymer Physics* **2007**, *45*, 597.
- [73] M. Asgarpour, F. Bakir, S. Khelladi, A. Khavandi, A. Tcharkhtchi, *Journal of Applied Polymer Science* **2011**, *119*, 2784.
- [74] S.-J. L. Kang, "Sintering: Densification, Grain Growth and Microstructure", Butterworth-Heinemann, 2004.
- [75] J. E. Mark, "Physical Properties of Polymers Handbook", Springer, New York, 2007.
- [76] J. D. Muller, A. Maazouz, "Sintering of Polymers: Comprehension, Modeling and Application to Rotomolding Process", in *10th ESAFORM Conference on Material Forming*, AIP Publishing, 2007, p. 907/824.
- [77] A. Hamidi, S. Farzaneh, F. Nony, Z. Ortega, S. Khelladi, M. Monzon, F. Bakir, A. Tcharkhtchi, *International Journal of Material Forming* **2015**, *1*.
- [78] C. T. Bellehumeur, M. Kontopoulou, J. Vlachopoulos, *Rheologica Acta* **1998**, *37*, 270.
- [79] S. Mazur, D. J. Plazek, *Progress in Organic Coatings* **1994**, *24*, 225.
- [80] R. J. Farris, J. E. Morin, "Thermoset Recycling Methods and Solid Article Produced", United States Patent, 2003.
- [81] M. Ristić, S. Milošević, *Science of Sintering* **2006**, *38*, 7.
- [82] S.-J. Liu, *International Polymer Processing* **1998**, *13*, 88.
- [83] S. Hambir, J. Jog, *Bulletin of Materials Science* **2000**, *23*, 221.
- [84] O. Pokluda, C. T. Bellehumeur, J. Vlachopoulos, *AIChE Journal* **1997**, *43*, 3253.
- [85] T. Kraft, H. Riedel, *Journal of the European Ceramic Society* **2004**, *24*, 345.
- [86] M. Schmid, A. Amado, K. Wegener, "Polymer Powders for Selective Laser Sintering (SLS)", 30th International Conference of the Polymer Processing Society, 2014, Cleveland, Ohio, 2014.

- [87] D. L. Bourell, T. J. Watt, D. K. Leigh, B. Fulcher, *Physics Procedia* **2014**, *56*, 147.
- [88] R. J. Crawford, J. L. Throne, "*Rotational Molding Technology*", William Andrew, 2001.
- [89] X. Li, N. Wang, G. Fan, J. Yu, J. Gao, G. Sun, B. Ding, *Journal of Colloid and Interface Science* **2015**, *439*, 12.
- [90] Y. Zhang, R. Wang, *Journal of Membrane Science* **2014**, *452*, 379.
- [91] R. S. Hebbar, A. M. Isloor, A. Ismail, S. J. Shilton, A. Obaid, H.-K. Fun, *New Journal of Chemistry* **2015**, *39*, 6141.
- [92] Saudi Basic Industries Corporation (Sabic), "Material Data Sheet - Ultem™ 1000P".
- [93] S. Béland, "*High Performance Thermoplastic Resins and Their Composites*", William Andrew, 1990.
- [94] R. O. Johnson, H. S. Burlhis, "Polyetherimide: A new high-performance thermoplastic resin", in *Journal of Polymer Science: Polymer Symposia*, Wiley Online Library, 1983, p. 70/129.
- [95] PlasticsEurope, "Plastics – The Facts 2015 An Analysis of European Plastics Production, Demand and Waste Data ", 2015.
- [96] S. M. Kurtz, "*The UHMWPE Handbook: Ultra-High Molecular Weight Polyethylene in Total Joint Replacement*", Academic Press, 2004.
- [97] Celanese Corporation, "Material Data Sheet - GUR® 2126".
- [98] Braskem, "UTEC - Ultra High Molecular Weight Polyethylene (UHMWPE)", 2013.
- [99] Quadrant AG, "Material Data Sheet TIVAR® 1000".
- [100] N. Beckmann, "Polypropylen-Nanokomposit auf Basis von MWCNT-dekorierten Polymerpulverpartikeln: Verarbeitung und Charakterisierung", Hochschule Wismar, Ed., 2015.
- [101] R. Strapasson, S. Amico, M. Pereira, T. Sydenstricker, *Polymer Testing* **2005**, *24*, 468.
- [102] Ineos Group Limited, "Typical Engineering Properties of Polypropylene", Datasheet, 2014.
- [103] S. D. Forero, FutureCarbon GmbH, "Leitfähiges Polymer-Komposit sowie Verfahren zu dessen Herstellung", Deutsches Patent- und Markenamt, Patent Number DE102010013210A1, Germany, 2011.
- [104] G. Mennig, K. Stoeckhert, "*Mold-Making Handbook*", Carl Hanser Verlag GmbH & Company KG, Munich, 2013.
- [105] F. M. Mirabella, A. Bafna, *Journal of Polymer Science Part B: Polymer Physics* **2002**, *40*, 1637.
- [106] C. Vasile, "*Handbook of Polyolefins*", CRC Press, New York, 2000.
- [107] H. Münstedt, *J Rheol* **2014**, *58*, 565.

-
- [108] S. Bakshi, J. Tercero, A. Agarwal, *Composites Part A: Applied Science and Manufacturing* **2007**, *38*, 2493.
- [109] T. McNally, P. Pötschke, P. Halley, M. Murphy, D. Martin, S. E. Bell, G. P. Brennan, D. Bein, P. Lemoine, J. P. Quinn, *Polymer* **2005**, *46*, 8222.
- [110] D. Olmos, C. Dominguez, P. Castrillo, J. Gonzalez-Benito, *Polymer* **2009**, *50*, 1732.
- [111] A. Maksimkin, S. Kaloshkin, V. Tcherdyntsev, D. Chukov, I. Shchetinin, *Journal of Applied Polymer Science* **2013**, *130*, 2971.
- [112] A. Romankiewicz, T. Sterzynski, W. Brostow, *Polymer international* **2004**, *53*, 2086.
- [113] P. Pötschke, T. D. Fornes, D. R. Paul, *Polymer* **2002**, *43*, 3247.
- [114] O. Valentino, M. Sarno, N. G. Rainone, M. R. Nobile, P. Ciambelli, H. C. Neitzert, G. P. Simon, *Physica E* **2008**, *40*, 2440.

Curriculum Vitae

Personal Details

Name Christian Otto
Date of Birth 30.12.1985 in Saarlouis
Nationality German

Education

Since 05/2013 **Doctorate** for the degree of Dr. rer. nat., University of Hamburg, MIN-Faculty, supervisor: Prof. Dr. V. Abetz

2012 – 2013 **Diplomarbeit**, *Lehrstuhl für Adhäsion und Interphasen in Polymeren, Universität des Saarlandes*
„Abscheidung von organischen Monomeren auf nativen Metalloberflächen“

2006 – 2013 **Dipl.-Ing der Werkstoffwissenschaft**, *University of Saarland*; Major: Non-Metals

1996 – 2005 **Allgemeine Hochschulreife**, *Albert-Schweitzer-Gymnasium, Dillingen*

List of Publications

Christian Otto, Ulrich A. Handge, Ortrud Aschenbrenner, Juliane Kerwitz, Clarissa Abetz, Volker Abetz,

Solvent-Free Preparation of Electrically Conductive Polyetherimide Membranes Using Carbon Nanotubes

Macromolecular Materials and Engineering 2015; (300) 12: 1246 – 1256.

(DOI 10.1002/mame.201500088)

Christian Otto, Ulrich, A. Handge, Prokopios Georgopoulos, Ortrud Aschenbrenner, Juliane Kerwitz, Clarissa Abetz, Anke-Lisa Metze, Volker Abetz,

Porous UHMWPE Membranes and Composites Filled with Carbon Nanotubes: Permeability, Mechanical and Electrical Properties

Macromolecular Materials and Engineering

(DOI 10.1002/mame.20160040)

Christian Otto, Ulrich A. Handge, Volker Abetz, Ortrud Aschenbrenner,

Sintering method, sintering product, filtration module and use

European Patent, EP 2982492

Safety Hazards

Table 11: Safety instructions and hazardousness of used chemicals and materials

| Material | GHS-Symbol | H-Phrases | P-Phrases |
|-----------------------------------|--------------|---|---|
| Multi-Walled Carbon Nanotubes | GHS07 | H319, H335 | P233, P261, P402, P403, P404 |
| Chloroform (as cleaning agent) | GHS07, GHS08 | H302, H331, H315, H319, H336, H351, H361d, H372 | P202, P260, P280, P305 + P351 + P338 |
| Ethanol | GHS02, GHS07 | H225, H255, H319 | P210, P233, P241, P243, P305 + P351 + P338 |
| Acetone (as cleaning agent) | GHS02, GHS07 | H225, H319, H336, EUH066 | P241, P243, P305 + P351 + P338, P403 + P235 |
| Polyethylene | - | - | - |
| Polypropylene | - | - | - |
| Polyetherimide | - | - | - |

Eidesstattliche Versicherung

Hiermit erkläre ich an Eides statt, dass ich die vorliegende Arbeit selbst verfasst habe und keine anderen Hilfsmittel als in der Arbeit angegeben verwendet habe. Diese Arbeit wurde nie in irgendeiner Form an anderer Stelle zur Prüfung eingereicht. Kein anderes Promotionsverfahren wurde an anderer Stelle versucht oder durchgeführt.

Statement in Lieu of an Oath

I hereby declare in lieu of an oath that I have written this thesis on my own and that I have not used any other resources or aids than the ones referred to in this thesis. This thesis has never been submitted in any form for any other examination. No other doctorate was attempted or pursued at a different location.

Christian Otto